Development of bond coat alloy(s) for Ni based superalloys for low emission gas turbine technology for H_2 rich Syngas

Eleftheria Karagianni

Department of Materials Science and Engineering

The University of Sheffield

Thesis submitted for the degree of Doctor of Philosophy

June 2015

"Dedicated to the memory of my beloved partner, Dr D. Myriounis"

"Αφιερωμένο στη μνήμη του πολυαγαπημένου μου συντρόφου, του Δημήτρη μου"

Table of contents

ACKNOWLEDGEMENTS

At this point, I would like to thank my family for their valuable support at every level. I have a real debt of gratitude to my parents and my sister for their unremitting zeal and helpfulness and for standing by me, especially towards the end of this thesis. Also a very special thanks to my beloved partner, Dimitris, who was the one who helped me love my science, who initiated me to start a PhD and helped me be committed to it and realize the joy of the experiment. Many thanks to my dearest friends and my university colleagues (Mr Jack Nelson, Mr Andrew Tweddle and Mr Gary Bywater) for helping and encouraging me to achieve my goals and realize my ambitions. I hope to give them more joy and happiness in the future. Finally, I would like to thank my supervisor Professor Panos Tsakiropoulos who truly believed in me all these years and for giving me the chance to start fulfilling my dreams.

Abstract

This thesis describes the research performed as part of the materials package of the FP7 project H2-IGCC to design, develop and evaluate new bond coat (BC) alloys that form in situ alumina oxide scales. Literature on bond coat alloys and processing techniques used for Ni based superalloys is reviewed. The experimental techniques used to prepare and characterise the alloys of this research are described. Five NiCrCoAl based bond coat type alloys, namely Ni-23Co-20Cr-8.5Al (EK1), Ni-23Co-20Cr-8.5Al-4Ta (EK2), Ni-23Co-20Cr-8.5Al-4Ta-0.6Y (EK3), Ni-23Co-20Cr-8.5Al-4Ta-0.6Y-0.8Hf (EK4) and Ni-23Co-20Cr-8.5Al-4Ta-0.6Y-0.8Hf-2Si (EK5) (wt%), were studied in the as cast, heat treated (1200 °C) and oxidised (975 °C in air) conditions.

The γ-Ni_{ss} and β-NiAl phases were stable in all the alloys. The synergy of Ta and Y and of Ta, Y and Si enhanced the stability of the γ'-Ni_3Al. The addition of Y stabilised Y containing intermetallics. The $\gamma + \beta$ eutectic was not observed in the alloys EK3 and EK5, which would suggest that Y and Si suppress its formation. During solidification the formation of the γ-Ni_{ss} and β-NiAl was accompanied respectively by partitioning of Al, Si and Ta to the melt, and Co, Cr, Si and Ta to the melt and Al to the β-NiAl. The partitioning of Al and Co between the γ-Ni_{ss} and β-NiAl was not changed by the synergies of different alloying elements however the partitioning of Cr to the γ-Ni_{ss} was increased by the synergy of Ta and Y and Ta, Y and Si. The alloying with Ta resulted to the highest Al + Cr and Cr contents in Ni_{ss} and NiAl in the as cast condition and this was maintained after heat treatment. The Al + Cr content in the $\gamma + \beta$ eutectic was essentially the same in the three alloys where the eutectic was formed but the Al/Cr ratio increased dramatically when the Ta was in synergy with Hf. Alloying with Ta had a dramatic effect on the volume fractions of γ-Ni_{ss} and β-NiAl. In the as cast condition the vol% of the β-NiAl was higher than the vol% of the γ-Ni_{ss} in the alloys EK2 and EK5, suggesting that alloying with Y and Hf tends to favour the γ-Ni_{ss} rather than the β-NiAl. There were changes in the vol% of the aforementioned phases after the heat treatment, with the vol% of the β-NiAl increasing in all alloys. The higher vol% of β-NiAl was still observed in the alloys EK2 and EK5. The addition of Si enhanced chemical inhomogeneities in the microstructure and there was formation of Si and Y rich areas in the solidified microstructure where Ta and Hf had also partitioned. After heat treatment the formation of intermetallic phases in those areas was accompanied by severe micro-cracking in the microstructure and internal oxidation.

Oxidation benefited from the reactive element addition(s). With the addition of reactive elements a significant amount of Al outward transport was reduced. Alloying with Si did not improve the oxidation rate and increased the depth below the scale where internal oxidation occurred. The "effectiveness" of reactive elements was compromised when the latter were simultaneously in synergy with Ta. The Ni_{ss} and NiAl respectively were the main supplier of Al and Cr for the growth of the scale. Overall, the "best" oxidation behaviour was exhibited by the alloy that tended to form equal volume fractions of γ-Ni_{ss} and β-NiAl, i.e., the alloy EK3. Alumina, chromia, spinels and nitrides were present in the scales formed on the alloys. GXRD confirmed the presence of transition aluminas and α-Al_2O_3. The morphologies of the aluminas were consistent with those reported in the literature. The spallation and cracking of scales was attributed to the formation and transformation(s) of transition aluminas to α-Al_2O_3 and the presence of reactive elements. Internal oxidation zones rich in Al formed below the scales. Diffusion zones rich in Cr formed below the internal oxidation zones. Nitrogen was analysed in all the diffusion zones. Ni rich phases were observed in the diffusion zones of the alloys EK2, EK3 and EK4 that contained Al, Co and Cr. In the substrate below the diffusion zone γ and γ'-Ni_3Al was observed in the alloys EK2, EK3, EK4 and EK5. In all the alloys the contamination by nitrogen extended below the diffusion zones. In γ, γ'-Ni_3Al and β-NiAl below the diffusion zone the concentration of nitrogen was around 5 to 10 at% but that of oxygen was < 1 at%. Below the diffusion zones a Cr rich phase was formed in EK2 and EK3 and a Ni rich phase was formed in EK4 and EK5. The latter phase had higher solubility for nitrogen compared with the former. New phase equilibria was established in the alloys EK2 to EK5 below the scale owing to the consumption of Al and Cr to form the scale and the contamination by oxygen and nitrogen.

Introduction

Since the 1960s the increased demand for improvement of the performance of gas turbine engines in aircraft and marine propulsion and in power generation led to significant technological developments and the development of thermal barrier coatings (TBCs). TBCs are multilayered systems which consist of a ceramic topcoat for thermal insulation, a thermally grown oxide (TGO) scale (alumina), and a metallic bond coat that provides resistance against oxidation and corrosion to the superalloy substrate. This project is part of the FP7 project H2-IGCC on the deployment of integrated combined cycle (IGCC) plants with CO_2 capture and storage (CCS). The aim and main objectives of the H2-IGCC project are to pave the way for commercial deployment of efficient, clean, flexible and reliable integrated combined cycle (IGCC) plants with CO_2 capture and storage (CCS) by 2020 and to provide and demonstrate technical solutions which will allow the use of state-of-the-art highly efficient, reliable gas turbines in the next generation of IGCC plants, suitable for combusting undiluted hydrogen-rich Syngas with low NO_x and also allowing for high fuel flexibility. In particular, the materials work package in which this work belongs, is expected to demonstrate cost-effective materials and coating technologies to overcome the component life-limiting problems of overheating and of hot corrosion, resulting from the higher temperatures and from residual contaminants in the Syngas. The work described in this thesis aims to design, develop and evaluate new bond coat (BC) alloys that form in situ alumina oxide scales. It is envisaged that in collaboration with H2-IGCC partners coating technologies will be selected to deposit BC alloy(s) on currently used substrate alloys [Tsakiropoulos, 2010].

The substrate materials in the H2-IGCC project are superalloys. The term superalloy was primarily used after World War II in an effort to describe a group of alloys developed for use in aircraft turbine engines that required high performance at elevated temperatures. Until now the range of applications where superalloys are used has expanded to many other areas including aircraft and gas turbines, rocket engines and power plants [tms.org].

Material work package will address the interdiffusion effect between bond coat and substrate, top coat and Calcium-Magnesium-Alumino-Silicate (CMAS). In H2-IGCC, materials operate in H2 rich environment, where oxidation and hot corrosion are likely to occur with the TBC. The degradation process for coatings involves loss of aluminium in two directions; outward loss by oxide formation and spallation and inward loss by

interdiffusion with the substrate. At the same time TBCs are susceptible to degradation by molten CMAS which deposits in advanced engines that operate at higher temperatures. CMAS attack may be severe near the surface and the interface with the substrate. There is a need for protective coatings in which the bond coat may be of two types, either an aluminide diffusion coating based on the β-NiAl phase or an MCrAlY (M = Ni, Co, or NiCo) overlay coating based on a mixture of β-NiAl and γ'-Ni_3Al or γ-Ni_{ss} phases. In order to provide thermal insulation to hot section metallic components and improved efficiency and performance of the gas turbine engines other partners are developing TBCs which would be multi-layered systems consisting of an outer layer, in charge of the CMAS resistance, and an inner layer in order to ensure the appropriate low thermal conductivity that is needed in the system [Tsakiropoulos, 2010]. In the project described in this thesis the focus is on gas turbine engines. Even though this work is relevant to land based gas turbines used for energy production, it is also relevant to aerospace because of the type of BC that is studied.

Our research strategy was to understand phase selection and stability at the BC/substrate interface in currently used systems in conventional plants, to understand the role of the alloying additions in BC and then to design new BC alloys for H2-IGCC environments. MCrAl-X based on where M = Ni, Co and X = Y, Ta, Hf.

1.1 Protective coatings and their microstructure

Superalloys suffer from chemical and mechanical degradation during operation at high temperatures. To protect the alloys from environmental degradation, protective coatings have been developed [Reed, 2008]. Thermal barrier coatings (TBCs) allowed the turbine inlet temperature (TIT) to increase by 278 °C (500 °F) by providing thermal insulation to hot section metallic components [Krämer et al., 2006], see figure 1.1. About half of this increase is due to a more efficient design for the air cooling of turbine blades and vanes, while the other half is due to improved superalloys and casting processes. The cooling that is now possible enables high-pressure turbine blades and vanes to operate with turbine inlet temperatures of typically 1343 °C (2450 °F), which is above the melting point of the superalloy substrate. Turbine inlet temperatures as high as 1571 °C (2860 °F) are now possible in several advanced aero-engines [ASM handbook, 1990].

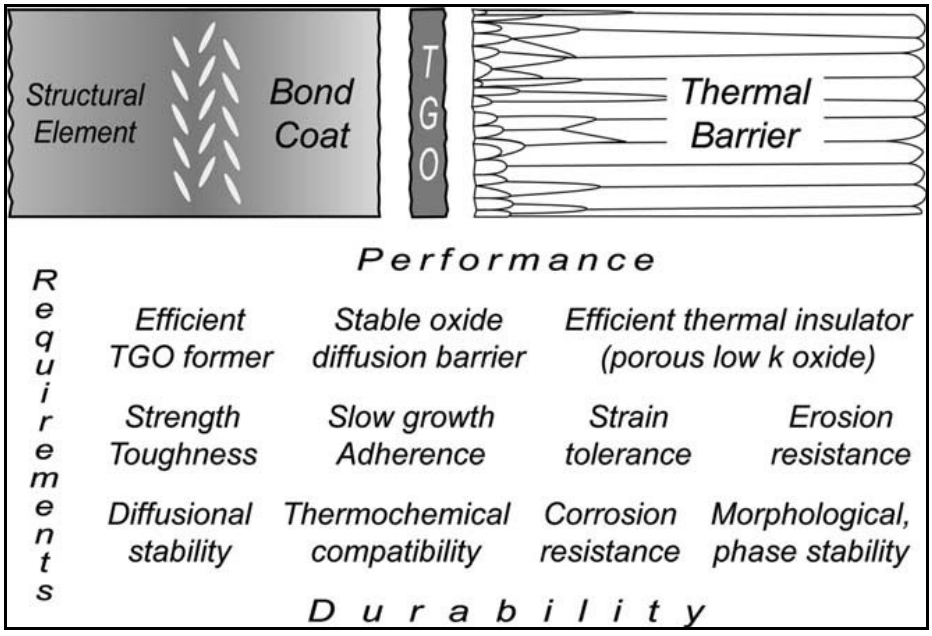

Figure 1.1 The materials of a thermal barrier coating [Levi, 2014]

The components of a TBC are (starting from the substrate) the bond coat (BC), the ceramic top coat and the thermally grown oxide (TGO) that is formed in situ after exposure of the material system (i.e., substrate + TBC) to temperature, see figure 1.2. [Krämer et al. 2006]. The role of the BC is to protect the substrate from high temperature corrosion (oxidation resistance). In the currently used material systems the TGO is alumina. The top coat provides thermal insulation and allows the material system to operate in environments where the temperature (turbine inlet temperature) is well above the melting point of the substrate and BC alloys. TBCs should fulfill the following requirements [Stöver, 2007]:

- be stable up to the operating temperature
- have low thermal conductivity (< 2 $Wm^{-1}K^{-1}$)
- have coefficient of thermal expansion (>9*10^{-6} K^{-1}) compatible with the substrate alloy
- be chemically resistant against high-temperature corrosion
- exhibit low sintering rate
- have acceptable fracture toughness

Bond coats, for example, could be aluminide coatings based on the β-NiAl or Ni_2Al_3 phases or MCrAlY (M = Ni, Co, or NiCo) overlay coatings based on a mixture of β-NiAl and γ'-Ni_3Al or γ-Ni_{ss} phases [Kang, 2010]. The aluminide coatings are obtained by diffusion and the MCrAlY ones by plasma spray or electron beam-physical vapor deposition EB-PVD [Levi, 2004]. The ceramic top coat is typically made of Y_2O_3-stabilized ZrO_2 (YSZ, 7 to 8 wt % Y_2O_3). YSZ has desirable properties that makes it the material of choice for the top-coat. It has one of the lowest thermal conductivities at elevated temperature of all ceramics, approximately 2.3 $W \cdot m^{-1} \cdot K^{-1}$ at 1000 °C [Padture et al., 2002]. The TGO layer is about 1-10 μm thick and is formed when the ceramic top-coat reacts with the bond coat at very high temperatures. This layer is engineered to form α-Al_2O_3. Alumina exists in multiple crystalline forms, of which the two most important ones are α-Al_2O_3 and γ-Al_2O_3. The latter has the structure of spinel, has solubility for water and is not stable in acid [Barron, 2010]. The former is the desirable high temperature form and is also known as corundum. In its crystal structure there are hexagonal close-packed array of oxygen (O^{2-}) ions and octahedral interstices are occupied by Al^{3+} ions. The bond coat is about 75-150 μm thick and in some cases it may also have more than one layers having

different composition. The substrate can be air cooled by internal hollow channels [Adelpour, 2010].

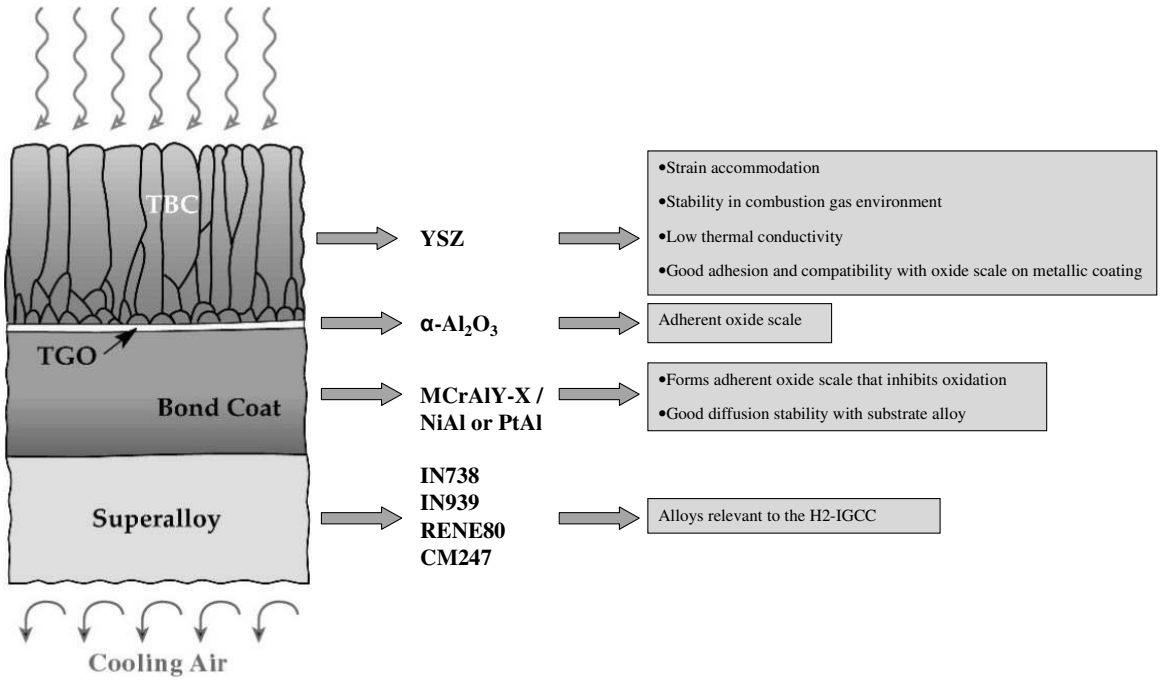

Figure 1.2 Structure of a protective coating, where the substrate alloys are some of the alloys currently used in industrial gas turbines (IGTs) for power generation [Adelpour, Strangman (1985)]

1.2 Processes used to deposit protective coatings on superalloy substrates

1.2.1 High velocity oxy-fuel (HVOF) process

The HVOF process requires the coating alloy to be available in powder form. Powders are mainly produced by gas atomisation. HVOF coatings are often found in IGTs. In HVOF, combustion between oxygen and fuel gas (hydrogen, kerosene, acetylene, propylene) is used to produce a high velocity thermal spray. The method of introducing the powder particles in the flame differs depending on the design of the HVOF system. In some systems powder particles enter into the flame zone axially in others radially and travel towards the substrate at high velocities. The powder partially melts and is

accelerated onto the substrate at velocities up to 2130 m/s at a high temperature, see figure 1.3. The fully molten or partially molten (i.e., semi-solid) powder particles splat on the substrate and solidify. The porosity in the coating depends on the volume fraction of liquid in the spray and the solidification conditions [Plasmatron, 2013]. The strength of the substrate-coating interface is controlled by the surface condition of the substrate (e.g., its surface roughness) as well as the velocity of the powder particles as they splat on the substrate.

For a given HVOF system, i.e., type of gun and fuel, atmosphere in spraying chamber, distance from gun to substrate, the state of each powder particle arriving on the substrate, i.e., whether its is fully or partially molten depends on its size. The volume fraction of liquid in the spray that arrives to the substrate surface depends on the distribution of powder particle sizes in the spray and on impact it is affected by the temperature of the substrate. Depending on all these parameters the HVOF process produces a coating that is low in porosity, has low amount of oxides in the as sprayed condition, has superior bond strength, higher density and higher hardness than other competitive vacuum spray processes [Ellison Surface Technologies (2010), Lima and Guilemany (2007), Brandl et al. (1997)].

Compared with other thermal spray techniques for coating applications like vacuum plasma spraying (VPS) and low pressure plasma spraying (LPPS), the HVOF process operates at atmospheric pressure and not in vacuum, therefore operating and production costs are considerably lower. Thus, using lower temperature jets during the application results in some remaining unmelted powder particles [Brandl et al, 1997].

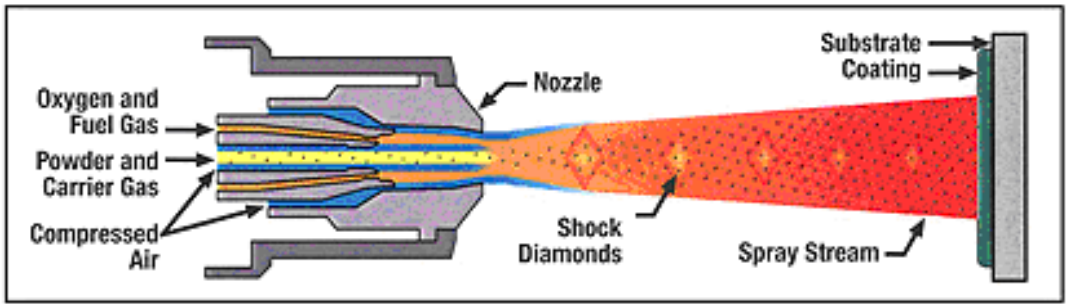

Figure 1.3 HVOF thermal spray coating technique [Plasmatron, 2013].

1.2.2 Plasma spraying (PS)

Plasma sprayed coatings are built upon particle-by-particle as the molten particles deposit on the substrate and solidify with high cooling rates (10^6 to 10^8 K/s), see figure 1.4. In order to accomplish uniform heating and acceleration of the sprayed material so as to produce a high quality coating, the material in particulate form must be introduced into the plasma at a uniform rate. Therefore, a narrow particle size range is preferred. Finer particles give denser deposits with less porosity. However, residual stresses can be high and oxide inclusions are formed by oxidation of the molten particles in the spray during flight. With PS the average composition of the coating can be very close to the average composition of the powder particle charge used for spraying, which is significant advantage compared with EB-PVD where accurate control of composition might be difficult owing to differences in evaporation rates. Plasma spraying cannot produce a fully dense coating without any porosity [Reed, 2008]. Air plasma spraying (APS) or vacuum plasma spraying (VPS) or low pressure plasma spray (LPPS) can be used. The LPPS process allows formation of extremely dense overlays with metallurgical bonding. This technology is applicable where HVOF and conventional plasma or flame spraying techniques are inefficient [Surface Modification Systems, 2010]. The APS process can be automated, has lower costs and gives good bond strength but higher coating porosity than the VPS process.

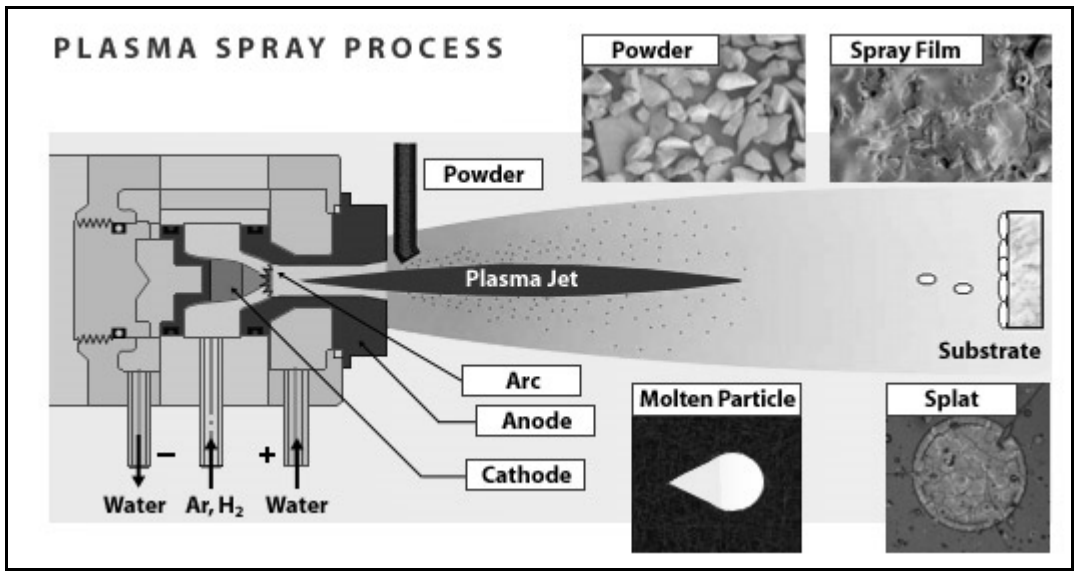

Figure 1.4 Schematic illustration of the plasma spray process [TSET, 2010].

1.2.3 Electron beam physical vapour deposition (EB-PVD)

Electron beam physical vapour deposition or EB-PVD is a physical vapour deposition process in which a target material is bombarded with an electron beam generated for example by a charged tungsten filament under high vacuum. The target material is in a water cooled copper crucible and the level of the molten metal is adjusted. A plum of evaporated atoms is produced by the electron beam. These atoms then "condense" on the substrate (the EB-PVD process is known as a line of sight process) where, following surface nucleation and growth, the coating is formed. The evaporation rate can be about 10^{-2} g/cm^2 sec. In EB-PVD deposition rates can be in the range 0.1 µm/min at relatively low substrate temperatures. The material utilization efficiency is very high. A schematic diagram of an EB-PVD system is shown in figure 1.5.

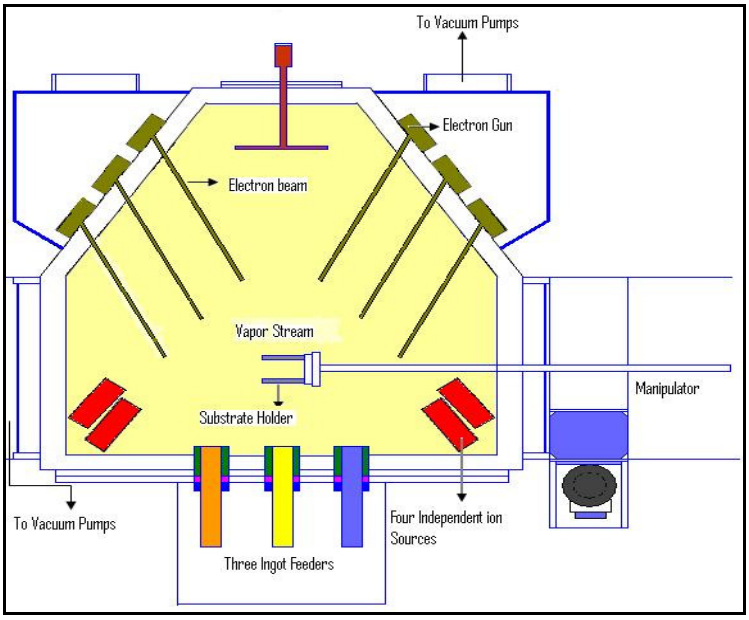

Figure 1.5 Electron beam physical vapour deposition [wikelectro, 2010].

A TBC that is formed using EB-PVD can have columnar colonies that grow competitively with each other and perpendicular to the substrate and are weakly bonded to their neighbour columns. This mode of growth gives the coating strain tolerance which is essential for its survival in service given the intrinsic brittleness of the coating and the stresses from thermal cycling in service. The coating quality is impaired when the surface to be coated is not perfectly clean, because small imperfections are not covered up and this

can result in a growth abnormality that is magnified as the coating thickens. Process parameters that are important for controlling the structure (i.e., size, regularity and orientation of columns) and architecture (i.e., uniformity of structure along substrate) of the coating are the rotation speed of the substrate and its temperature [Reed, 2008]. When the substrate temperature is 850 °C to 1050 °C the TBC density, hardness, erosion resistance and spallation life are improved. Internal tensile stresses build up in a coating deposited on a hot substrate. These can be converted to compressive stresses using high energy ions to bombard the coating [Wolfe and Singh, 2000].

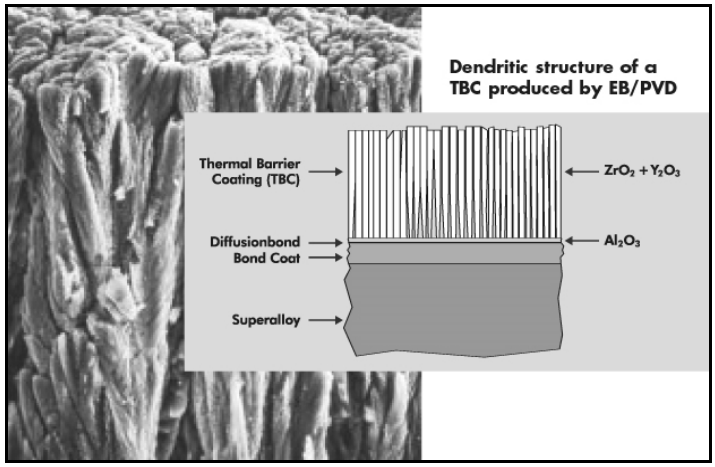

Figure 1.6 Columnar structure of a TBC produced by EB-PVD [ALD Vacuum Technologies].

1.3 Overlay coatings

Overlay coatings are one type of oxidation resistant coatings designed to protect and insulate the substrate from high temperatures. There is a strong interdependence between the overlay coating and the substrate composition, regarding their corrosion resistance and mechanical properties. Overlay coatings are often of the MCrAlY type where M is the alloy base metal, usually Ni, Co, or a combination of these two. These alloys are designed to provide good balance between oxidation resistance, corrosion resistance, and coating ductility but suffer from interdiffusion with the substrate [Nicholls (2000), Itoh and Tamura (1999)]. Oxygen-active alloying elements are added to this type of coatings such as Hf, Si, Ta, Y, W, Zr, Re, Nb, Ti etc. singly or in combination to increase oxide-scale adhesion and decrease oxidation rate.

In order to produce improved overlay coatings that are more resistant to hot corrosion (see section 1.7) (lower temperature -Type II hot corrosion) there is a need to increase the Cr content [Russo and Dorfman (2003), Nicholls (2000)]. These more complex alloy systems are often generically known as M-Cr-Al-X or M-Cr-Al-X-Y systems, where X refers to oxygen-active elements other than yttrium. Over-aluminising is used to enrich with Al the surfaces of coatings in coating systems used in IGTs fuelled with natural gas and achieving higher than normal temperatures [Kedward, 1969].

Interdiffusion occurs between the aluminium containing BC and the substrate alloy resulting in intermetallic formation, primarily β-NiAl or CoAl, depending on the elements in the substrate. The rate of interdiffusion decreases in the order NiCrAlY>CoCrAlY>CoNiCrAlY>NiCoCrAlY, where NiCo represents higher Co contents in comparison with Ni and CoNi [Stringer (1987), Itoh and Tamura (1999)].

Nowadays, overlay coating are applied to substrates using thermal and plasma spraying, (see sections 1.2.1 and 1.2.2) and electron beam physical vapour deposition (EB-PVD), (see section 1.2.3.) [Pomeroy, 2005]. The overlay coatings are thicker (mostly 125–200 μm though sometimes their thickness can reach ~300 μm) than diffusion coatings. Thus, the former coatings last longer than the latter ones under the same corrosion conditions. The cost of an overlay coating is typically two to four times the cost of a conventional aluminide or platinum-aluminide coating [Nicholls, 2000].

1.4 Diffusion coatings

Diffusion coatings are formed by enriching the surface of an alloy with either aluminium (aluminides), chromium (chromized), or silicon (siliconized) to improve environmental resistance of the substrate [Nicholls, 2003]. The diffusion coating process provides a chemically bonded coating which acts as a barrier against the diffusion of oxygen into the substrate. There exist different processes but pack cementation (see below) is the most widely used process owing to its low cost and adaptability.

Aluminide diffusion coatings are based on the β-NiAl intermetallic. The presence of β-NiAl in a coating increases the Al activity at the surface, so that a protective α-Al_2O_3 scale can form at high temperature (see figure 1.7a). The stability of the NiAl intermetallic phase is affected by interdiffussion phenomena at the coating system interfaces and the loss of Al (e.g., due to the TGO formation) in service. Inward diffusion happens when

there is low temperature and high activity (where aluminium or chromium diffuses inwards) and outward diffusion takes place when there is high temperature and low activity [Pochet, 1996]. Additionally, as the scale grows, several processes may reduce the adherence of the oxide scale to the alloy. This results in spallation of the scale, after which catastrophic oxidation may follow [Pochet, 1996], [Stiller, 2010]. The addition of Pt to conventional aluminide coatings improves the high temperature oxidation resistance, increases the protective life and introduces a diffusion barrier [Stiller, 2010], [Pochet, 1996]. Pt aluminide coatings are deposited with similar methods on the aluminide coatings but after electroplating the substrate with Pt (see figure 1.7b).

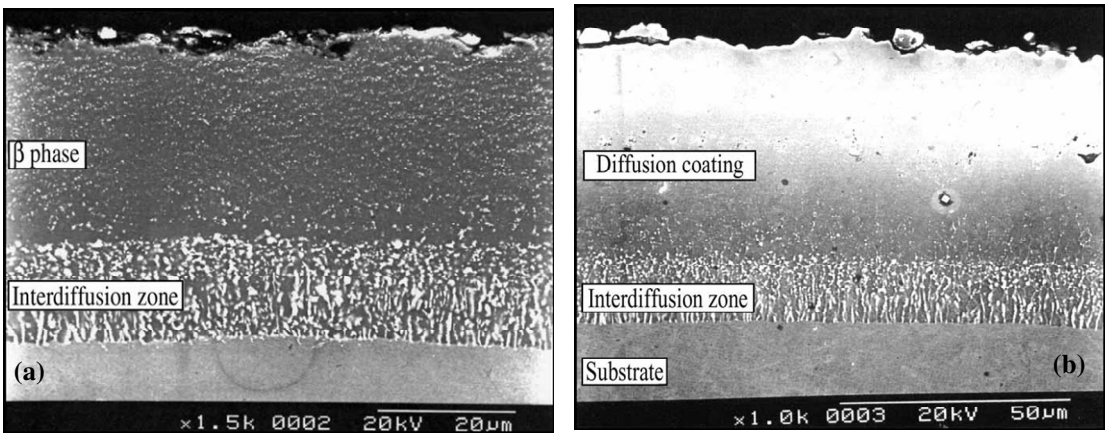

Figure 1.7 SEM back scatter electron images of (a) NiAl based pack aluminide on IN738 and (b) PtAl coatings [Nicholls, 2003].

1.4.1 Pack cementation

The pack cementation process falls in the category of chemical vapour deposition. The parts are loaded into box(es) that contain a mixture of powders: active coating material containing aluminium, activator (chloride or fluoride), and thermal ballast, such as aluminium oxide. These form the pack which is then heated at a temperature in the range 700 to 1100 ˚C in an Ar or H_2 atmosphere where gaseous aluminium halide forms, and diffuses to deposit Al metal. After the end of the process the so-called "green coating" is produced, which is too thin and brittle for direct use. A subsequent diffusion heat treatment leads to further inward diffusion and formation of the desired coating. The deposition can be characterised as being a low or a high activity deposition depending on

the Al activity on the substrate surface. Ni diffusion drives the coating formation in low activity coatings (which are deposited at high temperatures, usually in the range 1000 to 1100 °C) and Ni rich NiAl forms (it should be remembered that the NiAl has a homogeneity (solubility) range). Diffusion of Al drives the formation of high activity coatings that are usually deposited at 700 to 950 °C. In this case the intermetallics Ni_2Al_3 and β-NiAl can form. To even-out gradients in Al concentration and form NiAl in the coating the coatings are given a so called diffusion heat treatment at 1050 to 1100 °C.

The choice of coating in pack cementation is highly influenced by the substrate composition owing to interdiffusion between coating and substrate that "defines" the final coating microstructure. In this respect the case of Ti must be mentioned as it is a common alloying addition in Ni based superalloy substrates. Titanium diffuses into the coating and this leads to the formation of titania that is believed to break the continuity of alumina oxide scale.

Advantages of the pack cementation process

- the coating is metallurgically bonded to the substrate
- batch processing for high production rates
- can be used to coat large or small components
- coats both external and internal surfaces, even deep, small bores
- can be tailored to meet specific requirements
- economical process
-

1.5 Bond coat- Pt aluminides

As briefly discussed in section 1.4 NiAl coatings tend to suffer from interdiffusion with the substrate, see figure 1.8. This leads to formation of γ'-Ni_3Al and the vol% of β-NiAl is reduced. Pt provides a diffusion barrier. Platinum additions limit the outward diffusion of alloying elements like Ti, Ta etc. from the substrate, reduce the growth of internal voids, and thus improve scale adhesion and cyclic oxidation resistance [Nicholls (2003), Nicholls et al (1989)]. Other metals such as rhodium and palladium provide similar benefits to Pt [Pochet, 1996].

Oxidation/corrosion resistance is superior when the material is richer in Pt content, however, in this case the coating has less ductility and is phase unstable. Less than 10 μm of Pt are needed onto a Ni based alloy followed by aluminizing the Pt plated substrate at approx. 1050 °C using pack cementation. Single phase platinum aluminides are a continuous outer layer of PtAl with Al concentration around 15 to 25 wt% (see figure 1.9.). While they appear to perform well in high temperature oxidation/corrosion resistance which is the case in Type I hot corrosion environments (800-950 ˚C), they perform less well under Type II hot corrosion conditions [Nicholls, 2000] but they have enhanced ductility and better thermal phase stability. PtAl is a line compound and thus it is difficult to deposit. As Al gets lost from the coating the phase equilibria shifts in the Pt-Al system and new phase can form (stabilise), for example PtAl + Al_3Pt_5 [Perez et al., 2005]. These changes in phase equilibria will be accompanied by volume changes, and as the matrix is inherently brittle (essentially it is an intermetallic based alloy) voids and cracks will form [Pochet, 1996]. The so-called duplex aluminide coatings consist of NiAl and Pt rich aluminide and their formation is accompanied by volume expansion compared with volume contraction in the case of the Pt rich intermetallics.

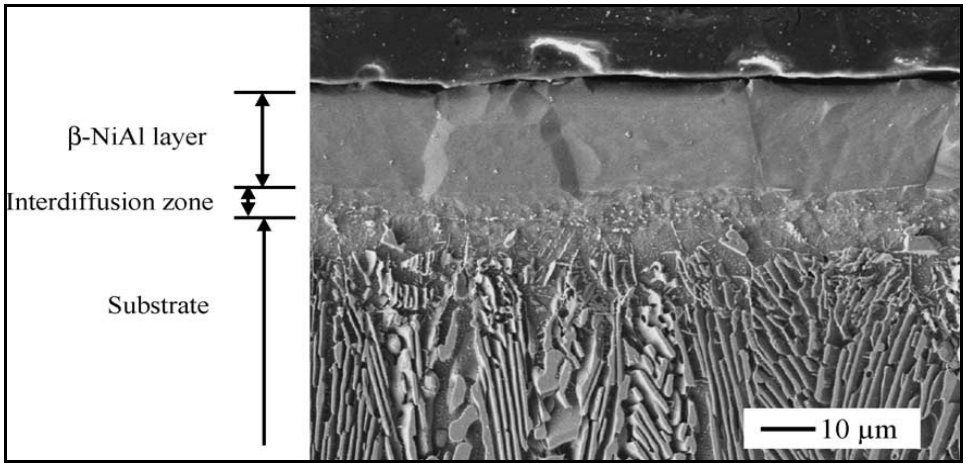

Figure 1.8 SEM image of a cross-section of a NiAl bond coat deposited at 1000 ˚C [Yu et al., 2004].

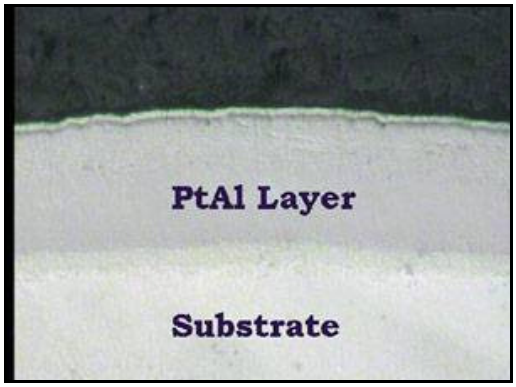

Figure 1.9 SEM image of PtAl coating on superalloy substrate [Creech and Barber, 1991].

1.6 Bond coat - MCrAlY based alloys

Typical MCrAlY-X bond coats (where M= Ni, Co (or combination of the two) and X= Re, Ta, Hf, Zr, Ti, Ta, Pd, Si) contain at least 4 elements, see Table 1.1. The typical microstructure of MCrAlY coatings is β-NiAl+γ-Ni_{ss}. The γ-Ni_{ss} phase improves the coating ductility (good for resistance to thermal fatigue). Cr gives these coatings excellent corrosion resistance combined with good oxidation resistance. The amount of Cr that can be added is limited depending on the effect it is expected to have on the substrate and the formation of Cr-rich phases in the coating [Thomas-Sourmail, 2013]. Al controls oxidation and thus its concentration is usually in the range 8 to 12 wt%. Increasing the Al concentration, though beneficial in terms of oxidation resistance, is bad for ductility. Si increases resistance to cyclic oxidation, but has an adverse effect on the liquidus temperature of the coating. It has also been suggested that Si affects phase stability. Si is thought to be very promising to overcome the problems of inherent brittleness, spalling and interdiffusion effects. Alloying is used to modify the composition of MCrAlY BC alloys, for example Si can replace Al and/or Cr [Grunling and Bauer, 1982]. The role of Y and Hf (which are known as reactive element (RE) additions in the literature that is relevant to BC alloys) is to improve the scale adhesion [Smeggil, 1987] while Y is also believed to "trap" S and thus prevent its segregation. In some MCrAlY BC alloys Re has been added to improve oxidation and fatigue properties [Czech et al., 1994] and it is also claimed that Re improves scale adhesion [Wright and Pint, 2005]. Tantalum (which is a key alloying addition in the alloys developed in the research described in this thesis) is also added to MCrAlY BC alloys to improve oxidation resistance.

The deposition of MCrAlY based alloys with/out the aforementioned alloying additions using pack cementation is challenging owing to the difficulties of controlling the activities of the elements in the pack to get the target composition for the coating [Smeggil, 1987]. Instead, APS, LPPS and EB-PVD are used for the deposition of MCrAlY bond coatings. After deposition, a heat treatment in vacuum allows interdiffusion with the substrate alloy and thus the adhesion of the coating is enhanced.

Table 1.1. Typical MCrAlY bond coat compositions (wt %) considered for coatings in IGCC plants, [Tsakiropoulos, 2010].

Coatings	**Ni**	**Co**	**Cr**	**Al**	**Y**	**Ta**	**Si**	**Re**
SV20	Bal	-	25	5.5	0.6	1	2.7	-
GT29	-	Bal	29	6	0.5	-	-	-
GT33	Bal	37	22	9	0.5	-	-	-
CoNiCrAlY	32	Bal	21	8	0.5	-	-	-
SC2931	30	31	30	8	0.6	-	-	-
SC2453	52	10	23	12	0.6	-	0.7	1.7
CoNiCrAlY	32	Bal	21	8	0.5	-	-	-

1.7 Type I and type II hot corrosion

Hot corrosion is a type of corrosion that results from the presence of salt contaminants such as sodium sulphate (Na_2SO_4), sodium chloride (NaCl) and vanadium pentoxide (V_2O_5) that combine to form molten deposits which damage the protective surface oxides. Alloy, environment and salt composition are important for “defining” the temperature where hot corrosion is important. Environments such as those encountered in coal gasifiers (used in syngas H2-IGCC plants) and gas turbines [Keienburg et al., 1985],

lead to the formation of solid and molten salts that take part in corrosion [Bose, 2007]. Hot corrosion has three forms of attack, Type I or high temperature hot corrosion, Type II or low temperature hot corrosion and vanadic corrosion. Depending on the alloy composition, the temperature and temperature cycles, the erosion processes etc, there will be a development of the above types of hot corrosion [Eliaz et al. 2002]. Hot corrosion develops in two stages, the initiation stage and the propagation stage. In the first stage where initiation takes place, hot corrosion is low as the breakdown of the surface oxide scale occurs. After that repair of the oxide is impossible and the propagation stage begins, that results in rapid consumption of the alloy. The initiation stage can be extended to be as long as the designed life limit unless the repair of the protective surface oxide scale is possible. Otherwise, once the coating penetration begins, the propagation stage is inevitable, the salts have access to the unprotected metal and exceedingly high corrosion rates occur till spallation of the component [Nicholls, 2000].

In Type I hot corrosion (800–950 °C) S is transported from (typically) Na_2SO_4 (i.e., from a sodium sulphate deposit) into the alloy via the oxide scale formed on the latter to form stable sulphide(s) with sulphide forming elements, e.g., Cr. The latter are molten at the above temperatures (e.g., NiS_2 is molten at 645 °C, Co_xS_y has liquidus at ~ 840 °C) and thus their formation has catastrophic consequences for the base alloy (component degradation) [Eliaz et al. (2002), Viswanathan (2001)]. BC alloys that have resistance to Type I hot corrosion are MCrAlY alloys with 25 wt%Cr and 6 wt%Al and platinum aluminide coatings [Goward, 1998].

Type II hot corrosion occurs in the temperature range 650–800 °C and involves the formation of base metal (nickel or cobalt) sulphates which require a certain partial pressure of sulphur trioxide for their stabilization. Therefore, chromising is of particular use for resistance towards Type II hot corrosion and has also been found to be of major benefit in protecting Ni-based alloys from corrosion by sulphatic deposits in chemical plants. These sulphates react with alkali metal sulphates to form low melting point compounds which prevent the metal from forming a protective oxide [Pomeroy, 2005]. Different types of bond coat alloys are shown in figure 1.10 where under high temperature oxidizing conditions, NiCrAlY and NiCoCrAlY overlay coatings outperform the cobalt based coating systems.

When fuels combust, accelerated corrosion occurs when vanadium containing deposits are found on components operating at high temperatures such as gas turbine engines. Vanadium oxides such as V_2O_5 are produced and react with sodium sulphate

(Na_2SO_4) in the environment forming low melting sodium vanadates ($Na_xV_yO_z$). Such deposits are very acidic and aggressive, particularly if they form a liquid phase which attacks the oxide scales [Bose (2007), Hancock (1987)].

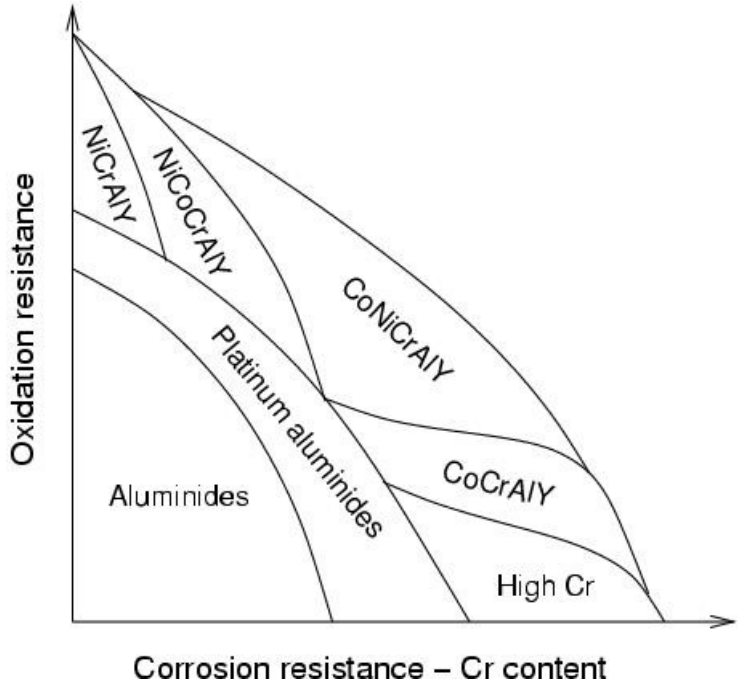

Figure 1.10 Optimum coating compositions for oxidation and hot-corrosion resistance [Schütze, 2000].

Transient (or transition) aluminas can form in the initial stages of oxidation and then transform to the desirable α-$A1_2O_3$, this is particularly true when oxidation occurs above 950 °C. In the early stages of oxidation Ni spinels can form, for example $Ni(Cr,A1)_2O_4$, and NiO. The growth of the latter is fast and then chromia forms beneath it a continuous layer. Then below the latter alumina forms in its metastable (i.e., transient or transition) form(s), before it transforms to α-$A1_2O_3$ [Prescott and Graham, 1992].

Uncoated superalloys with high Cr content (in the latest generation of superalloys the Cr content is significantly reduced owing to the additions of elements like Re that ehnace the formation of TCP phases like Laves, σ, μ) rely on in situ chromia formation for oxidation resistance. At high flow rates of the oxidising environment and T>1000 °C chromia becomes less effective as a protective scale owing to the formation of the volatile CrO_3 oxide. The protective properties of chromia are also lost in the presence of water because of the formation of volatile $Cr(OH)_3$. As mentioned earlier, the TGO in state of the

art coating systems is α-$A1_2O_3$, but SiO_2 has also been considered when developing coating systems as a protective oxide [Tsakiropoulos, 2012]. However, at elevated temperatures reduction of silica to the volatile SiO may occur or complex molten oxides can form [Wallwork and Hed, 1971].

Hot corrosion mechanisms have been studied experimentally and nowadays guide coating and superalloy development. Elements like chromium, platinum and silicon are preferable to be used and elements like molybdenum, tungsten and vanadium are meant to be avoided in the development of hot corrosion resistant coatings [Goward, 1998]. An example of modern coatings designed to operate under high temperature oxidation is the "SMARTCOAT" [Nicholls et al., 2002]. It consists of an MCrAlY base bond coat alloy, enriched first with chromium to enhance type II corrosion protection and then with an aluminium rich (β-NiAl) composition to increase high temperature oxidation resistance and type I hot corrosion (see section 1.7). The coating forms protective alumina scale at T>900 °C but at lower temperature re-formation of alumina is not quick enough to offer protection. Rapid formation of chromia was ensured by the coating design via the incorporation of an intermediate Cr rich layer to ensure formation of chromia to provide protection against Type II hot corrosion. That was done either through sourcing beneficial elemental additions (reservoir behavior) or by trapping detrimental elements (scavenger behavior) [Nicholls et al., 2002].

1.8 Crystal structure of aluminium oxide

It should be clear from the previous discussion that alumina is preferred to chromia for oxidation resistance at high (> 1000 °C) temperatures. The volatility issues disc used above for the Cr-O system are not met in the Al-O system. Furthermore, cations diffuse slower through alumina compared with chromia. The free energy of alumina formation is more negative than that of chromia (in other words alumina is more stable than chromia). Thus, if the alloy contains Al and Cr and chromia is formed as the scale, internal oxidation of Al will occur. The latter is undesirable. [Wallwork and Hed, 1971]. Thus, the optimum scale that coating designers wish to form is α-Al_2O_3.

As already discussed Al can form different oxides. Corundum (α-Al_2O_3) is the natural form but alumina can also be found naturally in hydrated forms [Adelpour, 2010].

The α-$A1_2O_3$ is the stable form at high-temperature. In the crystal structure of α-$A1_2O_3$ there are hexagonally close-packed oxygen ions and two thirds of the octahedral interstices are filled by trivalent cations. There are aluminas that are stable at lower temperatures. These have different structures compared with α-$A1_2O_3$ and with increase in temperature transform to a different alumina structure (transient alumina) and eventually to α-$A1_2O_3$ at high temperature. This very point will be revisited when the results of the oxidation study of the alloys developed in this thesis are discussed. At this stage it is suffice to say that their transformation is a reconstructive process with a continuous ordering of cations and restructuring of anions to the hexagonal close-packed arrangement in the rhombohedral structure [Prescott and Graham, 1992].

The microstructure of the TGO is usually columnar and the formation of the latter is attributed to the diffusion of O^{2-} ions and Al (respectively inward and outward diffusion). It has been suggested that the texture resulting from the columnar nature of growth of the alumina grains assists the control of the evolution of residual strains and the deformation of the TGO. The reactive element additions discussed earlier, for example Y, are believed to segregate to the g.bs of the TGO grains and in doing so to slow done (or even suppress) the diffusion of Al along the g.bs. This then allows the inward diffusion of oxygen ions to "control" the growth processes in the scale and to lead to the formation of an inward growing scale of columnar microstructure [Karadge et al., 2005].

1.9 Interdiffusion between bond coat and substrate

Coatings in general are not in thermodynamic equilibrium with the substrate alloys. Due to the compositional difference between the coating and the substrate, interdiffusion of various elements occurs when the coated alloy is exposed to high temperatures. Aluminium, which is one of the main constituents of the substrate and the coating, may affect both oxidation resistance and the overall phase stability of the coating. The main cause for the degradation of coatings is the loss of aluminium in two directions; outward loss by oxide formation and spallation, and inward loss by interdiffusion with the substrate, see figure 1.11. When aluminium diffuses towards the coating's surface it usually enhances formation of protective Al_2O_3 scale. When it diffuses inwards, towards the substrate can cause significant degradation, [Bose (2007), Smialek and Lowell (1974)].

An aluminium reservoir can be the NiCoCrAlY bond coat itself with its high aluminium content that will help the formation of a thermally grown oxide (TGO) layer. If this TGO layer is destroyed, it is supposed to heal out. Thus, if there is depletion in aluminium due to diffusion, there is not enough aluminium left for a new formation of TGO. On the other hand, alloying elements from the bond coat may diffuse outwards and disturb the adhesion of the TGO layer, e.g. titanium. The introduction of a diffusion barrier between substrate and bond coat is a suitable means to overcome this problem. Thus a "diffusion barrier" to prevent or retard the migration of aluminium from the coating into the substrate was required and this led to the development of Pt-A1 coatings [Jackson and Rairden, 1977], see section 1.5 above.

In both MCrAlY and NiAl-based coatings, the Al-rich β-NiAl phase plays the role of an Al reservoir for the formation of continuous, stable, and protective Al_2O_3 scale. β-NiAl has a solubility range which means that alloying is possible and coatings deposition easier but loss of Al means that two-phase equilibria will occur [Perez et al., 2005].

After high temperature exposure the Al-rich β-NiAl phase is dissolved because of depletion of Al from the coating [Perez et al., 2006]. The remaining β-NiAl phase regions often have the characteristic structure of a martensite. As Al is depleted, the average composition of the bond coat becomes increasingly enriched in Ni until reaching the single phase boundary at which point further depletion leads to the formation of γ'-Ni_3Al and if it goes further on at even longer exposure times, the composition can extend into the γ region of the phase diagram. In addition, martensitic structures within the β-NiAl phase field are formed as the phase boundary is approached. Whereas the Ms of the pure β-NiAl compositions is known to be generally around room temperature to 300 °C, the Pt, Co, and Cr in the bond coat increase the martensitic transformation temperature (Ms) temperature [Clarke and Levi, 2003].

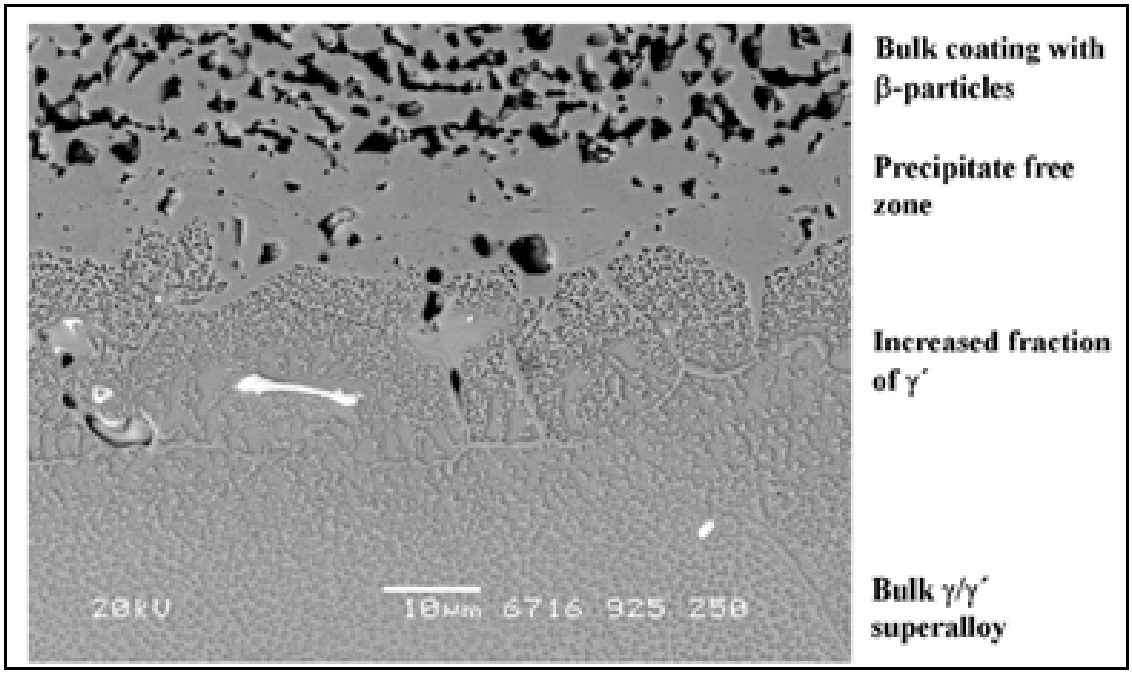

Figure 1.11 IN738 substrate coated with a MCrAlY BC alloy and heat treated at 925 C for 250 h. The image shows a precipitate free area in the inter-diffusion zone and the formation of γ'-rich layer on the substrate side [Dahl et al., 2006].

Loss of Al can occur by inter-diffusion and oxidation and the former can be more severe than the latter. Spallation of the scale (and thus exposure of the substrate to the oxidising environment) will accelerate the latter method of Al loss. The coating is considered to be non-effective when the NiAl is no more stable in its microstructure and when its Al content is <10 at% [Perez et al., 2006]. Figure 1.12 summarizes the main changes that occurred during high-temperature exposure of a coated turbine blade. The system consisted of zirconia based TBC with (Ni, Pt)Al BC and a ReneN5 (50Ni-17Cr-13Co-12Al-7Ta-4W-3Re-1Mo-Pt in at%) alloy as substrate. The alumina TGO formed (attributed to the oxidation of NiAl). There was outward Ni diffusion from the substrate and inward diffusion of Pt from the BC. In the outer β layer the NiAl exhibited tweed or martensitic substructure, which would suggest the transformation indicated in the figure 1.12. In the middle layer the β-NiAl (that may contain μ particles in the as-deposited condition) transformed to a β/γ' matrix that contained coarse μ particles (these could be present in the as-deposited condition) and $M_{23}C_6$ carbides. The NiAl had a tweed substructure or had transformed to martensite on cooling. The inner layer was a mixture of γ' and NiAl with a tweed microstructure (and contained σ, σ' and μ phases in the as-

received condition) transformed to γ' in service and the σ, σ' and μ phases coarsened and $M_{23}C_6$ carbides formed [Zhang and Heuer, 2005].

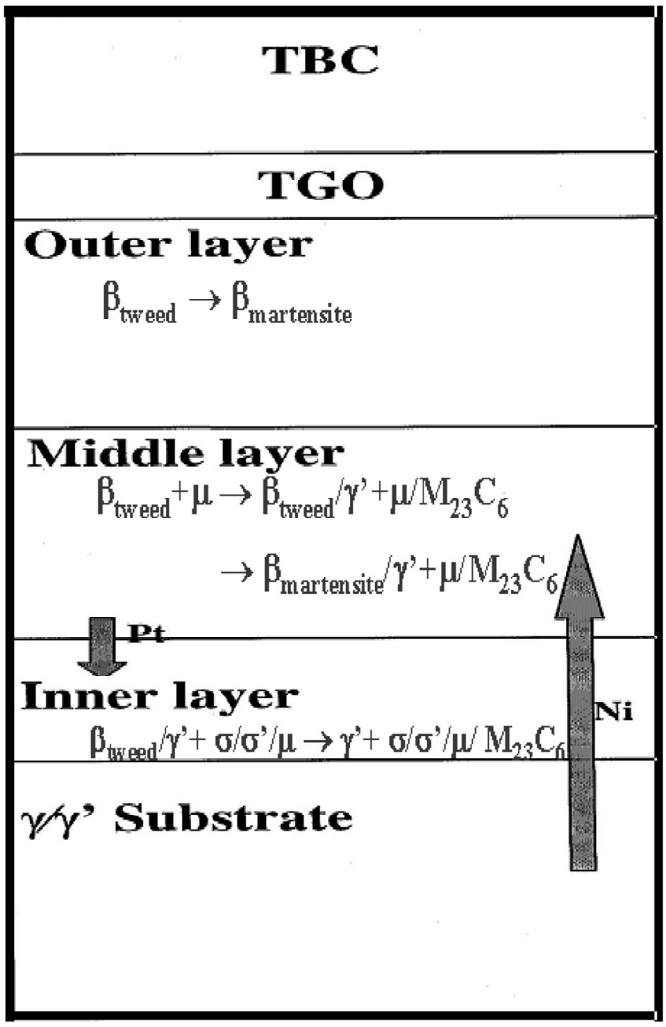

Figure 1.12 Schematic drawing showing interdiffusion in bond coat during service [Zhang and Heuer, 2005].

1.10 Phase equilibria

The three phases of interest to the research presented in this thesis are the γ-Ni_{ss} solid solution and the intermetallics β-NiAl and γ'-Ni_3Al, all of which are found on the Ni side of the NiAl binary phase diagram. Crystallographic data of these phases is shown in Table 1.2.

Table 1.2 Crystallographic data for the phases of interest to this study.

Phases	Space group	Crystal structure
γ-Ni_{ss}	Fm3-m	FCC
β-NiAl	Pm3-m	BCC (B2)
γ'-Ni_3Al	Pm3-m	FCC ($L1_2$)

Numerous publications exist for the Ni rich part of the Ni-Al phase diagram regarding the phase equilibria and solidification of Ni rich alloys but there is disagreement for the NiAl and Ni_3Al phases. Thus, there are disagreements for the phase diagram near the γ'-Ni_3Al composition. Some researchers including Singleton et al. (1986), Hansen and Anderko (1985) and Alexander and Vaughan (1937) show a peritectic reaction between β and γ' (see figure 1.13a) whereas other studies by Dupin (1995), Lee and Verhoeven (1994), Verhoeven et al. (1991), Bremer et al. (1988), Hilpert et al. (1987) and Schramm (1941) show a peritectic reaction between γ and γ' and a eutectic reaction between γ' and β separated by only 1 to 3 °C (see figures 1.13b) and 1.14). Based on the low velocity solidification studies by Lee and Verhoeven (1994) the phase diagram in figure 1.14 is considered to be the correct one. Trivedi (1995) observed lamellar and fibrous eutectic structures with β and γ' and bands of γ and γ' typical of a peritectic reaction. Verhoeven et al (1991) evaluated the eutectic temperature at 75 at% Ni in a solidifying sample. Their method was not accurate as it gave a value that is higher by 15 K than the corresponding value measured by differential analysis by Bremer et al. (1988) and Hilpert et al. (1987). The liquidus and solidus temperatures of the β-NiAl and γ-Ni_{ss} phases are considered to be well determined as both phases are in equilibrium with the liquid over a wide range of compositions. However, the γ'-Ni_3Al phase is in equilibrium with the liquid over less than 1 at% and several degrees only, which makes the measurement of the liquidus slope very difficult. All these reasons explain the difficulties and disagreements in calculating the positions of the γ' liquidus and solidus and why these uncertainties still remain. As long as these issues about the Ni-Al phase diagram remain unsolved the choice of Ni-Al phase diagram is crucial for the development of modern superalloys.

Further study of phase equilibria in the Ni-Al system using directional solidification experiments and modeling by Hunziker and Kurz (1999) provided data that allowed the Ni-Al phase diagram shown in figure 1.13b to be optimized as follows:

- There is a very small temperature difference between the stable and the metastable eutectic (see figure 1.14) which is less than 0.5 K
- Similar liquidus slopes for the γ-Ni_{ss} and γ'-Ni_3Al
- The solid composition of γ'-Ni_3Al is close to 76 at% Ni

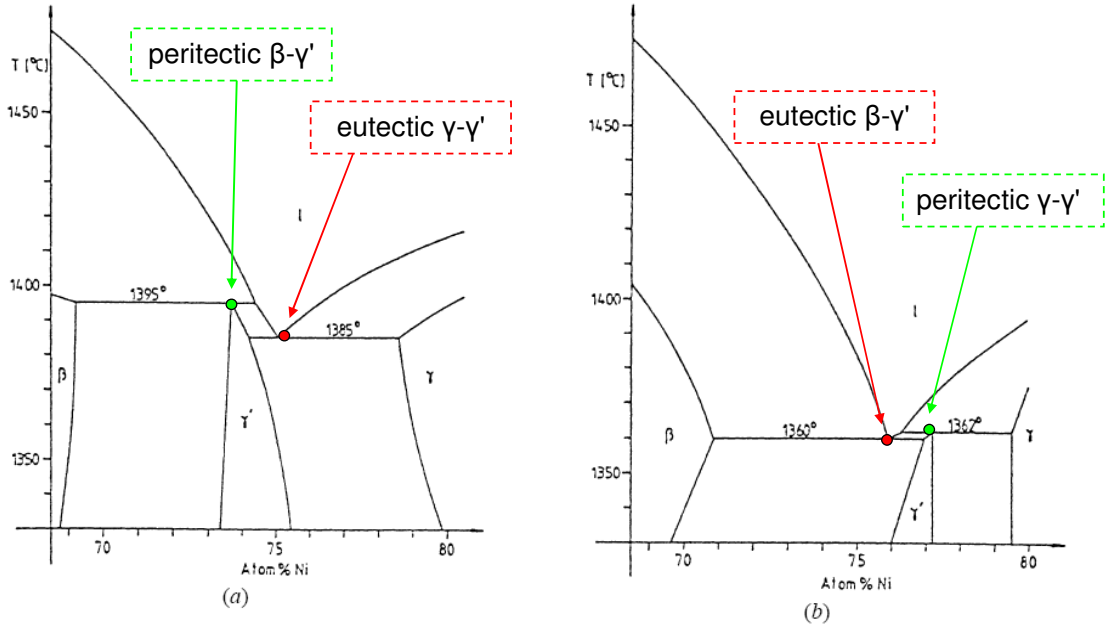

Figure 1.13 Two different versions of Ni-Al binary system (a) From Alexander and Vaughan (1937) (b) From Schramm (1941).

Thus, Hunziker and Kurz (1999) optimised the phase diagram to get agreement with the results of the solidification studies. The optimised phase diagram was proposed to have a peritectic between γ and γ', a eutectic between β and γ' (figures 1.13b and 1.14), with a very small difference between the temperatures of the stable β-γ' and the metastable β-γ eutectics, similar liquidus slopes for the γ and γ' phases, the composition of γ' at ~ 76 at% Ni, and a solidification range (freezing range) for the γ' of 2.3K.

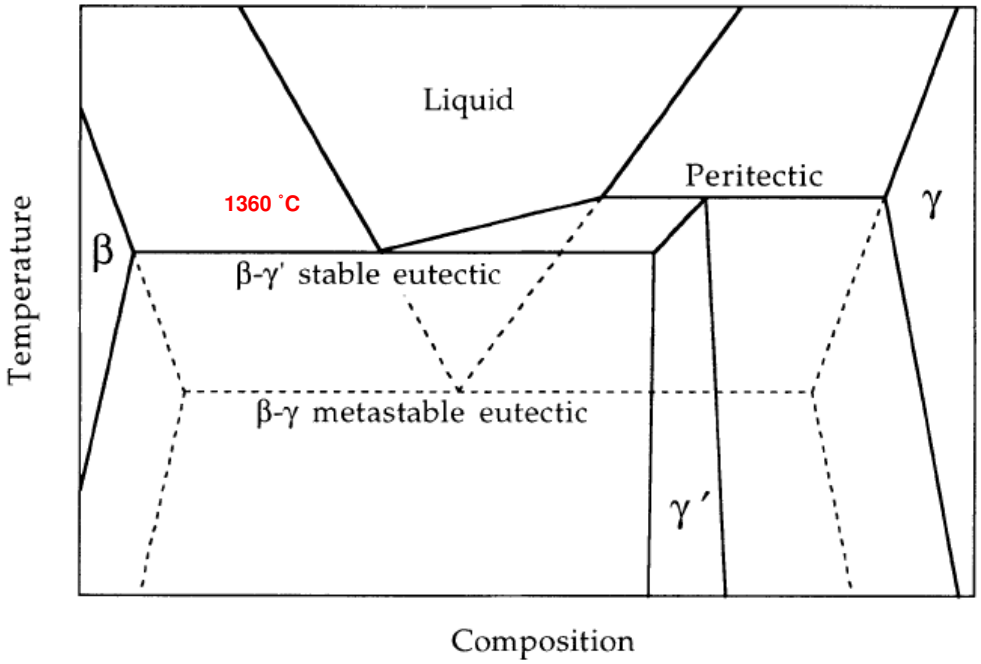

Figure 1.14. Equilibrium and metastable eutectics in the Ni-Al system, from Hunziker and Kurz (1999).

According to the ASM alloy phase diagram database there are eleven Al-Cr-Ni ternary diagrams that cover the full composition range. The earliest of these diagrams was published in 1974 and the most recent one in 1985. There are significant differences between the published diagrams regarding phase equilibria between β-NiAl, γ'-Ni_3Al and γ-Ni_{ss}. For example, 1027 ˚C and 1127 ˚C, isothermal sections published by Chart in 1980 show that Cr has no solid solubility in γ'-Ni_3Al while 1150 ˚C isothermal section published by Oforka in 1985 there is a solubility of about 10 at% of Cr in γ'-Ni_3Al which is lower than the solid solubility of 20 at% of Cr suggested by Jackson in his 1060 ˚C isothermal section published in 1978. Furthermore, there is disagreement as to whether there exists three-phase equilibrium between β-NiAl, γ'-Ni_3Al and γ-Ni_{ss}. According to Jackson (1978), three-phase equilibrium it is not possible at 1060 ˚C, and the same was concluded by Chart (1980) for 1027 ˚C. However, Chart (1980) gave three phase equilibria at 1127 ˚C as did Oforka (1985) at 1150 ˚C.

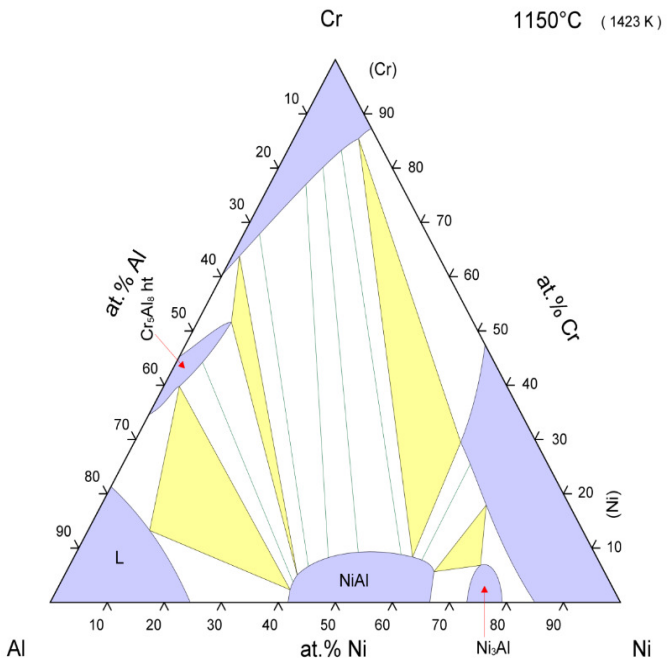

Figure 1.15 Isothermal section by Oforka at 1150 ˚C [ASM database].

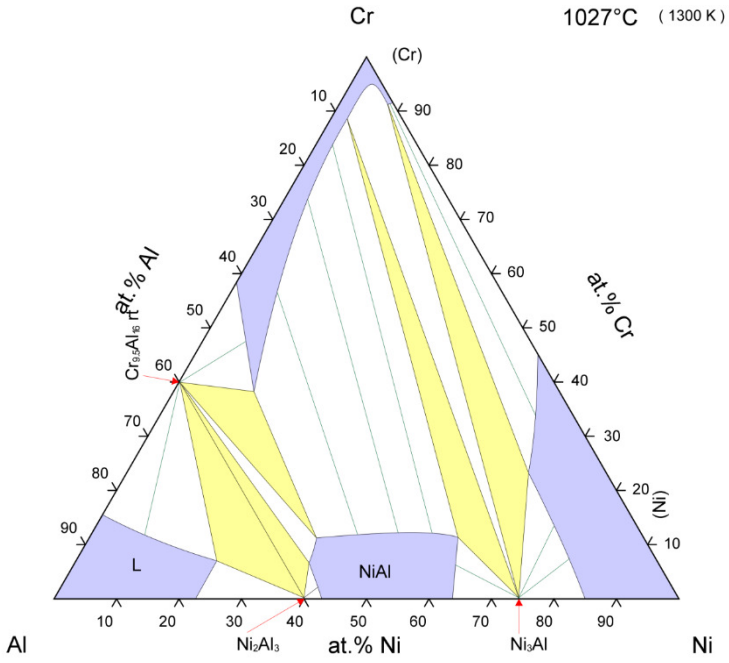

Figure 1.16 Isothermal section by Chart at 1027 ˚C [ASM database].

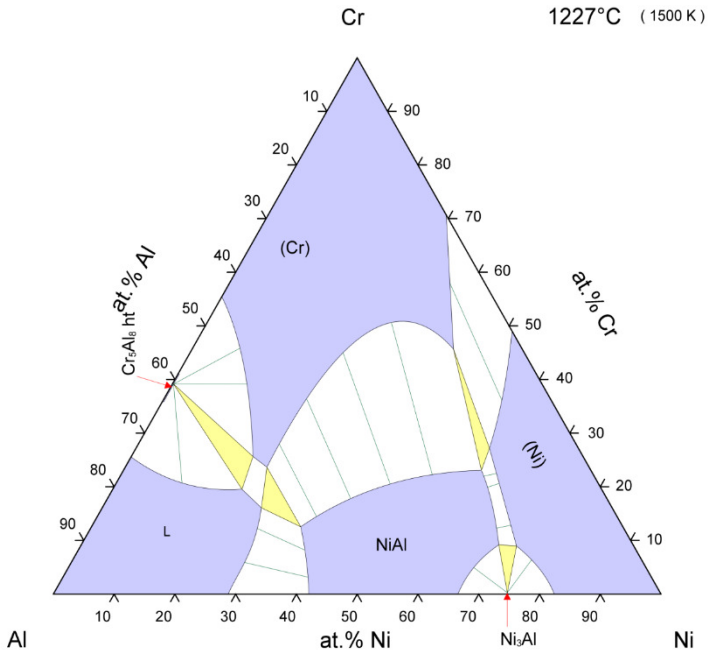

Figure 1.17 Isothermal section by Chart at 1127 ˚C [ASM database].

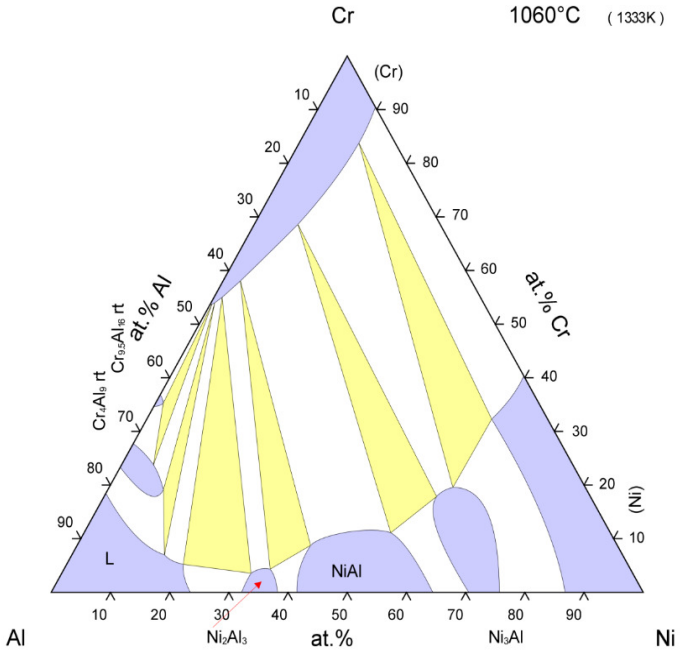

Figure 1.18 Isothermal section by Jackson at 1060 ˚C [ASM database].

There are numerous isothermal sections for the Ni-Al-Co system in the ASM database which show three-phase equilibria between β-NiAl, γ'-Ni_3Al and γ-Ni_{ss} but with significant differences, for the solubility of Co in γ'-Ni_3Al and the solubility of Al in γ'-Ni_3Al. Co is soluble in β-NiAl and there is also solubility of Co in Ni as the two elements form a complete solid solution. In some diagrams about 10 at% Co is soluble in γ'-Ni_3Al and in others as much as 25 at%. The solubility of Co in γ'-Ni_3Al is predicted to increase or decrease with temperature in some diagrams.

The above uncertainties about phase equilibria in Ni-Al and Ni-Al-X systems are inherent in existing thermodynamic databases for Ni superalloys, which have been shown in a recently completed "round robin" study [Tsakiropoulos, 2010] to affect the accuracy of predicted liquidus and solidus temperatures and volume fractions of phases for different heat treatment temperatures. The serious concern about the level of accuracies has favored a "re-assessment" of the Ni-Al-X phase equilibria and of the Ni superalloy databases.

1.11 Calcium-Magnesium-Alumino-Silicate (CMAS)

Deposits of molten calcium–magnesium alumino silicate, commonly known as CMAS, form (usually) in the top coat of TBCs (but there is increasing evidence that CMAS can also attack the BC) in aero engines at high temperatures when the oxidation environment has siliceous debris such as dust, sand, volcanic ash and runway debris. The siliceous debris forms glassy melts on TBC surfaces [Borom et al., 1996]. The molten CMAS penetrates the open structure of the top coat easily, causing the original top coat (usually YSZ in modern aedro engines) to dissolve in the CMAS and then the product of the dissolution process re-precipitates with a different morphology and composition. At low temperatures when the aforementioned contaminants are impacting as solid particles they can cause erosive wear or local spallation of the TBC. All these have as a result a minimal attack in the bulk of the coating but severe attack near the surface and the interface with the substrate, which is also partially dissolved by the melt. The damage mechanism depends on the exfoliation of discrete surface layers which are infiltrated with the molten CMAS as the latter freezes upon cooling and stresses arise due to the thermal expansion mismatch with the substrate [Krämer et al., 2006]. CMAS attack mainly affects high-performance jet engines that operate at high temperatures. In the case of land based electricity generation engines, it is practically harder to filter out the finest particles that

can be carried along with the input air and from alternative fuels such as Syngas [Levi et al., 2012].

1.12 H2 IGCC Process

The H2-IGCC project has been part of the European Union's 7th Framework Programme for Research and Development. H2-IGCC is part of the deployment for Integrated Gasification Combined Cycle (IGCC) with Carbon Capture and Storage (CCS) technology, based on low emission gas turbine technology operating with hydrogen rich Syngas, which increases the gas turbine efficiency and maximises fuel flexibility.

Syngas is a biofuel for high efficiency and low emission combined cycle power plant. In these power plants the gas turbines are making use of the high temperature combustion products in order to improve the efficiency of the power plant. Syngas is a fuel of hydrogen and carbon monoxide that is produced when coal is burnt in pure oxygen and steam in high pressure gasifiers. In these gasifiers, turbine-corroding gases are filtered out and the clean syngas is used in the gas turbine combustors. In order to improve energy efficiency of the plant, separation technologies can be used to produce hydrogen from syngas that can be fed into fuel cells and improve the energy conversion efficiency of the plant. This IGCC power plant is environmentally ideal as it captures and reuses CO_2.

As shown in figure 1.19 in a multishaft cycle in an IGCC power plant the hot exhaust gas from a gas turbine is utilized to generate steam in the steam turbine to provide power to drive a generator. This combination of gas and steam in IGCC plants give the highest efficiency electric power generation. In more detail in the IGCC power plant the hot exhaust gas from a gas turbine is used to generate steam in a steam cycle. The hot steam is expanded in a steam turbine providing power to drive a generator.

If H2 rich Syngas derives from coal in gas turbines combustion is not feasible with low NO_x systems. Current gas turbine technology for power and heat generation has been improved for natural gas. Barriers towards wider use of Syngas is the variability in composition and heating value of Syngas. Very high flow rates of cost intensive dilution gas (N_2, H_2O) are needed to combust Syngas in highly diluted diffusion flames and not control NO_x emissions.

The issues that apply to the BCs being used in H2 rich Syngas environment are the high temperature of gas therefore the BCs are exposed to higher temperature than

currently, therefore the interdiffusion increases and the fact that hot gas is more chemically aggressive it makes the CMAS related phenomena more serious.

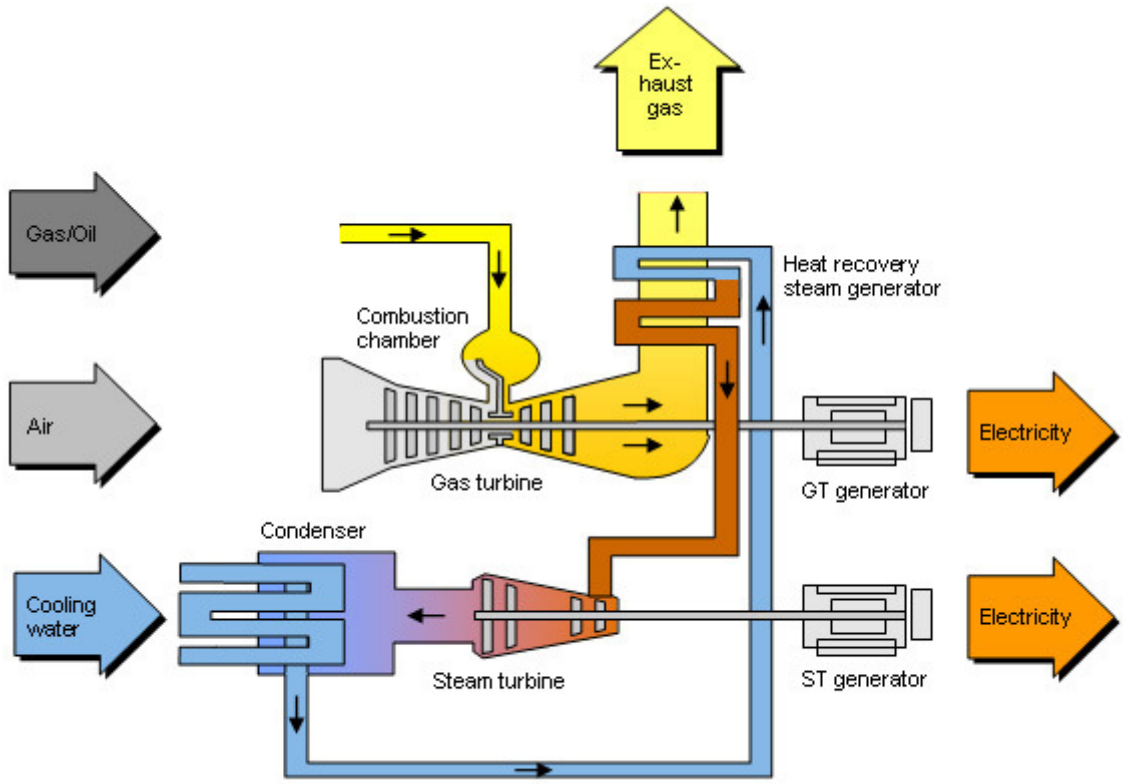

Figure 1.19 Schematic of a combined cycle power plant.

1.13 Substrate alloys

Ni based superalloys of interest to this project are the alloys IN738, IN939, RENE80 and CM247. These alloys contain transition metals (TMs) such as Co, Cr, Fe, Ti, Zr, Hf and refractory metals (RMs) such as Mo, W, Nb, Ta, Re and Al, B, Si and C.
Typical concentrations of the main alloying elements are given in Table 1.3.

Table 1.3. Typical concentrations (wt%) of the main alloying elements in the Ni superalloys of interest to this work [steelforge 2015 and iweb.tms 2015]

Ni superalloys of interest	Ni	Cr	Co	Mo	Fe	Al	Ti	Ta	W	Zr	C	B	Hf	Nb
IN 738	bal	16	8.5	1.7	-	3.5	3.5	1.7	2.5	0.05	0.09	0.010	-	2
IN 939	bal	22.4	19	-	-	1.9	3.7	1.4	1.6	0.1	0.15	0.010	-	1
RENE 80	bal	14	9.5	4	-	3	5	-	4	0.03	0.16	0.015	-	-
CM247	bal	8.1	9.2	0.5	-	5.6	0.7	3.2	9.5	0.015	0.07	0.015	1.4	-

1.13.1 Role of alloying elements

The elemental additions in Ni-base superalloys can be categorized as being

i. γ formers (elements that tend to partition to the γ matrix),
ii. γ' formers (elements that partition to the γ' precipitate),
iii. carbide formers and
iv. elements that segregate to the grain boundaries.

Gamma phase formers (or elements that partition to the γ-Ni) are Co, Cr, Mo, W, Fe (in other words Group V, VI and VII elements. These solutes have atomic sizes only 3-13% different than Ni. Elements that are γ' formers (or elements that partition to the γ') are the Al, Ti, Nb, Ta, Hf (in other words Group III, IV and V elements). The latter have atomic sizes that differ from Ni by 6-18%. The solutes forming carbides are Cr, Mo, W, Nb, Ta and Ti. Where the carbides are precipitated at the grain boundaries they have the tendency to improve the resistance to sliding and migration that would occur during diffusion creep. However, if they precipitate as a continuous grain boundary film, the fracture toughness of the alloy may be reduced, together with the ductility. Cr forms $M_{23}C_6$ and M_7C_3 in the grain boundaries so the hot corrosion resistance is improved and TCP

phases are promoted. Mo forms M_6C and MC in the grain boundaries. Nb forms NbC in the grain boundaries. The primary grain boundary elements are B, C, Zr and provide grain boundary strengthening and improve the creep strength and the ductility. Their atomic diameters are 21-27% different than Ni [TMS, 2010]. Reactive elements such as Y, Hf, Si and Zr when present in small concentrations as alloying constituents in the bond coat, they improve the adherence of Al_2O_3 and Cr_2O_3 scales and significantly reduce susceptibility to spallation during thermal cycling. Alloying with Al and Ti promotes the formation of the γ' phase. The γ' phase size can be precisely controlled by careful precipitation hardening heat treatments. Co, Fe, Cr, Re, Nb, W, Mo, Ta, V, Al, Ti are solid solution strengtheners both in the γ and γ' phases. Ta not only has a high strengthening effect in the matrix like Mo but it also increases the γ' volume fraction. Re leads to an improvement in creep strength. Some of the enhanced resistance to creep comes from the promotion of rafting by Re which partitions into the γ phase and makes the lattice misfit parameter more negative. Re reduces the overall diffusion rate in Ni based superalloys and retards coarsening [Tsakiropoulos, 2010]. Oxidation or corrosion resistance is provided by elements such as Al and Cr [TMS (2010), Levitin (2006), Sims et al. (1992)].

Excessive quantities of Cr, Mo, W and Re promote the precipitation of intermetallic phases which are rich in these elements [Krämer et al., 2006]. In Rene80, Cr, B, Zr, and Hf reduce oxygen embrittlement [Woodford, 2006]. In CM247, by decreasing the amount of Cr and increasing Re there is an increase in high temperature capability. Re increases high temperature creep strength but is harmful for high temperature corrosion [Gurrappa, 2008].

1.13.2 Manufacture of the alloys

The Ni based alloys IN738, IN939 and Rene80 can be conventionally casted (CC) or directionally solidified (DS) to obtain columnar grains parallel to the tensile axis or can have a single-crystal (SX) structure. CM247 is specifically designed for directionally solidified (DS) blades. The modified alloy CM247 LC, which is a low carbon alloy, demonstrates exceptional resistance to grain boundary cracking during directionally solidified (DS) casting [Tsakiropoulos (2010), Das et al. (2000)].

1.14 Mechanical integrity of bond coat

The mechanical integrity of the bond coats depends on the degradation of coatings resistance to high temperature which proceeds either by loss of coating constituents due to oxidation and corrosion, which results in loss of Al from coating to create a thin protective layer of Al_2O_3 on the surface, or by interdiffusion of the coating-substrate which results in diffusion of alloy elements into the coating [Rhys-Jones, 1989]. Coatings inspected after service show that often the TGO is wrinkled, wavy or convoluted and that contact with the BC is lost. The above have been attributed to the development of compressive stresses in the TGO that cause it to deform as it grows. It is also believed that the TGO grows laterally owing to the formation of new oxide at g.bs (via the diffusion of oxygen and Al, as discussed previously). A mechanism that has been suggested envisages the Al ions moving outward along short circuit paths in the alumina and the oxygen ions moving along the alumina g.bs [Prescott and Graham, 1992].

When degradation of the platinum-aluminide (PtAl) coating occurs it is due to loss of aluminium from the coating to form protective Al_2O_3 on the surface and this oxide is then spalled due to thermal cycles and erosion. Consecutively the coating provides additional aluminium to form new aluminium oxide [Bernstein, 1991]. Platinum improves the spalling resistance of the alumina scale either by reducing the stresses in the scale through an enhanced diffusional-creep process or through enhanced grain-boundary sliding [Das et al., 2000]. For instance, the Pt-Al coating provides superior cyclic-oxidation protection to CM-247 that becomes more prominent as the cyclic-oxidation temperature increases. Both alumina and spinel were formed during oxidation of the bare alloy and the coating and oxide spallation under cyclic oxidation of the coatings was thought to be a result of spinel formation [Das et al., 2000].

A key aspect that results in TGO spallation is the yttrium concentration in the bond coat. When it is decreased beneath a critical level then its positive effect on TGO adherence is lost. Oxide spallation might be affected by a number of factors such as the different stress generation and relaxation due to the presence of TBC and superalloy, the interdiffusion processes and the surface condition [Toscano et al., 2006]. TBC spallation life is lowest when the rate of oxidation is greatest and vice versa [Reed, 2008].

The coating system is designed to ensure that the surface temperature of the coated component is acceptable for the specific material. This is mainly the job of the top coat that provides thermal insulation and allows a temperature gradient to be established between the hot gases and the substrate surface. In a modern aero engine, the TET (turbine entry temperature) can be ~ 1500 °C and the surface temperature of a state of the art superalloy can be ~1125 °C. Failure of the coating and in particular coating spallation can cause creep and oxidation damage to the substrate. Thus, the integrity of the coating system is of paramount importance. In figures 1.20-1.22 some typical features of failures in coating systems (BC/TGO/YSZ) are shown.

Delamination cracks are common at the BC/top coat interface and occur during thermo-mechanical cycling. These cracks together with cracks in the TGO and the top coat contribute to damage development and the eventual failure of the coating system [Brodin et al., 2006]. The main failure mechanism depends on whether the operating conditions are predominantly isothermal or cyclic [Spitsberg et al., 2005]. Therefore the system durability is dominated by cracks evolving in the TBC and at the TBC/TGO interface. Coalescence along the TGO/bond coat interface constitutes only a small fraction of the life [Spitsberg et al., 2005]. However, there are additionally at least five different failure mechanisms [Evans et al., 2001] which depend on the bond coat chemistry and microstructure and the method used to deposit the thermal barrier layer.

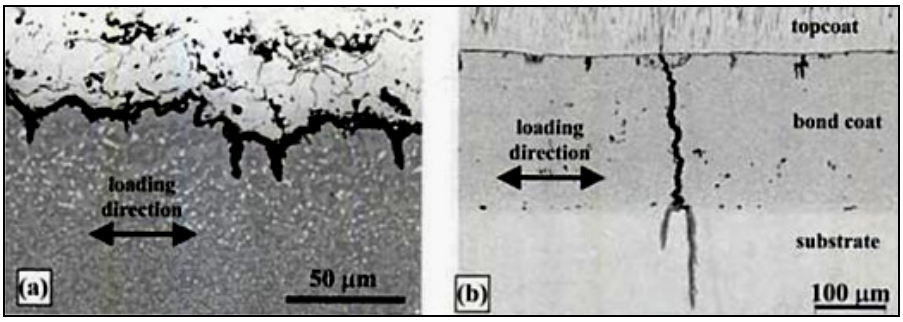

Figure 1.20 Cracking of TBC systems tested with high mechanical strain: a) topcoat-bond coat interface in a plasma sprayed coated specimen where several cracks started at the valleys of the interface and grew into the bond coat, b) cracking through the bond coat in an EB-PVD coated specimen where crack initiation is linked to inhomogeneities at the interface [McGaw et al., 2003].

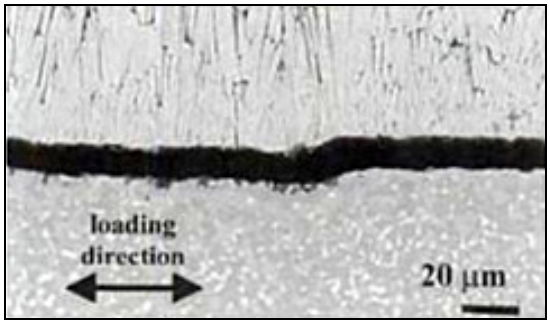

Figure 1.21 Centre of delamination of the topcoat from the bond coat in the EB-PVD coated specimen of Figure 1.20(b) tested with low mechanical strain [McGaw et al., 2003].

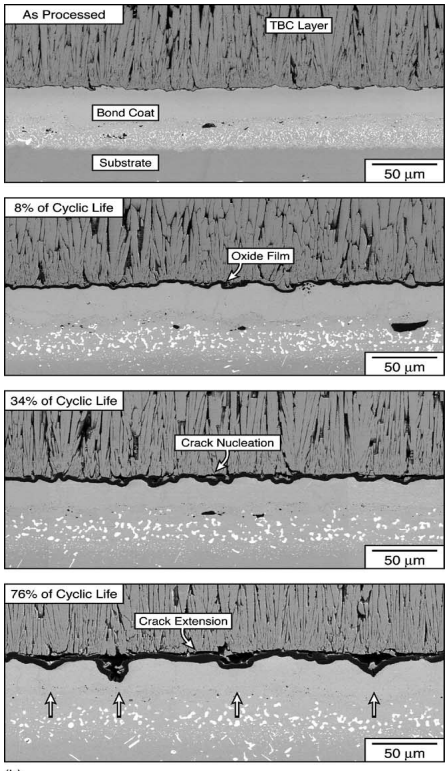

Figure 1.22 Failure of a TBC system, driven by a cyclic instability in the thermally grown oxide layer. The cross-sectional images detail the micro-structural and morphological evolution of the TBC system at various stages of life. The imperfections that ratchet and the resulting crack nucleation in the TBC are evident after only 34% of the cyclic life. Both grew with further cycling [Mumm et al., 2001].

Segregation of impurities at the BC/TGO interface leads to degradation. The latter is not threatening the life of the coating system when the TGO instability dominates, but

becomes important when the instabilities are suppressed and failure occurs by edge delamination mechanisms [Spitsberg et al., 2005]. In the literature various mechanisms have been identified and/or proposed to account for the failures of coating systems. Among these mechanisms dominate those that focus on thermal-expansion mismatch stresses, the oxidation of the BC, and the continuously changing compositions, microstructures, interfacial morphologies, and properties of the components of the coating system [Padture et al., 2002]. A summary of factors that are thought to contribute to failures of coating systems is given in Figure 1.23.

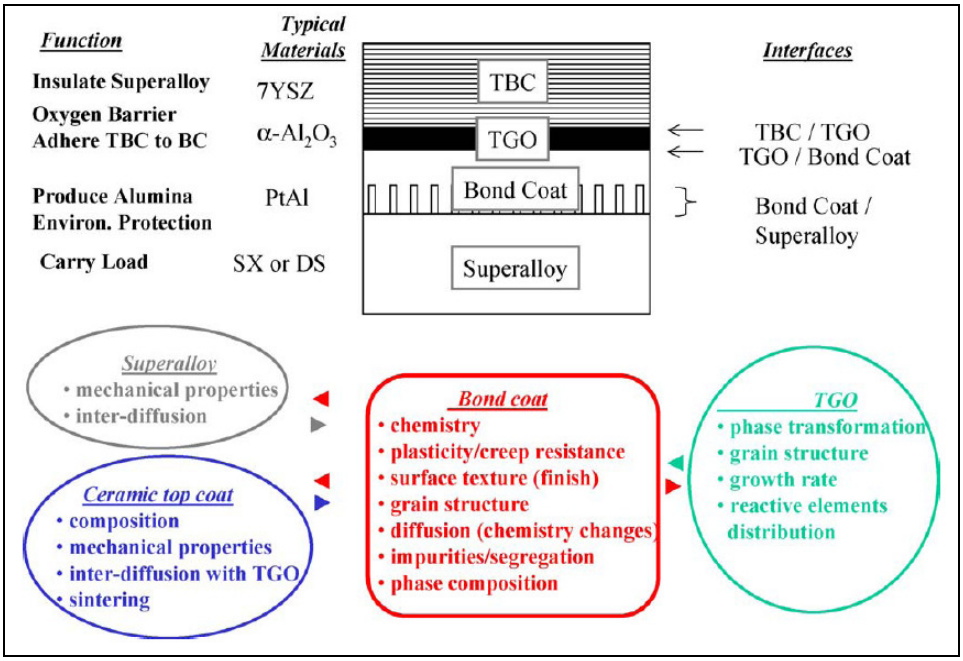

Figure 1.23 Schematic illustration of the factors that contribute to failure mechanisms of TBCs [Spitsberg and Moreb, 2005].

1.15 Mechanical properties

The high temperature strength of the coating is lower than that of the superalloy on which it is placed; as a result when it is subjected to loading, the yield stress of the coating is exceeded, so that the stresses in it are quickly relieved across the cross-section. When a thermal barrier coating is employed, the resistance to thermal cycling depends strongly upon the composition of the overlay coating onto which is placed [Reed, 2008].

The mechanical behavior of a TBC depends on the type of ceramic top coat (YSZ) and its thermal conductivity, thickness, and morphology, and on the continuity of the oxide scale (TGO) and the bond coat (BC). It also depends on the toughness, strength, ductility and coefficient of thermal expansion of the bond coat and on the properties of the substrate (superalloy). As a whole a TBC + substrate need to be tested in thermal mechanical/cycle fatigue and creep and for its thermal conductivity and thermal expansion behavior and its toughness, and strength. Special attention should be given to the mismatch in thermal expansion coefficients of superalloy substrate and TBC system which can cause thermal stresses during thermal cycling that will lead to TBC failure during operation by spallation. In this project other partners will evaluate the combination of ceramic top coat and bond coat in terms of thermal diffusivity, compatibility with the superalloy substrate and mechanical and environmental behavior of the whole TBC + substrate system as seen in Table 1.4.

Table 1.4 Properties of TBC materials.

Al_2O_3	T_m=2323 K[9] D_{th}=0.47*10^{-6} m^{2}s^{-1} (1273 K)[8] λ=5.8 W m^{-1} K^{-1} (1400 K)[10] E=30 GPa (293 K)[10] α=9.6*10^{-6} K^{-1} (1273 K) [13] v=0.26[10]
Al_2O_3 (TGO)	E=360 GPa (293 K)[13] α=8*10^{-6} K^{-1} (293-1273 K)[13] v=0.22[13]
NiCoCrAlY (BC of a TBC)	E=86 GPa (293 K)[13] α=17.5*10^{-6} K^{-1} (293-1273 K)[13] v=0.3[13]

where D_{th} = thermal diffusivity, E = Young's modulus, α = thermal expansion coefficient, λ = thermal conductivity, v = Poisson's number, T_m = melting point, TGO = thermally grown oxide on bond coat (BC) [Cao et. al, 2004]

Chapter 2 – Experimental Procedures

2.1 Selection of alloys

Failure of commercial TBCs occurs at the interface of the TGO with either the BC or the top coat. A major drawback for improving coating lifetimes is the oxidation of the bond coat. In this research the alloys were designed to form a protective α-Al_2O_3 scale during high temperature operation. One of the concerns is the good adhesion of the thermally grown oxide scale with the bond coat as any spallation of the Al_2O_3 scale would result in loss of the top coat. The substrate-bond coat system can affect the growth and adhesion of the oxide scale and the integrity of the BC-substrate interface. For a commercial metallic substrate like Rene80, there is a concern about possible inter-diffusion of elements between the two components of the coating system. The major concern is loss of Al from the bond coat below the critical level required for Al_2O_3 formation. In the case of Rene80, the uncoated substrate has low Al content ~3 wt%, therefore, it is unlikely that enough Al will diffuse from the substrate to the bond coat.

After careful study of the literature [see Chapter 1, Li et al. (2010), Musil et al. (1997)] where commercial BC alloys and their microstructures were studied, we concluded that our series of BC alloys should be of the MCrAlY type in an effort to minimize bondcoat/substrate interdiffusion, to improve resistance to hot corrosion, to form an adherent oxide scale and to have good compatibility with the top coat. Commercial alloys of interest were the Amdry 995 and Amdry 997 that provide oxidation resistance and maintain sulphur content at very low levels in the BC/TGO interface as segregation of sulphur at the BC/TGO interface reduces the TGO adhesion [Smialek et al, 1994]. Ta was used as an alternative element to Re to reduce material costs. Hf was added to improve the adherence of Al_2O_3 scales with the coating and Si to promote the adhesion of the BC/TGO [Padture et al. (2000), Pint et al. (2000)].

Chromium was added in our alloys to enhance high temperature strength, prevent internal oxidation which occurs at low aluminium content (8.5-16.2 wt%), and improve resistance to Type I and II corrosion (see section 1.7 in Chapter 1). Chromium and tantalum were also expected to be more effective under hot corrosion conditions in the aggressive environment of our project (Type II hot corrosion and H_2 rich environment). Ta

was also chosen to improve Al_2O_3 formation through spinel $TMTaO_4$ formation, where TM is a transition metal like Ti that exists in the RENE80 substrate. Chromium, cobalt and aluminium additions are vital for both types of hot corrosion, although high aluminium contents can lead to embrittlement of the bond coat. Yttrium, like the Hf addition improves adherence of the Al_2O_3 oxide scale with the coating and alleviates stresses from the thermal expansion mismatch. Hafnium also controls the Al_2O_3 growth as it is thought to precipitate at aluminium grain boundaries and restricts Al_2O_3 growth. Addition of silicon is also known to affect the growth kinetics of Al_2O_3 and the stability of Cr_2O_3, if formed [Tsakiropoulos, 2012].

The selection of the BC alloys of this study was informed by the results of the literature review and discussions with H2-IGCC project industrial partners who provided some data about commercial BC alloys used in conventional (i.e., not IGCC) plants. It has been decided to design Ni-Co-Cr-Al alloys with/without reactive element additions and additions of Y and Si that would be produced by solidification under conditions of high cooling rates to "simulate" the non-equilibrium conditions during BC deposition by LPPS (low pressure plasma spraying, see section 1.2.2 in Chapter 1) which are used by industrial partners in the H2-IGCC project. The alloys made in this work are identified with the codes EKi (i=1, 2, 3, 4 and 5), AC for the as cast condition, HT1 for the first heat treatment, HT2 for the second heat treatment and TGA for the oxidized condition. The alloy compositions are given in Table 2.1.

The alloys of this project given in Table 2.1 are bond coat alloys that contain Ni, Co, Cr, Al, Ta, Y, Hf and Si. In addition to the aforementioned roles of solute elements, the following was also taken into account when designing the alloys EKi (i=1 to 5). Ni forms stable, high melting point intermetallic compounds with aluminium such as β-NiAl and γ'-Ni_3Al. The presence of Al enhances oxidation resistance.

Table 2.1. The alloys selected for this work (nominal compositions, in at %).

Alloy and condition	Ni	Co	Cr	Al	Ta	Y	Hf	Si
EK1-AC	43.1	20.4	20.1	16.4	-	-	-	-
EK2-AC	42.7	20.1	19.8	16.3	1.1	-	-	-
EK3-AC	42.5	20.1	19.8	16.2	1.1	0.3	-	-
EK4-AC	42.4	20.1	19.7	16.2	1.1	0.3	0.2	-
EK5-AC	40.9	19.3	19.1	15.6	1.1	0.3	0.2	3.5

Co helps to improve corrosion resistance and strength at high temperatures and is believed to suppress the γ'-Ni_3Al and instead promote β-NiAl formation [Achar et al, 2004]. Co can also easily substitute nickel atoms and improve corrosion resistance in sulphur containing environment. Cr added to Ni-Al or Co-Al alloys reduces the critical level of Al needed to form protective $A1_2O_3$ scale. Furthermore, when Cr is alloyed with Ni and Co, and with minor additions of Al and Si (1-5%), it forms microstructures that are resistant to both type I (higher amounts are required ~ 25-40% Cr) and type II (lower amounts are required ~ 15-20% Cr) hot corrosion but decreases creep resistance. Y addition to Ni-Al or Co-Al alloys improves the adherence of Al_2O_3 scales to base material. At Y concentrations up to 0.01% the Y is in solid solution, above this level intermetallics can form. Hf enhances the grain boundary strength. Ta when added to Ni-Al or Co-Al alloys enhances their resistance to high temperature hot corrosion. Silicon, when alloyed with Ni or Ni-Cr, forms intermetallic compounds that are not as stable as those with Al. The dilution of Al in coatings by the diffusion of Ni out of the substrate is the process observed to occur most frequently. The existence of high contents of refractory metals such as Ta, W and Mo in the substrate seems to lower the nickel activity and also increase the stability against diffusion [Goward, 1986].

2.2 Preparation of ingots

Alloys were prepared using pure elements in forms of billets (Ni:99.99 wt%, Co:99.99 wt%, Cr:99.99 wt%, Al:99.99 wt%, Ta: 99.9 wt%, Y:99.95 wt%, Hf:99.9% and Si:99.9%). Small buttons of 10 g and approximately 2 cm in diameter were produced for each alloy. Alloys were prepared using clean melting elemental charges in a water cooled Cu crucible in an arc-melter that was evacuated to $8*10^{-5}$ Torr before melting in high purity argon atmosphere. Arc melting was used as it was the only facility available at this project and the fast cooling rates would be similar with PS. Arc melting was performed under a voltage of ~ 50 V and a current of ~ 600 A. Ti sponge was melted before the elemental charge to getter oxygen in the arc melter. A non-consumable W electrode was used and at least four melts were made to ensure homogeneity. The elements were melted in pairs because of their different melting points, for example for the alloy EK4 Ni and Hf were melted together, Co and Y were melted together, Cr and Ta were melted together and all these pilled up with Al in the bottom of the crucible to minimize Al loss.

2.3 Specimen preparation

Each button was mounted in bakelite and then sectioned using an ISOMET 5000 Buehler linear precision saw with an abrasive cutting wheel. The buttons were cut parallel to the bottom of the Cu crucible. Specimens from the bulk of the alloy/buttons were cut for use for microstructural characterisation. The specimens for use in microscopes were mounted in conductive bakelite. They were ground and polished using graded abrasive silicon papers of 400, 800 and 1200 grit. The specimens were then polished using 9 μm and then 3 μm water based diamond suspension and for the final polishing an acidic alumina suspension diluted with up to 50% water was used to ensure a smooth scratch free surface. The samples were then immersed in alcohol and cleaned in an ultrasonic bath. The buttons/ingots were cut parallel to the bottom of the Cu crucible, as illustrated below (figure 2.1) and all the samples were taken from the centre of the ingot in order to ensure that homogeneity and same cooling rates applied. Multiple melts and ingots were produced for the purposes of SEM/EDS, XRD, TGA as samples had to be taken as shown below from the same part of the ingot each and every time.

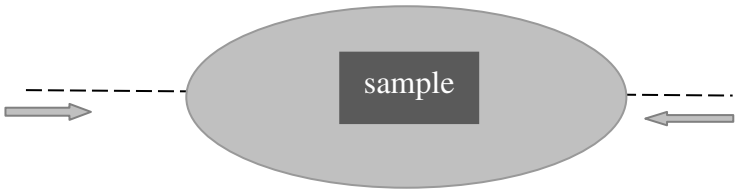

Figure 2.1 Schematic diagram of the catsed ingot and the place where the samples were taken from.

For the thermo-gravimetric (TGA) experiments small cubes ~ 3x3x3 mm^3 were cut from the bulk of the ingots. Their surfaces were manually ground to 1200 grit before TGA. The dimensions of each sample were measured using a micrometer and then the software "Measure Axio Vision" that was connected with an optical microscope in order to calculate their surface area. More information for the TGA experiments will be given in section 2.7.

2.4 Heat treatment (HT)

Specimens were taken from the bulk of the buttons for heat treatments. The first heat treatment (HT1) was for 24 hrs at 1200 ˚C and the second one (HT2) was another 24 hrs at 1200 ˚C, i.e., 48 hrs in total. The heat treatments took place in a muffle furnace in air and the specimens were placed in the hot zone of the furnce the temperature of which was monitored by the thermocouple. The specimens were heated with a heating rate of 3 degrees per min, then held at temperature for each 24 hrs period and then taken out and left to cool down in air at room temperature. The 1st heat treatment was decided to take place at 1200 ˚C for 24hrs as phase transformations happen quicker at high temperatures, the highest temperature that the alloy would experience in service and the substrate can operate are 1150 ˚C and also Ni-Cr-Al existing phase diagrams are around 1200 ˚C. The 2nd heat treatment was at 1200 ˚C for 48 hrs in order to check if phase transformations have finished or not and during plasma spraying the layers of powder are sprayed one on top of the other at high temperature so this is like a 2nd heat treatment.

2.5 X-ray diffraction (XRD)

For phase identification in the as cast and heat treated alloys and oxidised samples X-ray diffraction (XRD) was used. Phase analysis for the thin oxide scales formed on the

oxidised samples was performed with glancing angle X-ray diffraction (GAXRD). Individual phases and their crystal structures were identified using the JCPDS (Joint Committee of Powder Diffraction Standards) data. The specimens used for the XRD studies were not in powder form since the alloys could not be pulverized and thus texture effects from the microstructure are likely to have had an effect in the X-ray diffractograms.

2.5.1 Conventional X-ray diffraction

In this study a Siemens D5000 X-ray diffractometer was used for the XRD studies of the bulk microstructures of the as cast, heat treated and oxidised samples. The diffractometer used CuKα (λ=1.54178 Å) radiation that was excited by an acceleration voltage of 40 kV and a current of 30 mA. Every solid crystalline compound gives its own unique X-ray diffraction pattern, consisting of a set of 'Bragg peaks'. The positions of the peaks are related to the unit cell dimensions and symmetry. Peak intensities are determined by the 'distribution of atoms in the unit cell of every crystalline phase present in the sample'. The diffraction pattern for an alloy can be considered unique for each specific one. Therefore, when XRD data is collected, the diffraction patterns can be used to identify what phases are present in an alloy. This specific diffractometer (Siemens D5000) uses for phase analysis work Bragg-Brentano (also known as reflection) geometry. A scan range between 20-90 2θ was used to get diffraction data from both primary and secondary phase peaks. The step size 0.02 degrees per second was used to improve the signal to noise ratio to distinguish between two peaks that were very close to each other. XRD data was also collected for the sample holders and the Apiezon putty that was used to mount the samples.

In a cubic system with lattice parameter (unit cell side) a, the (hkl) planes are separated by:

$$d_{hkl} = \frac{a}{\sqrt{h^2 + k^2 + l^2}}$$

where d is the interplanar spacing of the (hkl) plane. The measured d spacing values may be affected by errors due to instrumental factors and by solute additions that change the positions of diffraction peaks compared with those expected from the JCPDS data.

2.5.2 Glancing angle X-ray diffraction

The Siemens D5000 X-ray diffractometer with CuKα (λ=1.54178 Å) radiation was also used for glancing angle X-ray diffraction. This technique is suitable for the study of thin films, like an oxide scale on an oxidised sample surface, by reducing the interference from the sample substrate and increasing the absorption path of the incident beam within the scale itself. In this technique, parallel, monochromatic X-rays fall on a sample surface at a fixed incidence angle and the diffraction profile is recorded by a detector. The penetration depth of X-rays in the material depends on the incidence angle (glancing angle). When the incidence angle of the X-ray beam decreases, the diffracted and scattered signals at the 2θ angle arise mainly from the limited depth from the surface and in this way the detection of the phases present in the scale is possible. By varying the glancing angle it is possible to undertake depth profiling of surface layers.

In order to avoid in our X-ray scans the signal interference from the substrate, the calculated depth should be smaller than the oxide scale thickness observed in backscatter electron images of the microstructure in a cross section of the oxidised alloy. Thus, we choose to stop at a glancing angle of 5˚ degrees. According to the literature when oxidation takes place at high temperatures transition aluminas may be observed during the initial stages of oxidation. In the literature the first phases to form have been identified as Ni(Al, $Cr)_2O_4$ and NiO. The NiO grows rapidly and Cr_2O_3 forms beneath it and eventually becomes continuous. Below Cr_2O_3, Al_2O_3 develops as a metastable phase and transformation of Al_2O_3 to α-Al_2O_3 occurs upon its incorporation into the external scale. Thus, by scanning the oxidised samples at two different glancing angles it was checked if Cr_2O_3 and α-Al_2O_3 formation or formation of any other oxide and whether one oxide had grown below another. The glancing angle ranges used for the as cast and the oxidised EK series alloys after exposure for 100 hrs at 975 ˚C were 2.5 and 5 degrees.

2.6 Scanning electron microscopy (SEM)

An objective of this project was to study the effects of alloying additions on the microstructure of the BC alloys, and to understand the role of the alloying additions on phase selection and stability and oxidation behavior. Therefore, imaging of the microstructures, phase identification and qualitative and quantitative characterization were

necessary. There were done using SEM with EDS and WDS.

SEM was the most useful analytical technique to be used in this project as it gave secondary electron (SEI) and backscattered electron (BSI) images of the alloys and X-ray elemental maps through EDS/WDS. Electrons bombard the surface of the specimen and a variety of different signals is generated (including secondary electrons, backscattered electrons, characteristic x-rays) that can be used for the specimen characterization. Using secondary electrons, scanning electron microscopy (SEM) expands the resolution range from a few micrometers to a few nanometers depending on the capabilities of the microscope. In addition to the higher lateral resolution, SEM also has a much greater depth of field compared with an optical microscope, due to the small size of the final lens aperture and the small working distance. The main differences between secondary electrons and backscatter electrons are that SEI can give information regarding surface topography and compositional contrast whereas BSI can be employed for imaging the differences in the mean atomic number of different constituents of the samples (compositional contrast). The lateral resolution in SEI ranges from 5 to 100 nm whereas in BSI from 5 to 1000 nm and the information depth they give is 5–50 nm from SEI and 30–1000 nm from BSI. Factors like the appropriate kV and spot size as well the specimen surface after correcting focus, magnification, astigmatism, brightness and contrast can affect accuracy of results.

The SEMs that were used in our research were a Philips PSEM 500 equipped with Link Analytical ANIO software, a JEOL JSM 6400 equipped with Oxford Instruments INCA software, a FEI Inspect FEG equipped with INCA software and a Hitachi SU70 UHR (ultra high resolution) analytical SEM equipped with SDD (silicon drift detector) x-Act detect and WDS 700 system with five crystals.

2.6.1 Energy Dispersive Spectrometry (EDS)

EDS (energy dispersive spectrometry) in principle converts the energy of each individual X-ray into a voltage signal of proportional size. EDS makes use of the X-ray spectrum emitted by a solid sample bombarded with a focused beam of electrons to obtain a localized chemical analysis in principle (see figure 2.2). All elements from atomic number 4 (Be) to 92 (U) can be detected in principle. Qualitative analysis mainly identifies the lines in the spectrum owing to the simplicity of X-ray spectra. On the other hand EDS

quantitative analysis, determines the concentrations of the elements present by measuring line intensities for each element in the sample and for the same elements in calibration standards of known composition.

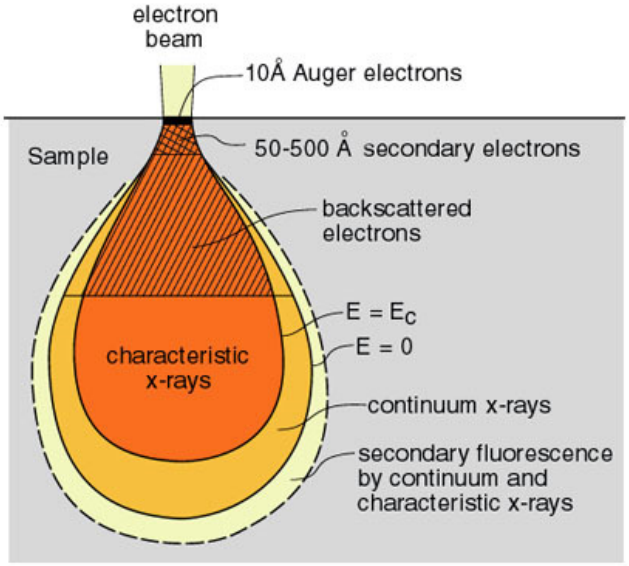

Figure 2.2 Schematic beam of electrons-specimen interaction volume [nau.edu].

The pear shape of the interaction volume is due to the characteristics of elastic and inelastic scattering. As electrons penetrate into the specimen they lose energy and thus the probability of elastic scattering increases which results in broadening of the interaction volume. Auger electrons coming from very close-to-surface are used for surface analysis whereas secondary and backscattered electrons are mostly used for SEM imaging and analysis. The characteristics X-rays are the main signals in EDS microanalysis to determine the chemical composition of the specimen. The interaction volume is a function of beam energy, specimen composition and beam incident angle. Equations 2.1 and 2.2 estimate the depth and width of the interaction volume respectively, for a perpendicular electron beam [nau.edu]:

$$x\ (\mu m) = 0.1\frac{(E_0)^{1.5}}{\rho} \quad (2.1)$$

$$y\ (\mu m) = 0.077\frac{(E_0)^{1.5}}{\rho} \quad (2.2)$$

where E_0 is the beam energy (keV) and ρ is the specimen density (g/cm^3). The beam energy is the kinetic energy of beam electrons which is equal to the SEM accelerating

voltage multiplied by the charge of electron. Therefore the accelerating voltage is a major factor to control the size of the interaction volume.

In our experiments most of the qualitative analysis for as cast and heat treated alloys took place in Inspect F whereas all the quantitative analysis was done in a Philips PSEM 500 and a JEOL 6400. An accelerating voltage of 20 kV was used for the analysis under which the electron beam size was about 1μm. Calibration for quantitative analysis was repeated almost every hour using a pure Co standard. High purity standards were used for EDS analysis for all elements such as Ni, Co, Cr, Al, Ta, Y, Hf and Si. Considering the spatial resolution, spot analysis was performed on particles of size $\geq$ 5 μm in diameter. Specimens were studied by EDS for large area analysis (0.5 mm x 0.5 mm), spot/point analysis and area analysis of eutectic microstructures. Large area analysis was taken at low magnification (x320) from several areas of the specimen. At least 5 large area analyses and point analyses were taken from different areas all around the samples. The analysis data presented in the thesis include the average, minimum and maximum values and the standard deviation.

2.6.2 Line scans and X-ray maps

Line Scans

The SEM electron beam is scanned along a preselected line across the sample while x-rays are detected for discrete positions along the line. Analysis of the x-ray energy spectrum at each position provides plots of the relative elemental concentration for each element versus position along the line. Line scans for our alloys, as cast and heat treated, were performed in a JEOL 6400.

Elemental Mapping

Characteristic x-ray intensity is measured relative to lateral position on the sample. Variations in x-ray intensity at any characteristic energy value indicate the relative concentration for the applicable element across the surface. One or more maps are recorded simultaneously using image brightness intensity as a function of the local relative concentration of the elements present. About 1 μm lateral resolution is possible. In our work elemental mapping was performed in a JEOL 6400, an Inspect F and a Hitachi SU70 for samples in as cast, heat treated and oxidised conditions.

2.6.3 Wavelength Dispersive X-ray Spectroscopy (WDS)

Wavelength dispersive X-ray spectroscopy (WDS) is a method used to count the number of X-rays of a specific wavelength diffracted by a crystal. Based on Bragg's law wavelength of the x-rays and the crystal's lattice spacings are related. Unlike the related technique of energy dispersive X-ray spectroscopy (EDS), WDS counts only the x-rays of a single wavelength at a time, not producing a broad spectrum of wavelengths or energies simultaneously therefore accuracy of WDS analysis is much higher. In our work, WDS was performed at 20 kV and a beam current of 8 nA, using a Hitachi SU70 for point analysis, qualitative and quantitative elemental mapping and qualitative and quantitative line scans for the oxidised alloys after exposure for 100 hrs at 975 ˚C. Pure elements of N, O, metals of Ni, Co, Cr, Al, Ta, Y, Hf, Si and Al_2O_3 and Cr_2O_3 compounds were used for standardization purposes. The oxygen and nitrogen concentrations were calculated based on SiO_2 and AlN standards.

To assist microstructural characterization of the oxidised specimens, qualitative and quantitative maps were used. The qualitative maps showed us what elements were present and where these elements where in the microstructure and this information was based on X-ray intensity. The quantitative maps converted the qualitative ones to quantitative information and then looked at every pixel in the qualitative maps to produce quantitative information at pixel level. This is useful for any changes in atomic or weight percentage from the raw data in the qualitative map.

2.7 Thermo-gravimetric analysis (TGA)

The temperature of the BC/substrate in gas turbines used for energy production operating in H2 rich Syngas environment will not exceed 1000 ˚C according to modelling work done by other partners in the H2-IGCC project, and most probably will be in the range 900-980 ˚C. Thus, the selected temperature for oxidation experiments was 975 ˚C. Thermo-gravimetric analysis (TGA) at 975 ˚C for 100 hrs was carried out with a Perkin Elmer Thermo-gravimetric Analyzer equipped with Pyris 1 TGA software. Cubic samples, 3x3x3 mm^3 in dimension were cut from the as cast alloys with an Isomet Buehler cutting machine with an Isocut diamond wafering blade. Their surfaces were ground to 1200 grit and the dimensions of each sample were measured using a micrometer and the Measure

Axio Vision software and the surface area was calculated. The sample weight was measured using a high accuracy scale before and after oxidation in order to verify in two different ways the weight change after the thermo-gravimetric analysis. Each sample was placed in a small alumina crucible that was positioned on the TGA balance, and then the balance was calibrated to the initial total weight. The sample was heated to the designed temperature (975 ˚C) and held at this temperature for 100 hrs. Then it was cooled in the furnace after isothermal oxidation was finished. Both heating and cooling rates in our experiments were 3 degrees per minute. The experiments took place in static air conditions where air was fed through a cylinder. The weight gain was calculated throughout the whole experiment but only the weight gain during the isothermal period is of interest and is calculated and used in the calculations in Chapter 5. All the samples were looked under SEM for structural oxide scale and microstructural characterization. They were carbon coated which gave high C content in the qualitative EDS spectra. A continuous curve of weight gain versus time was recorded by the software during the experiment. The weight gain was normalized against the initial surface area of the sample. Weight change/gain versus time graphs were plotted.

The oxide scales that formed after the thermo-gravimetric experiments were studied by glancing angle X-ray, see section 2.5.2. The cross sections of the oxidised alloys after 100 hrs at 975 ˚C were also studied. In order to study the cross sections of the oxidised samples the latter were cold mounted in epoxy resin. After grinding and polishing the cold mounted samples, carbon coating was applied for imaging and EDS/WDS analysis.

Chapter 3 – EK1, EK2 alloys

3.1 Introduction

Ni based superalloys in power plants are operating with a wide range of fuels using combined cycle power plant technologies. The increased demand for improvement of the performance of gas turbine engines in aircraft and marine propulsion and in power generation led to significant technological breakthroughs and the development of the thermal barrier coatings (TBCs). Ni based superalloys require protection for high temperature oxidation and type I and type II hot corrosion. MCrAlY overlay coatings are environmental protection coatings that can provide an optimized corrosion response over a wide range of turbine operating conditions that are likely to be encountered in utility turbines, working with multi-fuel capability.

Gas turbines are used either for propulsion or for energy production. Even though the research presented in this thesis is related with materials used in energy production, it is still relevant to aerospace because of the type of BC that is studied. BCs are usually of the MCrAlY type, which are similar to the BCs used in aerospace. In this specific FP7 EU project on H2-IGCC (Integrated Gasification Combined Cycle) plants, the materials are operating in H2 rich environment, where environmental problems like oxidation and hot corrosion are likely to occur with the BC. In this work new BC alloys are developed suitable for application using APS, therefore there are limitations in alloy design because of the availability of powders. Jülich, which is another partner in the FP7 project, is concentrating on the ceramic component of the TBC. The optimized coating will be evaluated by other partners in the project in simulated Syngas environment and for CMAS (calcium-magnesium-alumino-silicate) and CMAF (calcium-magnesium-alumino-iron) issues (see Chapter 1, section 1.11). The TGO that forms between the BC and the ceramic is usually Al_2O_3 or Al_2O_3 and Cr_2O_3 for the IGT's. In this particular project the BC's operating temperature is estimated to be between 920 to 980 ˚C. The aim of this project is to design, develop and evaluate BC alloys that form in situ Al_2O_3 oxide scales. Therefore, the interest is in the formation of high Al activity intermetallics in the BC, such as the β-NiAl or γ'-Ni_3Al.

The current study started with the selection of alloying elements based on commercial materials (see Chapter 1) in order to understand phase selection and stability in the bond coat in currently used systems in conventional plants and the role of the alloying additions in the bond coat in determining integrity and quality of the bond coat/substrate interface. Work on two selected bond coat alloys and the characterization of their microstructures will be discussed in this chapter. Cr and Al additions are very important in our study due to the fact that they play a crucial role for Type I and Type II hot corrosion (see Chapter 1, section 1.7). In Type I hot corrosion, Al is desirable whereas in Type II, Cr is desirable. Chromia is less effective in the presence of water vapor, Syngas environment in this project, therefore there is a need to have Al_2O_3 formation and thus a need to have high Al activity. Thus, there is an interest in the Cr and Al contents in the γ-Ni_{ss} and β-NiAl phases, in the as cast (AC) and heat treated (HT) conditions.

In this study is concentrated on Co and Cr rich, Ni-Co-Cr-Al based bond coat type alloys. This chapter is a report on the effects of Cr and Al in the as cast and heat treated (1200 ˚C/ 24hrs, 48hrs) microstructures of Ni-23Co-20Cr-8.5Al (wt %) (alloy EK1) and on the effect of Ta in the as cast and heat treated (1200 ºC/ 24hrs, 48hrs) microstructures of Ni-23Co-20Cr-8.5Al-4Ta (wt%) (alloy EK2) alloys which were investigated using scanning electron microscopy (SEM/EDS) and X-ray diffraction (XRD). The phases considered in the characterisation of the as cast and heat treated microstructures were the Ni_{ss} (γ), NiAl (β), Ni_3Al (γ' precipitates) and the lamellar eutectic (β-NiAl + γ-Ni_{ss}). It has been observed that both the size of the β intermetallics and the volume fraction of the lamellar γ-Ni_{ss} and β-NiAl in the microstructure, depend on time and temperature. Phase formation and stability with particular emphasis on solidification path and composition of phases will be discussed in this chapter.

3.2 Results

The materials system will consist of a directionally solidified (DS) nickel based superalloy RENE80 as substrate, a NiCoCrAl based bond coat (BC) applied by APS and a ceramic top coat like YSZ. Two bond coat alloys will be discussed in this chapter, the base alloy (EK1) with Ni, Co, Cr and Al additions and one alloy variant (EK2) with extra Ta addition. These alloys were studied in the as cast and heat treated conditions. The nominal compositions of the two BC alloys are given in Table 3.1.

Table 3.1. Nominal compositions of the alloys EK1 and EK2.

Alloy		Ni	Co	Cr	Al	Ta
EK1	wt %	48.5	23	20	8.5	-
EK1	at %	43.1	20.4	20.1	16.4	-
EK2	wt %	44.5	23	20	8.5	4
EK2	at %	42.7	20.1	19.8	16.3	1.1

3.2.1 Ni-20.4Co-20.1Cr-16.4Al (alloy EK1)

The EK1 alloy was designed to understand the basic composition with Cr and Al additions as the latter are important for Type I and Type II hot corrosion and tend to promote the formation of a protective oxide scale. Another objective was to study phase selection and stability under conditions of solidification at high cooling rates and to "simulate" the non-equilibrium conditions during BC deposition by APS [Eliaz et al. (2002), Goward (1998)]. In this alloy type, the Co addition is expected to stabilize the γ and β phases at all temperatures and at all Al levels and to suppress the γ' formation, as suggested by Achar et al. (2004).

3.2.1.1 As cast alloy (EK1-AC)

The average composition of the EK1 alloy in the as cast condition, as determined by EDS, is given in Table 3.2. Compared with the nominal composition, the alloy EK1 was slightly poorer in Co and Cr, less than 1 at%, and slightly richer in Al, around 1 at%. Considering the accuracy of the analysis technique (± 1%), this was considered satisfactory. The microstructure of the as cast alloy (EK1-AC), as suggested by the XRD data, contained the γ-Ni_{ss} solid solution and the intermetallics β-NiAl and γ'-Ni_3Al. In the SEM two phases were observed that exhibited light and dark contrast and a $(\beta+\gamma)_{eutectic}$, see Figure 3.1 and Table 3.2.

Table 3.2. EDS analysis data (at%) of the EK1 alloy in the as cast and heat treated conditions.

Area/Phase(s)	Ni	Co	Cr	Al
EK1-AC				
large area	42.9±0.2	19.7±0.4	19.9±0.1	17.6±0.5
γ (Ni_{ss})	42.5±0.3	21.4±1	20.5±0.6	15.7±1.4
β (NiAl) around γ (Ni_{ss}) (not in eutectic)	43.7±1.3	13±1.5	12.6±1.8	30.7±2.1
$(\beta+\gamma)_{eutectic}$	42.9±0.5	16.8±1.2	18.7±1.4	21.5±2.9
intermetallic phase lamellae in eutectic	43.9±0.8	15.1±1.5	15.6±1.9	25.4±2.8
γ (Ni_{ss}) between lamellae in eutectic	42.8±0.5	19.9±0.3	20.2±0.1	17.1±0.3
EK1-HT1 (1200 ˚C / 24 hrs)				
large area	43±0.2	19.6±0.3	19.4±0.08	17.9±0.2
γ (Ni_{ss})	42±0.1	21.6±0.2	22.1±0.2	14.1±0.2
β (NiAl)	45.8±1.3	11.8±0.2	9.4±1.5	32.9±0.7
prior $(\beta+\gamma)_{eutectic}$	43.5±0.5	18.3±0.9	17.7±1.3	18.6±5
EK1-HT2 (1200 ˚C / 48 hrs)				
large area	43.4±0.4	20.6±0.1	21.4±0.4	14.6±0.4
γ (Ni_{ss})	43.4±0.1	20.8±0.3	21.5±0.1	14.3±1.2
β (NiAl)	44.5±0.5	16.2±0.6	12±0.2	27.3±0.4

The lamellar eutectic was formed between γ-Ni_{ss} and β-NiAl as shown in figure 3.1 and its average composition was 42.9Ni-16.8Co-18.7Cr-21.5Al. The XRD data, figure 3.2, would suggest the presence of γ' in the microstructure. The peak identification was based on matching the superlattice and fundamental peaks from the database with the peaks from the diffractograms. The composition of some of the intermetallic lamellae was slightly poorer in Al compared with β-NiAl, Table 3.2 suggesting it could be γ'-Ni_3Al. It should be realized that the width of the intermetallic lamellae was not large, and thus errors in analysis are possible. The composition of γ in the lamellar eutectic was close to that elsewhere in the microstructure. The present microstructure was in agreement with those reported for coatings in the literature [Reed, 2008]. It is not clear though, whether the coating microstructures given in the literature are those in the as deposited condition or after heat-treatment (or after exposure to high temperature). There was also some variation in the EDS data for the β-NiAl, as shown by the standard deviation values in Table 3.2. Further analysis in β-NiAl regions showed that some β-NiAl where rich in Cr at% and had lower Al at% while others where rich in Al at% and had lower Cr at%.

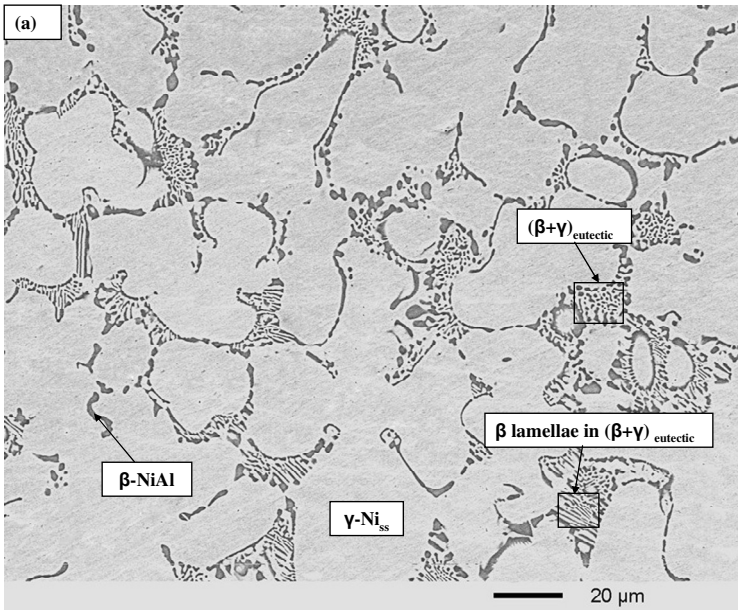

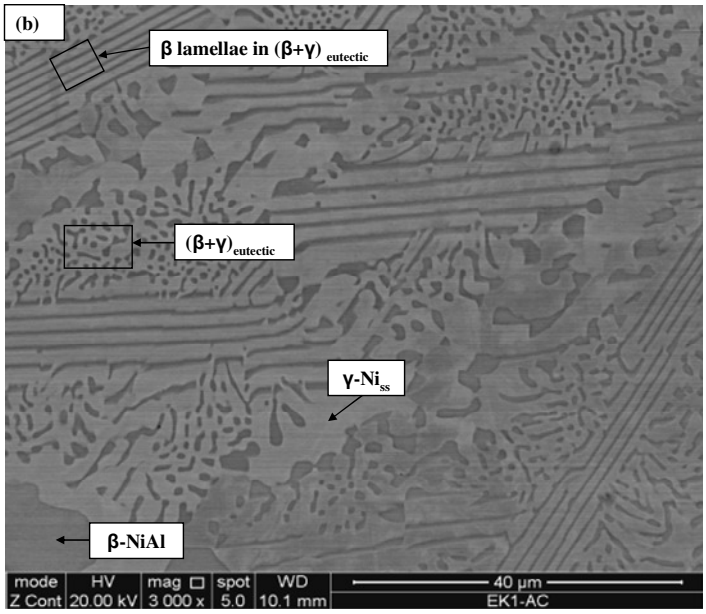

Figure 3.1 BSE images of the microstructure of EK1-AC.

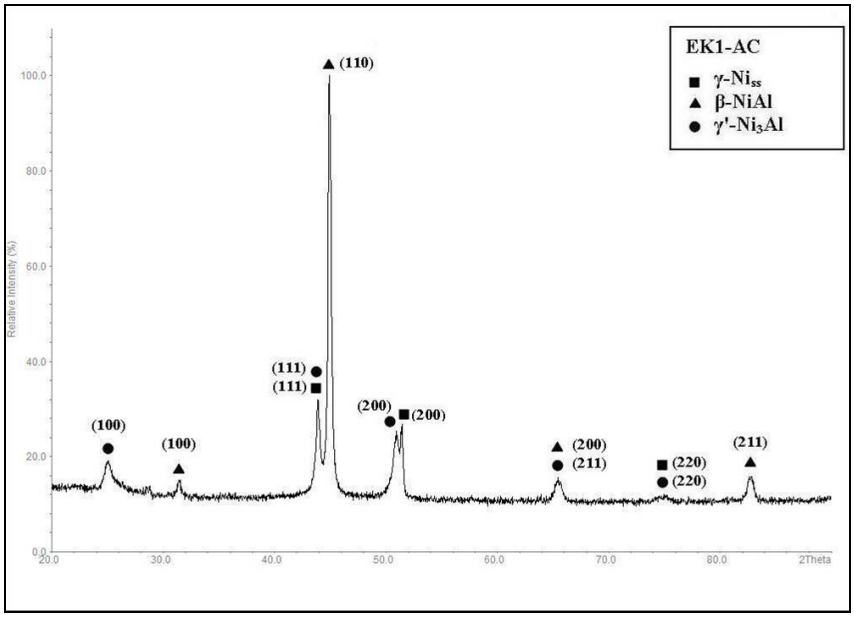

Figure 3.2 X-ray diffractogram of the EK1-AC.

3.2.1.2 Heat treated alloy (EK1-HT)

The first heat treatment (EK1-HT1) was for 24 hrs at 1200 ˚C. The large area analysis and the compositions of the phases are given in Table 3.2. For the former there was no significant difference in the average concentrations of the elements compared with

the as cast condition. The typical microstructure of the EK1-HT1 is shown in figure 3.3. After the first heat treatment two phases were present, namely the γ-Ni_{ss} and β-NiAl (see also Table 3.2). The β-NiAl was richer in Al compared with the as cast condition and its Co and Cr contents were slightly decreased.

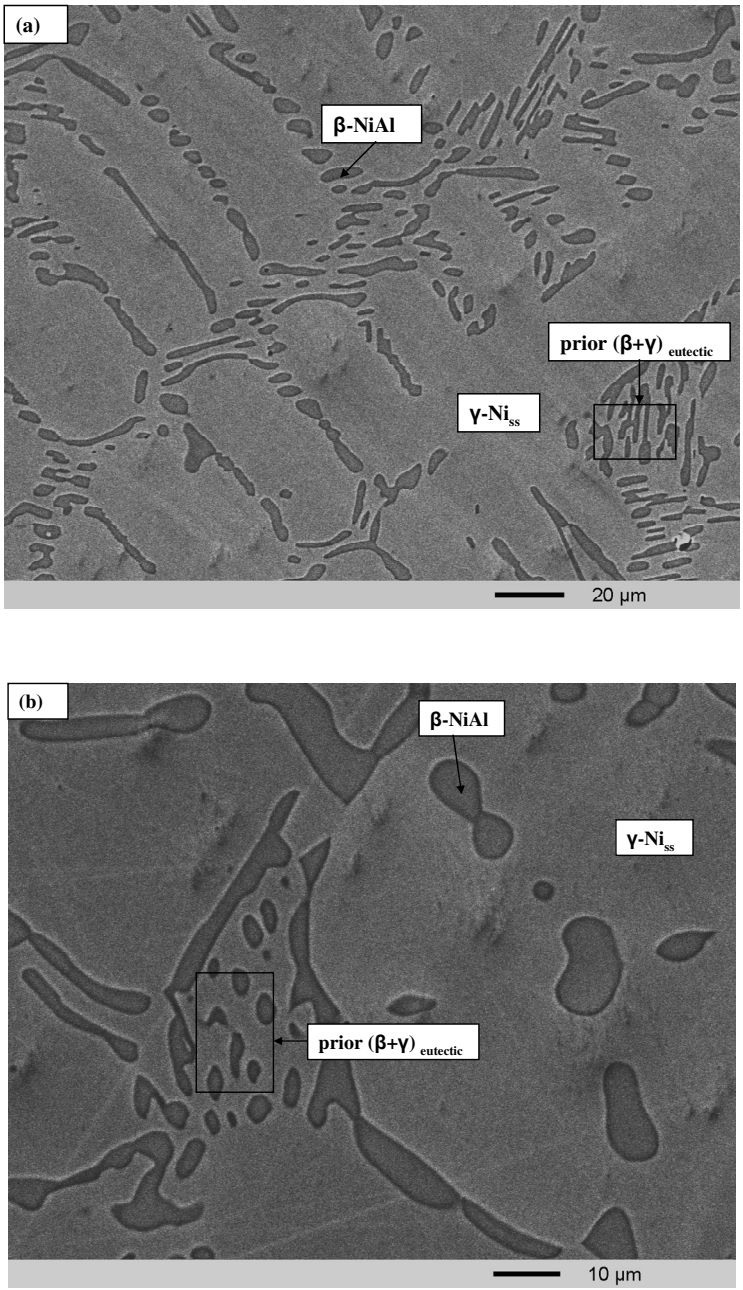

Figure 3.3 BSE images of the microstructure of EK1-HT1.

The XRD data (figure 3.4) would suggest the presence of the γ-Ni_{ss}, β-NiAl and γ´-Ni_3Al in the microstructure, however the EDS analysis did not confirm the presence of intermetallics with ~ 25 at% Al.

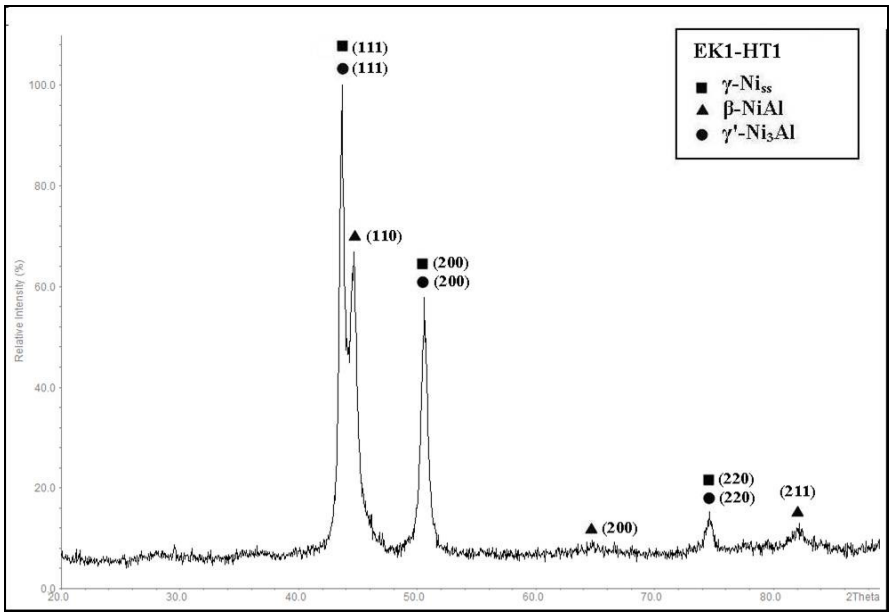

Figure 3.4 X-ray diffractogram of the EK1-HT1.

The second heat treatment (EK1-HT2) was for another 24 hrs at 1200 ˚C i.e., 48 hrs in total. The typical microstructure of the EK1-HT2 is shown in figure 3.5 and the EDS data is given in Table 3.2. The average composition of EK1-HT2 was poorer in Al compared with the as cast alloy. The XRD data (figure 3.6.) suggested the presence of γ-Ni_{ss}, β-NiAl and γ'-Ni_3Al but only the β-NiAl and γ-Ni_{ss} could be identified by EDS, see also Table 3.2 and figures 3.7. It should be noted that in the EK1-HT2 the major phase was the γ-Ni_{ss} with very low vol % of intermetallic, which could be imaged with difficulty using the Philips PSEM500 and Jeol 6400 SEMs. Using the Inspect F SEM, a second phase precipitation was observed in the γ-Ni_{ss} which was the β-NiAl as seen in figure 3.5.

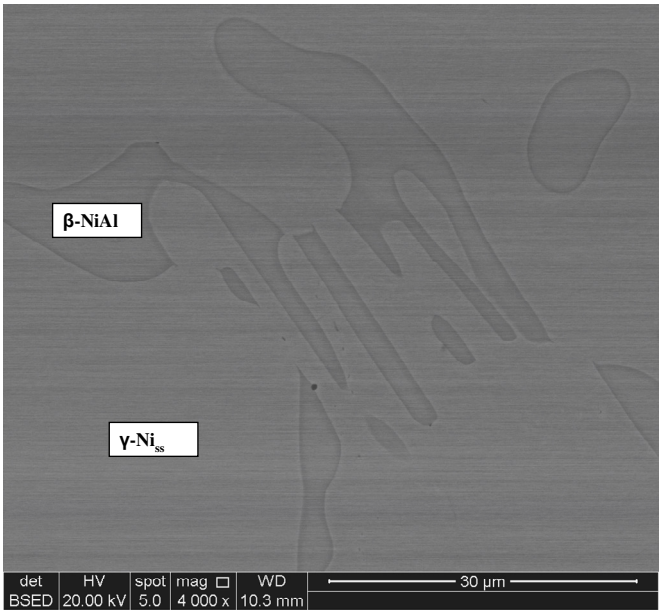

Figure 3.5 BSE image of the microstructure of EK1-HT2.

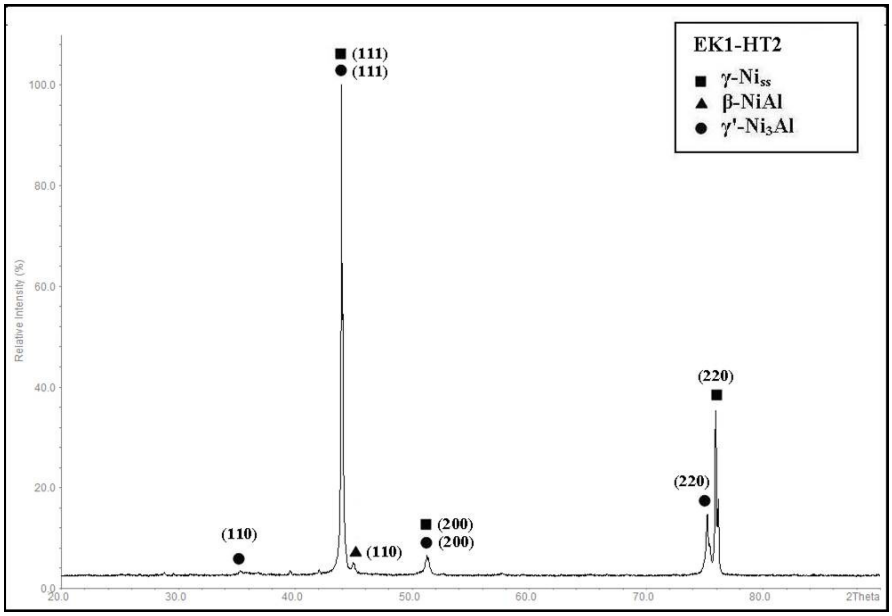

Figure 3.6 X-ray diffractogram of EK1-HT2.

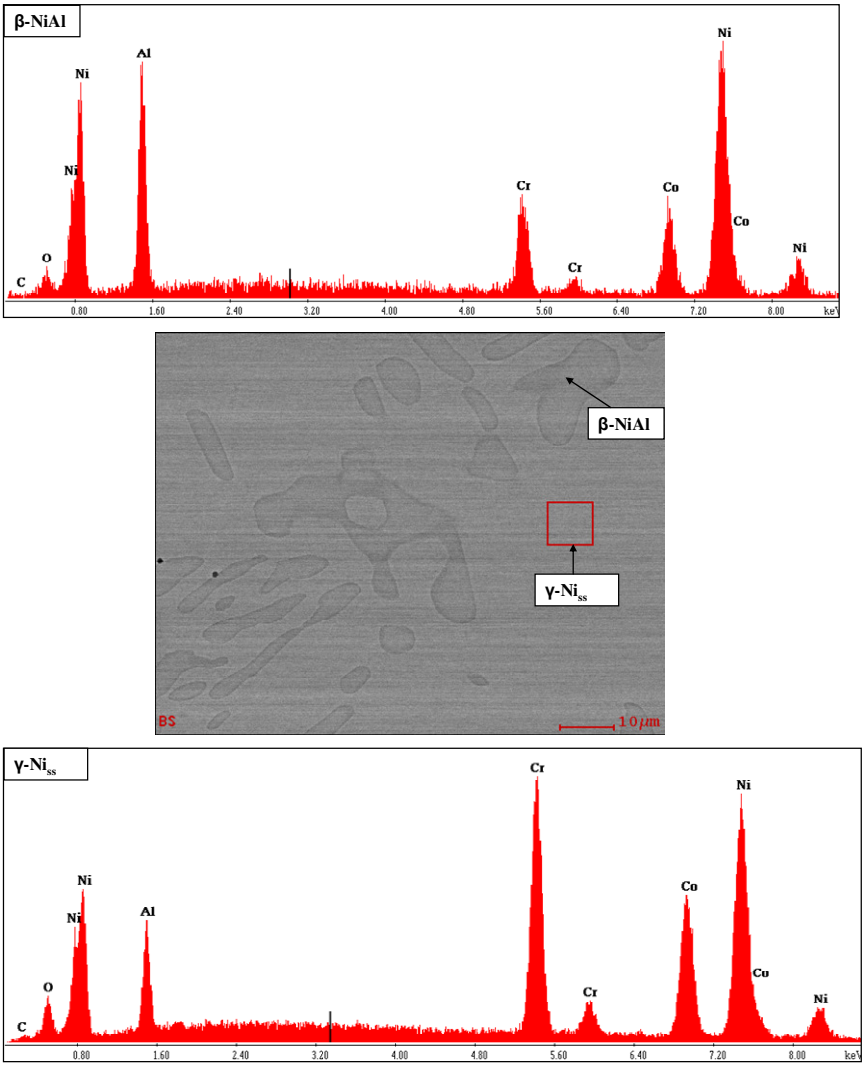

Figure 3.7 BSE image and EDS spectra of EK1-HT2 showing presence of Ni solid solution and NiAl intermetallic.

3.2.2 Ni-20.1Co-19.8Cr-16.3Al-1.1Ta (alloy EK2)

The EK2 alloy was designed in order to study the effects of Ta in the microstructure of MCrAlY alloys. Ta is used as an alternative alloying addition to the expensive Re. Ta was also expected to improve the refractiveness and oxidation resistance of the BC as well as to improve Al_2O_3 formation through spinel formation, and in synergy with Cr was expected also to improve the effectiveness of Cr in Type II hot corrosion behavior in H_2 rich environment [Pomeroy (2005), Viswanathan (2001), Schütze (2000)].

Table 3.3. EDS analysis data (at %) of EK2 alloy in the as cast and heat treated conditions.

Area/Phase(s)	Ni	Co	Cr	Al	Ta
EK2-AC					
large area	38.2±0.2	19.5±0.1	21.7±0.1	19.2±0.2	1.4±0.07
γ (Ni_{ss})	36.3±0.4	22.2±0.1	25.2±0.2	15.1±0.2	1.2±0.1
Ta rich γ (Ni_{ss})	36±0.5	19.9±1.8	25.2±2.9	14.4±2.2	4.5±2.8
β (NiAl)	39.6±0.5	15.7±0.2	15±0.5	28.4±0.8	1.1±0.1
$(\beta+\gamma)_{eutectic}$	37.8±0.3	19.4±0.4	20.9±0.9	20.7±1	1.2±0.2
EK2-HT1 (1200 ˚C / 24 hrs)					
large area	37.9±0.1	18.8±0.2	20.8±0.4	21±0.5	1.4±0.1
γ (Ni_{ss})	35.7±0.1	23.2±0.2	28.1±0.2	11.5±0.3	1.5±0.04
β (NiAl)	41.8±0.5	13.7±0.6	11.5±1	31.6±1.4	1.3±0.1
bright areas	35.3±0.5	22.4±0.7	26.9±1.4	13.7±1.8	1.6±0.05
EK2-HT2 (1200 ˚C / 48 hrs)					
large area	38.5±0.4	19.1±0.2	21.3±0.1	19.4±0.3	1.5±0.1
γ (Ni_{ss})	36.5±0.3	22.3±0.2	27±0.3	12.6±0.2	1.7±0.1
β (NiAl)	42.1±0.3	13.7±0.3	11.3±0.2	31.5±0.4	1.4±0.1

3.2.2.1 As cast alloy (EK2-AC)

The average composition of the as cast alloy (EK2-AC) is given in Table 3.3 and shows that the ingot was slightly poorer in Co and Cr, richer in Al and slightly richer in Ta compared with the nominal composition (Table 3.1). The microstructure consisted of γ-Ni_{ss}, β-NiAl intermetallic and a eutectic of these phases, see figure 3.8. As it can be seen from the BSE images, in EK2-AC there was micro-segregation of Ta in the γ-Ni_{ss}, see bright areas in figure 3.8. The scale of the eutectic varied in the ingot. According to the EDS data (Table 3.3) with the Ta addition the Cr content in the γ-Ni_{ss} increased compared with the EK1-AC, but the Co and Al contents were not different from those in the first alloy. Thus, Ta increased the solid solubility of Cr in the γ-Ni_{ss}. Ta also increased the Co and Cr concentrations in the eutectic compared with the first alloy.

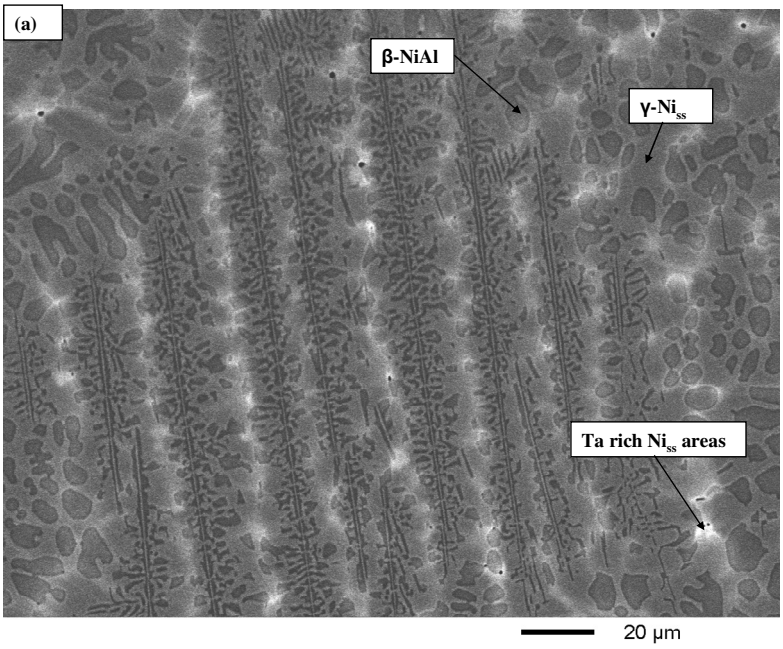

continued in the next page

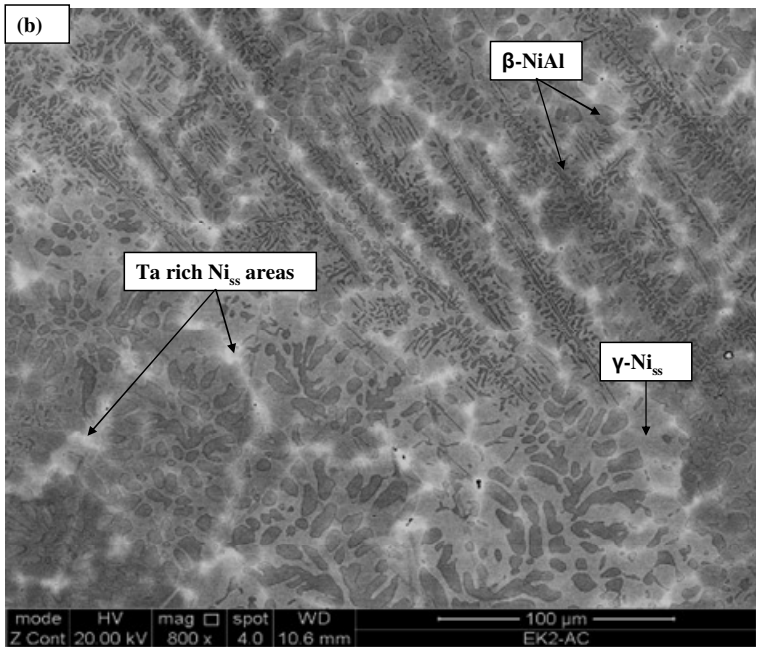

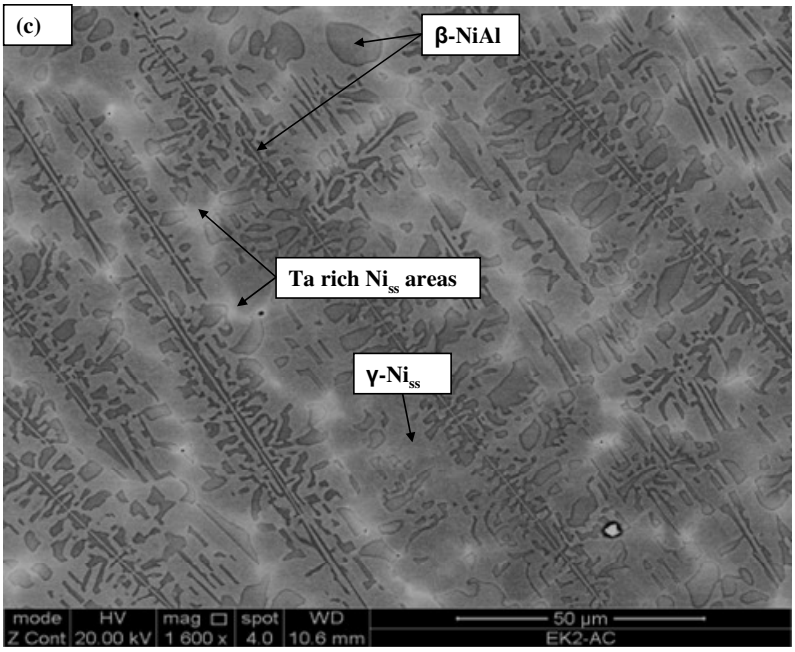

continued in the next page

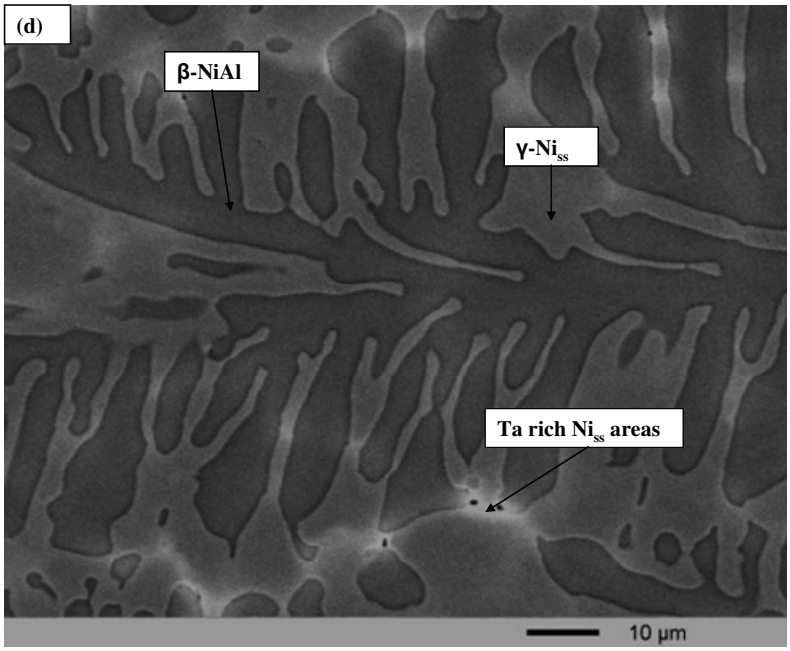

Figure 3.8 BSE images of the microstructure of EK2-AC.

The XRD data (figure 3.9) confirmed the presence of γ-Ni_{ss} and β-NiAl and suggested the presence of γ'-Ni_3Al. The peak at around $2\theta=61.8^{\circ}$ did not correspond to any of the above phases.

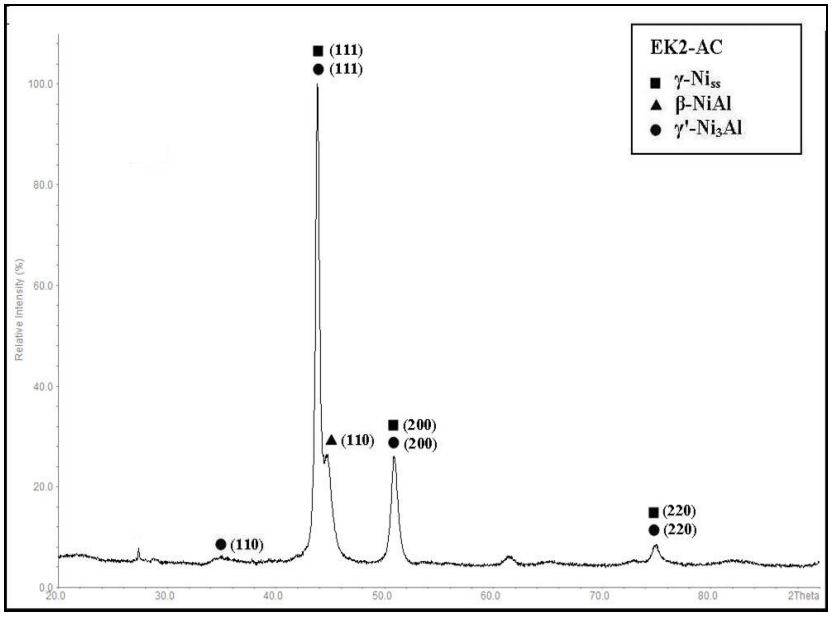

Figure 3.9 X-ray diffractogram of the EK2-AC.

3.2.2.2 Heat treated alloy (EK2-HT)

The first heat treatment (EK2-HT1) for the alloy was for 24 hrs at 1200 ˚C. Compared with the as cast alloy there was coarsening of the overall microstructure (figure 3.11). There were still some Ta rich areas in the Ni_{ss} that exhibited bright contrast. After the first heat treatment the Cr content of the γ-Ni_{ss} had increased and the Al content had decreased compared with the EK2-AC. The Co and Cr concentrations in β-NiAl had decreased and the Al concentration increased compared with the EK2-AC. The presence of γ-Ni_{ss} and β-NiAl in EK2-HT1 was confirmed by the XRD data (figure 3.12), which also suggested the presence of γ'-Ni_3Al. The peak at around 2θ=61.8 was not observed.

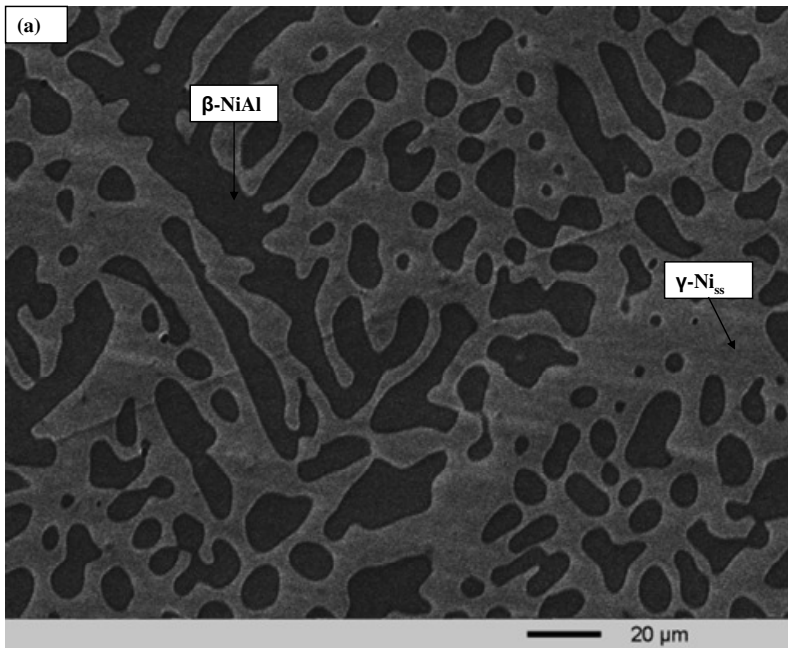

continued in the next page

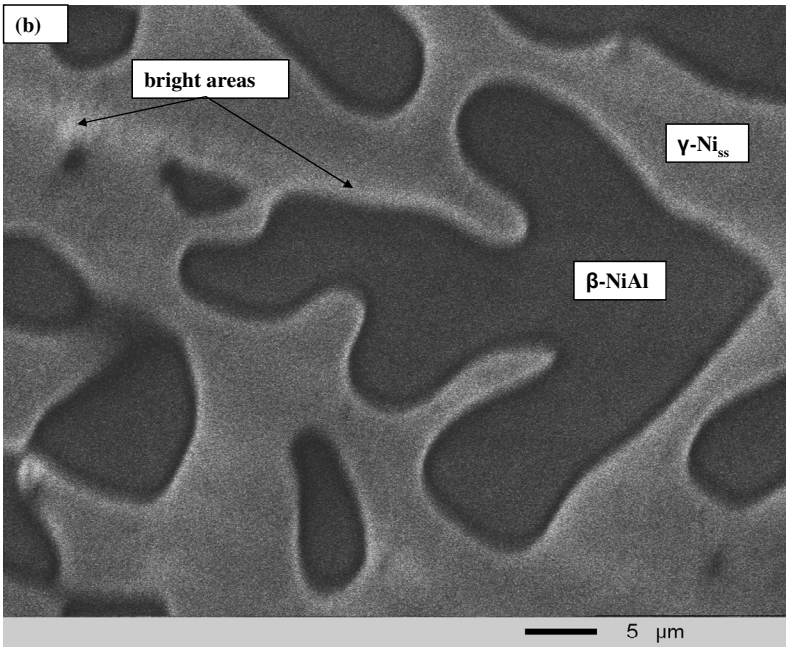

Figure 3.10 BSE images of the microstructure of EK2-HT1.

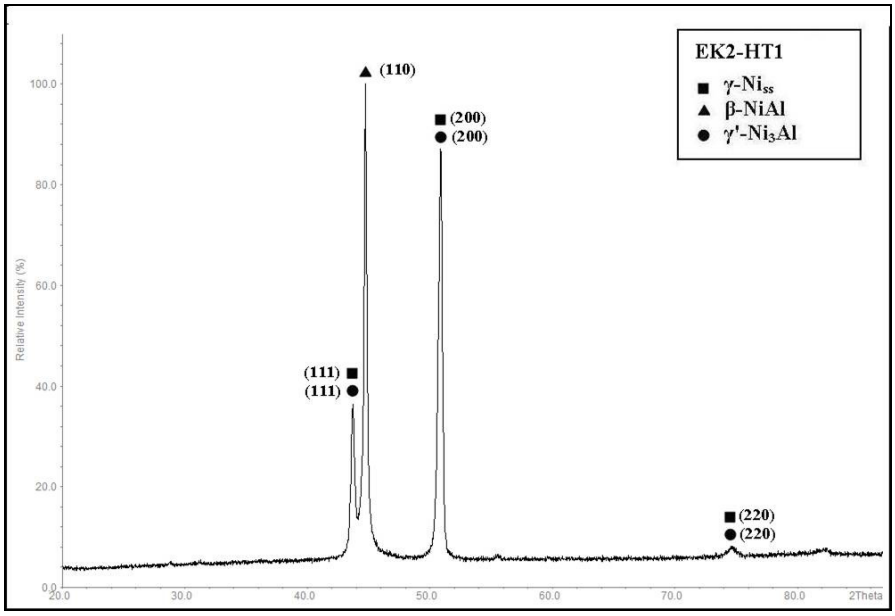

Figure 3.11 X-ray diffractogram of the EK2-HT1.

After the second heat treatment (EK2-HT2) i.e. total 48 hrs at 1200˚C, the microstructure of the EK2 alloy consisted of the γ-Ni_{ss}, β-NiAl and possibly γ'-Ni_3Al, as can be seen in the SEM images in figures 3.12. The microstructure had coarsened further. The phase identification was confirmed by qualitative EDS, as shown in figure 3.12c. The

same was the case for the β-NiAl. The presence of γ'-Ni_3Al in this condition was suggested by the XRD, see figure 3.13.

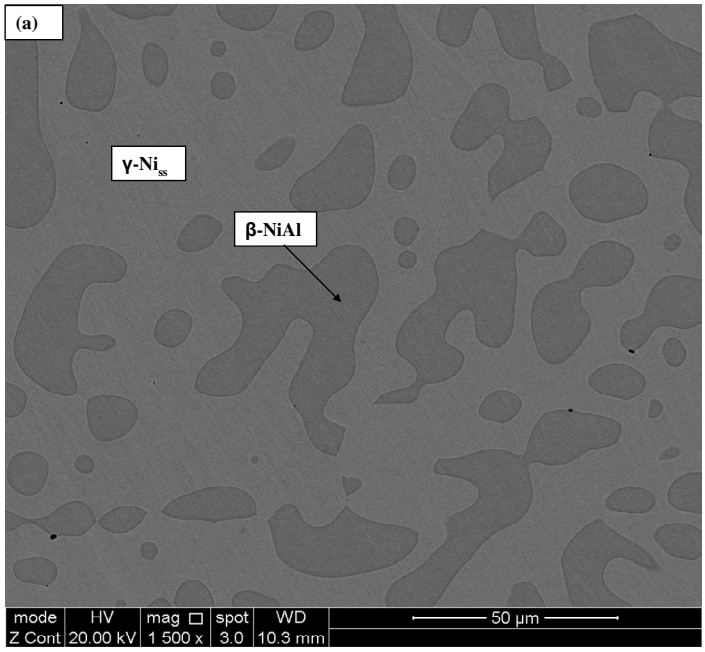

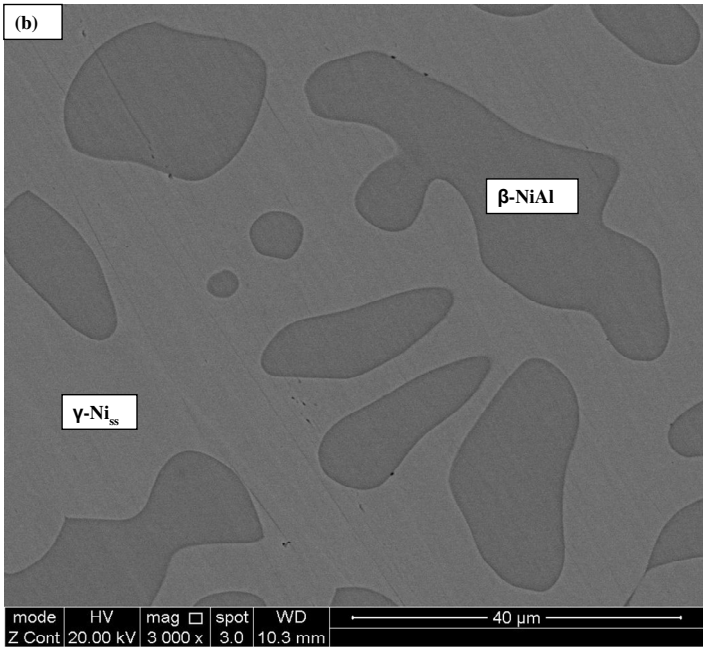

continued in the next page

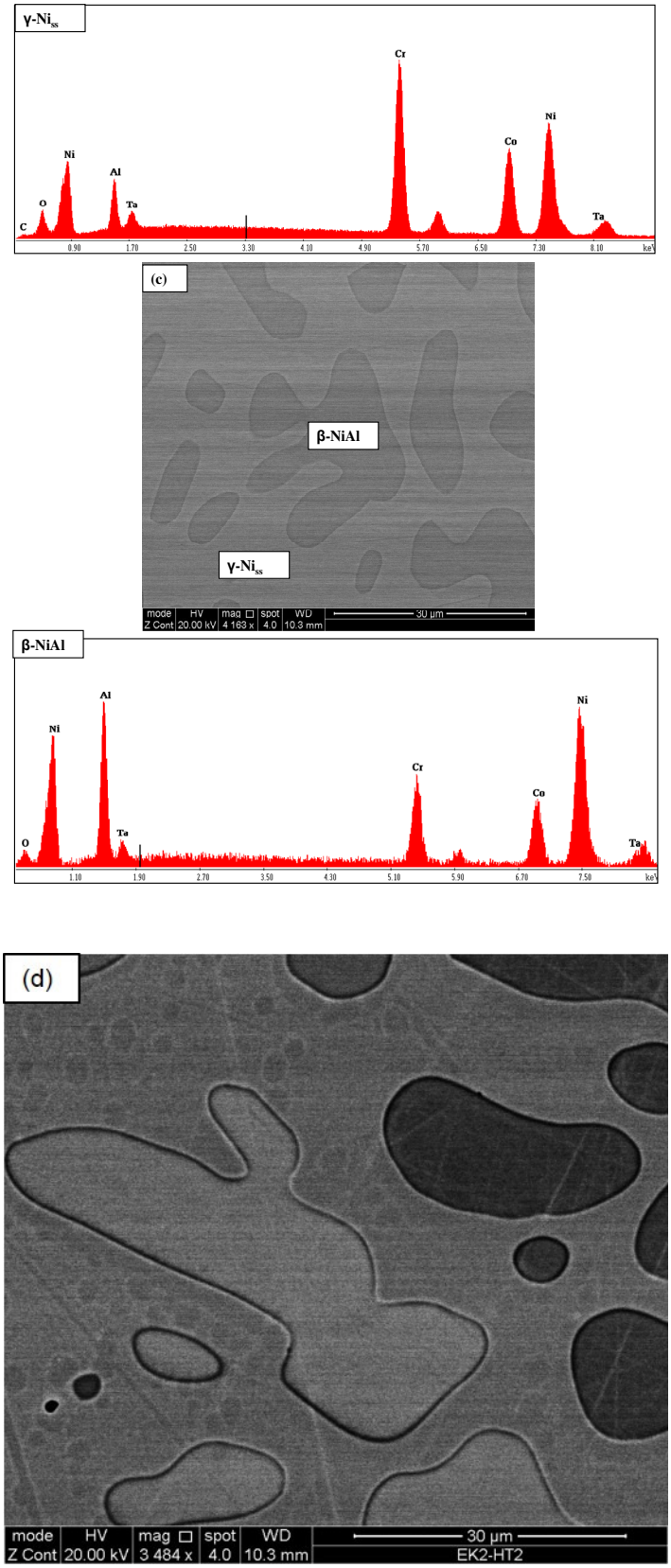

Figure 3.12 BSE images of the microstructure of EK2-HT2.

Therefore, in EK2-HT2 the phases present were the γ-Ni_{ss}, β-NiAl and γ'-Ni_3Al.

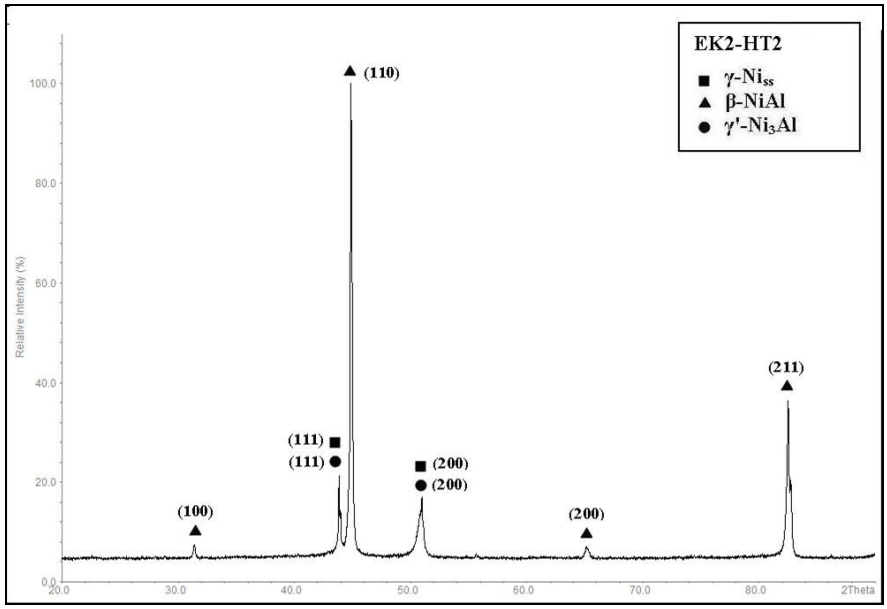

Figure 3.13 X-ray diffractogram of the EK2-HT2.

3.3 Discussion

The microscopy based studies confirmed the presence of two phases in the as cast alloys EK1 and EK2. For both alloys the XRD and EDS results confirmed the presence of the $(Ni)_{ss}$ (γ phase), the XRD suggested the presence of the ordered β-NiAl (B2) and γ'-Ni_3Al ($L1_2$) intermetallics and the EDS confirmed the presence of Al rich intermetallic phase, which formed a lamellar eutectic with the γ phase. In the heat treated alloy EK2-HT2 in the γ phase there were 1 – 3 μm precipitates of round or cubical shape, which is the morphology that is exhibited by the γ′ in Ni superalloys. The latter precipitates were observed only when a FEG-SEM (Inspect-F) was used but not with the other scanning electron microscopes used in this research. Precipitation of another phase in the γ phase in the EK1-HT alloy was not observed with FEG-SEM.

XRD studies of MCrAlY based bond coat alloys often suggest the presence of γ′ together with the dominant phases β-NiAl and γ [e.g., see Fritscher and Lee, 2005]. It has also been reported that Cr promotes the β-NiAl formation in Ni-Al-Cr alloys and the L → β + γ eutectic [Huang et al., 1985] and that the γ′-Ni_3Al is destabilized in MCrAlY alloys

as Ni/Co > 2 [Fritscher and Lee, 2005]. Tantalum, which is the addition in the EK2 alloy, encourages γ′ formation in Ni superalloys. Furthermore, the precipitation of γ′-Ni_3Al in γ with the morphology of the γ′ precipitates being similar to that observed in this study has been reported by Aurélie Vande Put et al (2010) in 70 - 80 μm thick sprayed NiCoCrAlYTa bond coats and Pt modified NiCoCrAlYTa bond coats after heat treatment. In this study the γ′-Ni_3Al in γ was observed using SEM and its size was ~ 0.4 μm.

Understanding the evolution of the microstructures of Ni-Al based alloys is challenging given the uncertainties (and disagreements over the years) about the Ni-Al binary phase equilibria (the phase equilibria close to the melting point of the γ′-Ni_3Al phase have been the subject of debate over the last 40 years) and consequently for the ternary Ni-Al-Cr phase equilibria, see chapter 1, section 1.10. Indeed, in the Ni-Al system alloys with compositions around Ni_3Al show a rather complicated phase selection and growth morphology sequence. This is an unsatisfactory situation because the Ni-Al binary forms the basis of modern superalloys (the seriousness of this problem was recently realized by users of Ni superalloys and a "re-evaluation" of thermodynamic data for these alloys is underway). As discussed in the section 1.10 (see figure 1.13) the "accepted" binary phase diagram is the one that exhibits a peritectic reaction between γ and γ′ at ~ 1362 ˚C and a eutectic between β and γ′ at ~ 1360 ˚C. Another version of the phase diagram gives a eutectic between γ and γ′ at ~ 1385 ˚C and a peritectic between β and γ′ at ~ 1395 ˚C. These binary phase diagrams are reproduced below in figure 3.14. Both diagrams show that the two intermetallics exhibit a solubility range for Al.

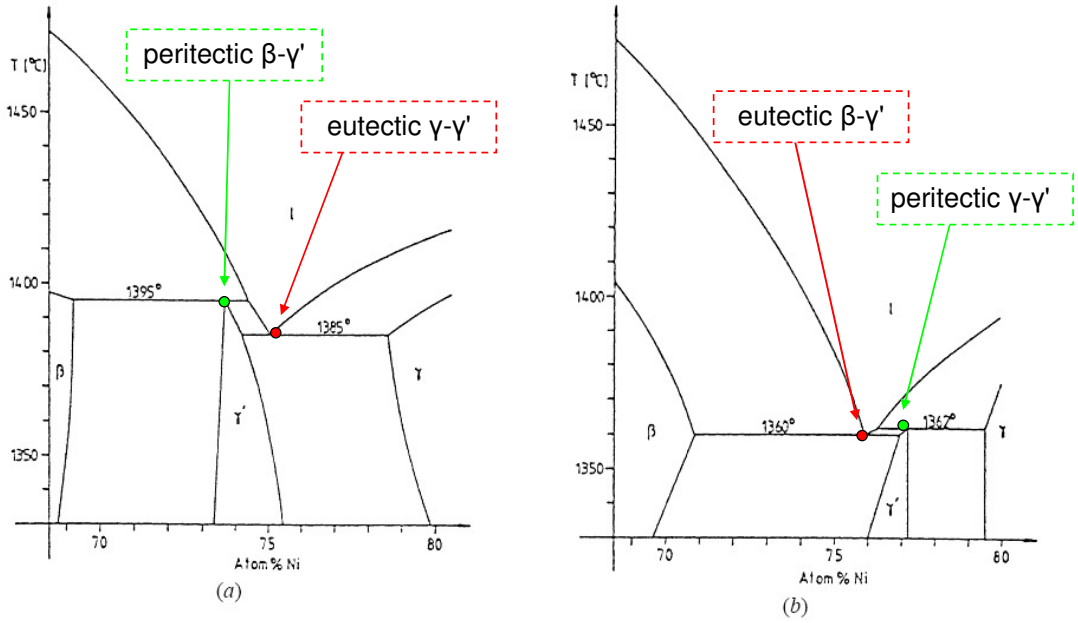

Figure 3.14 Versions of the Ni-Al binary system [Hunziker and Kurz, 1999].

Regarding the alloying additions, the phase equilibria data for Ni-Cr-Al shows that Cr has solid solubility in both the Ni_3Al and NiAl, for example in the former its s.s can be ~ 7.5 at% Cr at 1200 ˚C and ~ 15 at% Cr at 900 ˚C [Huang and Chang, 1999] and in the latter ~ 15 at% Cr and ~ 5 at% Cr at the same temperatures. In the case of Co, the Ni-Co-Al phase equilibria data shows that the NiAl and CoAl form a continuous solid solution phase and that the s.s of Co in the Ni_3Al decreases with increasing temperature, from ~ 30 at% Co at room temperature to ~ 18 at% Co at 1100 ˚C [Kainuma (1996), Protopopescu (1991)].

MCrAlY coatings are reported to have a dual-phase microstructure consisting of the γ $(Ni)_{ss}$ and β-NiAl phases with occasional γ′-Ni_3Al and α ($(Cr)_{ss}$). The coatings are applied using plasma spray techniques or EB-PVD, as discussed in chapter 1, section 1.2.2**,** in which the solidification conditions are far from equilibrium. For example, in LPPS the cooling rate is reported to be ~ 10^6K/s [Fritscher and Lee, 2005]. Under such conditions metastable phase formation and suppression or slowing down of solid state transformations (that would otherwise occur) during solid state cooling is possible. In the literature there are hardly any studies where MCrAlY coatings are compared in their conventionally cast and plasma sprayed conditions. The discussion below will highlight the reasons why such studies are crucial given the dependence of γ′-Ni_3Al and β-NiAl formation on solidification conditions.

The microstructures of the alloys EK1 and EK2 can be considered using the Ni-Cr-Al ternary phase equilibria [Fritscher (2003), Rogl et al (1991)] where in both alloys Co is calculated together with Ni (because of their s.s) and in the alloy EK2 the Ta is calculated with Ni (the maximum s.s of Ta in Ni is about 11 at%). The liquidus projection of the Ni-Cr-Al system is shown in figure 3.15.

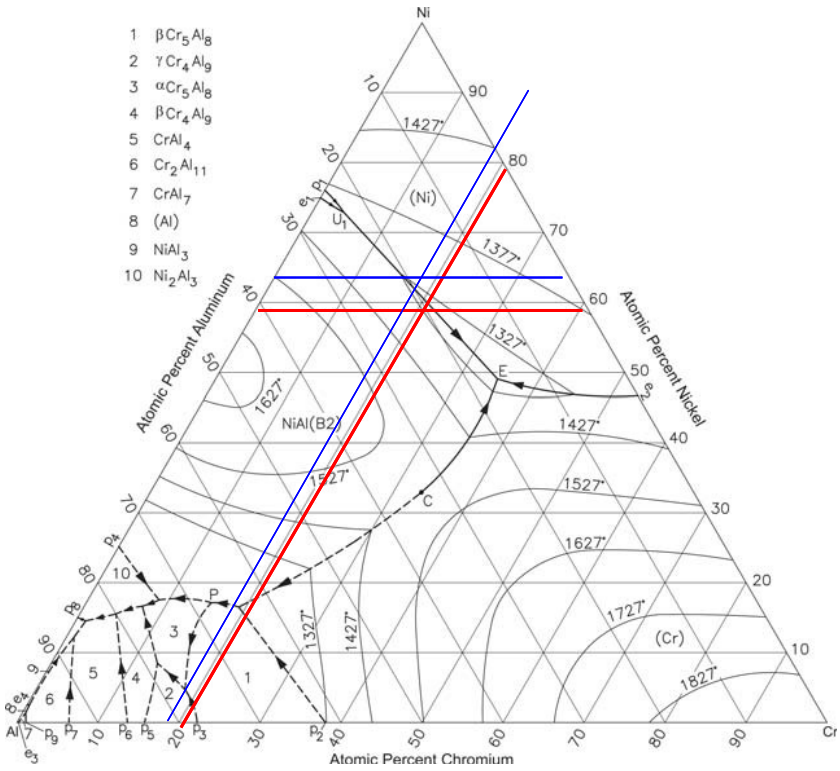

Figure 3.15 Al-Cr-Ni computed liquidus projection [Huang and Chang, 1999].

where the red full lines correspond to EK2-AC for the composition 59.1Ni-21.7Cr-19.2Al (at%) and the blue full lines correspond to the EK1-AC for the composition 62.6Ni-19.9Cr-17.6Al (at%), see Tables 3.2 and 3.3. In the Ni-Al-Cr liquidus projection the EK1-AC alloy falls in the γ field (γ primary phase) and very close to the γ + B2 eutectic, which means that as the temperature drops the γ + B2 eutectic will form. In the same projection the EK2-AC alloy falls almost on the γ + B2 eutectic, which could explain the high volume fraction of the latter in this alloy (see section 3.2). Bezencon et al (2003) also reported isopleths of the NiCoCrAl system, which were calculated with ThermoCalc and a commercial Ni database (neglecting Y), where an alloy with nominal composition Ni-23Co-20Cr-8.5Al-0.5Y-trace Ta (wt%), (i.e., essentially an alloy of the same composition as EK2) was expected and was observed to have γ + β eutectic microstructure.

The invariant eutectic reaction L → B2 + γ (Ni) + α (Cr) exists in the Ni-Al-Cr ternary, see figure 3.15., and experimental work has located it at 1320 ˚C ± 10 ˚C [Rogl, 1991]. In the quaternary Ni–Co–Cr–Al system, in which the actual alloy EK1 belongs, the above eutectic reaction still has one degree of freedom and therefore freezing occurs over a melting range.

Metastable β + γ eutectic is possible in the Ni-Al system according to the "accepted" Ni-Al binary phase diagram (see figure 3.16). In this diagram, β and γ phases are in equilibrium with the liquid over a range of compositions around ~ 25 at% Al. Hunziker and Kurz (1999) grew β + γ eutectics in directionally solidified Ni-24.5Al (at%) alloys at 10, 30 and 100 μm/s and Lee and Verhoeven (1994 (b)) observed β + γ eutectic down to 0.8 μm/s. The "average" composition of the metastable eutectic was ~ 24.5 at% Al [Lee and Verhoeven, 1994 (b)] and the calculated transition between γ plane front and β + γ eutectic solidification was given at ~ 22-21.8 at% Al by Hunziker and Kurz (1999). Modelling of competitive growth in a positive temperature gradient by these researchers predicted formation of the β + γ eutectic at <u>all</u> velocities down to 1 μm/s. The stable eutectic (i.e., the β + γ′ eutectic) was <u>not</u> predicted to form <u>above</u> 10 μm/s. According to Assadi et al (2006) the growth of NiAl becomes sluggish as its Al content increases.

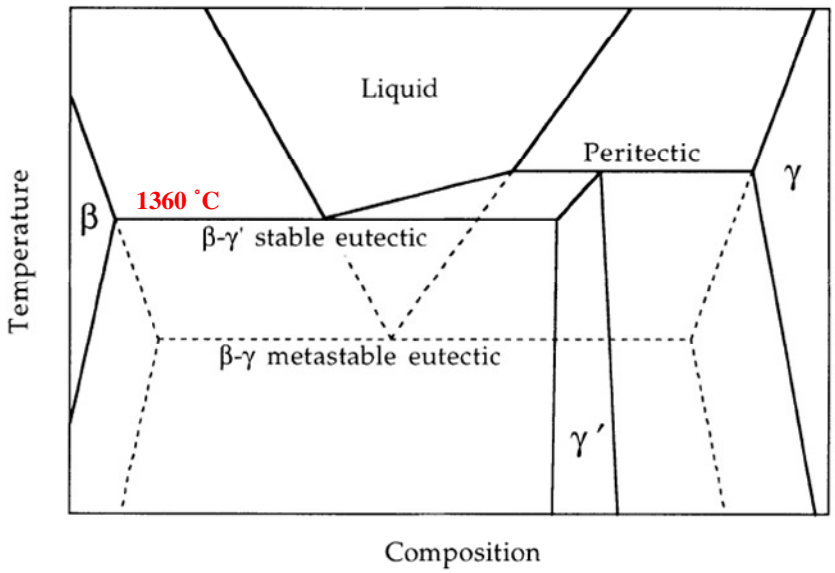

Figure 3.16 Equilibrium and metastable eutectics in the Ni-Al system [Hunziker and Kurz, 1999].

Jianqiang Li et al (2001) studied the dependence of β and γ′ formation on cooling rate in conventionally cast 12 mm thick buttons (dT/dt ~ 10 K/s) and rapidly solidified 70 μm thick ribbons (dT/dt ~ 10^5 to 10^6 K/s) of Ni_xAl_{100-x} (x=70, 75 and 80) alloys and reported that the vol% of γ′ increased and of β decreased as the cooling rate increased. In the ribbons the β ($L1_o$) martensite was formed during solid state cooling and disappeared after annealing.

The ternary Ni-Cr-Al phase equilibria (see figure 3.15) would suggest the formation of eutectic in the as solidified microstructures of the alloys EK1 and EK2. According to the XRD and EDS data there was no α (Cr) in the as solidified microstructures of the alloys EK1 and EK2. The finest spacing between eutectic lamellae in EK1-AC was ~ 10^{-6} m, which, according to the data of Hunziker and Kurz corresponds to growth velocity for the β + γ eutectic ~ 1800 μm/s and the "coarsest" spacing was 3 10^{-6} m, which corresponds to growth velocity for the β + γ eutectic ~ 150 μm/s (see figure 3.17 which is from Hunziker and Kurz, 1999). In the case of EK2-AC the finest spacing between eutectic lamellae was 4.5 10^{-6} m, which corresponds to growth velocity for the β + γ eutectic ~ 38 μm/s and the "coarsest" spacing between eutectic lamellae was 15 10^{-6} m, which corresponds to growth velocity of the β + γ eutectic ~ 1.6 μm/s. Furthermore, the average Al content of the eutectic in the as cast alloys was 21.5 and 20.7 at% Al for EK1-AC and EK2-AC, respectively. The above data for EK1 and EK2, when considered in the context of the work discussed previously and data about the s.s of Cr and Co in NiAl, provides further support for the presence of β and β + γ eutectic in the as cast microstructures of the two alloys.

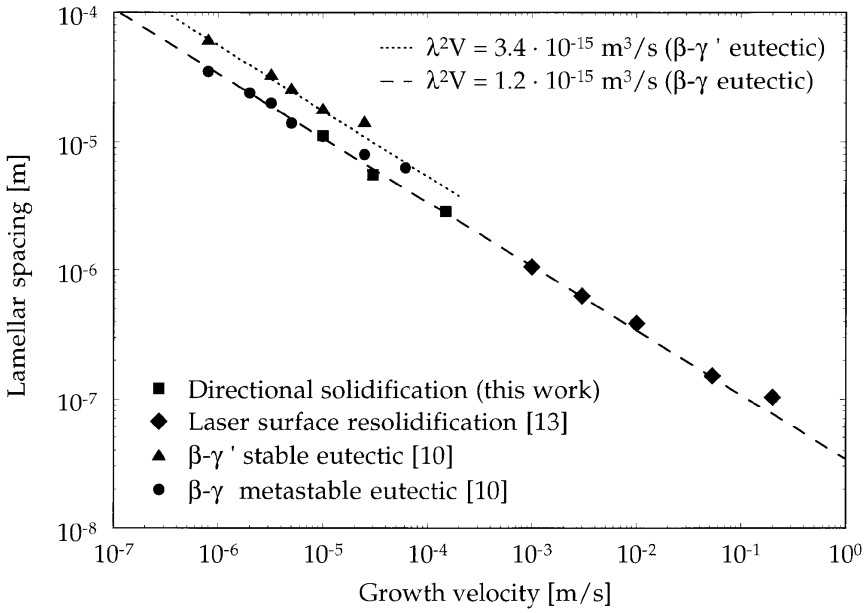

Figure 3.17 Eutectic lamellar spacing vs growth velocity and λ^2V=constant lines, for the stable (β-γ') and metastable (β-γ) eutectics [Hunziker and Kurz, 1999].

The segregation of elements in the cast alloys can be quantified with a solute partition coefficient $k'_i = C_i^{\gamma}/C_i^{\gamma-\beta\ eutectic}$ where i corresponds to the different elements and C_i is the measured concentration of element i in either the γ phase or the γ + β eutectic. The results for EK1-AC are $k'_{Al} = 0.73$, $k'_{Cr} = 1.1$ and $k'_{Co} = 1.27$ and for EK2-AC are $k'_{Al} = 0.73$, $k'_{Cr} = 1.21$, $k'_{Co} = 1.14$ and $k'_{Ta} = 1$ and 3.75, meaning (a) that Al partitions to the γ + β eutectic and Cr, Co and Ta to the Ni_{ss} and (b) that the addition of Ta does not affect the partitioning of Al but enhances the partitioning of Co and Cr.

Because the solid state diffusion coefficients are relatively large in the Ni-Al system, solidification microstructures can change significantly during cooling. Lee and Verhoeven (1994 (b)), from their study of quenched directionally solidified interfaces of Ni-Al binary alloys, reported that upon quenching a metastable interface between the β and γ phases in the (metastable) β + γ eutectic would decompose into the γ′ phase and that this reaction can occur so rapidly that it might not be possible to quench fast enough to preserve the interface between the β and γ phases at room temperature. On this basis, and given that the XRD suggested presence of the γ′ in the EK1-AC and EK2-AC microstructures, if this phase was indeed present its most likely location would be at the interfaces between β and γ phases in the β + γ eutectic. This could explain why the compositions of some of the intermetallic lamellae in the eutectic in EK1-AC were slightly

poorer in Al (see section 3.2.1.1). The addition of Ta in the alloy EK2 would be expected to decrease diffusivity in this alloy, which should make the aforementioned decomposition into the γ′ phase more difficult, compared with EK1. This would explain why only one analysis of intermetallic lamella in EK2-AC gave a composition close to the γ′ phase (39.4Ni-17Co-16.8Cr-25.6Al-1.2Ta (at%)).

The heat treated microstructures of the two alloys can be now considered using isothermal sections for the Ni-Al-Cr system. Figures 3.18 to 3.21 are the isothermal sections at 1200 ˚C, 1150 ˚C, 1050 ˚C and 1000 ˚C.

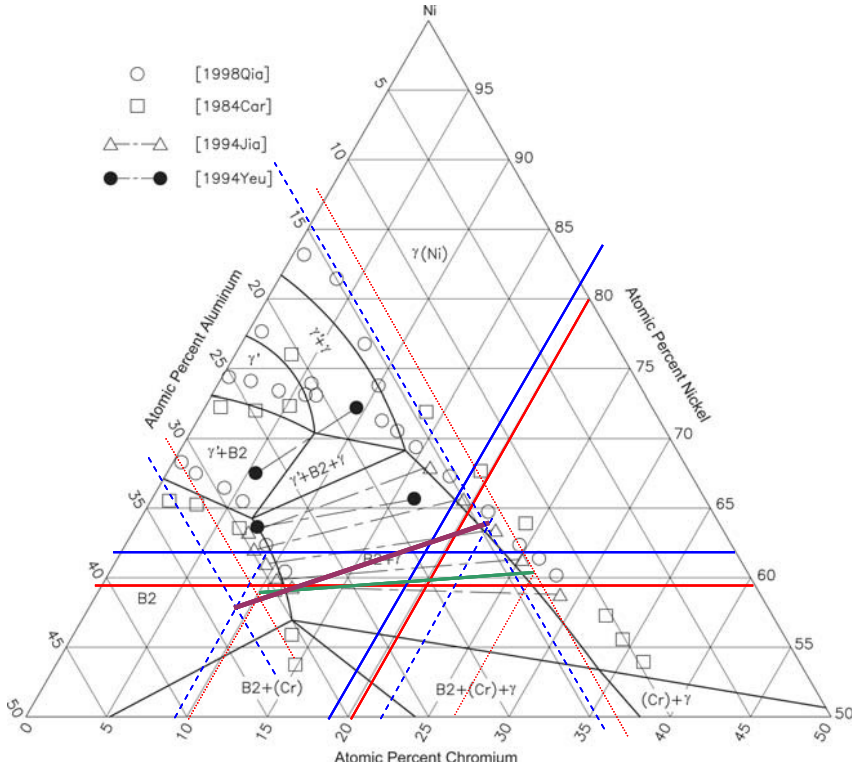

Figure 3.18 Al-Cr-Ni computed isothermal section at 1200 °C [Dupin et al, 2001].

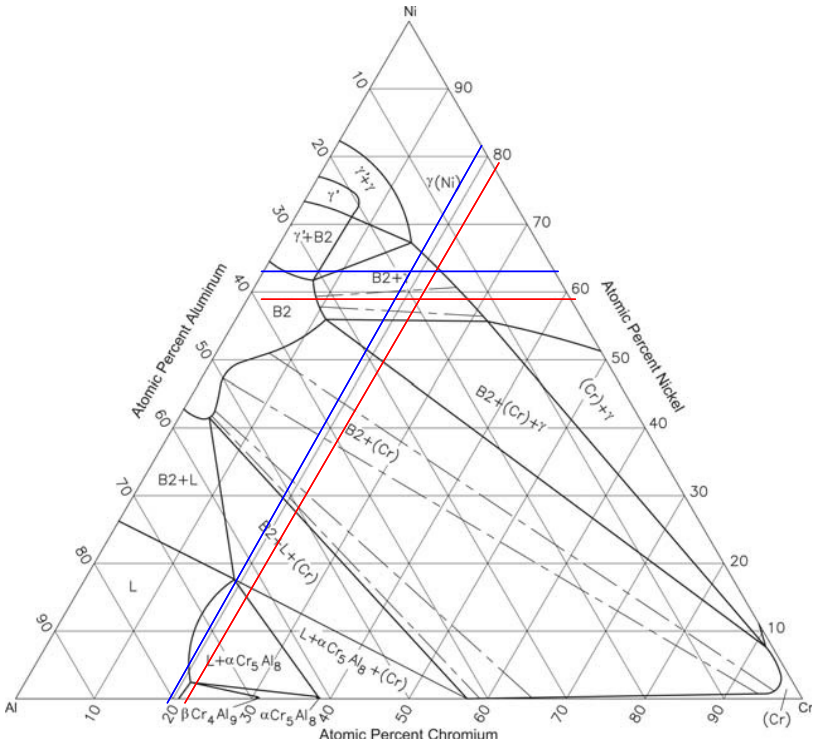

Figure 3.19 Al-Cr-Ni computed isothermal section at 1150 °C [Huang and Chang, 1999].

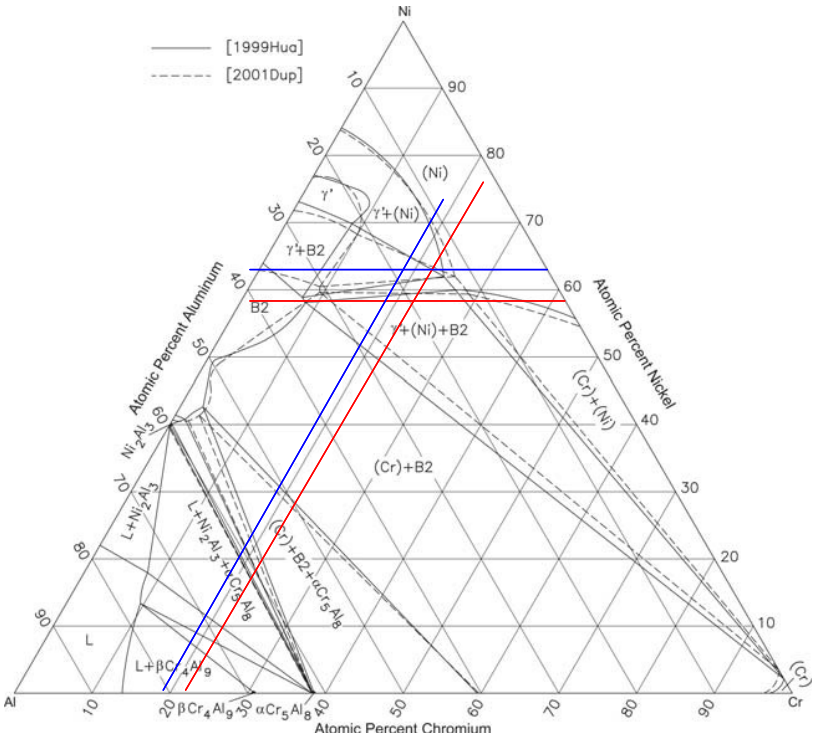

Figure 3.20 Al-Cr-Ni computed isothermal section at 1050 °C [Huang and Chang (1999), Dupin et al. (2001)].

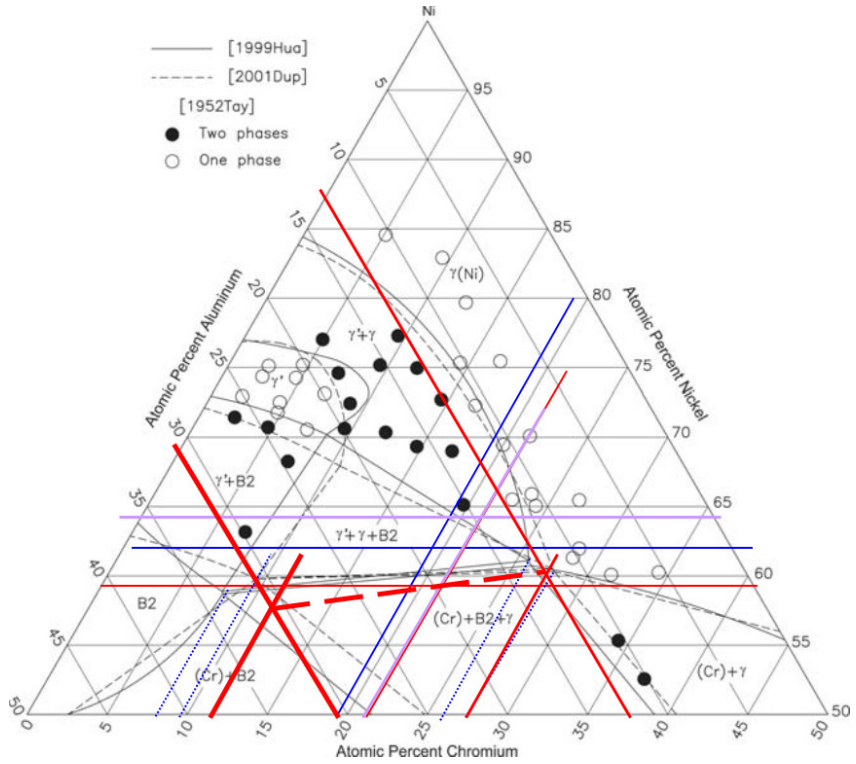

Figure 3.21 Al-Cr-Ni computed isothermal section at 1000 °C [Dupin et al. (2001), Huang and Chang (1999)].

In these figures the thin red full lines correspond to EK2-HT2 for the composition 59.1Ni-21.3Cr-19.4Al and the thin blue full lines correspond to the EK1-HT1 for the composition 62.6Ni-19.5Cr-17.9Al. In both alloys Co is calculated together with Ni (because of their s.s) and in EK2 the Ta is also calculated with Ni (the maximum s.s of Ta in Ni is about 11 at%).

In the 1200 ˚C isothermal section (figure 3.18) both alloys fall in the B2 (NiAl) + γ region. For the EK2 alloy the dotted red lines give the Cr and Al contents of each phase, which are given in the data in Table 3.3 and help to define the tie line for this alloy (green line), which is in excellent agreement with the experimental tie lines given in this part of the two phase field in the phase diagram. For the EK1 alloy the dashed blue lines give the Cr and Al contents of the two phases, which are given in the data in Table 3.2, and help to define the tie-line for this alloy. The observed microstructures at 1200 ˚C can be explained by the phase equilibria only for the EK1-HT (because in EK2-HT2 there is precipitating of γ′ in the γ).

The solid state partitioning of elements between the γ-Ni_{ss} and β phases can be calculated using the solid state partitioning coefficient $k_i^{\gamma/\beta} = C_i^{\gamma}/C_i^{\beta}$ where i corresponds to the different elements and C_i is the measured concentration of element i in either the γ phase or the β phase. The results for EK1-HT1 are $k_{Al}^{\gamma/\beta} = 0.43$, $k_{Cr}^{\gamma/\beta} = 2.35$ and $k_{Co}^{\gamma/\beta} = 1.83$ and for EK1-HT2 are $k_{Al}^{\gamma/\beta} = 0.52$, $k_{Cr}^{\gamma/\beta} = 1.79$ and $k_{Co}^{\gamma/\beta} = 1.28$, meaning (a) that Al partitions to the β and Cr, Co to the Ni_{ss} and (b) that upon longer exposure to temperature the partitioning of Al to the β increases and the partitioning of Co and Cr to the Ni_{ss} phase decreases. The results for EK2-HT1 are $k_{Al}^{\gamma/\beta} = 0.36$, $k_{Cr}^{\gamma/\beta} = 2.44$, $k_{Co}^{\gamma/\beta} = 1.69$ and $k_{Ta}^{\gamma/\beta} = 1.15$ and for EK2-HT2 are $k_{Al}^{\gamma/\beta} = 0.4$, $k_{Cr}^{\gamma/\beta} = 2.39$, $k_{Co}^{\gamma/\beta} = 1.63$ and $k_{Ta}^{\gamma/\beta} = 1.21$, meaning (a) that Al partitions to the β and Cr, Co and Ta to the Ni_{ss} and (b) that upon longer exposure to temperature the partitioning of these elements between β and γ does not change significantly. Comparison of the data for $k_i^{\gamma/\beta}$ for the two alloys shows that alloying with Ta affected the partitioning behavior of Al, Co and Cr between the two phases.

In the 1150 ˚C isothermal section (figure 3.19) both alloys also fall in the two phase B2 + γ field. Only the two phase β and γ microstructure of EK1-HT1 can be explained by the phase equilibria at 1150 ˚C.

In the 1050 ˚C isothermal section (figure 3.20) the γ′ + (Ni) + B2 phase field is labeled incorrectly, it should be B2 + (Ni) + (Cr) or B2 + γ + α(Cr). In this isothermal section the alloy EK1 falls in the three phase γ′ + γ + B2 field and is very close to the two phase γ + B2 field. Thus the two phase β and γ microstructure of the EK1-HT could also be explained by the phase equilibria at 1050 ˚C, if small errors were allowed in the phase fields in the isothermal section in figure 3.21.

In the 1050 ˚C isothermal section (figure 3.20) the alloy EK2-HT falls in a three phase field but this is the wrong field (B2 + γ + (Cr) field) as no (Cr) was observed in the NiAl. This alloy is also close to the two phase γ + B2 field.

In the 1000 ˚C isothermal section (figure 3.21) the pink lines in correspond to EK1-HT2 for the composition 64Ni-21.5Cr-14.6Al (at%). The alloy falls in the two phase γ+γ′ region but if it is assumed that the compositions of the phases in Table 3.2 correspond to γ and γ′ rather that γ and B2 then the tie line does not make sense (falls outside the γ+γ′ two phase field).

The alloy EK1-HT1 (62.6Ni-19.4Cr-17.9Al) falls in the three phase B2 + γ + γ′ field with the blue dotted lines giving the Cr concentrations in the B2 and γ respectively as ~ 8 at% Cr and ~ 26 at% Cr and the corresponding Al concentration of the B2 and γ respectively as ~ 33 at% Al and 13 at% Al from the calculation of Huang and Chang and ~ 9.5 at% Cr and 27. 5 at% Cr and the corresponding Al concentration of the B2 and γ respectively as ~ 31.5 at% Al and 12.5 at% Al from the calculation of Dupin et al. (2001). Only the B2 compositions from the two calculations are in good agreement with the experimental data in Table 3.2.

If there was γ′ in EK1-HT1, then its Cr and Al contents calculated from the corner of the B2 + γ + γ′ triangle would be ~ 8at% Cr and 22 at% Al respectively from the calculation of Huang and Chang (1999) and ~ 10.5at% Cr and 23 at% Al from the calculation of Dupin et al. (2001). These values are not close with the experimental data. If the γ′ was indeed present in the EK1 alloy (which seems unlikely according to Ni-Al-Cr phase equilibria), most probably it will be of nanometer size and precipitated in the γ (as suggested by the results for EK2-HT2 and Aurélie Vande Put et al., 2010), but would be of smaller size than the γ′ in EK2-HT (beyond the resolution of FEG-SEM), which could explain why it was not observed by FEG-SEM.

The alloy EK2-HT2 (thin red lines) is very close to the two phase B2 + γ field that separates the B2 + γ + γ′ three phase field from the B2 + (Cr) + γ three phase field, and falls in the latter in the above (1000 ˚C) isothermal section.

The microstructural data (accepting that the fine precipitates in γ are due to precipitation of γ′) would suggest that the alloy EK2-HT2 had a three phase B2 + γ + γ′ microstructure but the chemical analysis data available from this research is only for two phases, namely the B2 and γ. The compositions of the two phases are indicated by the intercepts of the thick red lines and are on the same line (tie line?) with the alloy composition (thick dashed line).

Figure 3.23 shows the fractions of phases as a function of temperature for the alloy EK2, which were calculated using a commercial Ni database. The data shows that the phases predicted at 1200 ˚C, 1150 ˚C and 1050 ˚C are the γ and β and the β, γ and a Cr rich phase at 1000 ˚C, with the γ′ being present below 950 ˚C.

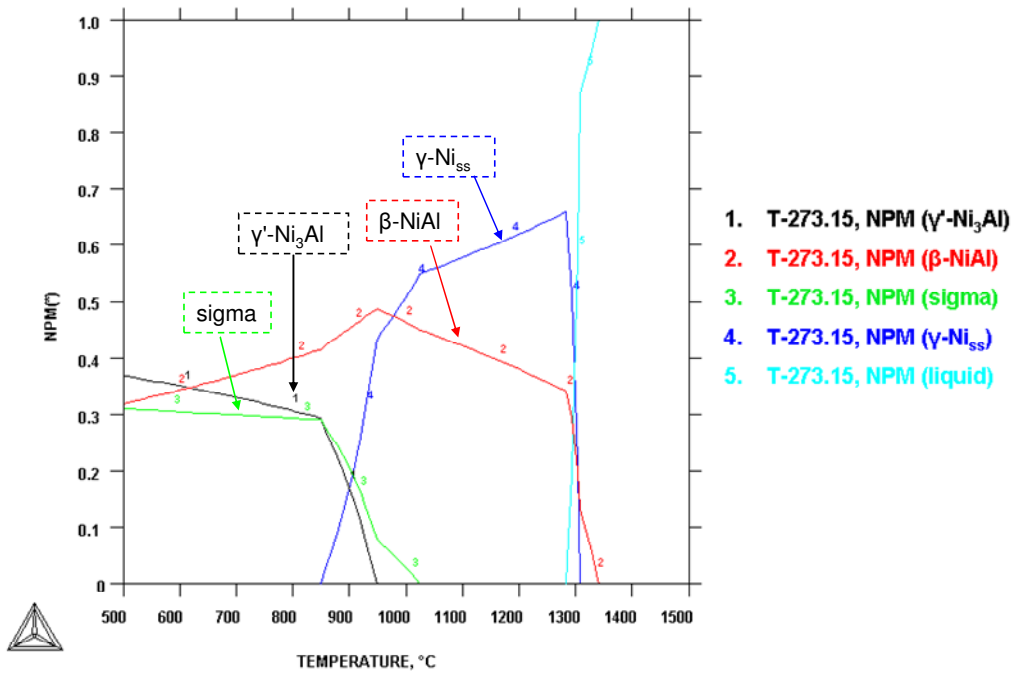

Figure 3.22 Thermodynamic calculations for alloys EK1 and EK2.

In conclusion, the available phase equilibria can explain only the microstructure of the alloy EK1. According to the EDS data for the alloys EK1 and EK2 given in the Tables 3.2 and 3.3, the addition of Ta increased the solid solubility of Cr in the γ-Ni_{ss}. This is considered beneficial for the bond coat in a hydrogen rich environment owing to the effectiveness of Cr in Type II hot corrosion behavior. Table 3.4 shows the Cr/Al ratio in the γ-Ni_{ss} phase in the two alloys. For both alloys this ratio increased after the heat treatment. In percentage terms the increase was more significant in the alloy EK2. After the second heat treatment, the Cr/Al ratio was 20% higher compared with the alloy EK1, in the as cast and heat treated conditions.

Table 3.4 The Cr/Al ratio in the γ-Ni_{ss} (the two ratio values for EK2-AC are given owing to the formation of Ta rich γ-Ni_{ss} in the cast alloy).

Alloy	AC	HT1	HT2
EK1	1.3	1.6	1.5
EK2	1.7 1.8	2.4	2.1

Another effect of the addition of Ta in the alloy EK2 was to reduce slightly the content of Al in NiAl in the as cast condition and after the first heat treatment compared with the alloy EK1 and to stabilize it to about 31.5 at% Al in the EK2 (Tables 3.2 and 3.3). The s.s of Cr in the NiAl increased with the Ta addition, and like Al, stabilized after the second heat treatment. The Al/Cr ratio in the NiAl was higher in the alloy EK1-AC and EK1-HT1 compared with the EK2-AC and EK2-HT1 (Table 3.5), owing to the higher Cr content in the intermetallic in EK2, but was lower in the EK1-HT2 compared with the EK2-HT2. The data would thus suggest that the Ta addition was beneficial for the NiAl as with prolonged exposure to high temperature its Al/Cr ratio increases by about 31% compared with the cast condition.

Table 3.5 The Al/Cr ratio in the β-NiAl.

Alloy	**AC**	**HT1**	**HT2**
EK1	2.4	3.5	2.3
EK2	1.9	2.75	2.8

The Ta addition also had a significant effect on the volume fraction of phases (Table 3.6). Indeed, in the alloy EK2 the dominant phase was the NiAl and its volume fraction was almost double that in the alloy EK1.

Table 3.6 Effect of Ta on the vol % of phases in the two alloys.

Alloy	**AC**		**HT1 (1200 ˚C / 24 hrs)**	
	γ-Ni_{ss}	β-NiAl	γ-Ni_{ss}	β-NiAl
EK1	74	26	67	33
EK2	43	57	38	62

3.4 Conclusions

In this chapter two MCrAl based alloys of nominal compositions (Ni-20.4Co-20.1Cr-16.4Al (alloy EK1) and Ni-20.1Co-19.8Cr-16.3Al-1.1Ta (alloy EK2) were studied in the cast and heat treated conditions in order to understand the effect of the addition of Ta has in the microstructure. The microstructures of both alloys contained the γ-Ni_{ss} and β-NiAl and a $\beta + \gamma$ eutectic in the as cast condition. The γ'-Ni_3Al probably had formed in the EK1-AC during solid state cooling at the β/γ interface and in the EK2-HT via precipitation in the γ-Ni_{ss}. Tantalum almost doubled the vol% of β-NiAl, which became the dominant phase in EK2. Tantalum also increased the solid solubility of Cr in the γ-Ni_{ss}. In both alloys the Cr/Al ratio in the γ-Ni_{ss} phase increased after the heat treatment and was 40% higher in the alloy EK2. The Ta addition caused an increase of the Al/Cr ratio in the β-NiAl by about 47% compared with the as cast condition. The available phase equilibria for Ni-Cr-Al could account for the microstructures only of the alloy EK1 in both conditions and for EK2 only in the as cast condition.

Chapter 4 – EK3, EK4, EK5 alloys

4.1 Introduction

The bond coat alloys developed in this study are designed to form alumina TGO owing to its favourable properties as protective and slow-growing oxide (see section 5.1). Alumina provides a better scale than chromia, which however has a better adhesion to the substrate. Alumina has a lower coefficient of thermal expansion (CTE) than the zirconia topcoat ($8*10^{-6}$ K^{-1} vs $11.5*10^{-6}$ K^{-1} by Cao et al. 2004), thus the strain is increased with the thickness of the TGO. Fracture occurs in the alumina TGO and its interfaces with the substrate and the topcoat. Reactive elements (RE) such as Hf and Y can be used to alleviate some of the problems of the alumina TGO. It is thought that RE additions improve the behaviour of alumina via enhanced oxide-scale plasticity, pegging or modification of oxide growth mechanisms [Whittle and Stringer, 1980]. This chapter focuses on the effects of the synergy of Ta with the reactive elements Y and Hf and with Si additions on the microstructure of cast and heat treated (1200 ˚C) NiCoCrAl based bond coat alloys. The alloys to be considered in this chapter are the alloys EK3, EK4 and EK5 with the nominal compositions given in Table 4.1.

4.1.1 Selection of alloys

The choice of alloying additions in the BC is important for determining its performance in service and the integrity and quality of the BC/substrate interface. Reactive elements in the bond coat are thought to promote adhesion and improve the thermal expansion matching with the substrate.

The nominal composition of the alloy EK3 was Ni-23Co-20Cr-8.5Al-4Ta-0.6Y (wt%). The Y was added to improve the oxide scale (TGO) adhesion. There is a “school of thought” that Y reduces the oxidation rate [Allam et al., 1978]. However, there are conflicting reports on this issue with some evidence suggesting that Y has either no effect or even a harmful effect on weight gain compared with the same alloy without Y addition [Kuenzly and Douglass, 1974]. Sulphur is expected to induce de-adhesion and spallation

when present at the substrate/BC interface. Yttrium limits the interfacial segregation of sulphur by gettering impurities like sulphur. The latter is thought to occur via the formation of Y_2O_2S compounds that reduce sulphur diffusion. Yttrium is also expected to affect the growth of the alumina scale. The distribution of Y in the coating depends on the manufacturing technique and the coating composition [Nallan, 2000]. Beneath the alumina scale Y oxidises and forms yttria or Y-aluminate. The latter has been reported to exist as isolated islands in the alumina scale or to extend between the BC and the TGO as finger like oxides possibly linked with Y rich precipitates formed in the BC [Sartwell, 2012]. The oxide fingers or pegs (which can also form with Hf additions) limit spallation. Residual stress measurements have shown that the TGO stresses are higher in the presence of Y [Bose, 2007]. This has been attributed to the yttria dispersion in the TGO resulting in higher creep strength and elimination of stress relaxation. Furthermore, the lifetime of TBCs on bond coats with Y or Hf addition is significantly higher than on those without Y addition. It is believed that the presence of yttrium in the bond coat increases the thermal-expansion coefficient and helps alleviate the stresses arising from the thermal-expansion mismatch between the ceramic top-coat and the underlying metal [Wang 2004, Vangas 1980].

Hf in general plays a similar role with that of Y. Hafnium like Y promotes scale adhesion [Pint et al., 1998] and improves the spallation resistance of a TBC [Reed et al., 2003]. Silicon is also considered to be beneficial for limiting alloy oxidation and for improving the CTE of the bond coat. In the EK4 alloy 0.8 wt% of Hf was added and the nominal composition was Ni-23Co-20Cr-8.5Al-4Ta-0.6Y-0.8Hf (wt%). Addition of hafnium in the bond coat in TBC is expected to enhance the grain boundary strength and also to increase the adhesive strength of the TGO-BC alloy interface and is important for the oxidation resistance of the bond coat [Smeggil 1987, Goward 1986].

In the alloy EK5 with nominal composition Ni-23Co-20Cr-8.5Al-4Ta-0.6Y-0.8Hf-2Si (wt%) the Si was added to increase the resistance to both oxidation and hot corrosion since the synergy of chromium and silicon is beneficial against Type II hot corrosion. It has also been suggested by Jiang (2010), Shirvani (2004) and Grunling (1982) that Si affects phase stability in BC alloys.

4.2 Results

The nominal compositions of the alloys EK3, EK4 and EK5 are given in Table 4.1 whereas the actual ones that were determined by EDS are given in Table 4.2. In the alloy EK3, where Y was the new alloying addition, the Cr content was decreased by 2.4 at% whereas the Al content was increased by 3 at%, compared with the nominal composition given in Table 4.1. In the alloy EK4, where Hf was the new alloying addition the Cr content was slightly lower whereas the Al and Ta contents were higher compared with the nominal composition. In the alloy EK5, Si was the new alloying addition and by comparing the nominal with the actual composition in Tables 4.1 and 4.2, is shown that Co, Cr and Ta contents were slightly decreased and the Al and Si contents were increased significantly. These differences in composition demonstrated how difficult it is to get the nominal composition in the cast alloy owing to the wide range of melting points of the alloying elements.

Table 4.1 Nominal compositions of the alloys EK3, EK4 and EK5.

Alloy		**Ni**	**Co**	**Cr**	**Al**	**Ta**	**Y**	**Hf**	**Si**
EK3	wt%	43.9	23	20	8.5	4	0.6	-	-
EK3	at%	42.5	20.1	19.8	16.2	1.1	0.3	-	-
EK4	wt%	43.1	23	20	8.5	4	0.6	0.8	-
EK4	at%	42.4	20.1	19.7	16.2	1.1	0.3	0.2	-
EK5	wt%	41.1	23	20	8.5	4	0.6	0.8	2
EK5	at%	40.9	19.3	19.1	15.6	1.1	0.3	0.2	3.5

Table 4.2 Actual compositions of the alloys EK3, EK4 and EK5.

Alloy		Ni	Co	Cr	Al	Ta	Y	Hf	Si
EK3	wt%	45.4	22.3	16.9	9.6	5.5	0.3	-	-
EK3	at%	41.4	20.3	17.4	19.2	1.6	0.1	-	-
EK4	wt%	45.4	22.1	16.3	9.9	6	0.1	0.2	-
EK4	at%	41.5	20.1	16.9	19.6	1.8	0.1	0	-
EK5	wt%	44	20.5	19.6	8.7	2.7	0.7	1.8	4
EK5	at%	38.7	18	17.5	16.7	0.8	0.4	0.5	7.4

4.2.1 Ni-20.1Co-19.8Cr-16.2Al-1.1Ta-0.3Y (alloy EK3)

The EK3 alloy was designed in order to study the effects of Y in its microstructure. As already discussed Y is expected to improve the adherence of Al_2O_3 scale to the base material and the oxidation resistance of the BC [Reed, 2008], see the introduction (section 4.1.1).

Table 4.3 EDS analysis (at%) data of the EK3 alloy in the as cast and heat treated conditions.

Area/Phase(s)	Ni	Co	Cr	Al	Ta	Y
EK3-AC						
large area	41.4±0.1	20.3±0.4	17.4±0.3	19.2±0.7	1.62±0.04	0.1
γ (Ni_{ss})	40.6±0.4	22.5±0.6	19.3±0.8	15.8±1	1.4±0.6	0.2
β (NiAl)	42.4±0.5	14.4±0.1	10.6±0.2	30.9±0.7	1.64±0.3	0
Y rich intermetallic phase	38.8±2	14.3±1.7	12.8±2.2	11.1±2.5	1.3±0.1	21.6±5
EK3-HT1 (1200 ˚C / 24 hrs)						
large area	41.7±0.3	20.4±0.2	17.3±0.1	18.9±0.3	1.5±0.1	0.04
γ (Ni_{ss})	40.7±0.2	23.2±0.2	21.4±0.4	13.1±0.5	1.6±0.1	0
β (NiAl)	44.4±0.8	13.9±1.1	9±1.4	31.5±2.1	1.1±0.1	0
M_5Y	50.5±1.3	12.4±0.5	6.7±1.3	15.2±0.6	0.3±0.2	14.7±1.2
EK3-HT2 (1200 ˚C / 48 hrs)						
large area	41.9±0.5	20.4±0.4	17.3±0.5	18.6±0.8	1.6±0.1	0.3
γ (Ni_{ss})	41.1±0.7	22.7±0.3	20.1±0.4	14.4±0.5	1.7±0.1	0
β (NiAl)	44.2±0.1	13.8±0.3	8.4±0.1	32.4±0.3	1.2±0.1	0
M_5Y	51.6±0.2	12.1±0.3	5.2±0.3	15.3±0.5	0.1	15.7±0.2
M_xY_z	10.4±3.9	5.7±1.9	6±2.3	1.8±0.5	0	76.4±8.5

4.2.1.1 As cast (EK3-AC)

The average composition of the as cast alloy (EK3-AC) is given in Table 4.3 and shows that the ingot was poorer in Cr and richer in Al and Ta contents compared with the nominal composition. The microstructure consisted of γ-Ni_{ss} and β-NiAl intermetallic and an Y rich intermetallic phase and a second phase in the γ-Ni_{ss}, which is believed to be the γ'-Ni_3Al, see figures 4.1 and 4.2. It should be noted that the fine second phase in the γ-Ni_{ss} could be seen only when the high resolution SEM (Inspect F) was used. As it can be seen from the BSE images, in figures 4.1 and 4.2 in EK3-AC there was micro-segregation in the microstructures. Based on the results of EK2-AC and the composition of EK3 the micro-segregation was attributed to both the Ta and Y additions. The scale of the intermetallics varied in the ingot. According to the EDS data (Table 4.3) the Cr content in the γ-Ni_{ss} (with γ'-Ni_3Al) was lower compared with the EK2-AC which could be due to the lower Cr content in the alloy, but the Co and Al contents were not different from those in the EK2 alloy. Similar decrease in the Cr content was observed in the β-NiAl intermetallic compared with the EK2-AC and its Al content was slightly increased.

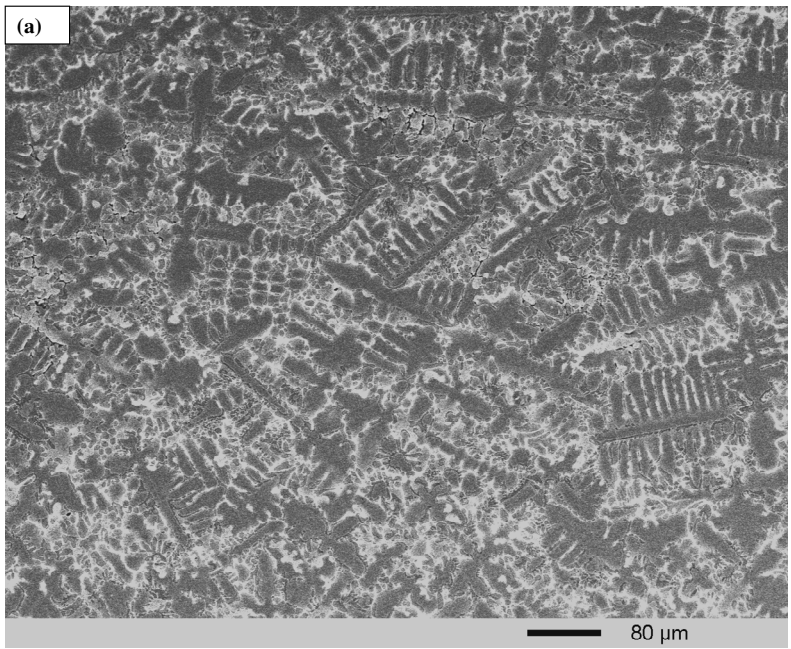

continued in the next page

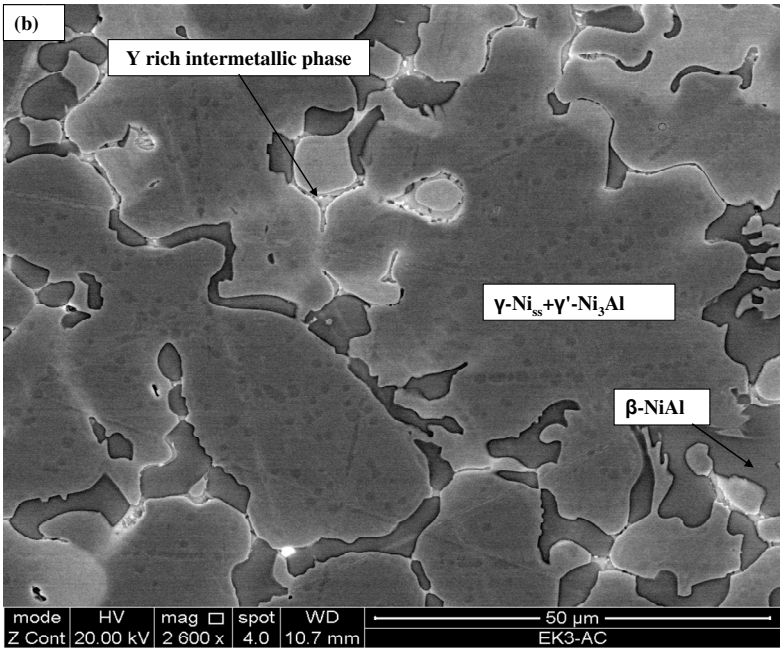

Figure 4.1 BSE images of the microstructure of EK3-AC.

The XRD data (figure 4.3) confirmed the presence of γ-Ni_{ss} and β-NiAl and suggested the presence of γ'-Ni_3Al in the microstructure, which is believed to be the second phase formed in the γ-Ni_{ss}, as seen in figure 4.1b. EDS analysis confirmed the presence of an Y rich intermetallic phase, which could be the M_5Y_Z (Y~25-26 at%). In the XRD diffractograms only one peak could correspond to the former intermetallic, but this peak coincided with other phases. The addition of Y in the alloy EK3 had a dramatic change in the architecture of the microstructure. The γ-β eutectic seen in EK2-AC was not observed in the alloy EK3.

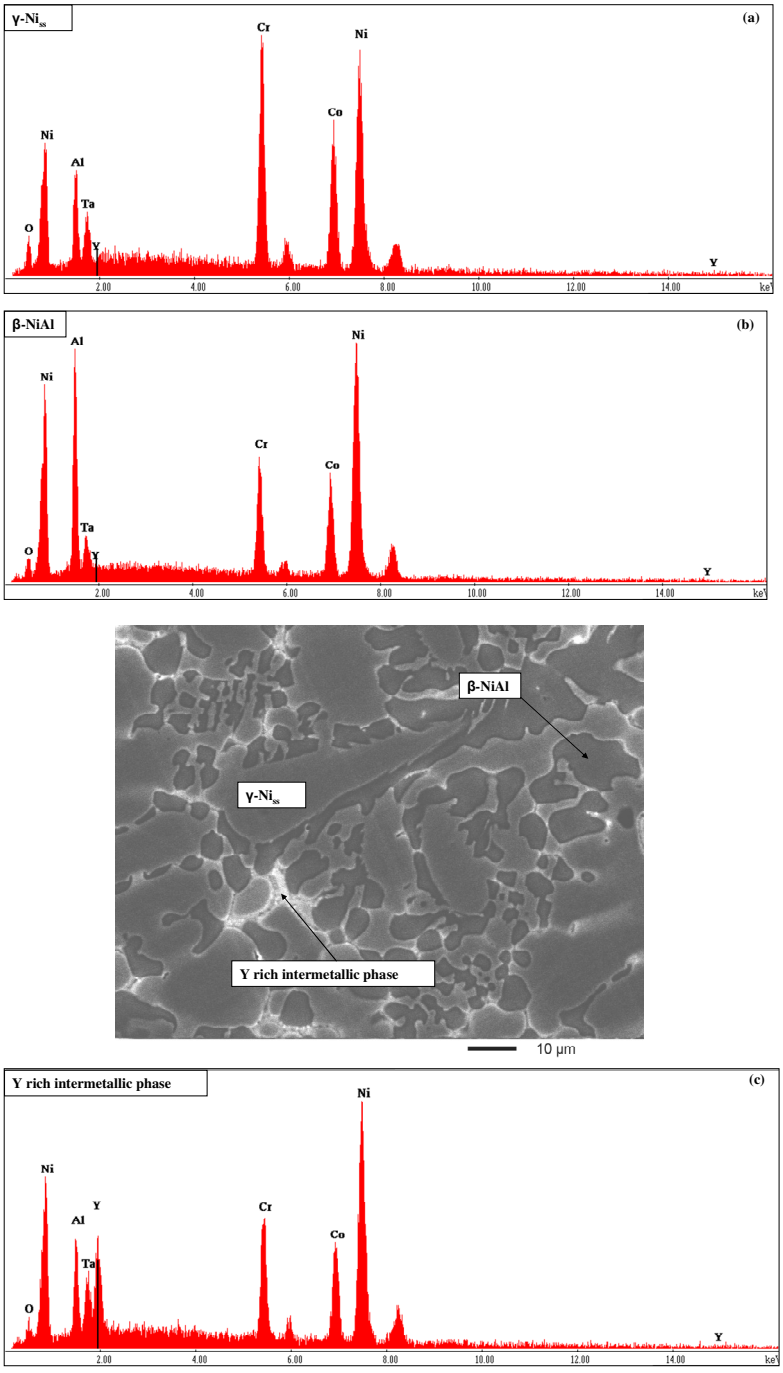

Figure 4.2 BSE image and EDS spectra of the EK3-AC showing presence of (a) γ-Ni_{ss}, (b) β-NiAl and (c) Y rich intermetallic phase.

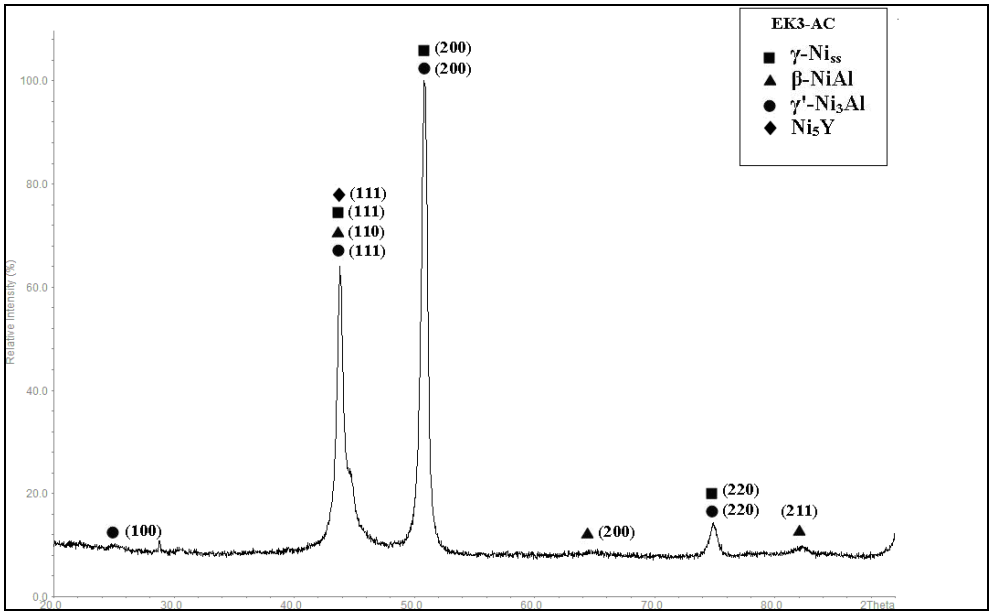

Figure 4.3 X-ray diffractogram of the EK3-AC.

4.2.1.2 Heat treated (EK3-HT)

The first heat treatment for the alloy (EK3-HT1) was for 24 hrs at 1200 ˚C. Compared with the as cast alloy the β-NiAl intermetallics had coarsened. There were Y rich areas present at the interface of β-NiAl and γ-Ni_{ss} that exhibited white contrast (figure 4.4). After this heat treatment the γ'-Ni_3Al precipitates that were present in the as cast condition (figure 4.1) could not be seen easily. The composition of the Y rich intermetallics corresponded to M_5Y (Table 4.3) and compared with the EK3-AC, it was richer in Al and poorer in Co, Cr and Ta. In the γ-Ni_{ss} the Cr content was increased and the Al was decreased compared with the EK3-AC. In the β-NiAl the Al content increased and the Cr content decreased in comparison with the as cast alloy. The presence of γ-Ni_{ss}, β-NiAl and M_5Y in EK3-HT1 was confirmed by the XRD data (see figure 4.5), where there was also one peak could be attributed to γ'-Ni_3Al.

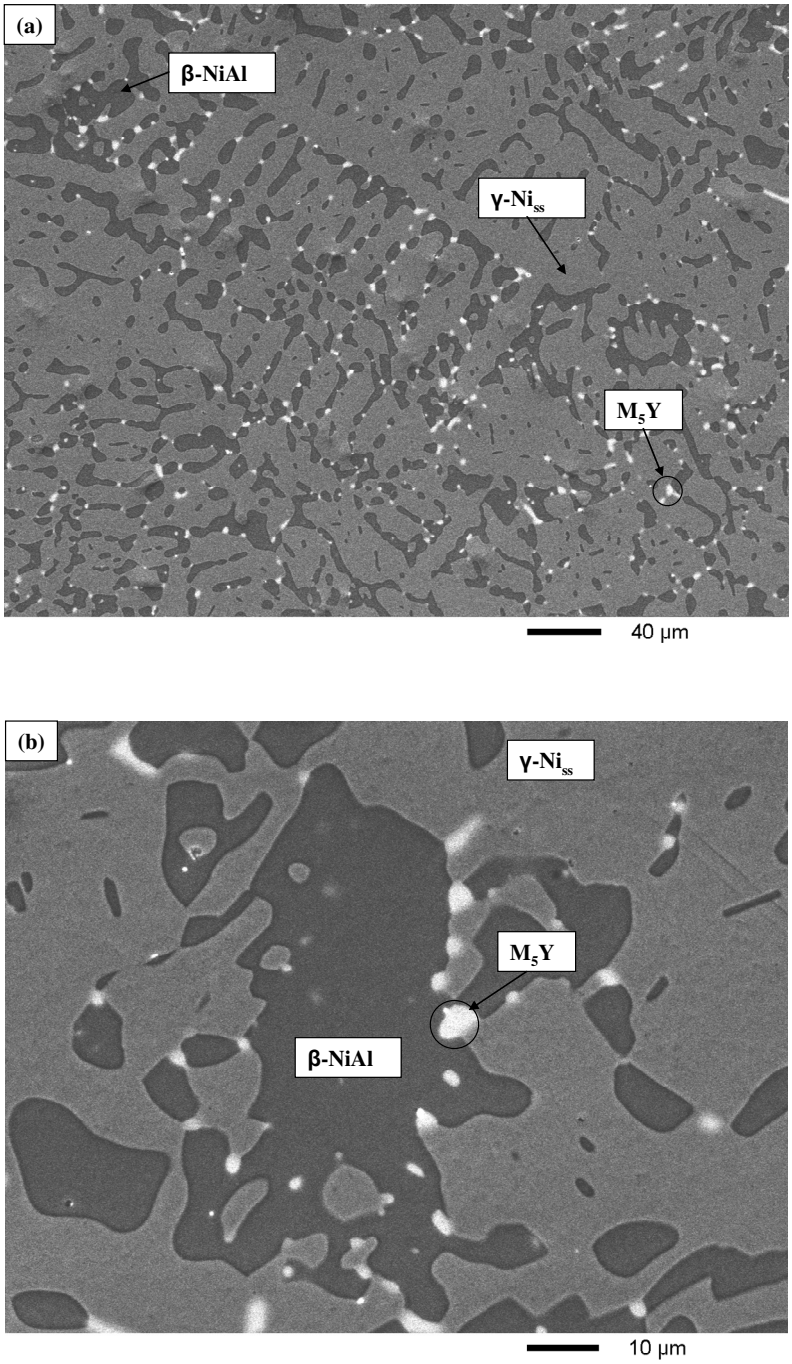

Figure 4.4 BSE images of the microstructure of EK3-HT1.

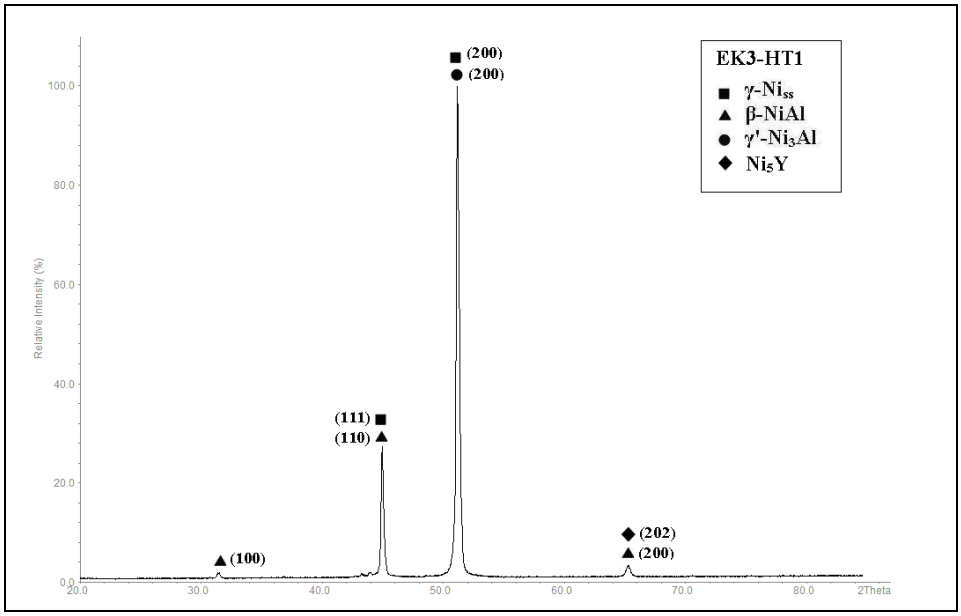

Figure 4.5 X-ray diffractogram of EK3-HT1.

After the second heat treatment (EK3-HT2) at 1200 ˚C for another 24 hrs (i.e., 48 hrs in total) the alloy microstructure consisted of the γ-Ni_{ss}, β-NiAl, M_5Y, M_xY_z and γ'-Ni_3Al as can be seen in figures 4.6 and 4.7. There was evidence for the precipitation of γ'-Ni_3Al in the γ-Ni_{ss}, see figure 4.6. The microstructure had coarsened even further after this heat treatment (solute rich areas at the γ-Ni_{ss} - β-NiAl interface was eliminated. The EDS data (see Table 4.3) for the Y rich areas had high standard deviation which is the reason why these intermetallics have been labelled M_xY_z. The Ni, Co, Cr and Al contents were significantly lower in M_xY_z compared with M_5Y, whereas the Y content was lower in the M_5Y and close to the Ni_5Y stoichiometry. The compositions of the Y rich intermetallics corresponded to Ni_5Y and NiY_3. The XRD data (see figure 4.8) suggested the presence of γ-Ni_{ss}, β-NiAl and γ'-Ni_3Al and there were no peaks corresponding to Ni_5Y or NiY_3.

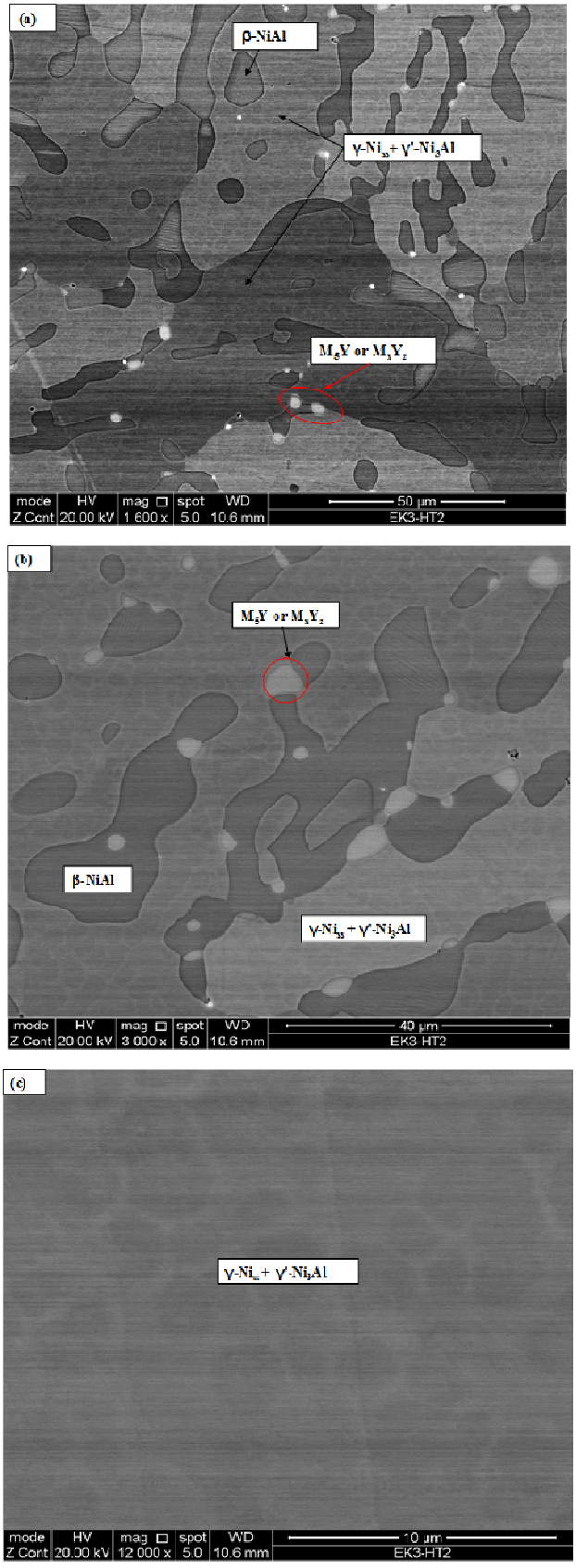

Figure 4.6 BSE images of the microstructure of EK3-HT2.

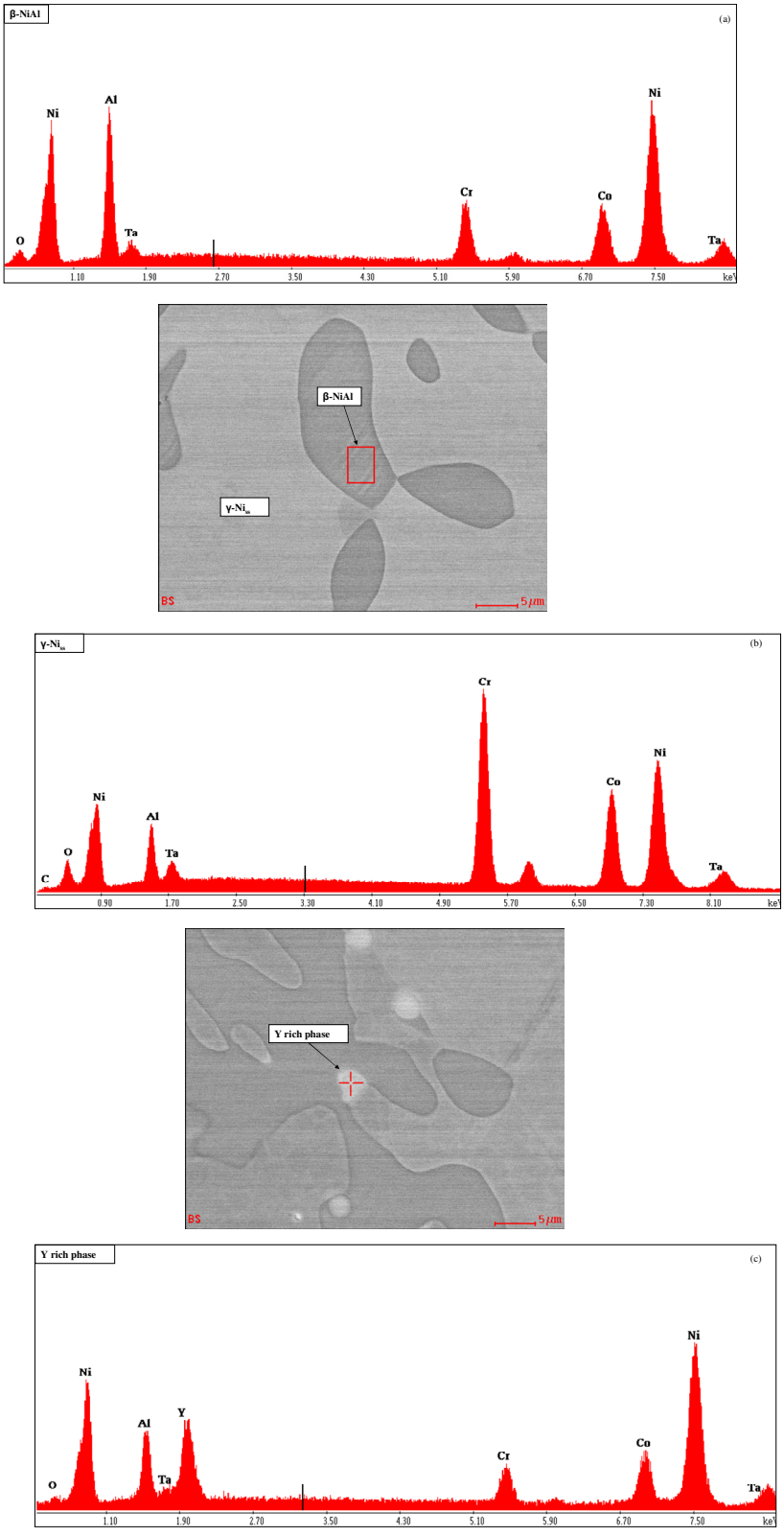

Figure 4.7 BSE images and EDS spectra of the EK3-HT2 showing presence of (a) γ-Ni_{ss}, (b) β-NiAl and (c) Y rich phase.

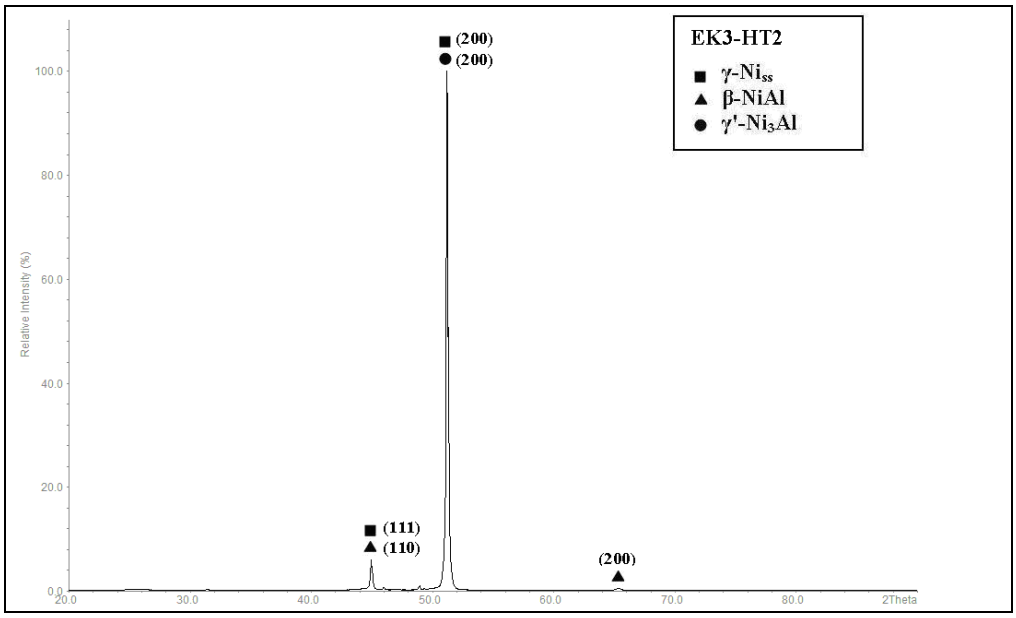

Figure 4.8 X-ray diffractogram of EK3-HT2.

4.2.2 Ni-20.1Co-19.7Cr-16.2Al-1.1Ta-0.3Y-0.2Hf (alloy EK4)

The EK4 alloy was designed in order to study the synergistic effects of Ta with two reactive elements (RE) (Y and Hf) being simultaneously present in the microstructure. Hf is expected to increase the adherence of the Al_2O_3 scale with the BC and to improve hot corrosion resistance and oxidation resistance [Unocic and Pint 2010, Gupta and Duvall 1984], see also introduction (see section 4.1.1).

4.2.2.1 As cast (EK4-AC)

The average composition of the as cast alloy (EK4-AC) is given in Table 4.4 and shows that the ingot was richer in Cr and poorer in Al compared with the nominal composition. The as solidified microstructure of EK4 is shown in figures 4.9 and 4.10. The microstructure contained the solid solution γ-Ni_{ss} and the intermetallic β-NiAl and white contrast areas, the latter were observed in BS imaging (figure 4.9). The former two phases, γ-Ni_{ss} and β-NiAl, were confirmed by the XRD data (see figure 4.11) and the EDS data (see Table 4.4). The XRD also suggested the presence of $Ni_{17}Y_2$.

Table 4.4 EDS analysis (at%) data of EK4 alloy in the as cast and heat treated conditions.

Areas/Phase(s)	Ni	Co	Cr	Al	Ta	Y	Hf
EK4-AC							
large areas	41.5±0.4	20±0.1	16.9±0.2	19.6±0.4	1.8±0.1	0.1	0
γ (Ni_{ss})	40.5±0.6	22.2±0.5	20.2±0.3	15.4±0.4	1.7±0.2	0	0
β (NiAl)	42.3±1.1	15.5±0.5	10.9±0.9	29.8±0.6	1.4±0.3	0	0
$(\beta+\gamma)_{eutectic}$	35.7±12.5	16.7±1.3	12.4±1.6	27±2.8	1.3±0.2	0	0
white contrast areas	45.9±0.7	15.6±1	10±1.8	14.5±2.4	3.6±0.6	5.3±1.1	5±1.3
EK4-HT1 (1200 ˚C / 24 hrs)							
large area	42±0.3	20±0.2	17.2±0.2	19±0.6	1.7±0.1	0.1	0
γ (Ni_{ss})	40.3±0.3	23.5±0.1	22.1±0.4	12.2±0.4	1.8±0.1	0	0
β (NiAl)	44.7±0.3	13.5±0.3	8.3±0.2	32±0.3	1.4±0.1	0	0
black contrast Al rich phase	40±1.3	19.8±2.1	17.4±3	20.8±3.9	1.8±0.1	0	0
black contrast Cr rich phase	38.4±0.2	22.8±0.8	21.7±0.1	15±0.6	1.9±0.3	0	0

white contrast phase	50.2±0.5	11.9±0.4	6.7±0.2	15.8±0.2	1.4±0.1	11.9±0.3	1.9
bright contrast phase	23.2±8.3	8.6±2	5.7±0.5	5.1±4	28.4±5.7	6.7±4	22.1±4.4
EK4-HT2 (1200 ˚C / 48 hrs)							
large area	41.8±0.2	19.9±0.2	17.1±0.2	19.3±0.2	1.7±0.1	0.1	0
γ (Ni_{ss})	40.4±0.2	23.5±0.1	21.8±0.4	12.2±0.3	1.8±0.1	0	0
β (NiAl)	44.9±0.4	13.1±0.2	7.7±0.2	32.8±0.4	1.3±0.1	0	0
white contrast featureless	29.8±1.4	18.1±1.6	17.7±1.9	6.2±0.9	12.4±3.4	2.6±0.9	13±3.1
white contrast areas with other phases present	47.3±7	12.4±1	6.6±1.5	14.6±2.6	1.5±1.5	12.5±2.1	3.3±4.7

The β-NiAl intermetallic had formed a eutectic with the solid solution, similar to that seen in EK2-AC. Segregation of Ta, Y and Hf at the interface of the γ-Ni_{ss} with β-NiAl can be seen in the white contrast areas in the BSE images in figure 4.9 and in figure 4.10. The bright contrast areas were rich in Ta, Y and Hf. The EDS analysis suggested that these areas contained ~5 at% Y and 5 at% Hf. If we allow for Hf solid solution in the Y containing intermetallic, then Y+Hf ~ 10 at% which could be the $Ni_{17}Y_2$ intermetallic suggested by the XRD. There was no evidence (at the resolution of FEG-SEM) of γ'-Ni_3Al precipitation in the γ-Ni_{ss}, even though the XRD data contained peaks that corresponded to this intermetallic.

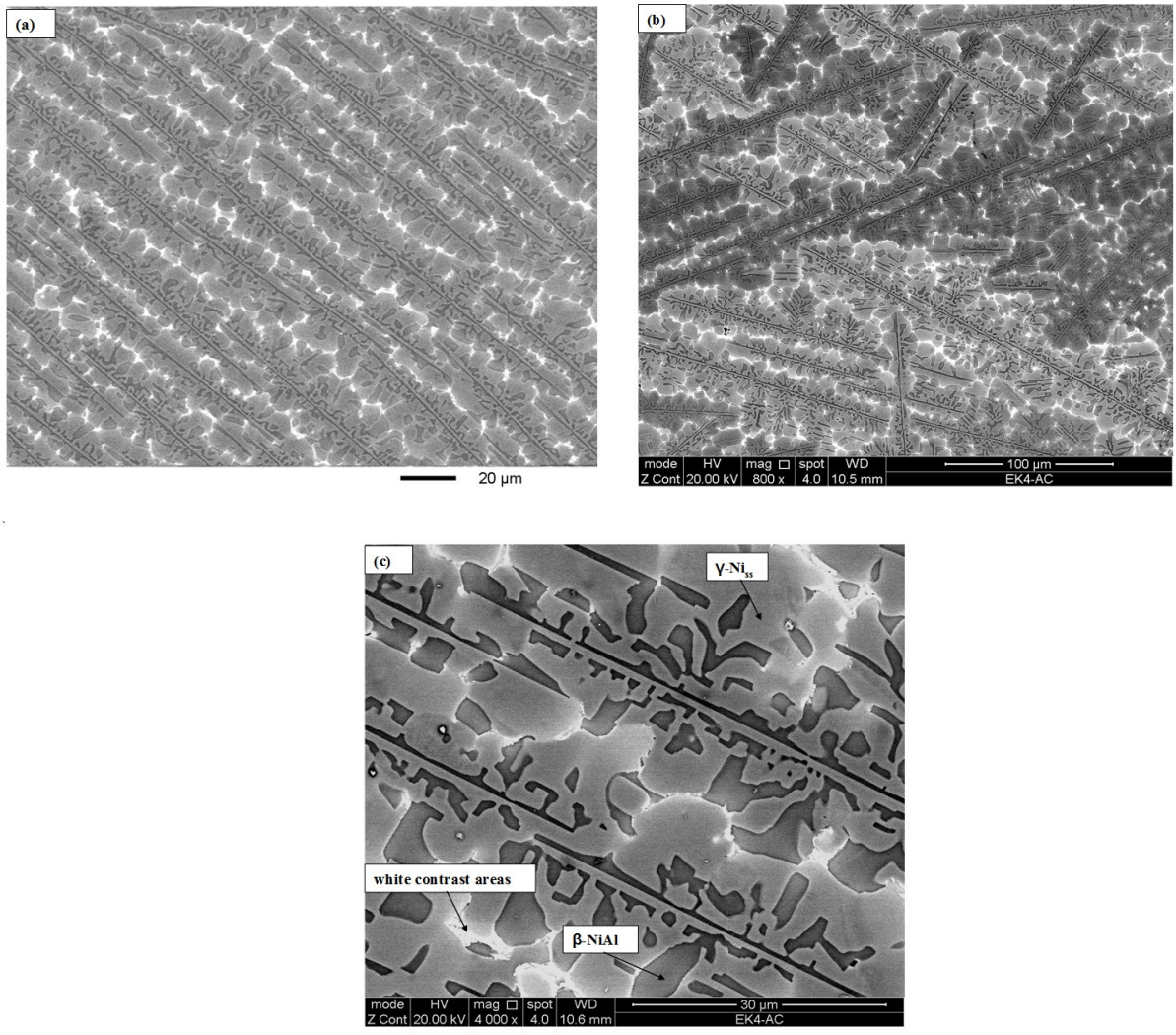

Figure 4.9 BSE images of the microstructure of EK4 alloy in the as-cast condition.

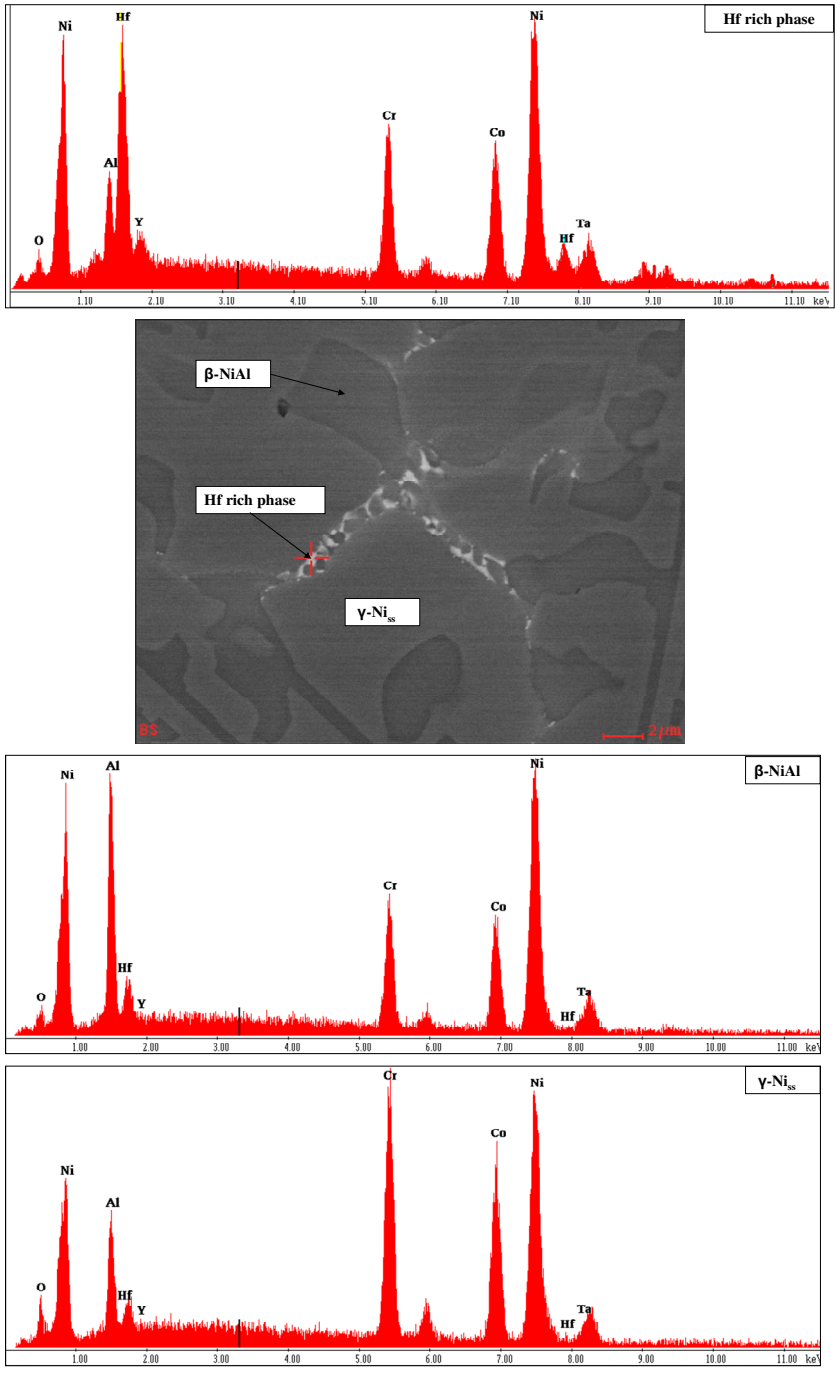

Figure 4.10 BSE image and EDS spectra of the EK4-AC alloy showing presence of (a) Hf rich phase, (b) β-NiAl and (c) γ-Ni_{ss}.

.

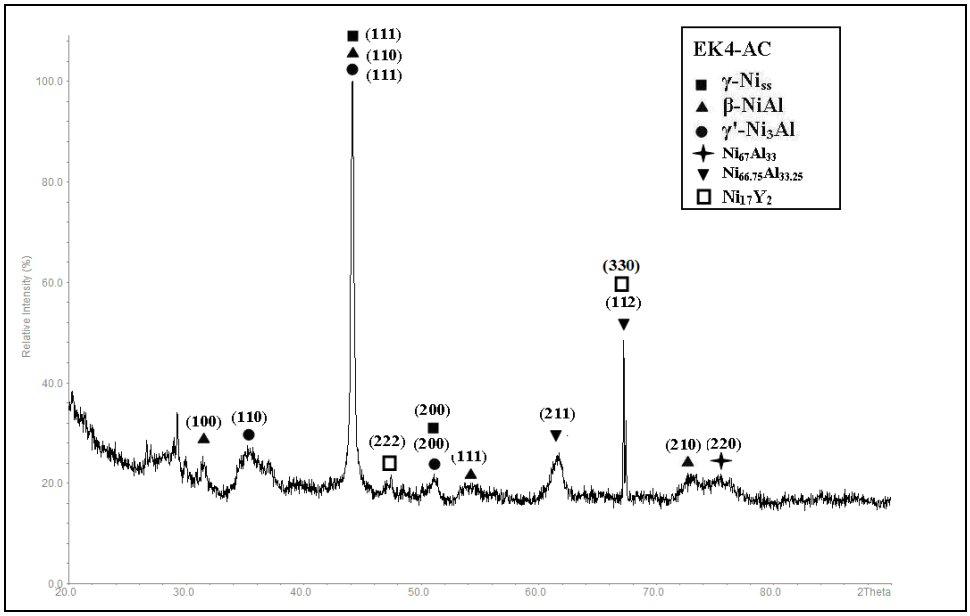

Figure 4.11 X-ray diffractogram of the EK4-AC.

4.2.2.2 Heat treated (EK4-HT)

The first heat treatment (EK4-HT1) was for 24 hrs at 1200 ˚C. Compared with the as cast alloy the microstructure was coarsened, and new phases were formed that were either rich in Y or Ta and Hf and with compositions different from the white contrast phases in EK4-AC (Table 4.4). The presence of γ-Ni_{ss} and β-NiAl in EK4-HT1 was confirmed by the XRD data (figure 4.13), which also suggested the presence of γ'-Ni_3Al. However, no γ' particles were seen in the γ-Ni_{ss}. In the XRD diffractograms there were also some peaks that could correspond to the Ni_5Y and $Ni_{17}Y_2$ phases. The white contrast phase with Y~11.9 at% could be the $Ni_{17}Y_2$ and if there was solid solution of Hf in the Y rich intermetallic then Y+Hf ~15 at % and the phase could be the Ni_5Y also suggested by the XRD. The Co and Cr concentrations in β-NiAl had decreased and Al concentrations increased compared with the EK4-AC. After this heat treatment the Co and Cr contents in the γ-Ni_{ss} had increased whereas the Al content decreased. In the Ni_{ss} there were precipitates exhibiting black contrast, see figure 4.12. These were free of Y and Hf and were rich either in Al or in Cr, see Table 4.4. The Cr rich black contrast phase had Cr~21.7 at% and Al~15 at% and the Al rich black contrast phase had Cr~16 at% and Al~22.7 at%. The composition of the former was similar to that of the γ-Ni_{ss} in the EK4-AC. There were also brighter contrast phases; one of them had low Ta (1.4 at%) and Hf (1.9 at%) but high

Y (11.9 at%) content which could be Ni_5Y or $Ni_{17}Y_2$ (see above) and the other had high Ta (28.4 at%) and Hf (22.1 at%) and low Y (6.7 at%) content. The chemical analysis of the latter phase was difficult owing to its size which would explain the high standard deviations. Some of the areas of white contrast were found to have other phases present in them (figure 4.12b).

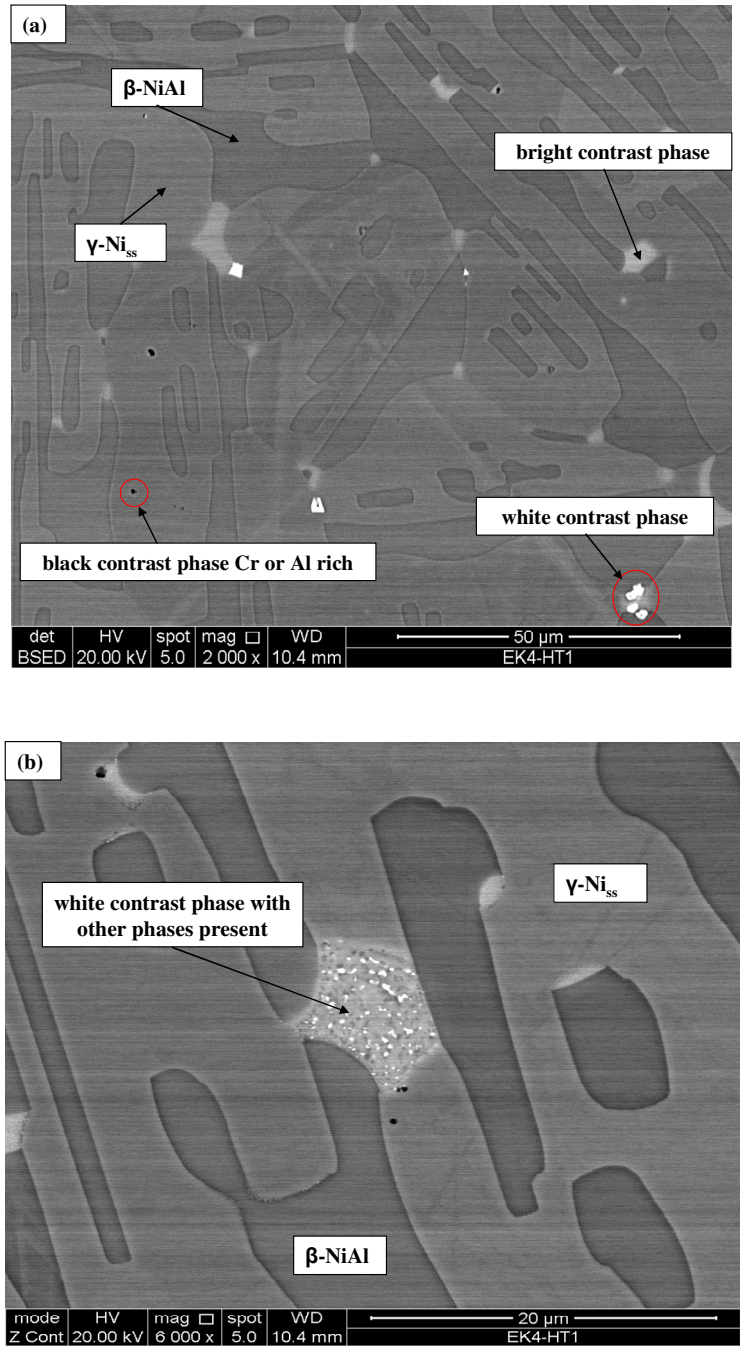

Figure 4.12 BSE images of the microstructure of the EK4-HT1, (a) x2000, (b) x6000.

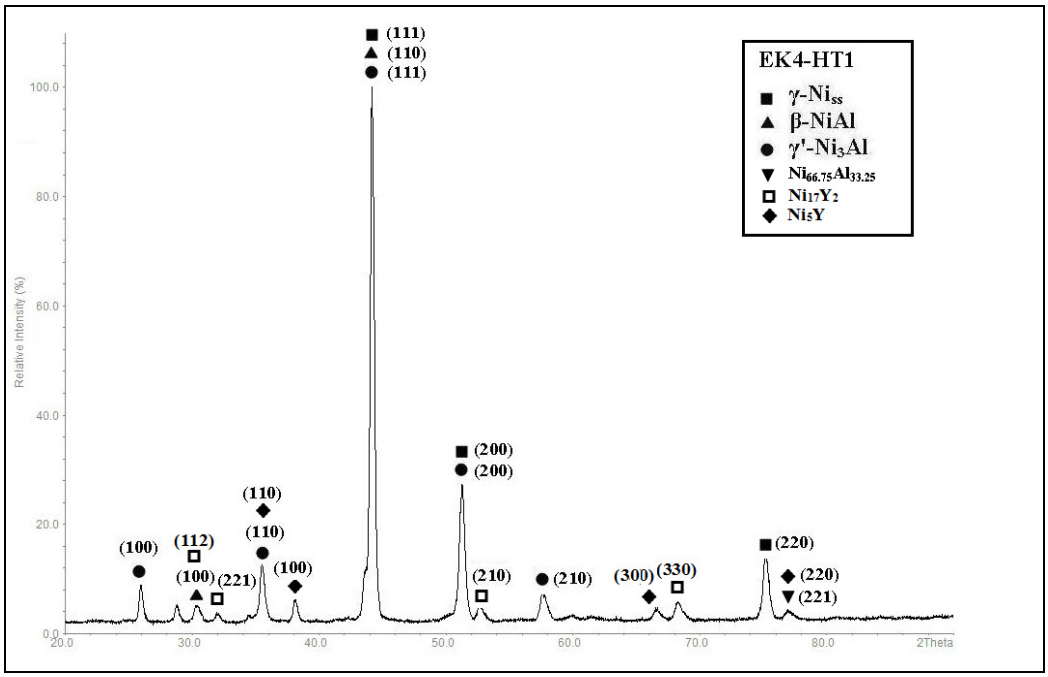

Figure 4.13 X-ray diffractogram of the EK4-HT1.

The second heat treatment (EK4-HT2) was for another 24 hrs at 1200 ˚C, i.e., 48 hrs at 1200 ˚C in total. The typical microstructure of the EK4-HT2 is shown in figure 4.14. The microstructure had coarsened further compared with EK4-HT1 and consisted of γ-Ni_{ss}, β-NiAl, fine precipitates decorating the γ/β interfaces, white contrast featureless areas and white contrast areas with other phases present in them, see figure 4.14 to 4.16. The latter areas were observed in the γ-Ni_{ss} near its interface with β-NiAl. The XRD figure 4.16 confirmed the presence of γ-Ni_{ss} and β-NiAl and there were peaks that could attributed to the $Ni_{17}Y_2$ and Ni_5Y phases. The γ' that was suggested by XRD was not observed. The average composition of the EK4-HT2 was similar with the as cast alloy and with EK4-HT1, see Table 4.4 After the second heat treatment the compositions of both the γ-Ni_{ss} and β-NiAl were unchanged compared with the EK4-HT1. The fine precipitates decorating the γ/β interfaces were Y rich or Hf and Ta rich, see figure 4.15a, b and 4.16. The white contrast featureless areas were Ta and Hf rich, see Table 4.4. The white contrast areas with other phases present were Y rich and contained Ta and Hf, see figures 4.14d, 4.15e and Table 4.4. The black contrast phases observed in the EK4-HT1 were not present in the EK4-HT2. The similarity of the composition of the black contrast Cr rich phase in EK4-HT1 with the γ-Ni_{ss} in EK4-AC would suggest that the black contrast phase was formed

from partitioning of solutes in the γ-Ni_{ss} during HT and that the latter was completed in HT2. However, partitioning of solute continued to play a role in the formation of the white contrast phases, compare their compositions for HT1 and HT2, in Table 4.4.

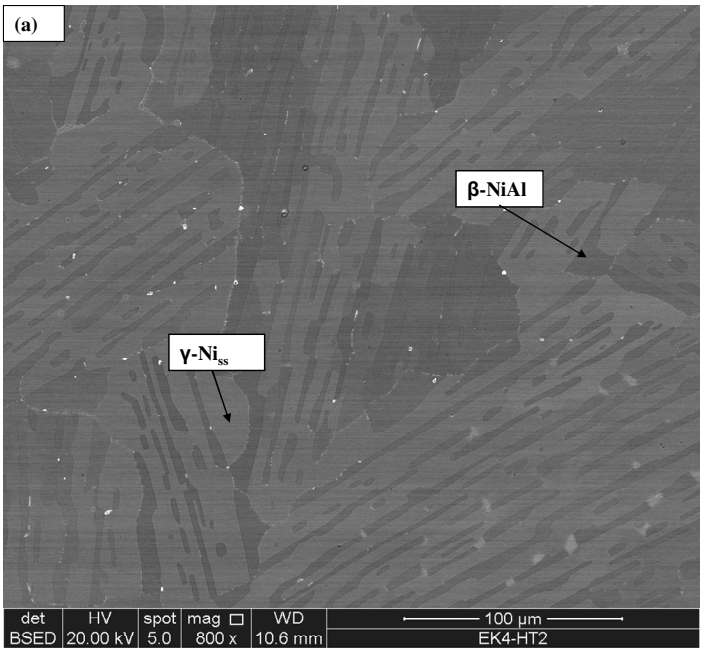

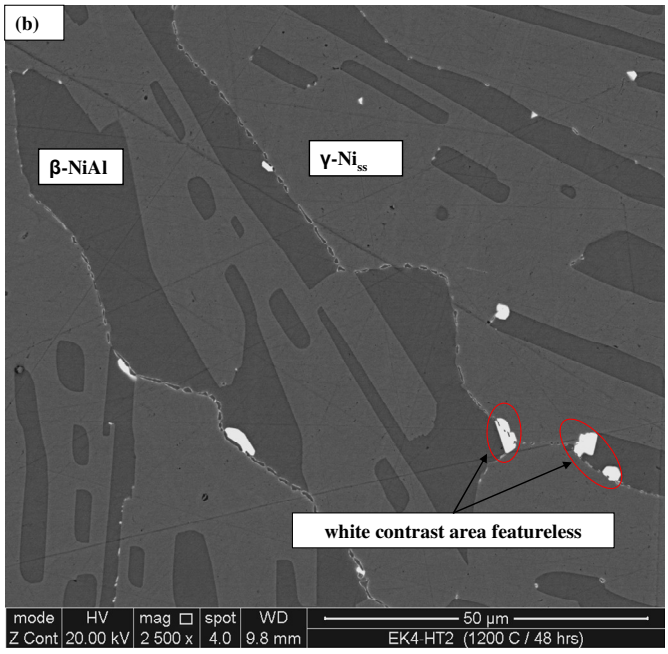

continued in the next page

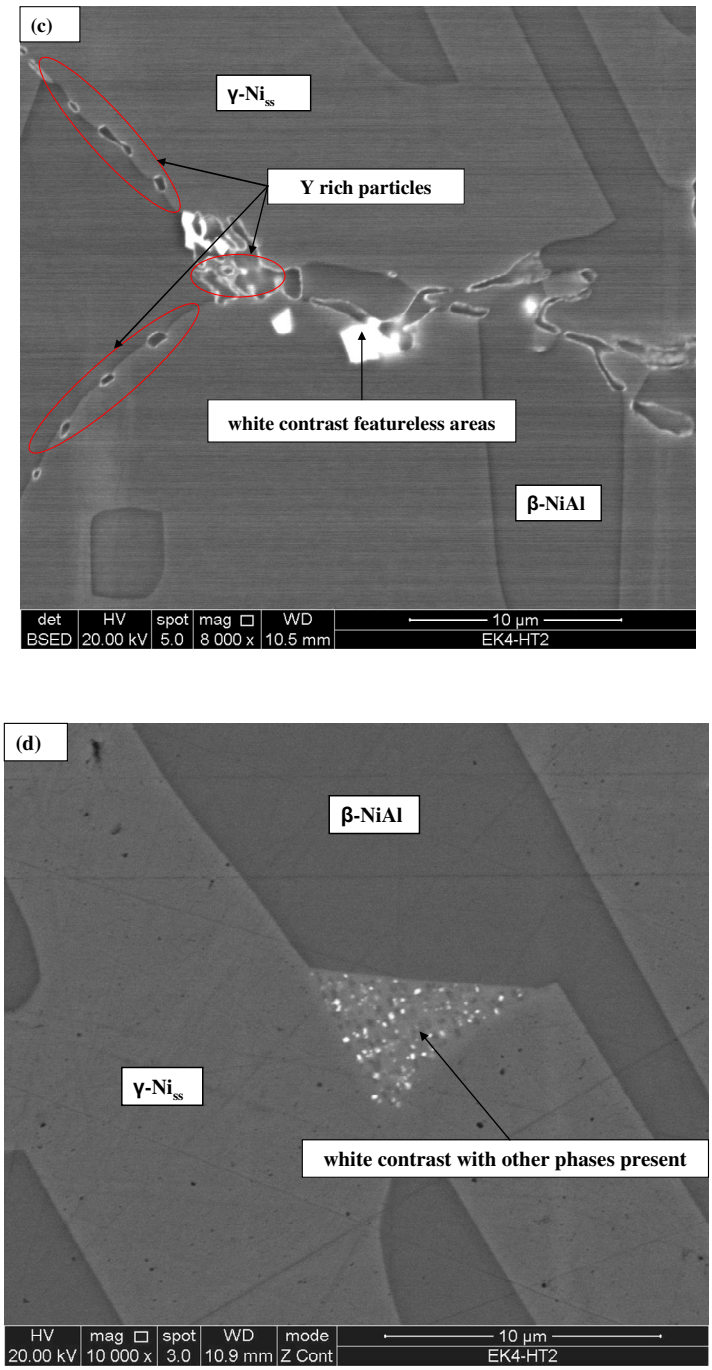

Figure 4.14 BSE images showing the microstructure of EK4-HT2 (a) x800, (b) x2500, (c) x800, (d) x10000.

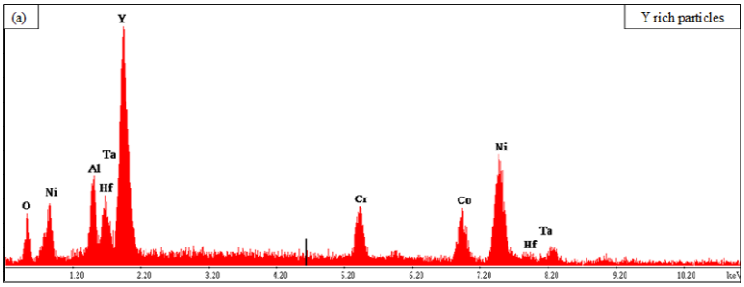
(a)
Y rich particles
Y
Ta
Al
Hf
Ni
O
Cr
Co
Ni
Ta
Hf

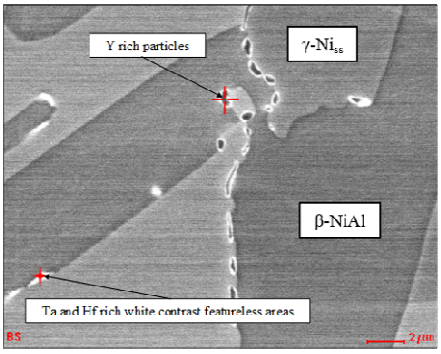
Y rich particles
γ-Ni$_{ss}$
β-NiAl
Ta and Hf rich white contrast featureless areas
BS
2 μm

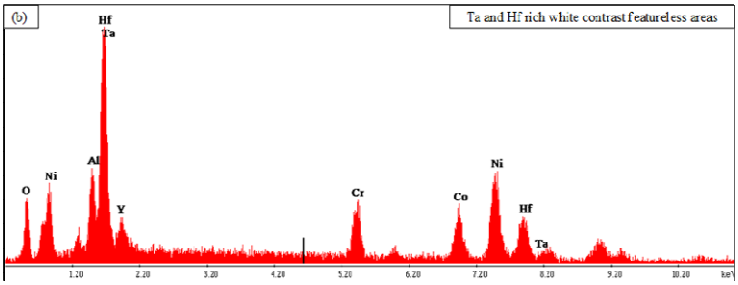
(b)
Ta and Hf rich white contrast featureless areas
Hf
Ta
Al
Ni
O
Y
Cr
Co
Ni
Hf
Ta

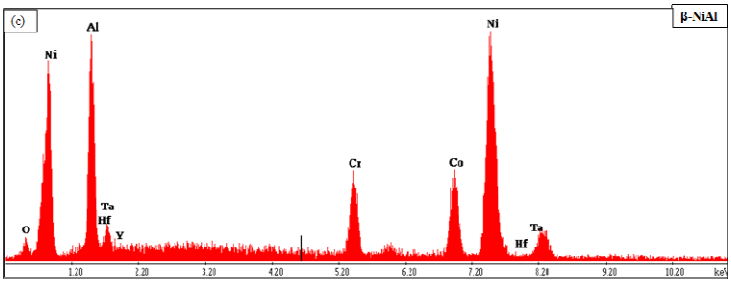
(c)
β-NiAl
Al
Ni
Ni
Ta
Hf
Y
O
Cr
Co
Ta
Hf

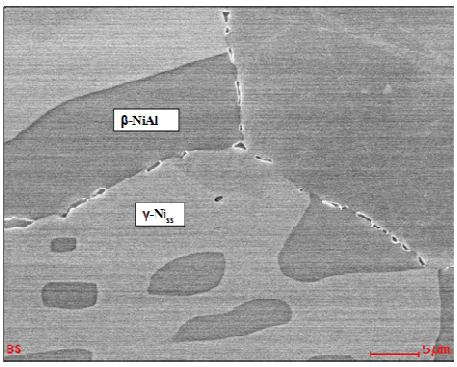
β-NiAl
γ-Ni$_{ss}$
BS
5 μm

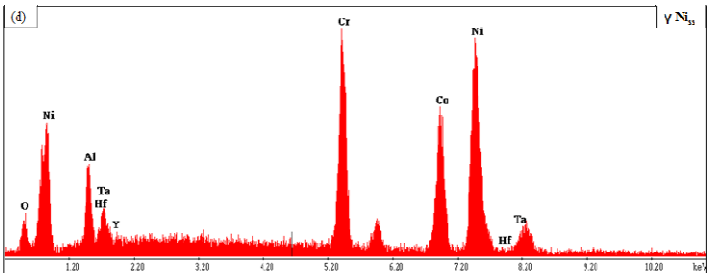
(d)
γ Ni$_{ss}$
Cr
Ni
Co
Ni
Al
Ta
Hf
O
Y
Ta
Hf

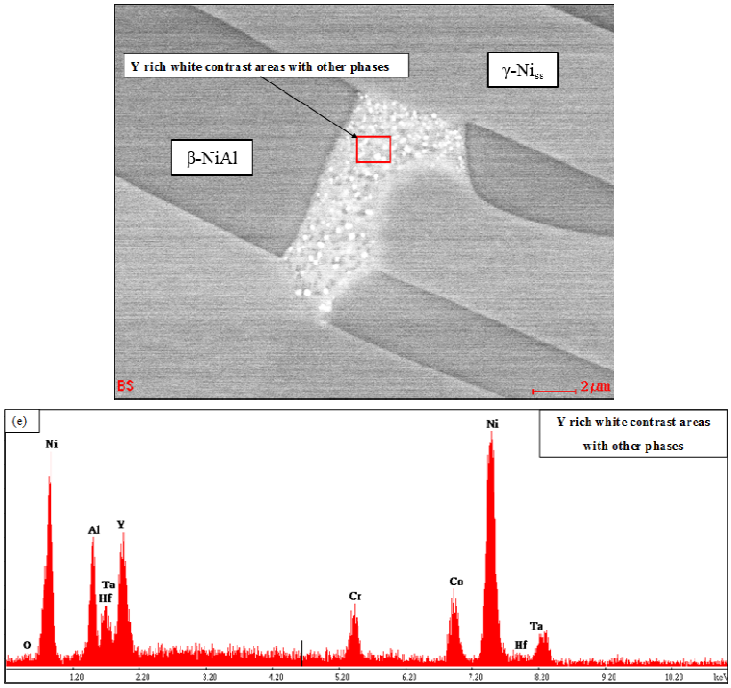

Figure 4.15 BSE images and EDS spectra of EK4-HT2 showing presence of (a) Y rich particles, (b) Ta and Hf rich white contrast featureless areas, (c) β-NiAl, (d) γ-Ni_{ss} and e) Y rich white contrast areas with other phases.

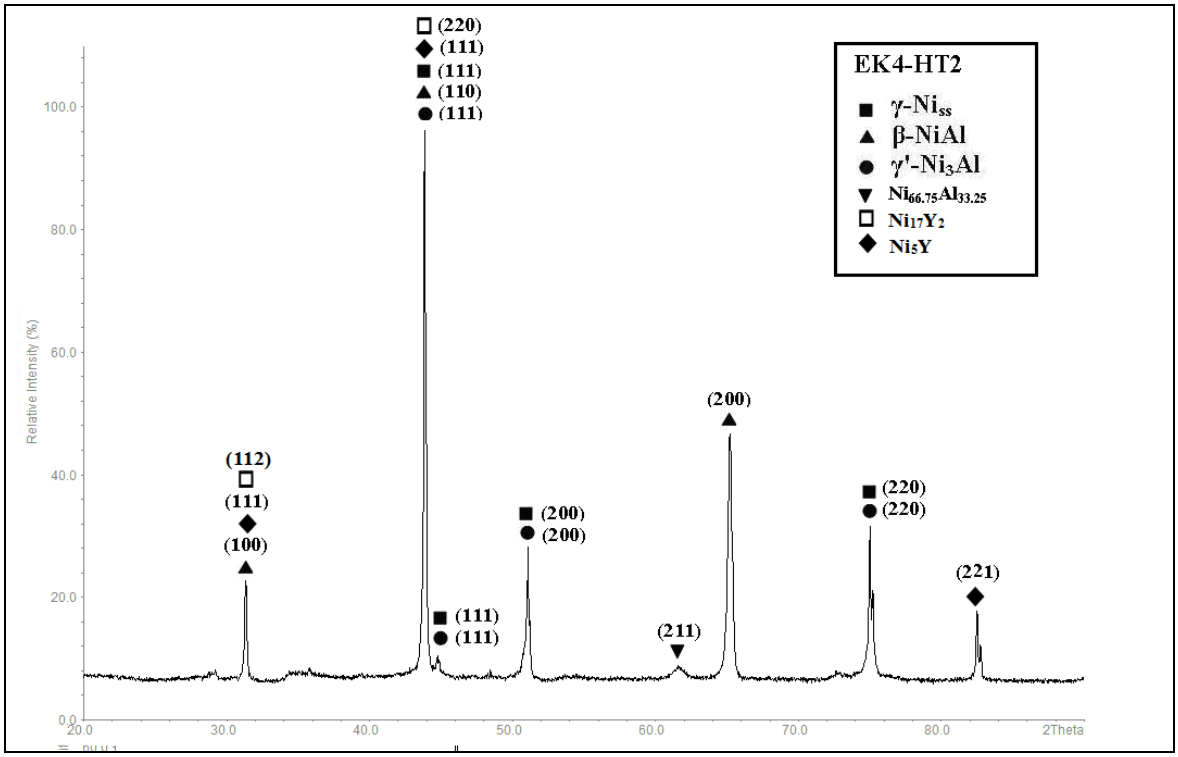

Figure 4.16 X-ray diffractogram of EK4-HT2.

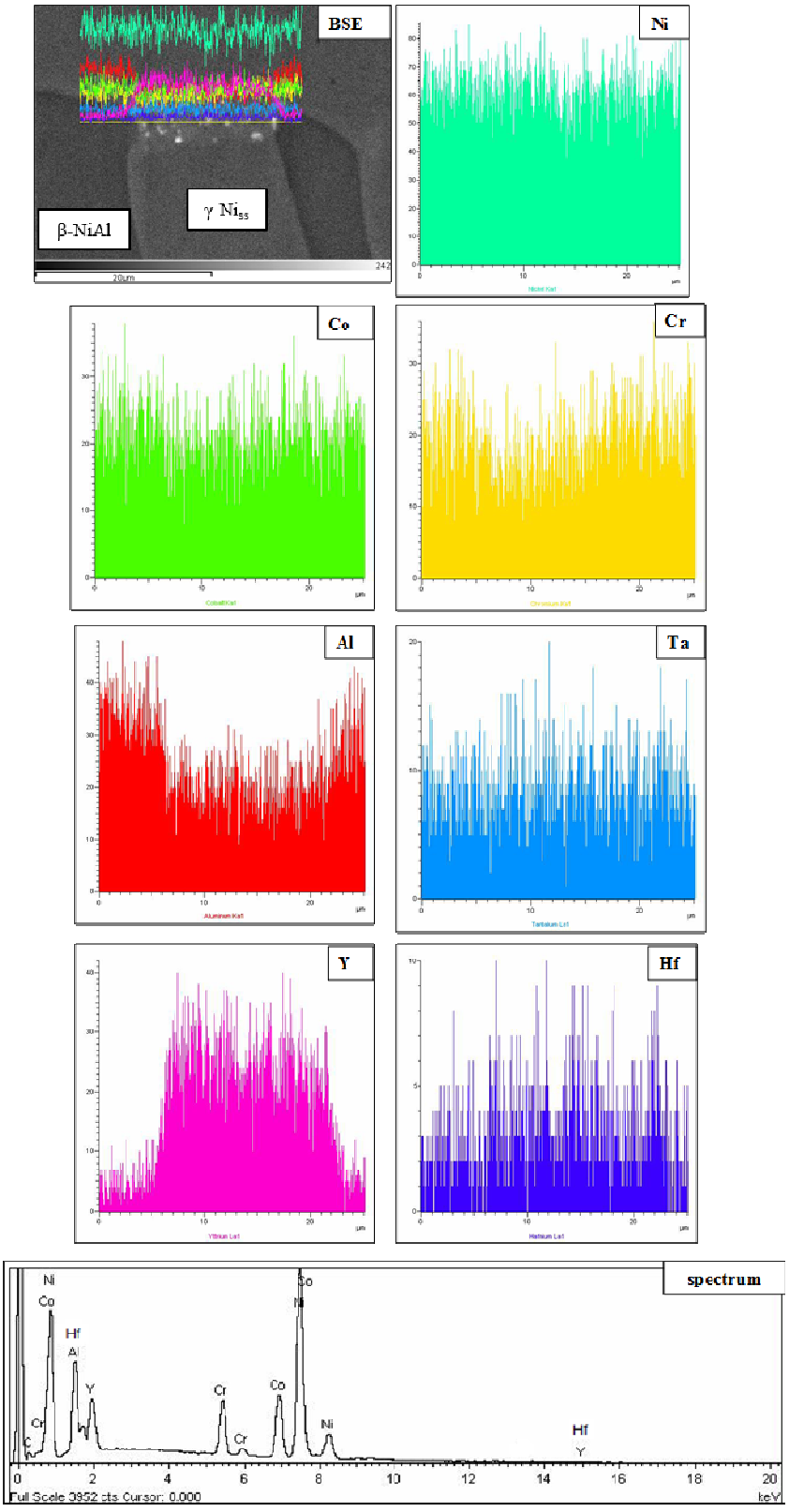

Figure 4.17 BSE image of EK4-HT2 and line scans showing distributions (detected by EDS) of Ni, Co, Cr, Al, Ta, Y and Hf.

4.2.3 Ni-19.3Co-19.1Cr-15.6Al-1.1Ta-0.3Y-0.2Hf-3.5Si (alloy EK5)

The EK5 alloy was designed in order to study the synergistic effects of Ta, Y, Hf and Si in an MCrAlY BC designed to operate at high temperatures. As suggested by Gupta and Duvall (1984), active elements such as yttrium and hafnium are expected to improve the oxide scale adherence with the BC and elements such as silicon and tantalum are added to improve hot corrosion resistance and protect the oxide scale from spallation and are also expected to reduce the oxide scale growth.

4.2.3.1 As cast (EK5-AC)

The average composition of the as cast alloy (EK5-AC) is given in Table 4.5 and shows that the ingot was slightly poorer in Co and Cr and slightly richer in Al and significantly richer in Si content compared with the nominal composition. The as solidified microstructure of this alloy can be seen in figure 4.18 and exhibited features seen in the EK4 alloy in the as cast condition. There was some weak evidence of a second phase in the solid solution see figure 4.18b. The microstructure consisted of the γ-Ni_{ss}, the β-NiAl intermetallic, a white contrast area, see figures 4.18 to 4.21, and a grey contrast area that was formed with the white one see figure 4.19, 4.20. According to the EDS data (Table 4.5) the Cr and Al contents in the γ-Ni_{ss} increased and decreased, respectively, and the Al content decreased in the β-NiAl, compared with EK4-AC and in both phases the solid solubility of Si was significant. Based on the EDS spectra taken from EK5-AC (see figures 4.19 and 4.20) and the EDS data in Table 4.5, the grey contrast area was rich in Y and Si and the white contrast area was rich in Ta, Hf and Si. The white contrast areas were formed in the same areas as with the EK4 alloy; they were poorer in Al and Y and richer in Ta and exhibited high solid solubility of Si.

Table 4.5 EDS analysis (at%) data of the EK5 alloy in the as cast and heat treated conditions.

Phase(s)	Ni	Co	Cr	Al	Ta	Y	Hf	Si
EK5-AC								
large area	38.7±0.9	17.9±0.2	17.5±0.5	16.7±0.5	0.8±0.9	0.4±0.2	0.5±0.2	7.4±2.4
γ (Ni_{ss})	37.1±0.4	21.8±0.1	23.3±0.5	10.9±0.6	1.1±0.5	0.2	0.1	5.3±0.6
β (NiAl)	40.8±0.4	14.1±0.2	11.4±0.3	26.7±0.2	0.6±0.4	0.5	0.3	6±0.7
white contrast area	34.3±0.9	16±0.7	11.7±2.1	4.3±0.9	8.3±1.7	1.5±0.3	4.1±0.7	19.6±3.3
grey contrast area	40.5±0.8	14.8±0.5	14.1±1.2	8.1±2	1.9±0.2	6.4±0.3	1±0.1	13.2±0.7
EK5-HT1 (1200 ˚C / 24 hrs)								
large area	38.9±0.6	17.5±0.3	17.2±0.3	16.6±0.2	0.4	0.2	0.5	8.6±1.3
γ (Ni_{ss})	36.7±0.4	21.5±0.4	24.1±0.3	9.4±0.2	1.1±0.5	0	0.2	7±1
β (NiAl)	41.5±0.3	13.7±0.1	10.2±0.2	22±5.7	0.3	0.2	0.5	7.7±0.9

A white contrast areas with other phases	41.7±1.9	14.1±1	12.1±0.9	6.9±1.1	1.6±1.3	5±2.5	2.4±1	16.1±1.4
grey contrast areas in A (Y and Si rich)	41.4±1.4	15.4±1.3	13.4±0.8	6.1±0.6	2.6±0.6	4.4±2.1	2.6±0.6	14.1±0.4
white contrast areas in A (Ta, Hf and Si rich)	32.5±1	13.8±0.1	2.3±0.1	1.7±0.5	13.2±0.8	0.4	7.2±0.6	29±2.9
B white contrast featureless areas	33.2±0.7	13.3±0.2	2.1±0.2	1.3±0.1	10.1±0.6	0.6±0.2	8.2±0.6	31.1±1.3
EK5-HT2 (1200 ˚C / 48 hrs)								
large area	39.9±0.5	17.8±0.4	17.5±0.4	15.4±0.5	0.4±0.5	0.1	0.6	8.2±1
γ (Ni_{ss})	38.4±1	21.2±0.2	23.2±0.4	8.8±0.2	0.7±0.6	0	0.2	7.3±1.6
β (NiAl)	43.4±0.6	13.3±0.2	9.5±0.1	25.5±0.2	0.4	0.2	0.3	7.3±0.8
white contrast phase (Ta, Hf and Si rich)	32.7±1.1	13.4±0.4	2.2±0.4	1.5±0.3	11.2±0.8	0.5	7.1±1.3	31.3±3

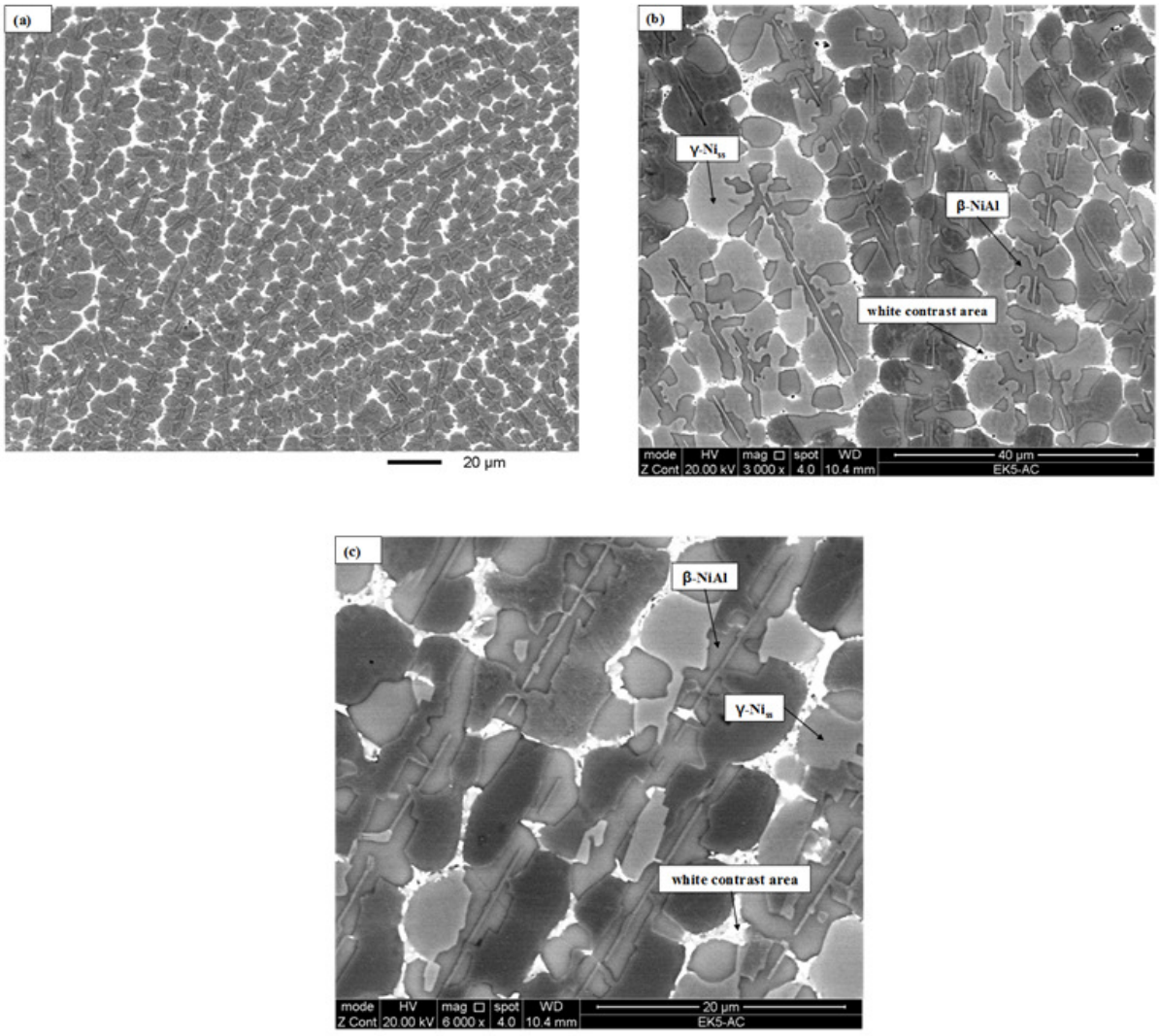

Figure 4.18 BSE images of the microstructure of EK5 alloy in the as-cast condition.

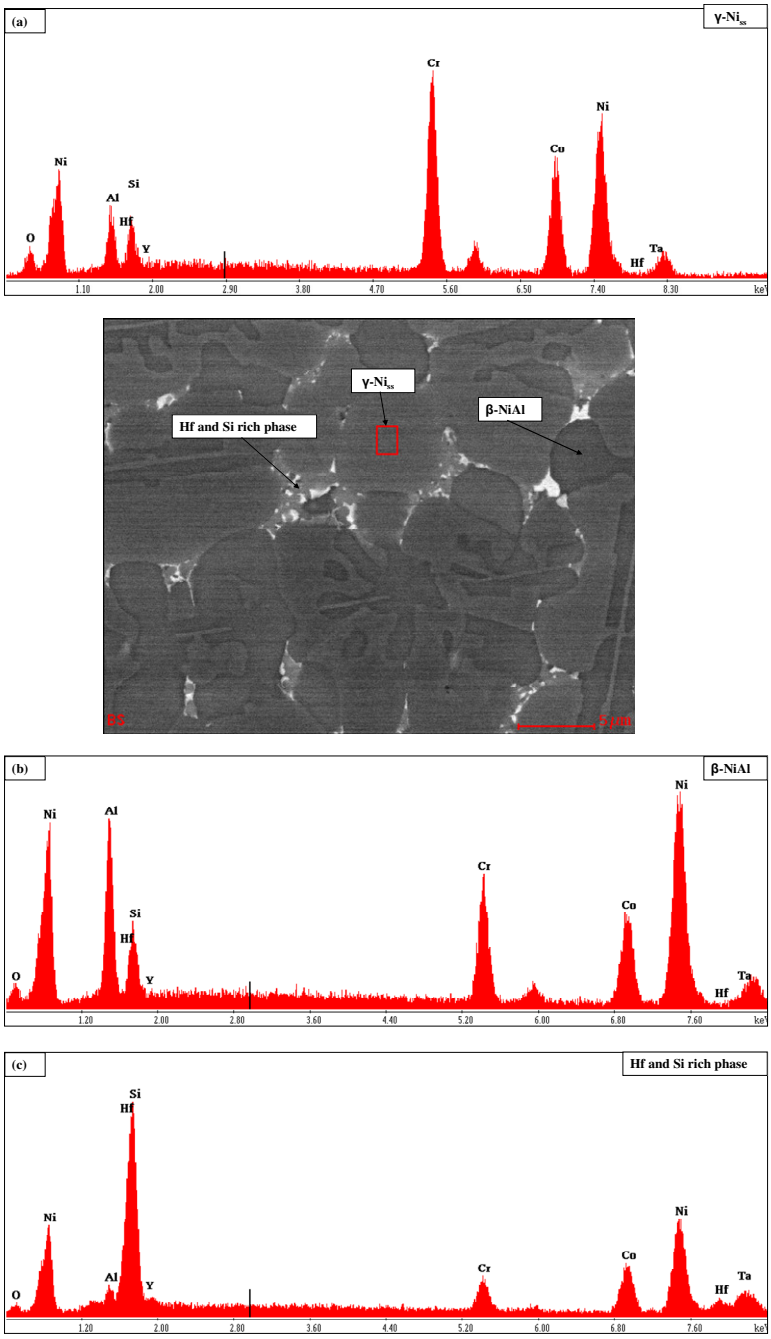

Figure 4.19 BSE image and EDS spectra of the EK5-AC showing presence of (a) γ-Ni_{ss}, (b) β-NiAl and (c) Hf and Si rich phase (grey contrast areas formed with white contrast areas).

continued in the next page

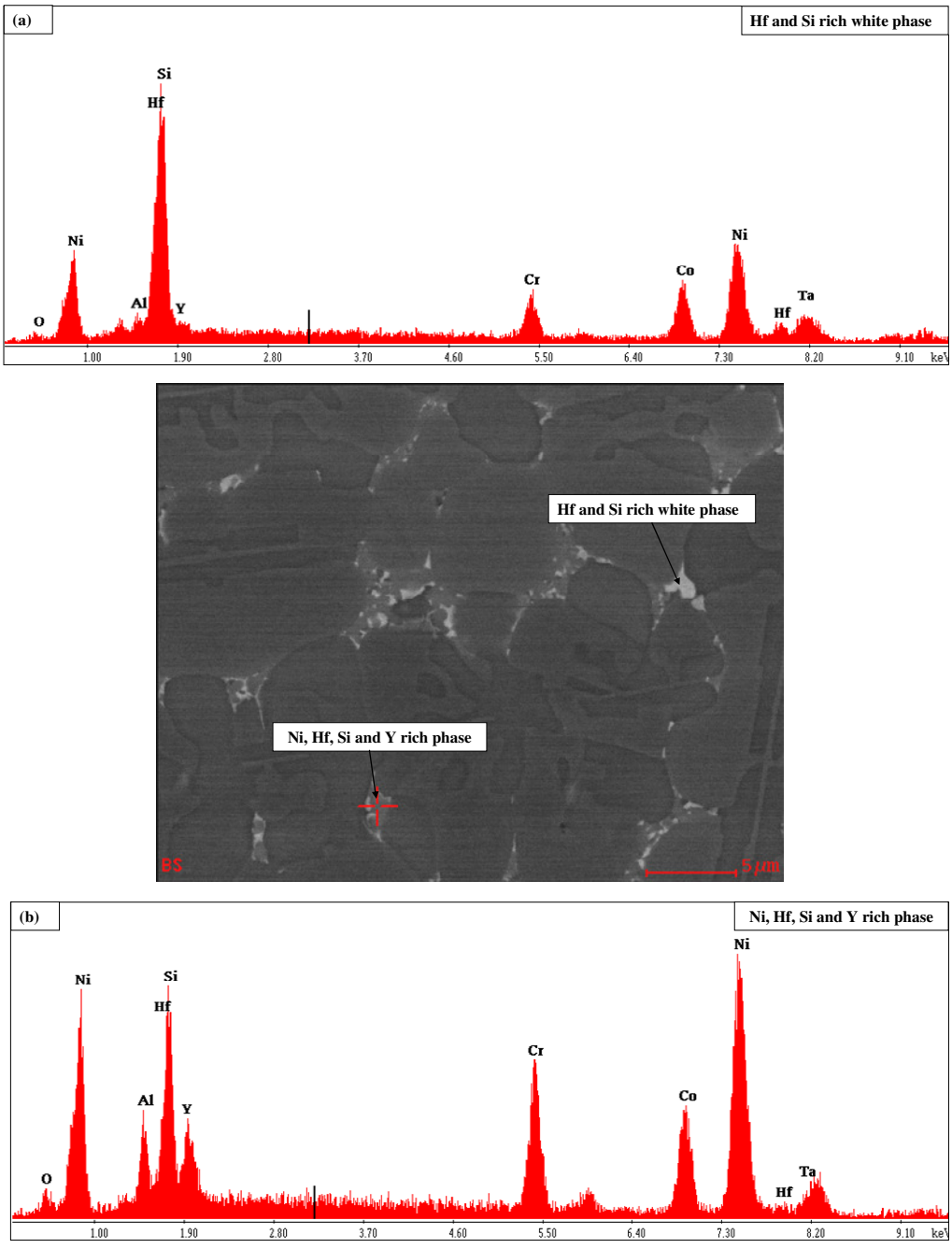

Figure 4.20 BSE image and EDS spectra of the EK5-AC showing presence of (a) Hf and Si rich white phase and (b) Ni, Hf, Si and Y rich phase.

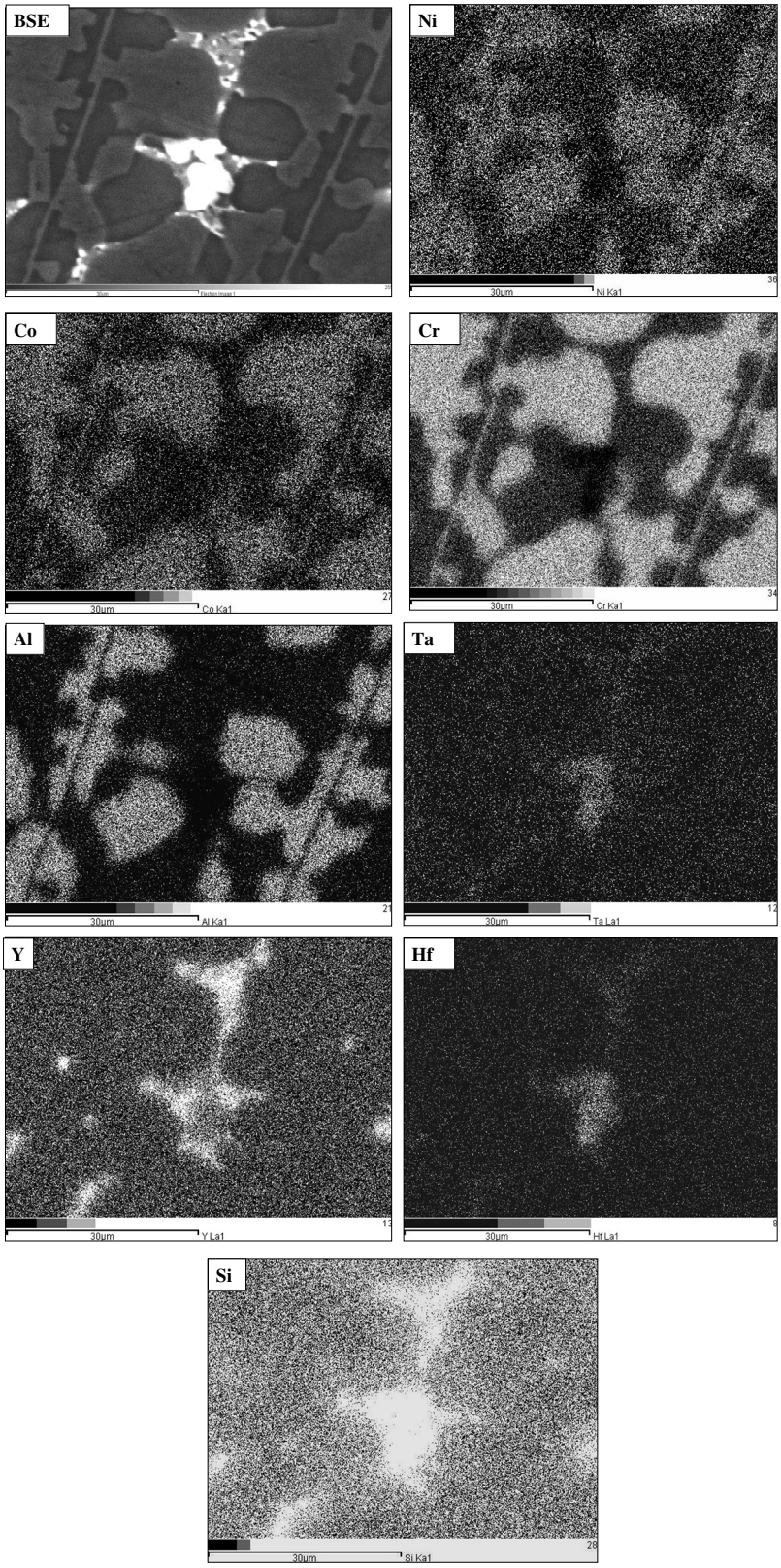

Figure 4.21 BSE image and qualitative elemental maps of Ni, Co, Cr, Al, Ta, Y, Hf and Si taken from the EK5-AC.

The XRD data (figure 4.22) confirmed the presence of γ-Ni_{ss} and β-NiAl and suggested the presence of γ'-Ni_3Al and Ni_5Y and $Ni_{17}Y_2$. If the γ'-Ni_3Al was present, it would have formed in the γ-Ni_{ss}. Thus, it is suggested that the second phase seen in γ-Ni_{ss} (figure 4.18b) was the γ'-Ni_3Al.

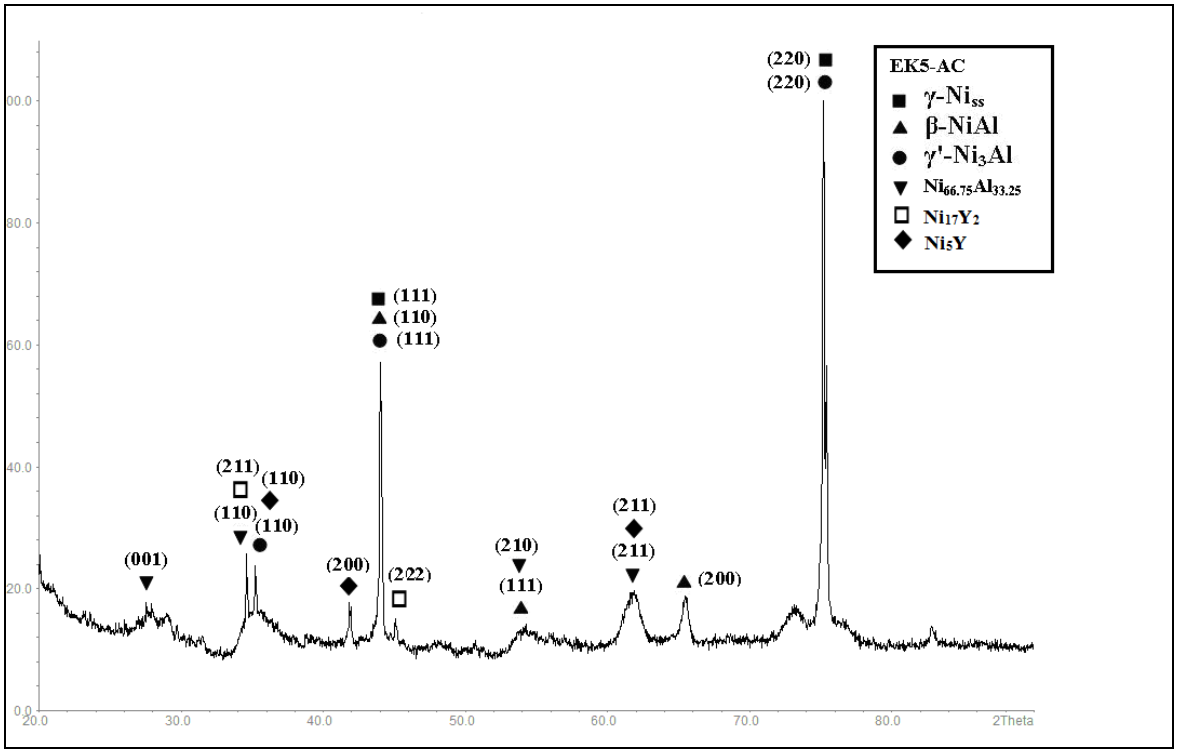

Figure 4.22 X-ray diffractogram of the EK5-AC alloy.

4.2.3.2 Heat treated (EK5-HT)

The first heat treatment (EK5-HT1) for the alloy was for 24 hrs at 1200 ˚C. The average composition of the EK5-HT1 was similar with the one of the as cast alloy (Table 4.5). There was coarsening of the overall microstructure. The microstructure of EK5-HT1 is shown in figure 4.23a,b and consisted of γ-Ni_{ss}, β-NiAl, white contrast areas with features or featureless, see figure 4.23c, which under high magnification and in particular after observation in high resolution SEM were found to be white contrast areas with and without internal microstructure, see figure 4.24. There were also cracks formed along the Ni_{ss}/NiAl interfaces in the as cast and heat treated (figures 4.23a, b) and through the white contrast areas and in NiAl grains (figure 4.23 b). The white contrast areas with features or

featureless were observed at the grain boundaries or junctions of γ-Ni_{ss} and β-NiAl grains, figures 4.23, 4.24.

The areas that exhibited white contrast under low magnification or when observed under non-high resolution SEM, were found to be either featureless, or to consist of two phases of white and grey contrast or three phases of white, grey and dark contrast, see figure 4.25 a,b. The areas with two phases were either a mixture of white and grey contrast phases (figure 4.27) or grey contrast phase surrounded by thin layer of white contrast phase (figure 4.25b). In the white areas with three phases, the dark contrast phase was NiAl, the grey phase was rich in Y and Si, see figures 4.25 and Table 4.5. Some white contrast areas with three phases were formed inside a grey contrast phase, see figure 4.26. In some cases the white contrast featureless areas were "massive" and facetted, see figure 4.27.

There was also evidence of fine precipitates exhibiting white contrast. These precipitates were observed at interfaces, see figure 4.28 and/or inside NiAl grains, see figures 4.28 and 4.29 with precipitates forming close to the grey phase and/or white phase (see figures 4.28, 4.30 and 4.31) and sometimes forming in bands, see figure 4.32 (a, b). Finally, there was evidence of second phase inside the Ni_{ss}, which is suggested to be Ni_3Al, in accordance with the results for previous alloys (see figure 4.33).

Quantitative analysis of the phases present in EK5-HT1 was possible only under a non-high resolution SEM, where some of the fine details exhibited in the white contrast areas observed in the microstructure could not be resolved. The EDS analysis data is shown in Table 4.5. Both the Ni_{ss} and NiAl had become richer in Si and the average Al content of the latter had decreased after this heat treatment. However, the standard deviation for the Al analysis in NiAl was high; this was attributed to precipitation of fine white contrast phase in it. The white and grey contrast areas in the white contrast areas as indicated in Table 4.5, were found to be respectively rich in Ta, Hf and Si and in Si and Y. The latter (rich in Si and Y) was also richer in Al and Cr compared with the former (rich in Ta, Hf and Si).

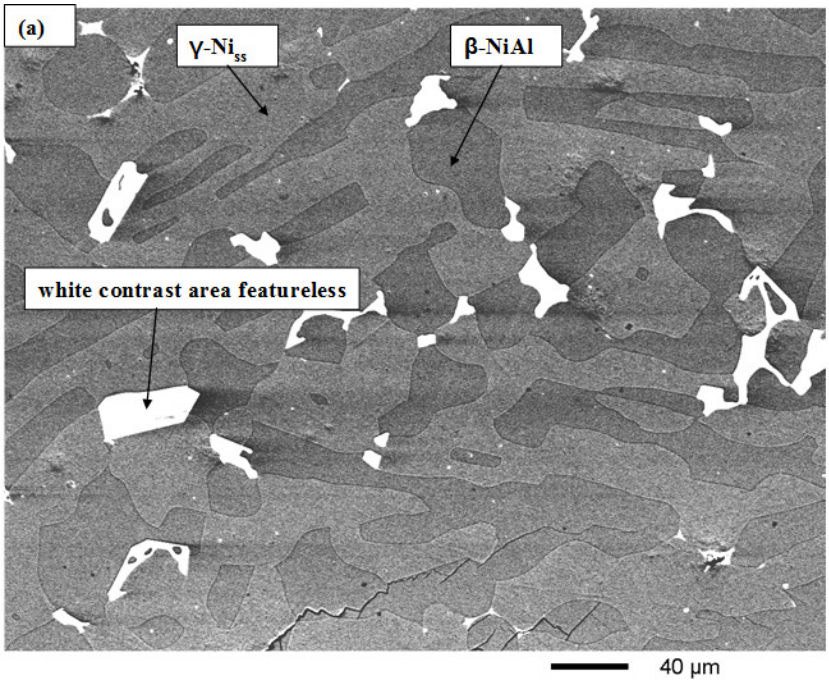
(a)
γ-Ni$_{ss}$
β-NiAl
white contrast area featureless
40 µm

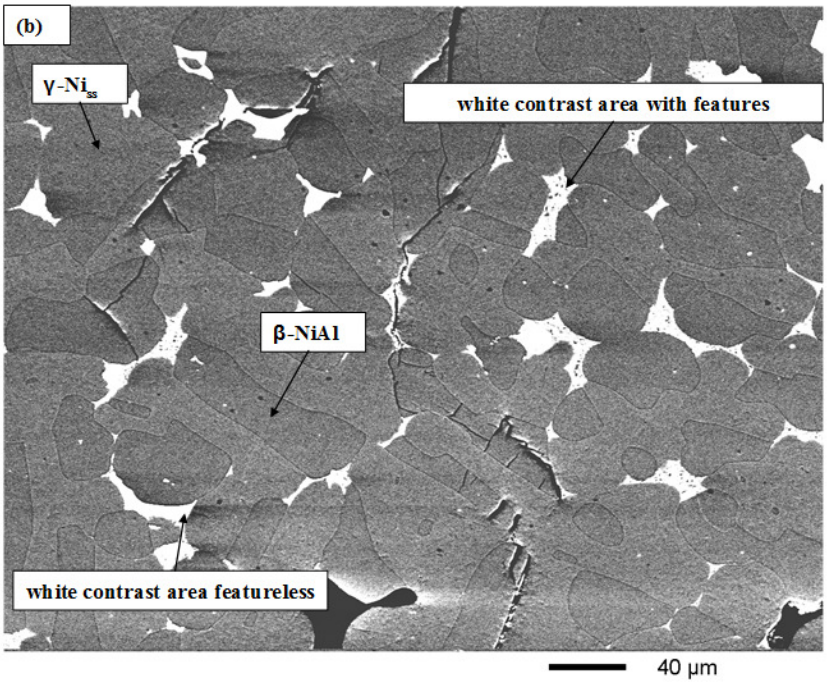
(b)
γ-Ni$_{ss}$
white contrast area with features
β-NiAl
white contrast area featureless
40 µm

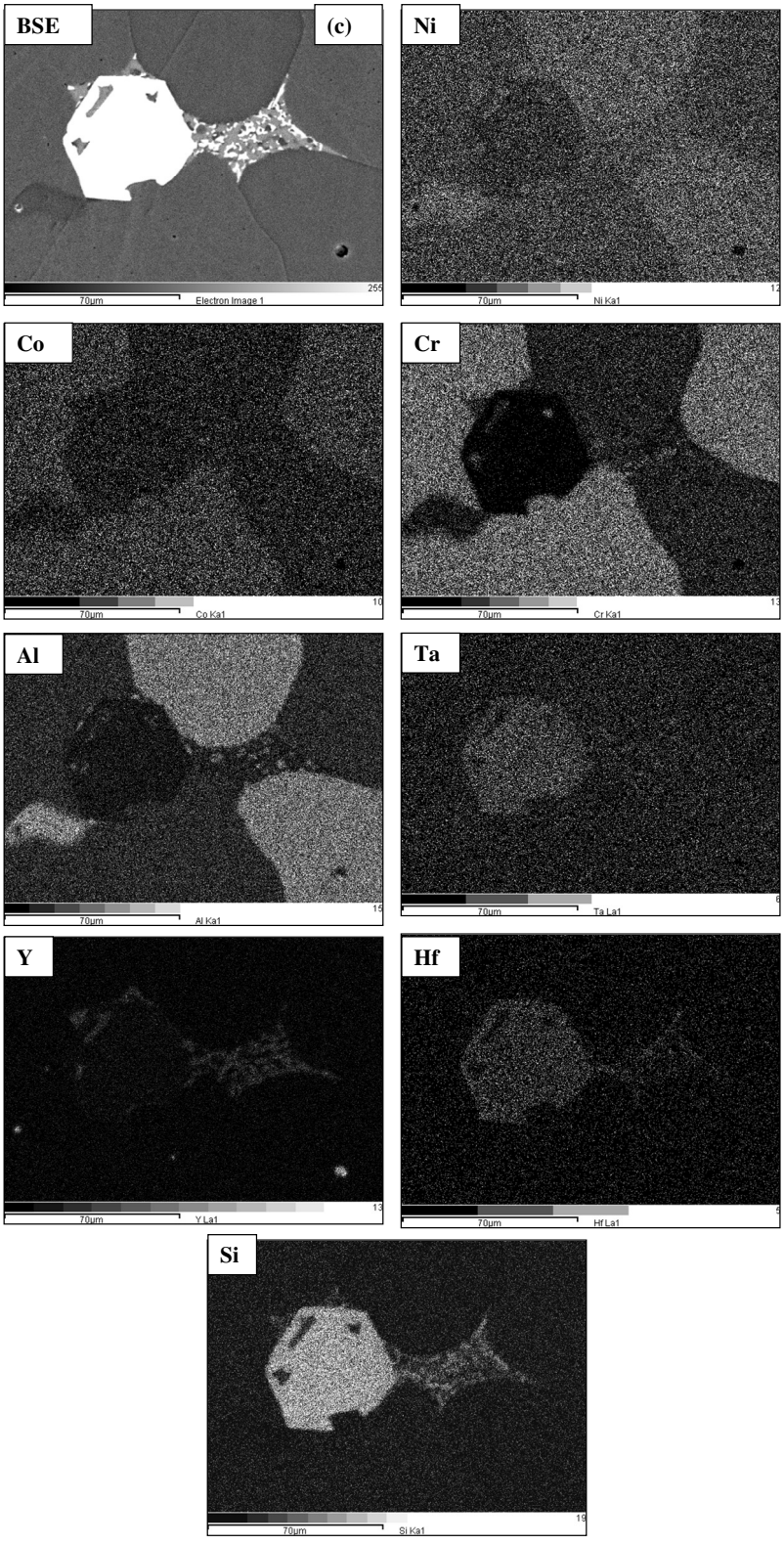

Figure 4.23 (a), (b) BSE images and (c) X-ray maps showing the microstructure of EK5-HT1 consisting of γ-Ni_{ss}, β-NiAl and white contrast areas with features or featureless.

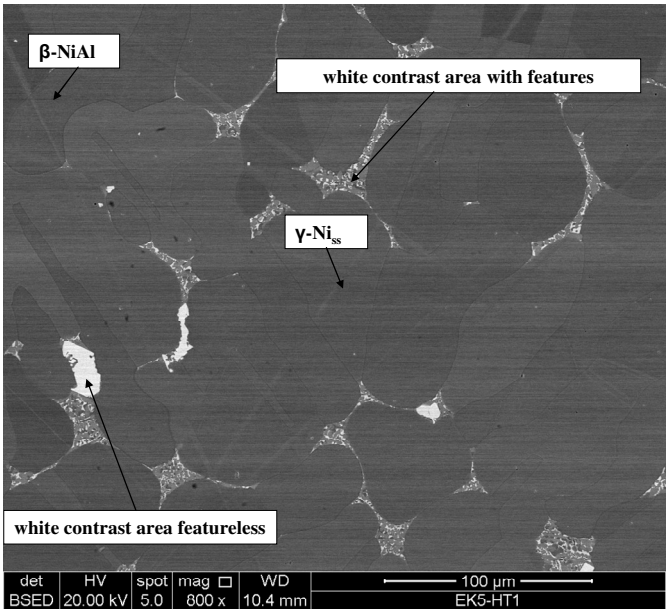

Figure 4.24 BSE image showing the microstructure of EK5-HT1 consisting of γ-Ni_{ss}, β-NiAl and white contrast areas with and without internal microstructure.

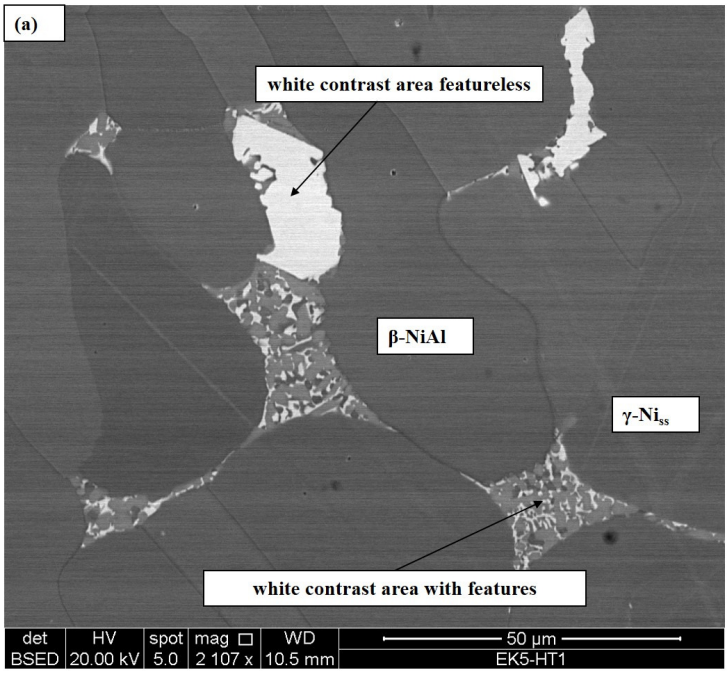
(a)
white contrast area featureless
β-NiAl
γ-Niss
white contrast area with features
det HV spot mag WD
BSED 20.00 kV 5.0 2 107 x 10.5 mm
50 µm
EK5-HT1

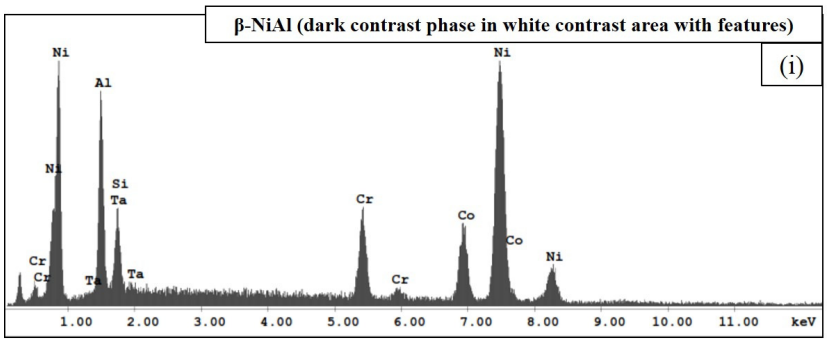
β-NiAl (dark contrast phase in white contrast area with features)
(i)
Ni
Al
Ni
Si
Ta
Cr
Cr
Ta
Ta
Cr
Co
Ni
Co
Ni
1.00 2.00 3.00 4.00 5.00 6.00 7.00 8.00 9.00 10.00 11.00 keV

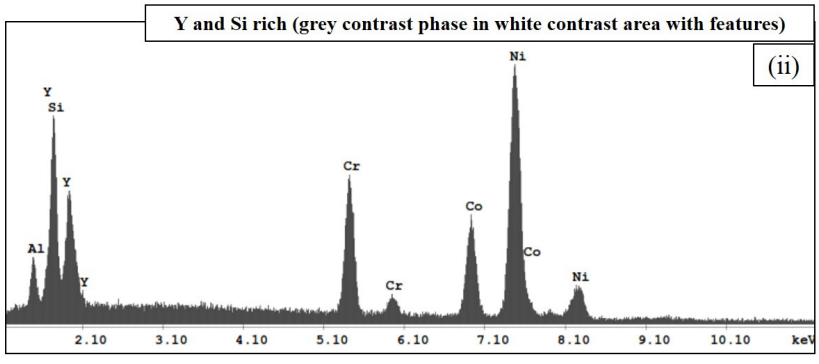
Y and Si rich (grey contrast phase in white contrast area with features)
(ii)
Ni
Y
Si
Y
Al
Y
Cr
Cr
Co
Co
Ni
2.10 3.10 4.10 5.10 6.10 7.10 8.10 9.10 10.10 keV

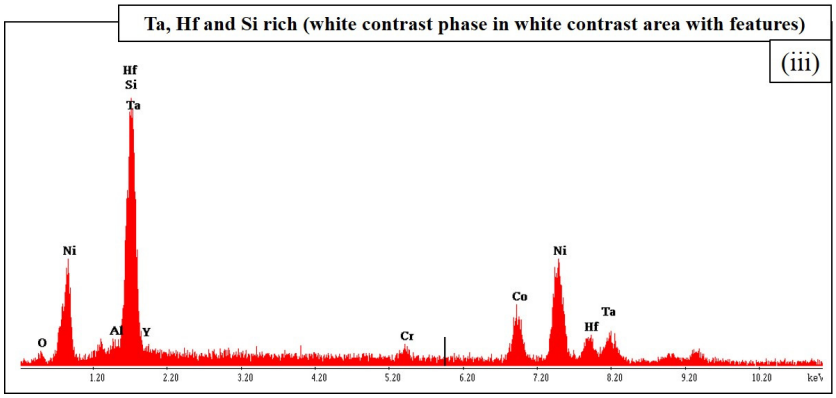
Ta, Hf and Si rich (white contrast phase in white contrast area with features)
(iii)
Hf
Si
Ta
Ni
O
Al
Y
Cr
Co
Ni
Hf
Ta
1.20 2.20 3.20 4.20 5.20 6.20 7.20 8.20 9.20 10.20 keV

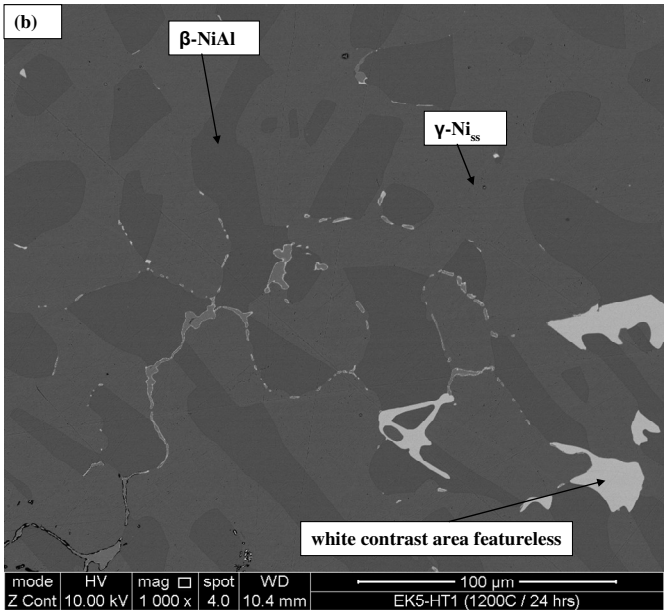

Figure 4.25 BSE images showing the microstructure of EK5-HT1 consisting of γ-Ni_{ss}, β-NiAl and white contrast areas with and without internal microstructure (a) BSE image and EDS spectra showing the dark contrast phase which is β-NiAl (i), the grey contrast phase rich in Y and Si (ii) and the white contrast phase rich in Ta, Hf and Si (iii) and (b) grey contrast phases surrounded by thin layer of white contrast phase.

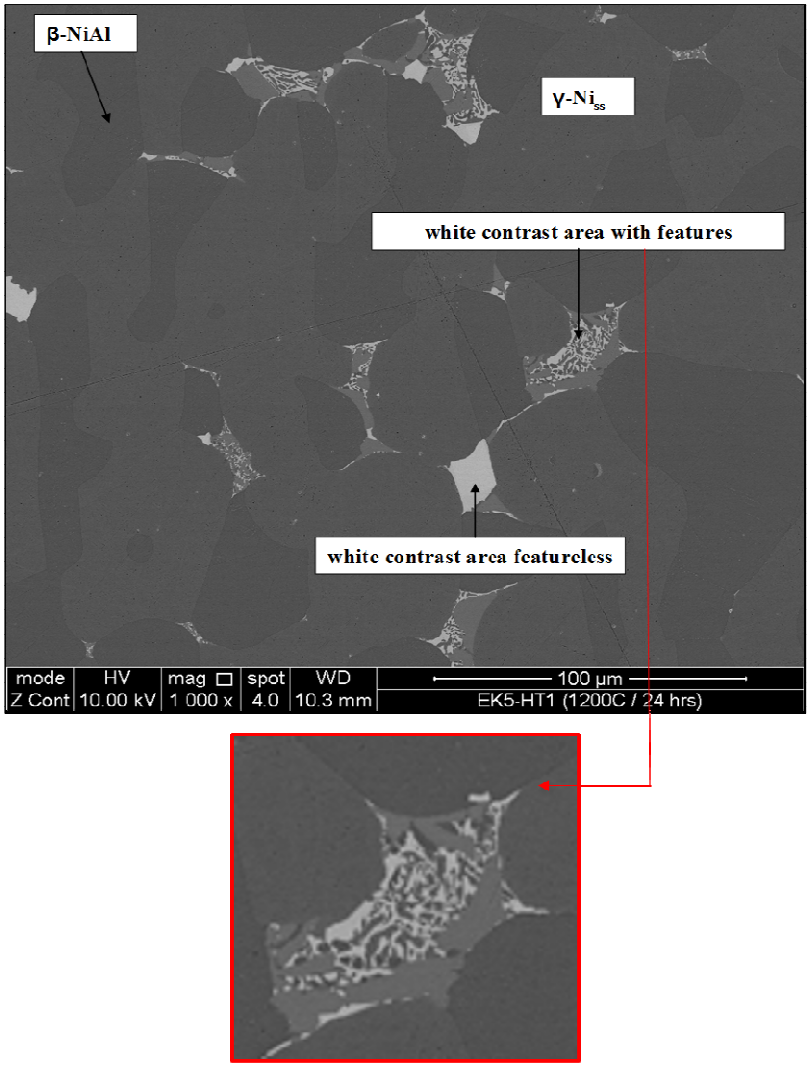

Figure 4.26 BSE image showing the microstructure of EK5-HT1 consisting of γ-Ni_{ss}, β-NiAl and white contrast areas with and without features. Some white contrast areas with three phases are formed inside a grey contrast phase.

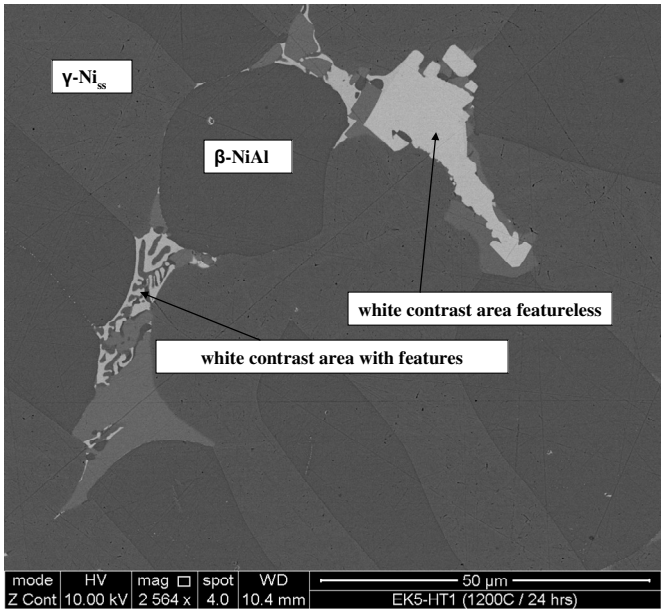

Figure 4.27 BSE image showing the microstructure of EK5-HT1 consisting of γ-Ni_{ss}, β-NiAl and white contrast areas with and without features. Some white contrast featureless areas were "massive" and facetted.

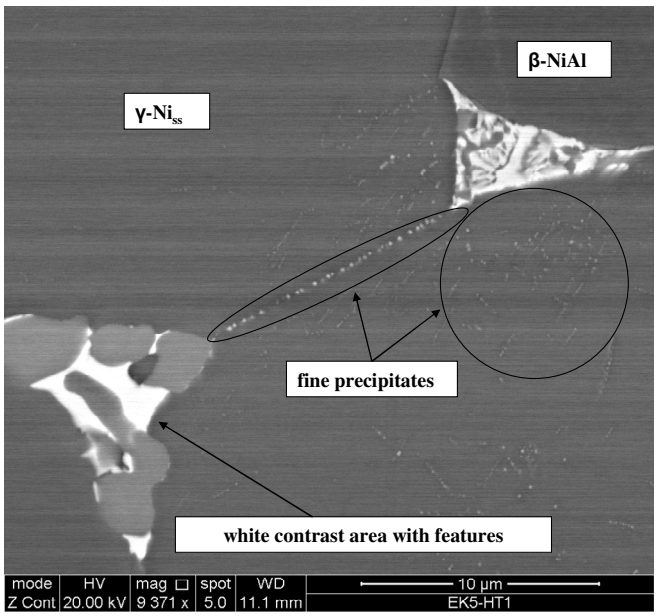

Figure 4.28 BSE image showing the microstructure of EK5-HT1 consisting of γ-Ni_{ss}, β-NiAl and white contrast areas with and without features. Evidence of fine precipitates exhibit white contrast.

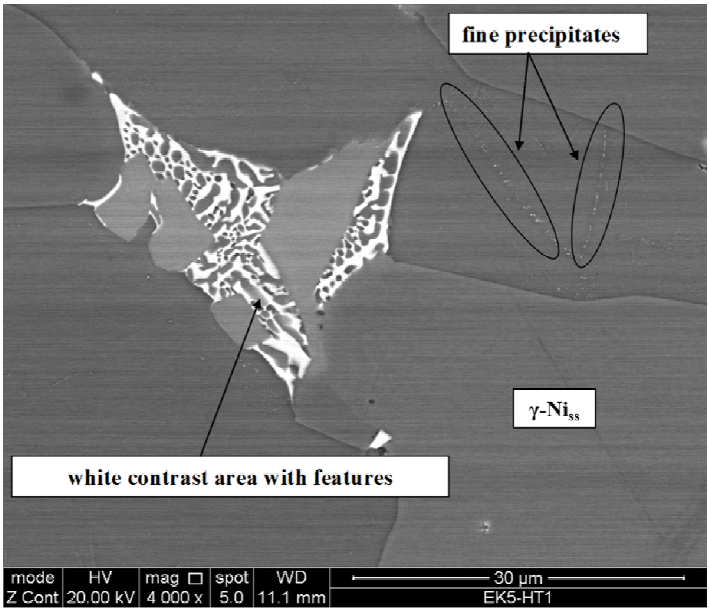

Figure 4.29 BSE image of EK5-HT1 showing fine bright contrast precipitates in β-NiAl.

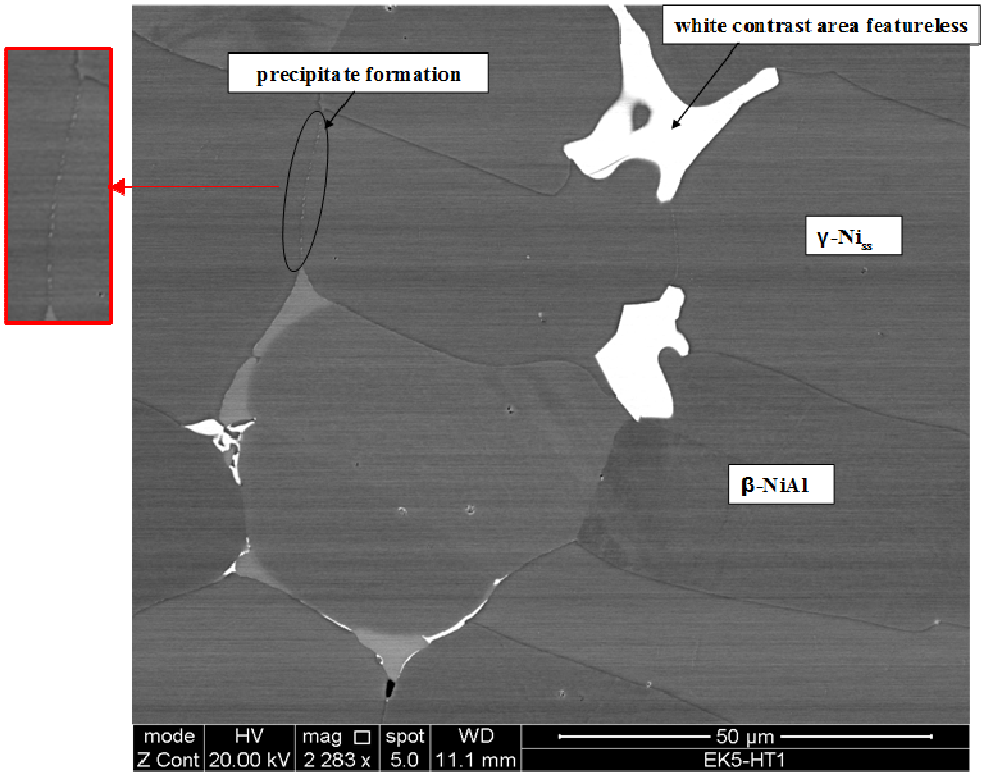

Figure 4.30 BSE image showing the microstructure of EK5-HT1 consisting of γ-Ni_{ss}, β-NiAl and white contrast areas without features. Evidence of fine precipitates exhibiting white contrast.

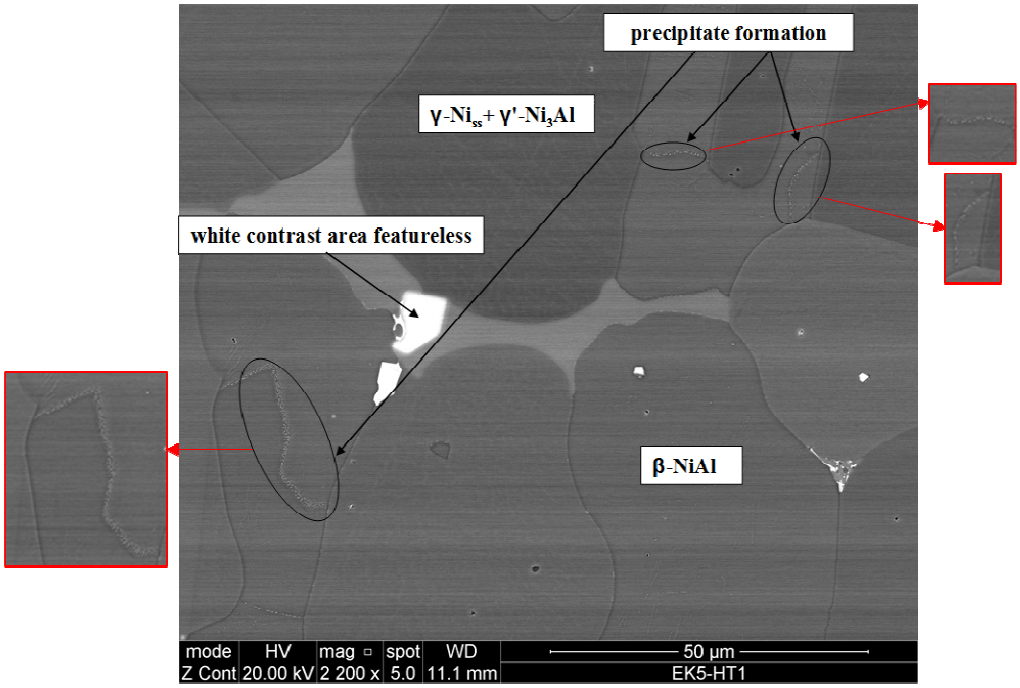

Figure 4.31 BSE image showing the microstructure of EK5-HT1 consisting of γ-Ni_{ss}, β-NiAl and white contrast areas without features. Evidence of fine precipitates exhibiting white contrast in the β-NiAl.

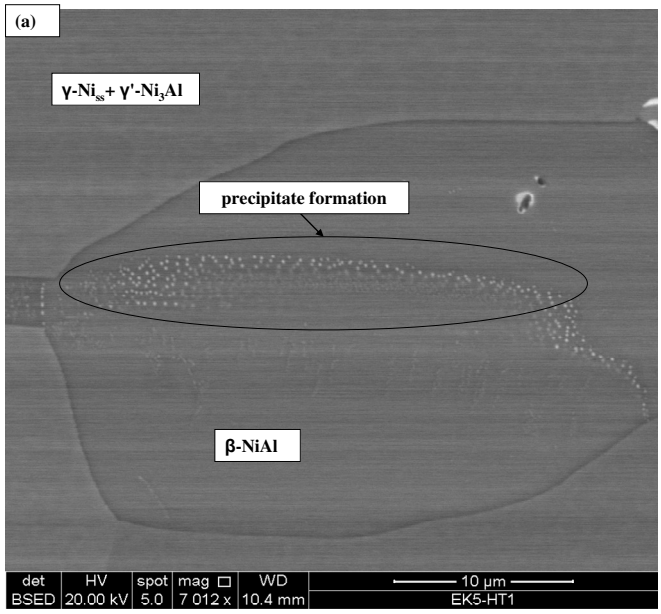

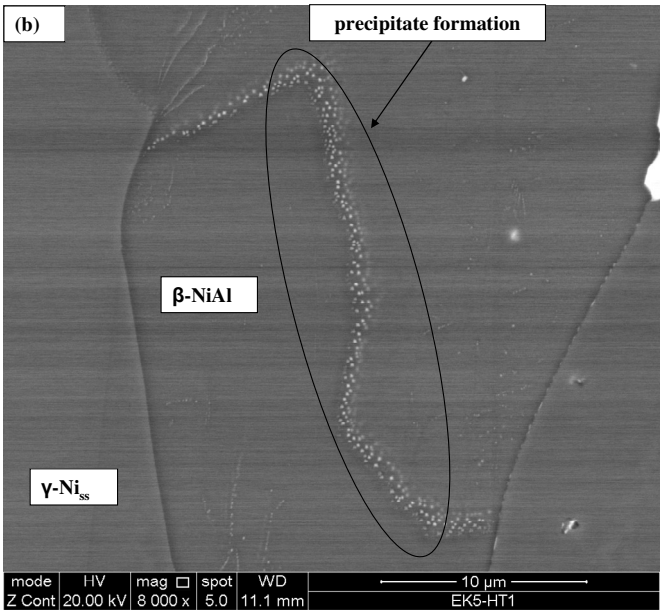

Figure 4.32 BSE images showing the microstructure of EK5-HT1 consisting of γ-Ni_{ss}, β-NiAl and evidence of fine precipitates exhibiting white contrast in the β-NiAl.

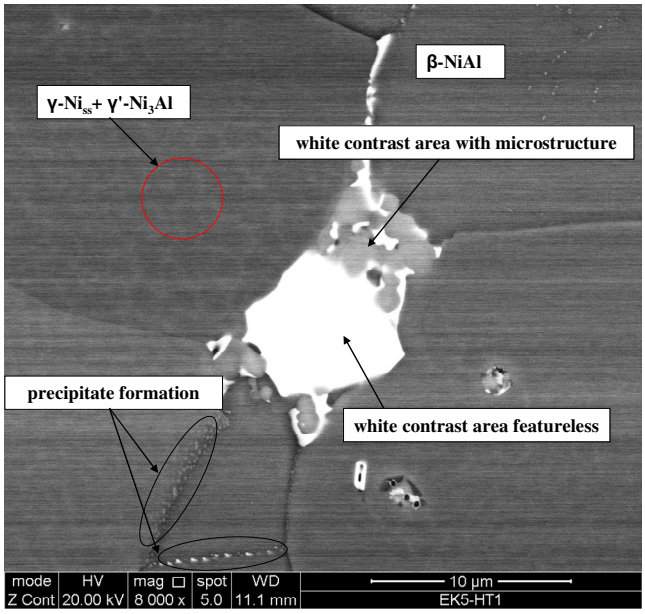

Figure 4.33 BSE image showing the microstructure of EK5-HT1 consisting of γ-Ni_{ss}, β-NiAl, white contrast areas with and without features. Evidence of fine precipitates exhibiting white contrast and evidence of second phase formation inside the γ-Ni_{ss} which is suggested to be γ'-Ni_3Al.

The presence of γ-Ni_{ss}, β-NiAl and γ'-Ni_3Al in EK5-HT1 was confirmed by the XRD data (figure 4.34), which also suggested the presence of Ni_5Y, $Ni_{17}Y_2$, α-Cr. The non-identified peaks in figure 4.34 are attributed to the other phases observed in the microstructure.

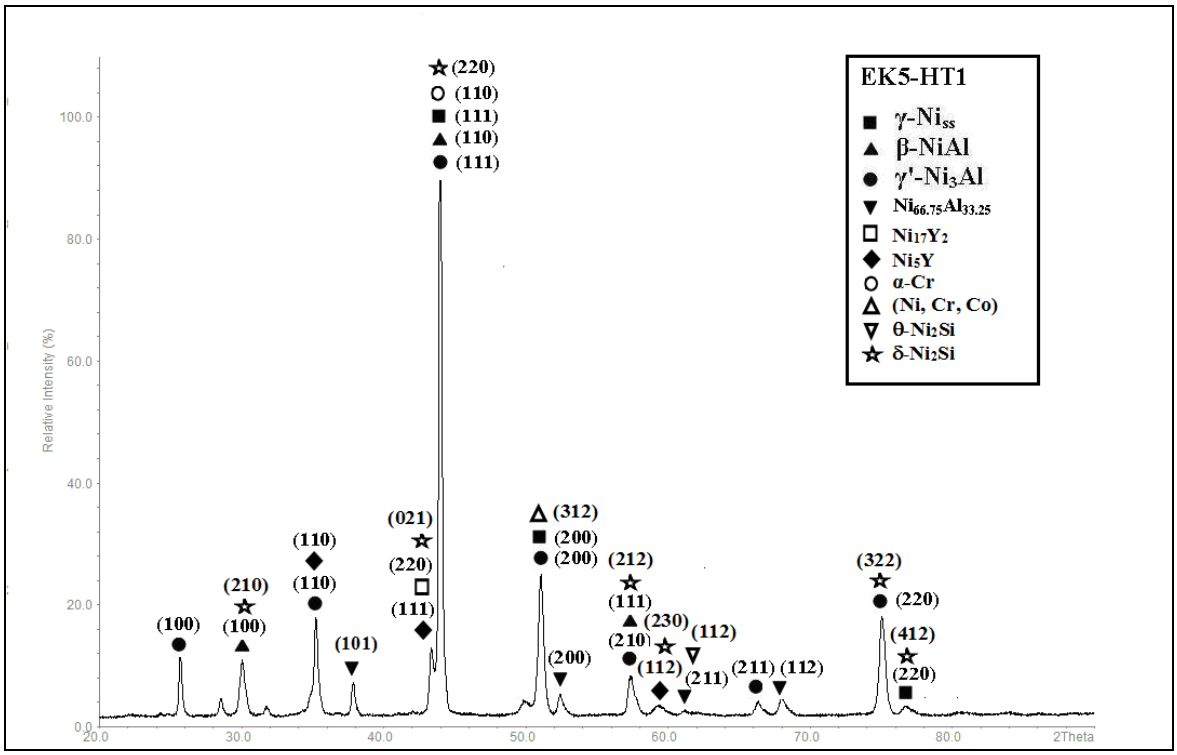

Figure 4.34 X-ray diffractogram of EK5-HT1.

The second heat treatment (EK5-HT2) was for another 24 hrs at 1200 ˚C (48 hrs in total). The average compositions of the EK5-HT2 was slightly poorer in Al compared with EK5-AC and EK5-HT1, whereas Co and Cr concentrations did not change significantly. At low magnification the microstructure of EK5-HT2 exhibited Ni_{ss}, NiAl and white contrast areas at their interfaces and/or grain boundaries (see figure 4.35). Upon study at higher magnifications the white contrast areas were found to be featureless (see figure 4.36) and Ta, Hf and Si rich (see Table 4.5 and figures 4.37, 4.38 and 4.39) or to be surrounded by and/or surround a black contrast phase (see figure 4.40). Some grey contrast phases were also observed that were surrounded by a black contrast phase (see figure 4.41a) and these were observed on interfaces or grain boundaries and were often surrounded by a white contrast phase, this feature was also observed in EK5-HT1 (see

figure 4.41b). There was also evidence of Ni_3Al formation in the bulk of Ni_{ss} (see figure 4.36 and figure 4.39). Precipitation of fine white contrast particles in β-NiAl, like the ones observed in EK5-HT1 was also seen (see figure 4.42), but this was rather rare. The grey contrast areas were Y rich (see figures 4.37, 4.38) and the black contrast phase was Al and O rich (see figure 4.43), the latter suggesting internal oxidation during the prolonged heat treatment. The above characteristic features of the black, grey and white contrast phases can also be seen in the line scans in figures 4.44 and 4.45 and the X-ray maps in figure 4.46. The XRD data confirmed the presence of Ni_{ss}, NiAl and Ni_3Al and suggested the presence of $Ni_{17}Y_2$ and α-Cr (see figure 4.47).

As was the case in EK5-HT1, quantitative analysis of the phases present in EK5-HT2 was possible only under a non-high resolution SEM, where the large white contrast areas could be analysed. The EDS analysis data is shown in Table 4.5 and shows essentially no change in the composition of the Ni_{ss} and NiAl compared with EK5-HT1. However, in the NiAl the standard deviation for the Al content was small, which could be attributed to the lack of fine precipitates in this phase in EK5-HT2.

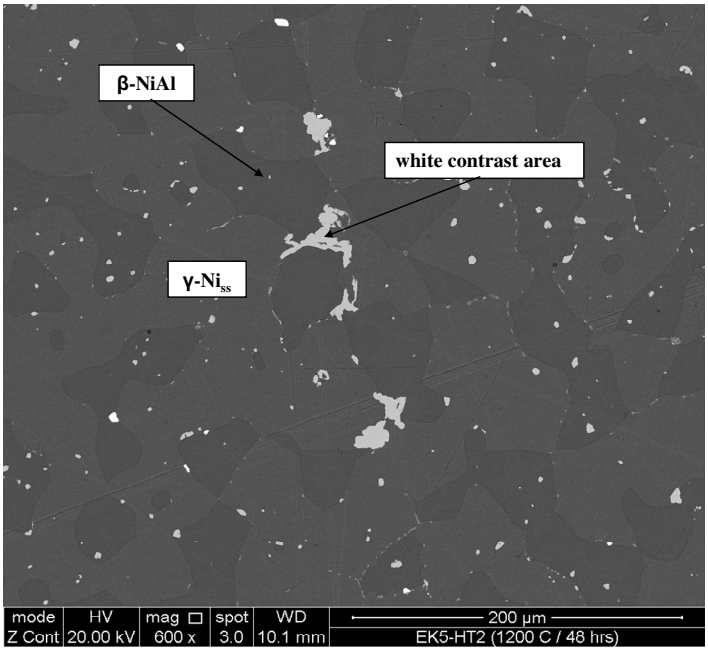

Figure 4.35 BSE image showing the microstructure of EK5-HT2 consisting of γ-Ni_{ss}, β-NiAl and white contrast areas without features at their interfaces.

The composition of the featureless white contrast areas had changed very little between the two heat treatments, which would suggest that this is a stable phase. The Si and Al content of these areas, which could be as high as ~36 at%, could suggest that they correspond to Ta and Hf rich silicide. The formation of alumina at Ni_{ss} and NiAl interfaces and/or grain boundaries points to internal oxidation upon prolonged heat treatment and was not surprising given the cracking along the above features that was observed in EK5-HT1.

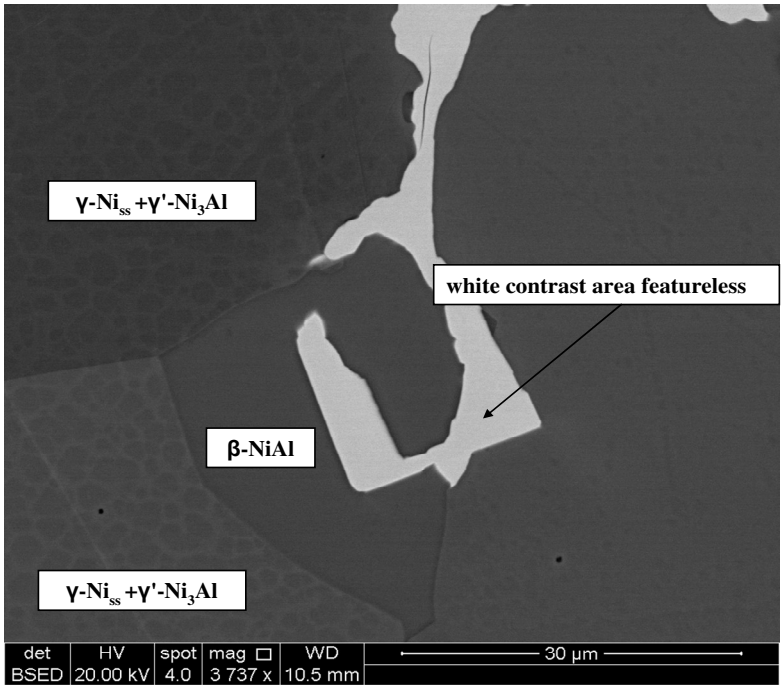

Figure 4.36 BSE image showing the microstructure of EK5-HT2 consisting of γ-Ni_{ss}, β-NiAl and white contrast featureless areas.

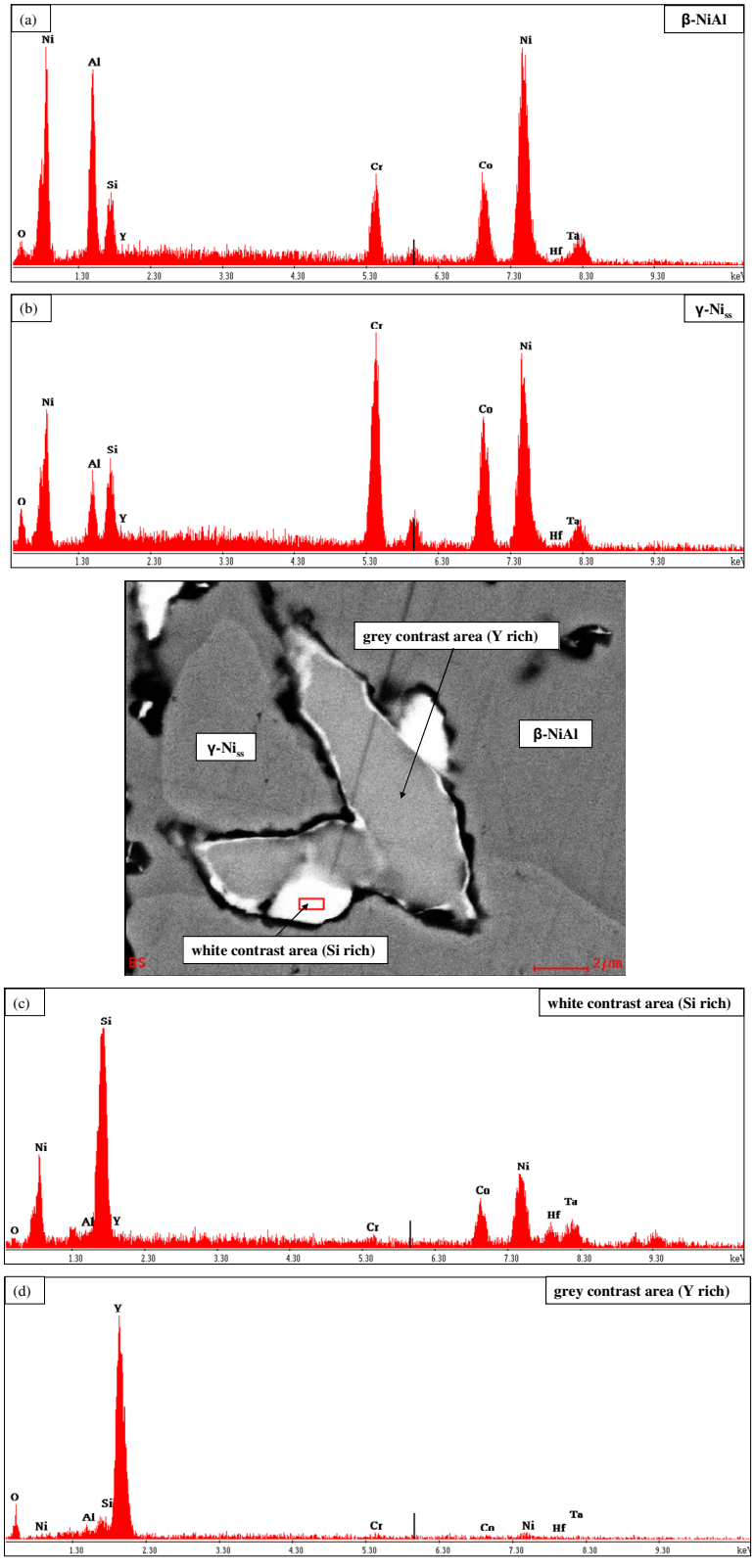

Figure 4.37 BSE image and EDS spectra showing the microstructure of EK5-HT2 consisting of γ-Ni_{ss}, β-NiAl, white contrast areas (Si rich) and grey contrast areas (Y rich).

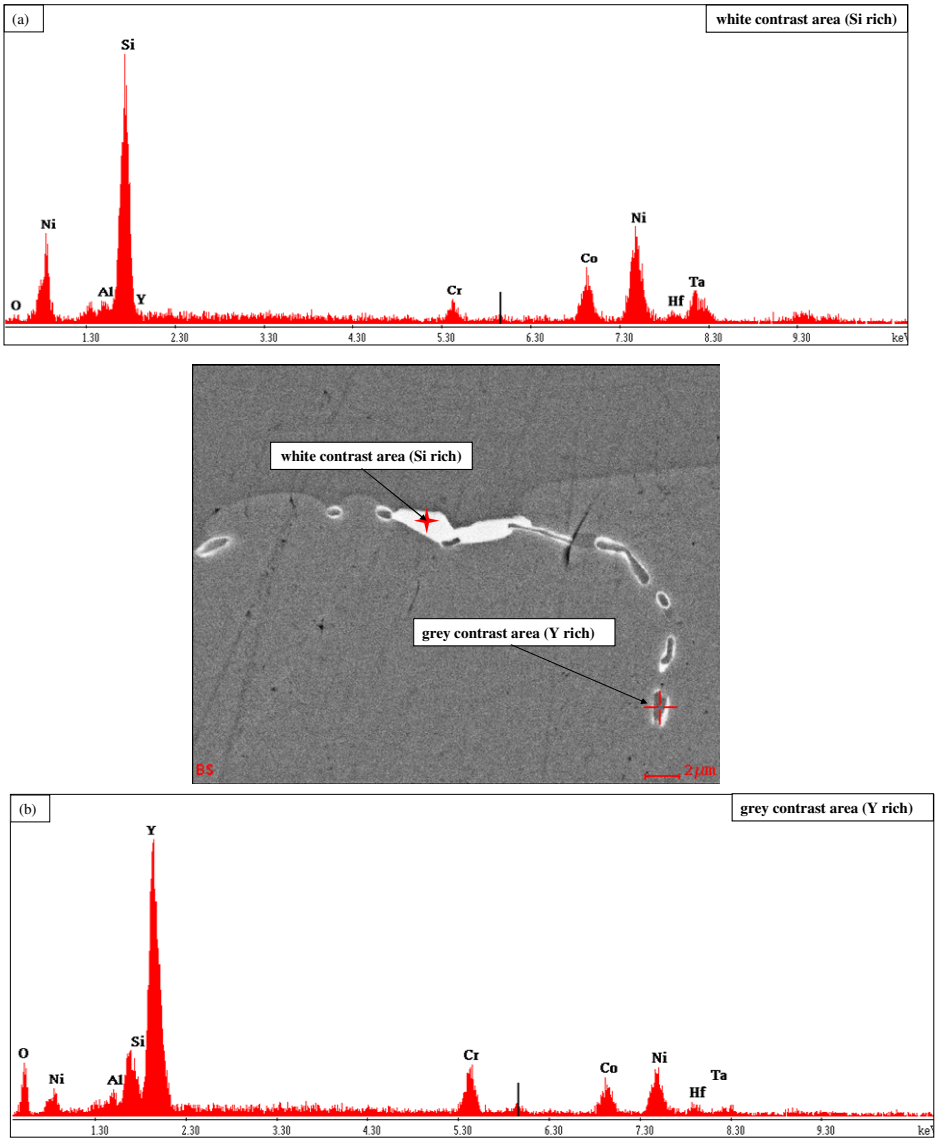

Figure 4.38 BSE image and EDS spectra showing the microstructure of EK5-HT2 consisting of white contrast areas (Si rich) and grey contrast areas (Y rich).

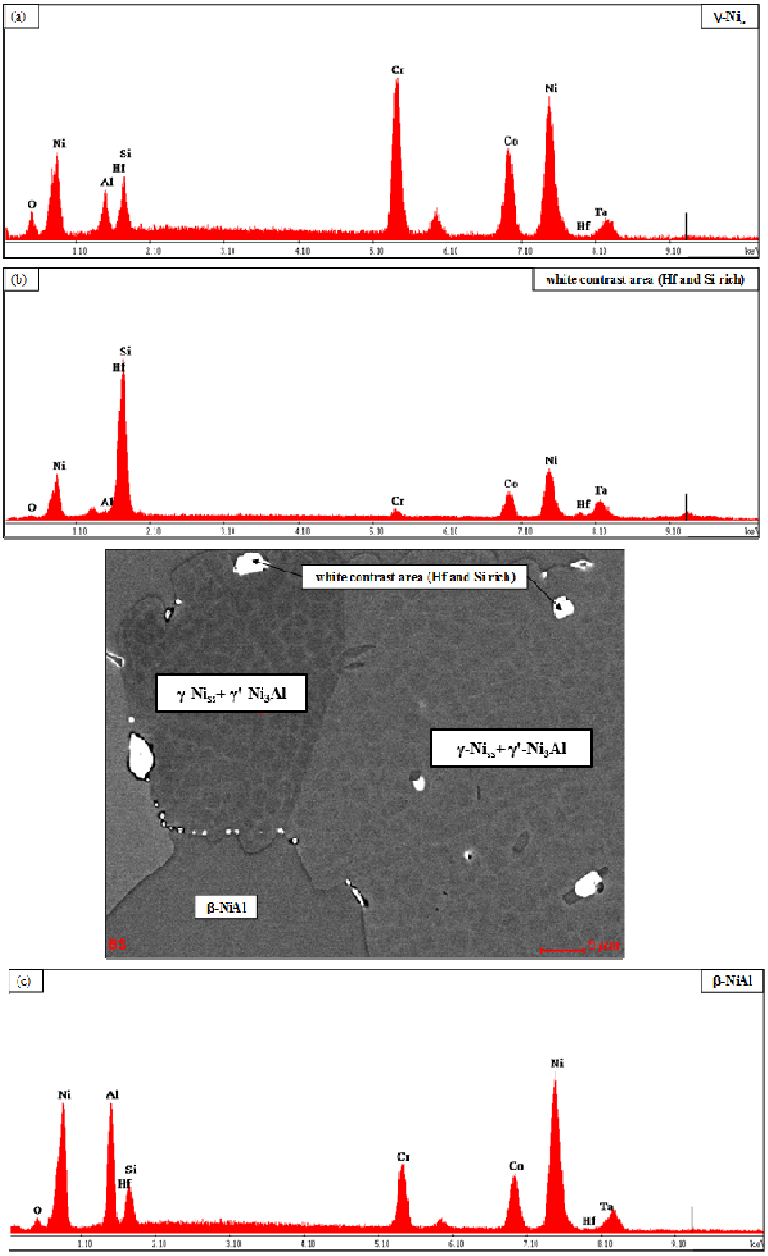

Figure 4.39 BSE image and EDS spectra showing the microstructure of EK5-HT2 consisting of γ-Ni_{ss}+ γ'-Ni_3Al, β-NiAl and white contrast areas (Hf and Si rich).

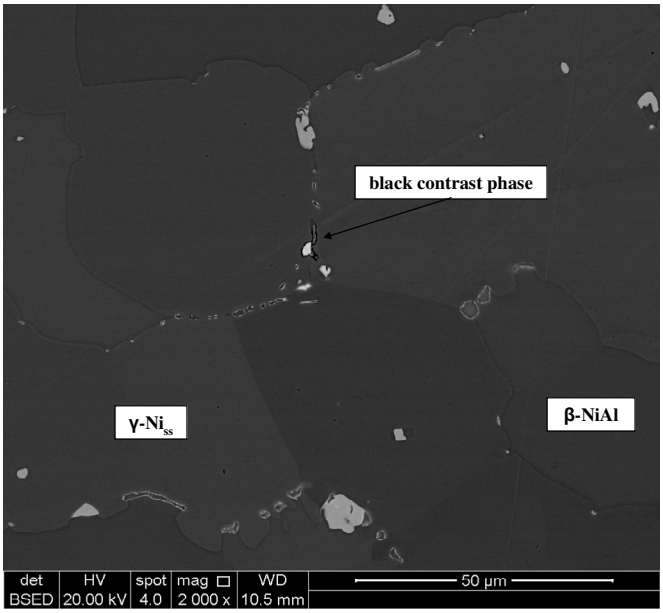

Figure 4.40 BSE image showing the microstructure of EK5-HT2 consisting of γ-Ni_{ss}, β-NiAl and black contrast phases.

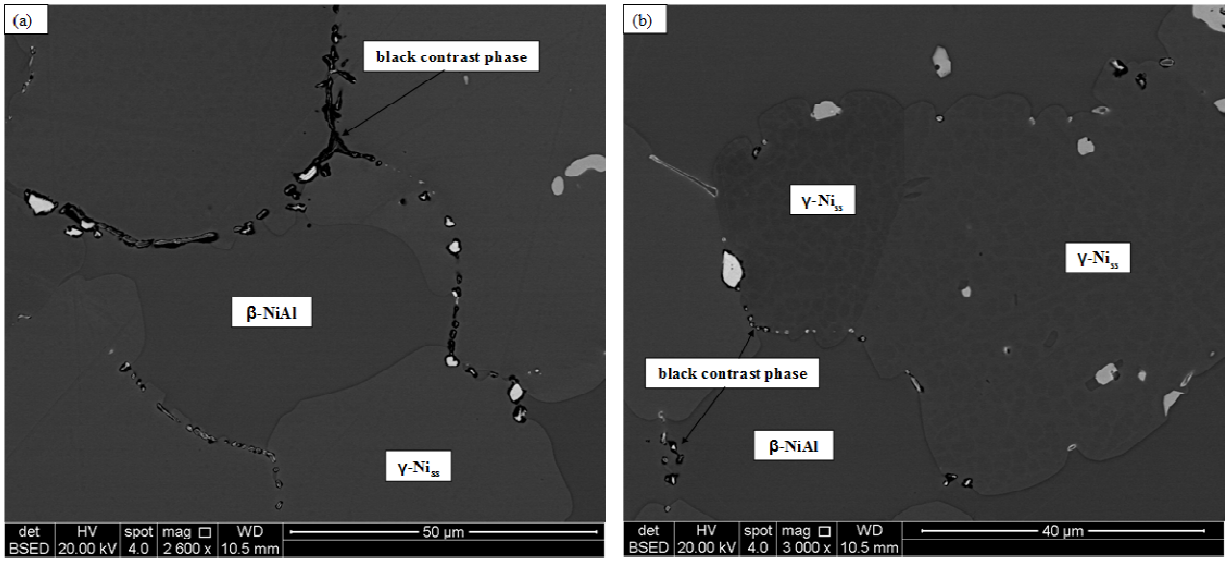

Figure 4.41 BSE images showing the microstructure of EK5-HT2 consisting of γ-Ni_{ss} and β-NiAl and (a) grey contrast phase surrounded by black contrast phase and (b) grey contrast phase surrounded by white contrast phase (towards the top left corner).

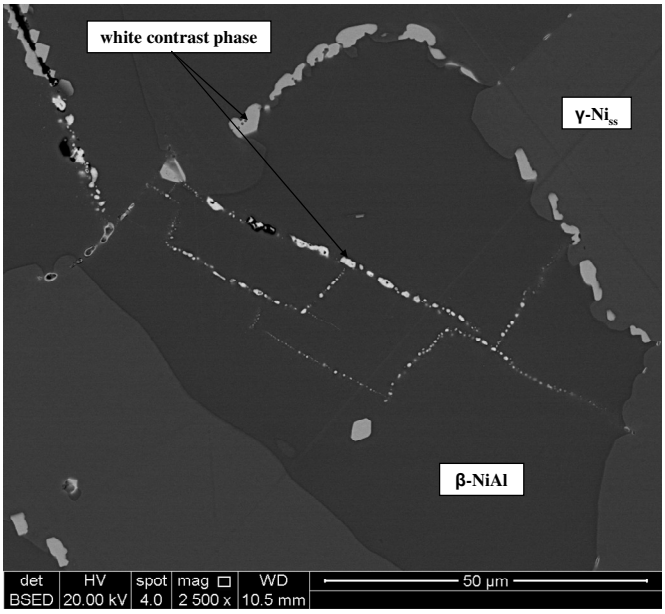

Figure 4.42 BSE image showing the microstructure of EK5-HT2 consisting of γ-Ni$_{ss}$, β-NiAl and precipitation of fine white contrast particles in β-NiAl.

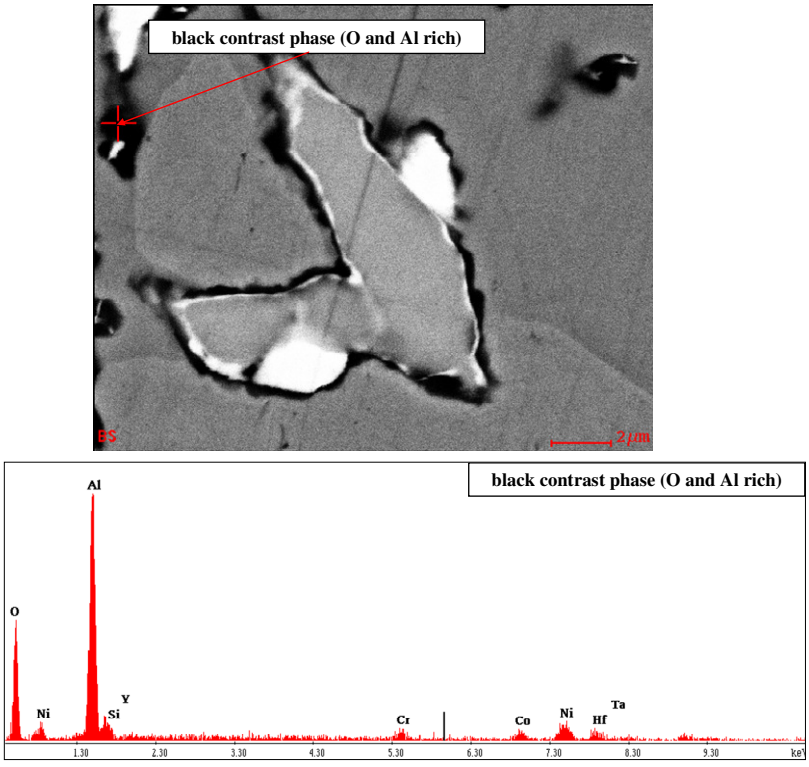

Figure 4.43 BSE image and EDS spectrum showing black contrast phase Al and O rich in the microstructure of EK5-HT2.

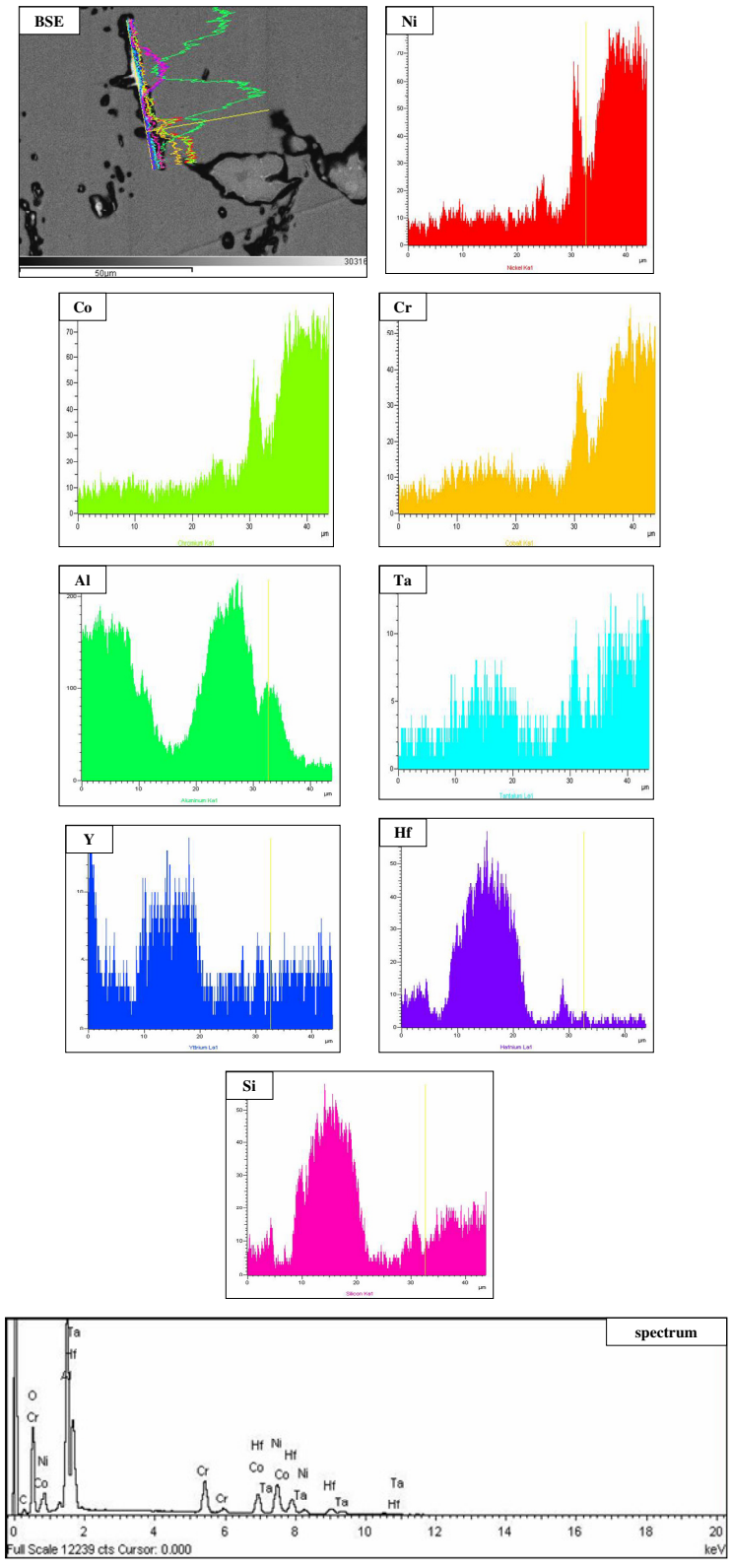

Figure 4.44 BSE image showing the microstructure of EK5-HT2 and line scans showing distributions (detected by EDS) of Ni, Co, Cr, Al, Ta, Y, Hf and Si. The line scan crosses a white contrast phase which is rich in Si, Hf, Y and Ta.

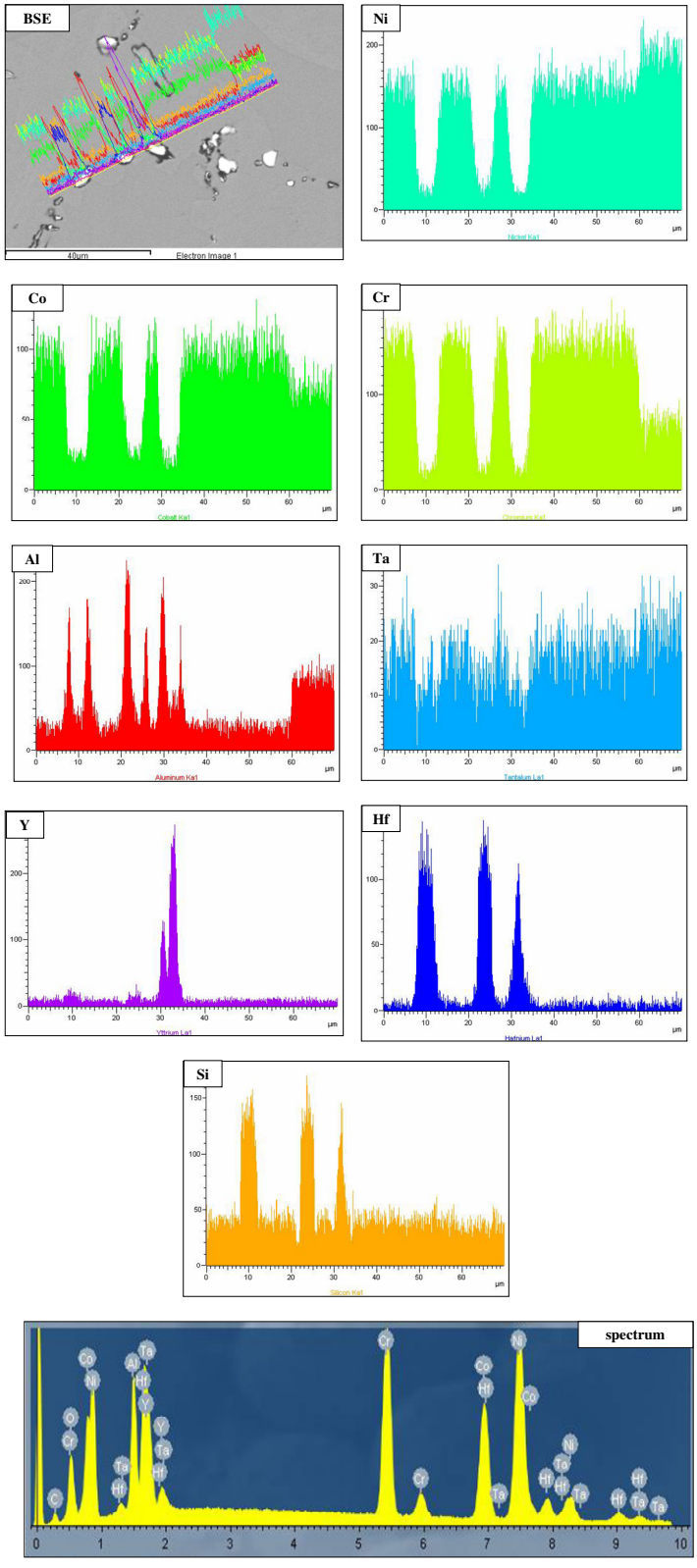

Figure 4.45 BSE image showing the microstructure of EK5-HT2 and line scans showing distributions (detected by EDS) of Ni, Co, Cr, Al, Ta, Y, Hf and Si. The three white contrast phases are rich in Si, Hf and one of them is also rich in Y.

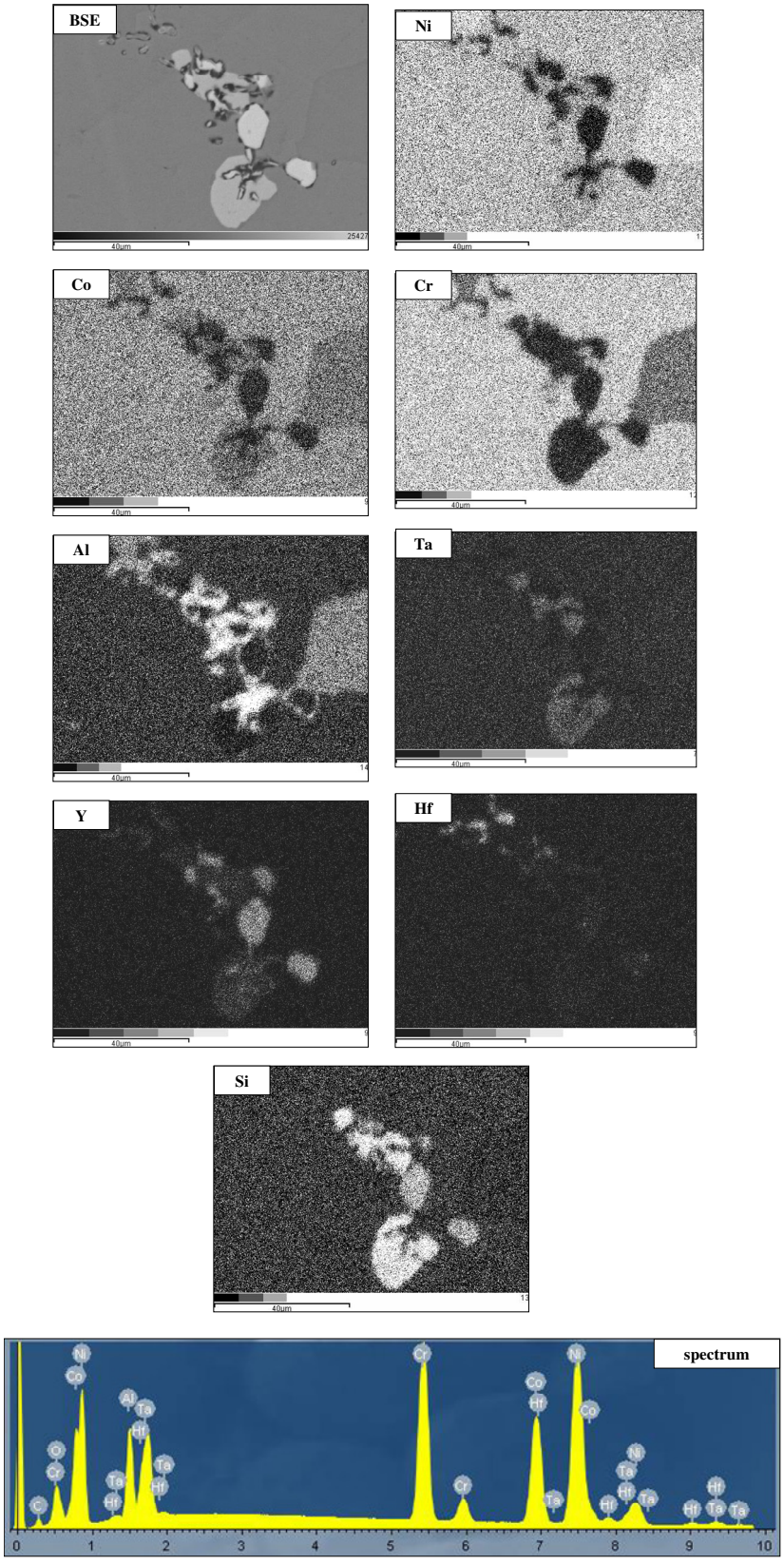

Figure 4.46 BSE image and qualitative elemental maps of Ni, Co, Cr, Al, Ta, Y, Hf and Si taken from EK5-HT2.

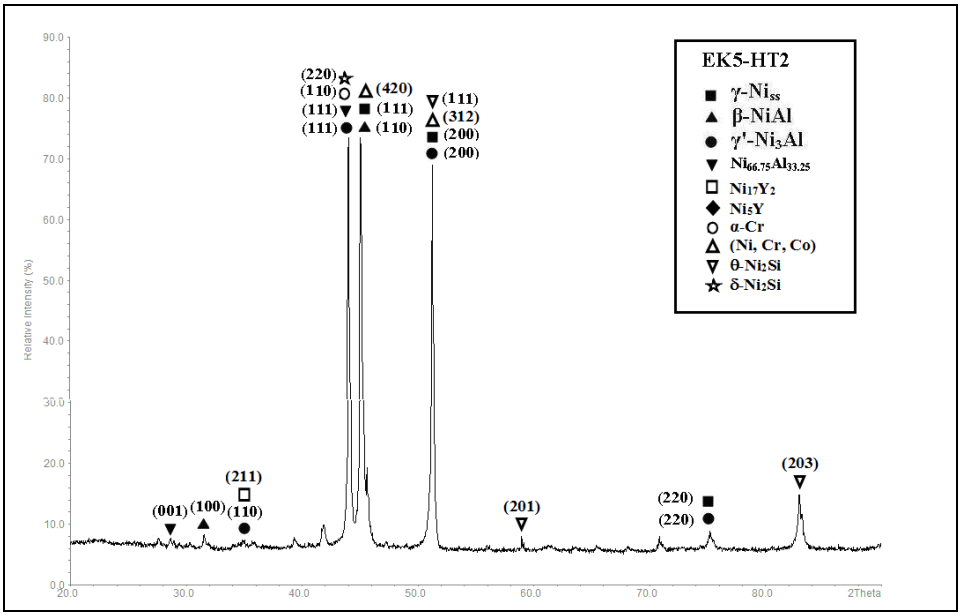

Figure 4.47 X-ray diffractogram of EK5-HT2.

4.3 Discussion

As far as the Ni-Al system is concerned, alloys with compositions around Ni_3Al show a rather complicated phase selection and growth morphology sequence. Four different crystal structures are involved around that composition with the possibility of single phase or eutectic growth and with subsequent solid state transitions. This makes the explanation of the resulting final microstructure sometimes speculative [Assadi et al., 1998]. The main phases observed in the cast and heat treated alloys EK2, EK3, EK4 and EK5 confirmed that the phase equilibria that was "established" by the synergy of Ni-Co-Cr-Al in the alloy EK1, namely the stable γ-Ni_{ss} and β-NiAl phases, was not altered by the synergy of Ta with Y, Ta, Y and Hf and Ta, Y, Hf and Si. The latter synergies however had an effect on the stability of γ'-Ni_3Al (as far as the presence of this intermetallic could be confirmed at the level of resolution of FEG-SEM in addition to the XRD data) and of the $\gamma + \beta$ eutectic. In the alloys with Y, i.e., the alloys EK3, EK4 and EK5, there was evidence for the presence of Y containing intermetallics in their microstructures. The latter were suggested to be the $Ni_{17}Y_2$ and Ni_5Y phases by the XRD data. The former has been reported to form in Y containing BC MCrAlY type alloys [Naumenko et al., 2009].

During solidification the formation of the γ-Ni_{ss} was accompanied by partitioning of Al, Si and Ta to the melt, with the only exception being the alloy EK5 where the Ta partitioned to the γ-Ni_{ss} rather than the melt, see Table 4.6. Furthermore, the formation of the β-NiAl was accompanied by partitioning of Co, Cr, Si and Ta to the melt and of Al to the β-NiAl during solidification, with the data for Ta for the alloy EK3 suggesting partitioning of Ta to the β-NiAl, see Table 4.7. Assadi et al calculated the relationship between the S/L interface temperature and the solid and liquid compositions at the interface for different growth velocities and predicted invertible partitioning of solute only between the ordered β-NiAl and the liquid for normalised growth velocities V/V_n greater than 0.3 (where $V_n = D_i/\lambda$ with D_i the interface diffusivity (= $6\ 10^{-8}\ m^2s^{-1}$) and λ the jump distance (=10^{-9}m)) [Assadi et al., 1995]. In contrast, for disordered solid solutions where the partition coefficient never becomes larger than 1 if its equilibrium value is smaller than 1 (or vice versa). Thus their prediction is that under non equilibrium conditions segregation should occur, i.e., at growth velocities greater than 18 ms^{-1}. Such growth velocities are considered unlikely during the solidification of the alloys of this study. The change in the values of the partitioning coefficients $k_{Ta}^{L/\gamma}$ and $k_{Ta}^{L/\beta}$ from less than one to greater than one respectively for the alloys EK5 and EK3 is thus either a real effect of alloying or an error due to difficulties with EDS analysis of Ta (see below).

Table 4.6 Partition coefficient* $k_i^{L/\gamma} = C_i^{\gamma}/C_i^{L}$ for solute elements (i) in the alloys EK1 to EK5 where C_i^{γ} and C_i^{L} are the concentration of element i in the γ-Ni_{ss} and Liquid respectively (C_i^{L} is the concentration of element i in large area analysis of alloy).

alloy	$k_{Al}^{L/\gamma}$	$k_{Cr}^{L/\gamma}$	$k_{Co}^{L/\gamma}$	$k_{Ta}^{L/\gamma}$	$k_{Si}^{L/\gamma}$
EK1	0.9	1	1.1	-	-
EK2	0.8	1.2	1.1	0.9	-
EK3	0.8	1.1	1.1	0.9	-
EK4	0.8	1.2	1.1	0.9	-
EK5	0.6	1.3	1.2	1.4	0.7

Table 4.7 Partition coefficient $k_i^{L/\beta} = C_i^{\beta}/C_i^{L}$ for solute elements (i) in the alloys EK1 to EK5 where C_i^{β} and C_i^{L} are the concentration of element i in the β-NiAl and Liquid respectively (C_i^{L} is the concentration of element i in large area analysis of alloy) (data "rounded up" to first decimal point).

alloy	$k_{Al}^{L/\beta}$	$k_{Cr}^{L/\beta}$	$k_{Co}^{L/\beta}$	$k_{Ta}^{L/\beta}$	$k_{Si}^{L/\beta}$
EK1	1.7	0.6	0.7	-	-
EK2	1.5	0.7	0.8	0.8	-
EK3	1.6	0.6	0.7	1.01	-
EK4	1.5	0.6	0.8	0.8	-
EK5	1.6	0.7	0.8	0.8	0.8

In the solidified microstructures the partitioning of Al and Co between the γ-Ni_{ss} and β-NiAl phases was not changed by the synergies of different alloying elements (see Table 4.8), the partitioning of Cr to the γ-Ni_{ss} was increased by the synergy of Ta and Y and Ta, Y and Si (Table 4.8), Ta partitioned to the γ-Ni_{ss} but when it was in synergy with Y in the alloy EK3 the latter element "pushed" the Ta to the β-NiAl.

Table 4.8 Partition coefficient $k_i^{\gamma/\beta} = C_i^{\gamma}/C_i^{\beta}$ for solute elements (i) in the cast alloys EK1 to EK5 where C_i^{γ} and C_i^{β} are the concentration of element i in the γ-Ni_{ss} and β-NiAl respectively (data "rounded up" to first decimal point).

alloy	$k_{Al}^{\gamma/\beta}$	$k_{Cr}^{\gamma/\beta}$	$k_{Co}^{\gamma/\beta}$	$k_{Ta}^{\gamma/\beta}$	$K_{Si}^{\gamma/\beta}$	$K_{Y}^{\gamma/\beta}$	$K_{Hf}^{\gamma/\beta}$
EK1	0.5	1.6	1.7	-	-	-	-
EK2	0.5	1.7	1.4	1.1	-	-	-
EK3	0.5	1.8	1.6	0.9	-	-	-
EK4	0.5	1.9	1.4	1.2	-	-	-
EK5	0.4	2	1.6	1.8	0.9	0.4	0.3

As the solutes partitioned between the two main phases, namely the γ-Ni_{ss} and β-NiAl, and the melt during solidification the Al + Cr contents of the aforementioned phases were "established" and according to the data in Table 4.9 the addition only of Ta in the alloys EK2 gave the highest Al + Cr contents in the γ-Ni_{ss} and β-NiAl. The higher Cr content in γ-Ni_{ss} was in the alloy EK2 (high Cr/Al ratio compared with most of the other alloys, Table 4.9) and the higher Cr content in the β-NiAl was also in the alloy EK2 (lowest Al/Cr ratio compared with the other alloys, Table 4.9). In other words, alloying with Ta resulted to the highest Al + Cr and Cr contents in the two main phases.

Table 4.9 The **A** = Al + Cr content (at%) and **B** = Cr/Al and **Γ** = Al/Cr ratio in the γ-Ni_{ss} and β-NiAl in the as cast (AC) and heat treated (HT) alloys EK1 to EK5.

alloy	**AC**				**HT1**				**HT2**			
	phase				**phase**				**phase**			
	γ- Ni_{ss}		**β-NiAl**		**γ- Ni_{ss}**		**β-NiAl**		**γ Ni_{ss}**		**β-NiAl**	
	A	**B**	**A**	**Γ**	**A**	**B**	**A**	**Γ**	**A**	**B**	**A**	**Γ**
EK1	36.2	1.3	41.1	2.4	36.2	1.6	40.7	2.2	35.8	1.5	39.3	2.3
EK2	**40.3**	1.7	**43.4**	1.9	**39.6**	2.4	**43.1**	2.8	**39.6**	2.1	**42.8**	2.8
EK3	35.1	1.2	41.5	2.9	34.5	1.6	40.5	3.5	34.5	1.4	40.8	3.9
EK4	35.6	1.3	40.7	2.7	34.3	1.8	40.3	3.9	34	1.8	40.5	4.3
EK5	34.2	2.1	38.1	2.3	33.4	2.6	32.2	2.2	32	2.6	35	2.8

The γ + β eutectic was not observed in the alloys EK3 and EK5, which would suggest that Y and Si suppress its formation. The Al + Cr content in the γ + β eutectic was essentially the same in the three alloys but the Al/Cr ratio increased dramatically when the Ta was in synergy with Hf (Table 4.10). This can be understood by considering the partitioning of solutes between the two main phases and the eutectic. The data in Table 4.10 shows that alloying with Ta, and Ta and Hf respectively decreased and increased the partition coefficients of Al and Cr and that this effect was particularly stronger for the partitioning of solutes between the β and the eutectic. Thus, the highest Al/Cr ratio for EK4 was due to the partitioning of Al and the high Al + Cr content due to the partitioning of Cr.

Table 4.10 Partition coefficient $k'^{j}_{i} = C_i^j/C_i^{(\gamma-\beta)\ eutectic}$ for solute elements (i) in phase j = β, γ and Cr+Al content and Al/Cr ratio for the γ-β eutectic in the cast alloys EK1, EK2 and EK4.

alloy	Partition coefficient				Cr + Al	Al/Cr
EK1	$k'^{\gamma}_{Al} = 0.7$	$k'^{\gamma}_{Cr} = 1.1$	$k'^{\gamma}_{Co} = 1.3$	-	40.2	1.1
	$k'^{\beta}_{Al} = 1.4$	$k'^{\beta}_{Cr} = 0.7$	$k'^{\beta}_{Co} = 0.8$	-		
EK2	$k'^{\gamma}_{Al} = 0.7$	$k'^{\gamma}_{Cr} = 1.2$	$k'^{\gamma}_{Co} = 1.4$	$k'^{\gamma}_{Ta} = 1$	41.6	1
	$k'^{\beta}_{Al} = 1.4$	$k'^{\beta}_{Cr} = 0.7$	$k'^{\beta}_{Co} = 0.8$	$k'^{\beta}_{Ta} = 0.9$		
EK4	$k'^{\gamma}_{Al} = 0.6$	$k'^{\gamma}_{Cr} = 1.6$	$k'^{\gamma}_{Co} = 1.3$	$k'^{\gamma}_{Ta} = 1.3$	39.4	2.2
	$k'^{\beta}_{Al} = 1.1$	$k'^{\beta}_{Cr} = 0.9$	$k'^{\beta}_{Co} = 0.99$	$k'^{\beta}_{Ta} = 1.1$		

A calculated primary phase selection map where only the growth competition of the γ-Ni_{ss}, γ′-Ni_3Al and β-NiAl was considered show that there is an extremely narrow regime of predominance of the γ′-Ni_3Al [Assadi et al, 1998]. The presence of the γ′-Ni_3Al in all the cast alloys was suggested by XRD but it was corroborated by high resolution FEG-SEM only in two of the studied alloys. Indeed, the γ′-Ni_3Al was "observed" in the cast alloys EK3 and EK5 (and also after their heat treatment) while in the alloy EK2 evidence for the γ′-Ni_3Al intermetallic was found only after the second heat treatment. The above would suggest that the synergy of Ta and Y and of Ta, Y and Si enhanced the stability of the γ′-Ni_3Al.

Following the two heat treatments in the coarsened microstructures the γ-Ni_{ss} and β-NiAl phases were stable. After the first heat treatment (HT1) the partition coefficient $k_i^{\gamma/\beta} = C_i^{\gamma}/C_i^{\beta}$ for each solute element (i) was remarkably stable, particularly for Al and Cr, but with the exception of Ta in the alloy EK5, see Table 4.11. The same was the case for the second heat treatment (HT2) for the alloys EK2 to EK5 but the partition coefficients for Al and Cr in EK1 were different from those in the other alloys (Table 4.12), which would suggest that the microstructure of EK1 was less thermally stable.

Table 4.11 Partition coefficient $k_i^{\gamma/\beta} = C_i^{\gamma}/C_i^{\beta}$ for solute elements (i) in the heat treated (HT1) alloys EK1 to EK5 where C_i^{γ} and C_i^{β} are the concentration of element i in the γ-Ni_{ss} and β-NiAl respectively.

alloy	$k_{Al}^{\gamma/\beta}$	$k_{Cr}^{\gamma/\beta}$	$k_{Co}^{\gamma/\beta}$	$k_{Ta}^{\gamma/\beta}$	$K_{Si}^{\gamma/\beta}$	$K_{Hf}^{\gamma/\beta}$
EK1-HT1	0.43	2.35	1.83	-	-	-
EK2-HT1	0.36	2.44	1.69	1.15	-	-
EK3-HT1	0.42	2.4	1.67	1.5	-	-
EK4-HT1	0.38	2.7	1.74	1.3	-	-
EK5-HT1	0.43	2.4	1.6	3.7	0.9	0.4

Table 4.12 Partition coefficient $k_i^{\gamma/\beta} = C_i^{\gamma}/C_i^{\beta}$ for solute elements (i) in the heat treated (HT2) alloys EK1 to EK5 where C_i^{γ} and C_i^{β} are the concentration of element i in the γ-Ni_{ss} and β-NiAl respectively.

alloy	$k_{Al}^{\gamma/\beta}$	$k_{Cr}^{\gamma/\beta}$	$k_{Co}^{\gamma/\beta}$	$k_{Ta}^{\gamma/\beta}$	$K_{Si}^{\gamma/\beta}$	$K_{Hf}^{\gamma/\beta}$
EK1-HT2	0.52	1.79	1.28	-	-	-
EK2-HT2	0.4	2.39	1.63	1.21	-	-
EK3-HT2	0.44	2.4	1.64	1.4	-	-
EK4-HT2	0.37	2.8	1.8	1.4	-	-
EK5-HT2	0.35	2.4	1.6	1.8	1	0.7

The partition coefficients $k_i^{\gamma/\beta} = C_i^{\gamma}/C_i^{\beta}$ for each solute element (i) in each alloy in the as cast and heat treated conditions are compared in Table 4.13. The data shows similar trends for Al, Co, Cr and Ta in the alloys EK2, EK3 and EK4. The data would suggest that $k_{Ta}^{\gamma/\beta} < 1$ for EK3-AC is incorrect, probably due to analysis errors. The same might be the case for $k_{Ta}^{\gamma/\beta} = 3.7$ for EK5-HT1 (EDS analysis of Ta in the presence of Hf and Si is considered “tricky”).

Table 4.13 Partition coefficient $k_i^{\gamma/\beta} = C_i^{\gamma}/C_i^{\beta}$ for solute elements (i) in the as cast and heat treated (HT1, HT2) alloys EK1 to EK5 where C_i^{γ} and C_i^{β} are the concentration of element i in the γ-Ni_{ss} and β-NiAl respectively.

alloy	$k_{Al}^{\gamma/\beta}$	$k_{Cr}^{\gamma/\beta}$	$k_{Co}^{\gamma/\beta}$	$k_{Ta}^{\gamma/\beta}$	$K_{Si}^{\gamma/\beta}$	$K_{Hf}^{\gamma/\beta}$
EK1-AC	0.51	1.63	1.65	-	-	-
EK1-HT1	0.43	2.35	1.83	-	-	-
EK1-HT2	0.52	1.79	1.28	-	-	-
EK2-AC	0.53	1.68	1.41	1.1	-	-
EK2-HT1	0.36	2.44	1.69	1.15	-	-
EK2-HT2	0.4	2.39	1.63	1.21	-	-
EK3-AC	0.5	1.82	1.56	0.85	-	-
EK3-HT1	0.42	2.4	1.67	1.5	-	-
EK3-HT2	0.44	2.4	1.64	1.4	-	-
EK4-AC	0.52	1.85	1.43	1.2	-	-
EK4-HT1	0.38	2.7	1.74	1.3	-	-
EK4-HT2	0.37	2.8	1.8	1.4	-	-
EK5-AC	0.41	2.04	1.55	1.8	0.88	0.33
EK5-HT1	0.43	2.4	1.6	3.7	0.9	0.4
EK5-HT2	0.35	2.4	1.6	1.8	1	0.7

As the solutes partitioned between the two main phases, namely the γ-Ni_{ss} and β-NiAl, during the heat treatment, the Al + Cr contents of the aforementioned phases did not change compared with the as cast alloys, the only exception being the alloy EK5 where there was decrease of the Al + Cr content (see Table 4.9). As was the case in the cast alloy, the addition only of Ta in the alloys EK2 gave the highest Al + Cr contents in the γ-Ni_{ss} and β-NiAl. The higher Cr content in γ-Ni_{ss} was in the alloy EK2 (high Cr/Al ratio compared with most of the other alloys, Table 4) and the higher Cr content in the β-NiAl was also in the alloy EK2 (lowest Al/Cr ratio compared with the alloys EK2 to EK5, Table 4.9). In other words, the alloying with Ta resulted to the highest Al + Cr and Cr contents in the two main phases in the cast conditions and this was maintained after the two heat treatments.

The alloying with Ta had a dramatic effect on the volume fractions of the two main phases. In the as cast condition the vol% of the β-NiAl was higher than the vol% of the γ-Ni_{ss} in the alloys EK2 and EK5, suggesting that alloying with Y and Hf tends to favour the γ-Ni_{ss} rather than the β-NiAl. There were changes in the vol% of the aforementioned phases after the heat treatment, with the vol% of the β-NiAl increasing in all alloys. The higher vol% of β-NiAl was still observed in the alloys EK2 and EK5 (see Table 4.14).

Table 4.14 Volume fractions of the γ-Ni_{ss} and β-NiAl phases in the cast and heat treated (HT2) alloys.

alloy	**As cast**		**Heat treated**	
	γ- Ni_{ss}	**β-NiAl**	**γ- Ni_{ss}**	**β-NiAl**
EK1	74	26	67	33
EK2	43	57	38	62
EK3	68	32	52	44
EK4	68	30	68	32
EK5	48	52	35	65

In the alloy EK3 the Ni_5Y intermetallic was present in the microstructure according to the XRD data. The other phases that were corroborated by XRD and EDS were the γ-Ni_{ss}, β-NiAl and γ′-Ni_3Al. In the Ni-Al-Y system the β-NiAl and γ′-Ni_3Al can be in

equilibrium with the Ni_5Y. This is considered as further evidence for the stability of the Ni_5Y in EK3.

In the alloy EK4 the XRD data suggested the presence of the Ni_5Y and $Ni_{17}Y_2$ in the microstructure. In the Ni-Al-Y system the above intermetallics can be in equilibrium with the γ-Ni_{ss} and the β-NiAl and γ′-Ni_3Al can be in equilibrium with the Ni_5Y. The γ′-Ni_3Al was not observed in this alloy. It is thus most likely that the $Ni_{17}Y_2$ is stable in EK4.

In the alloy EK5 the XRD data pointed to the presence of Ni_5Y and $Ni_{17}Y_2$ in the microstructure. Considering the aforementioned phase equilibria in the Ni-Al-Y system and the presence of the γ-Ni_{ss}, β-NiAl and γ′-Ni_3Al in the microstructure, it is suggested that both the Ni_5Y and $Ni_{17}Y_2$ intermetallics can form in EK5 (see below).

The above discussion has confirmed the positive effects of alloying with Ta on the Cr and Al contents of the two main phases in the alloys of this study. Alloying with Ta however caused chemical inhomogeneity in the microstructure and Ta in synergy with the other key elements like Hf, Si and Y that are added to BC alloys to improve the performance of the TGO (see section 4.1) enhanced the stability of other intermetallic phases in the microstructure after exposure to high temperature. In the previous chapter the effect of the Ta addition in the microstructure of EK2 was discussed. In this alloy (EK2) there was evidence of Ta segregation in the γ-Ni_{ss} consistent with the partitioning of Ta to this phase ($k_{Ta}^{\gamma/\beta}$ = 1.1, see Table 4.8). Ta rich areas in the γ-Ni_{ss} (and thus chemical inhomogeneity in the γ-Ni_{ss}) were still observed after the first heat treatment of EK2 but not after the second one, consistent with the low diffusivity of Ta owing to its high melting point. The addition of Y in the alloy EK3 led to the segregation of Y in the γ-Ni_{ss} and the formation of a Y containing intermetallic in the solidified microstructure (the standard deviation of the analysis of this phase was large, this phase could be either Ni_3Y or Ni_5Y, the latter was suggested by the XRD, see discussion above) and did not affect the solid solubility of Ta in γ-Ni_{ss}. According to the EDS data (Table 4.3), the partitioning behaviour of Ta changed ($k_{Ta}^{\gamma/\beta}$ = 0.9, see Table 4.8). The latter value for the partition coefficient of Ta is not considered reliable (see above). The Y rich areas persisted in the γ-Ni_{ss} in the heat treated microstructures where Ni_5Y and NiY_3 intermetallics were formed (see above) at γ/β interfaces.

The addition of Ta, Hf and Y in the alloy EK4 increased the chemical inhomogeneity of its microstructure. Hafnium, Ta and Y rich areas were observed in the γ-Ni_{ss} consistent with the partitioning of Ta in this phase (as was the case in EK2) and with

the areas of chemical inhomogeneity observed in EK2 and EK3. Following heat treatment there was precipitation of second phases in the aforementioned areas (fig. 4.12, 4.14, 4.15), which would point to the existence of a supersaturated solid solution and new phases that were either rich in Y or in Ta and Hf were formed in the microstructure (Table 4.4 and figs 4.12 to 4.16) in the areas where chemical inhomogeneity existed in the cast alloy.

In the alloy EK5 the addition of Si enhanced chemical inhomogeneities in the microstructure (figs. 4.19 to 4.21) and there was formation of Si and Y rich areas in the solidified microstructure where Ta and Hf had also partitioned (fig. 4.21). After heat treatment the formation of intermetallic phases in those areas (fig. 4.24 to 4.26) was accompanied by severe micro-cracking in the microstructure (fig. 4.23) and internal oxidation (fig. 4.37). Fine precipitates were formed in the microstructure figs 4.28 to 4.32, which according to Naumenko et al (2009) were α-Cr. The presence of this phase was also suggested by the XRD data. The Si rich phase formed after heat treatment could be based on Ni_2Si with Si + Al ~ 33 at% and could be either the δ-Ni_2Si (Si=33.3 at%) or θ-Ni_2Si (Si=33.3 to 41 at%) [Chandrasekaran et al., 2006]. The XRD suggested evidence for the existence of these intermetallics in the microstructures of EK5-HT1 and EK5-HT2. In the preceding discussion it was suggested that both the Ni_5Y and $Ni_{17}Y_2$ intermetallics can form in EK5. It should be noted that Ni_3Al and Ni_3Si are isostructural (complete solid solubility between them) [Chandrasekaran et al., 2006] and that in the Ni-Si-Y system [ASM, database] there is equilibrium between Ni, Ni_3Si and $Ni_{17}Y_2$, which would provide further support for the stability of $Ni_{17}Y_2$ in EK5, and that in the Ni-Si-Al system [Chandrasekaran et al., 2006] there is equilibrium between NiAl, Ni_3Al and θ-Ni_2Si, which would suggest that the θ- Ni_2Si phase could form in the alloy EK5.

4.4 Conclusions

In this chapter three MCrAl based alloys of nominal compositions (Ni-20.1Co-19.8Cr-16.2Al-1.1Ta-0.3Y (alloy EK3), Ni-20.1Co-19.7Cr-16.2Al-1.1Ta-0.3Y-0.2Hf (alloy EK4) and Ni-19.3Co-19.1Cr-15.6Al-1.1Ta-0.3Y-0.2Hf-3.5Si (alloy EK5) were studied in the as cast and heat treated conditions in order to understand the effect of the alloying additions like of Ta, Y, Hf and Si and the synergistic effects of them in the microstructure and phase stability. The microstructure of these three alloys contained the γ-Ni_{ss} and β-NiAl in as cast and heat treated conditions and was confirmed both by EDS

and XRD results. The γ′-Ni_3Al probably had formed in the all of the three alloys in as cast and heat treated conditions as suggested by the XRD data but its stability was affected by the synergy of Ta, Y, Hf and Si either by destabilizing it or by enhancing it as in EK3-AC, EK3-HT2, EK5-HT1 and EK5-HT2. Therefore, FEG-SEM evidence of its formation was found only in EK3-AC (see fig. 4.1a), EK3-HT2 (see fig. 4.6a, b, c), EK5-HT1 (see figs 4.31, 4.32a. 4.33) and EK5-HT2 (see fig. 4.36) via precipitation in the γ-Ni_{ss}. Eutectic between β+γ was confirmed only in the EK4-AC which got destabilised after the heat treatments.

Synergistic effects of Ta, Y, Hf and Si did not affect the stable γ-Ni_{ss} and β-NiAl phases. However, alloying additions had highly affected the stability of γ′-Ni_3Al and of the γ + β eutectic. They have also enhanced the formation of intermetallics rich in Y and Si such as Ni_3Y, Ni_5Y, $Ni_{17}Y_2$, Ni_3Si and θ- Ni_2Si and/or δ-Ni_2Si.

Tantalum had positive effects on Cr and Al in the γ-Ni_{ss} and β-NiAl and promoted chemical homogeneity in the microstructures. Ta with Y, Hf and Si enhanced the stability of intermetallics in the BC alloys therefore they are expected to improve the performance of the oxide scale. Ta segregated and partitioned in γ-Ni_{ss} creating Ta rich areas after HT1 of EK2. Alloying with Ta affected volume fractions of both γ-Ni_{ss} and β-NiAl in EK2 and EK5 alloys by favouring the β-NiAl formation.

Alloying with Y led to its segregation in γ-Ni_{ss} and formation of Y containing intermetallics such as Ni_3Y, Ni_5Y and $Ni_{17}Y_2$ without affecting solid solubility of Ta in the solid solution. Yttrium rich areas were formed at the γ/β interfaces after the heat treatments.

Hafnium addition in synergy with Y favoured γ-Ni_{ss} formation rather than β-NiAl, with the vol% of the β-NiAl being significantly decreased in EK4 alloy. However, Y with Ta and Hf increased chemical homogeneity of the microstructure in γ-Ni_{ss} with Ta partitioning similarly with EK2 alloy.

Silicon addition created more complex microstructures, chemically inhomogeneous with Si and Y rich areas where Ta and Hf had also partitioned. The microstructures contained the γ-Ni_{ss} and β-NiAl phases and also fine α-Cr precipitates as well as other intermetallics after the heat treatment with micro cracking and internal oxidation. In EK5 alloy, β-NiAl formation was favoured with increased vol% compared to the γ-Ni_{ss}.

Chapter 5 – Oxidation

5.1 Introduction

Commercial thermal barrier coating systems (TBCs), typically consist of a metallic bond coat (BC) applied on a Ni based superalloy (substrate) and a ceramic top coat, like yttria-stabilized zirconia (YSZ) that is applied by plasma spraying (PS) or electron beam-physical vapour deposition (EB-PVD). The bond coat needs to be resistant to oxidation because the YSZ cannot stop the transport of oxygen and thus cannot protect the substrate from oxidation.

The oxidation of Ni base superalloys and coatings have been studied in the temperature range 600 to 1300 ˚C and in different oxidizing atmospheres such as air, O_2, CO_2-CO and H_2O-H_2 [Brumm et al., 1994]. The oxidation of bond coats is one of the common failure mechanisms in commercial TBCs and a barrier for improving the coating lifetime. The BC alloys that were studied in this work were designed in order to form in situ a protective α-Al_2O_3 scale during operation at 975 ˚C.

Several factors were considered before designing the bond coats, including operating temperatures, operating environments such as H_2 rich Syngas and CMAS attack, microstructural stability of the bond coats, melting points of alloying elements and compositions of both bond coat and substrate among many others. Our primary concern though was to evaluate the oxidation of the new BC alloys through isothermal oxidation, the adhesion of the α-Al_2O_3 scale to the metal substrate and their spallation and the outward loss of solutes due to oxide formation.

This chapter attempts to discover and isolate issues related to oxidation of the bond coats. In this study five alloys were produced and tested in their as cast condition under isothermal oxidation in air at 975 ˚C for 100 hrs. The aim was all these alloys to form an alumina scale that will resist cracking and spallation and produce acceptable oxide scale growth rates. The first bond coat alloy was the alloy EK1 (Ni-20.4Co-21Cr-16.4Al at%) and the four other alloys had one extra alloying addition each time as alloying is an effective way to improve oxidation behaviour of MCrAlY based materials. The alloying additions were the elements Ta, Y, Hf and Si. The design/selection criteria for the alloys

EK1 to EK5 were discussed in chapter 2. The role of the alloying additions on oxidation resistance was studied using XRD and SEM with EDS and WDS, see chapter 2.

5.2 Results

5.2.1 Thermo-gravimetric analysis at 975 ˚C

Cubes of 3x3x3 mm^3 were cut from the bulk of the as cast alloys for the TGA studies. The dimensions of each sample were measured using a micrometre and the Measure Axio Vision software and the surface area was calculated, see chapter 2. Particles on the surface of a sample due to metallographic preparation, such as silicon carbide might affect oxidation locally. Therefore, the specimens that were prepared using grinding and polishing were ultrasonically cleaned in alcoholic bath (see chapter 2). The samples were weighted using an accurate scale to measure the weight change after the thermo-gravimetric analysis. After each oxidation experiment, the recorded data for weight change during the isothermal period was plotted as weight change per unit surface area as a function of time to determine the oxidation kinetics, see figure 5.1. The total weight change of the alloys EK1, EK2, EK3, EK4 and EK5 is summarized in Table 5.1 together with the parabolic rate constants (k_p) of each alloy. The rate constants were calculated using equation 5.1 [Schütze, 2000]. In Table 5.1 also are given the n values for the oxidation reaction kinetics from equation 5.2 [Khanna, 2000, Menon et al, 2001].

$$(\Delta w/A)^2 = k_p t \qquad (5.1)$$

$$\Delta w/A = kt^n \text{ and } \ln(\Delta w) = \ln k + n \ln t \qquad (5.2)$$

where Δw is the weight change of the specimen, A is the surface area of the specimen, k_p is the parabolic rate constant, t is the exposure time and the value of n is obtained as the slope in log-log plot. Formation of thick oxide layer or spallation of oxide scale was not observed in any of the alloys. The TG samples before and after isothermal oxidation are shown in figure 5.2.

Table 5.1 Weight gains, oxidation rate constants, n and R^2 values of the alloys after isothermal oxidation at 975 ˚C for 100 hrs.

Alloy code	**Weight gain (g/cm^2)**	**k_p ($g^2/cm^4 * sec^1$)**	**n***	**R^{2**}**
EK1	0.00097 (100 h)	$2.6 * 10^{-12}$	0.5	0.94
EK2	0.00067 (100 h)	$1.2 * 10^{-12}$	0.6	0.92
EK3	0.00036 (100 h)	$3.6 * 10^{-13}$	0.46	0.92
EK4	0.00047 (100 h)	$6.1 * 10^{-13}$	0.46	0.95
EK5	0.00041 (100 h)	$4.6 * 10^{-13}$	0.44	0.9

* n value close to 0.5 means that the oxidation follows a parabolic law. When n>0.5 or n<0.5 it means that the oxidation is faster or slower than parabolic oxidation kinetics [Menon et al, 2001, Perkins et al, 1989, Perkins et al, 1987].

** R^2 is the fitting parameter, the closer the R^2 value is to 1, the better the fitting

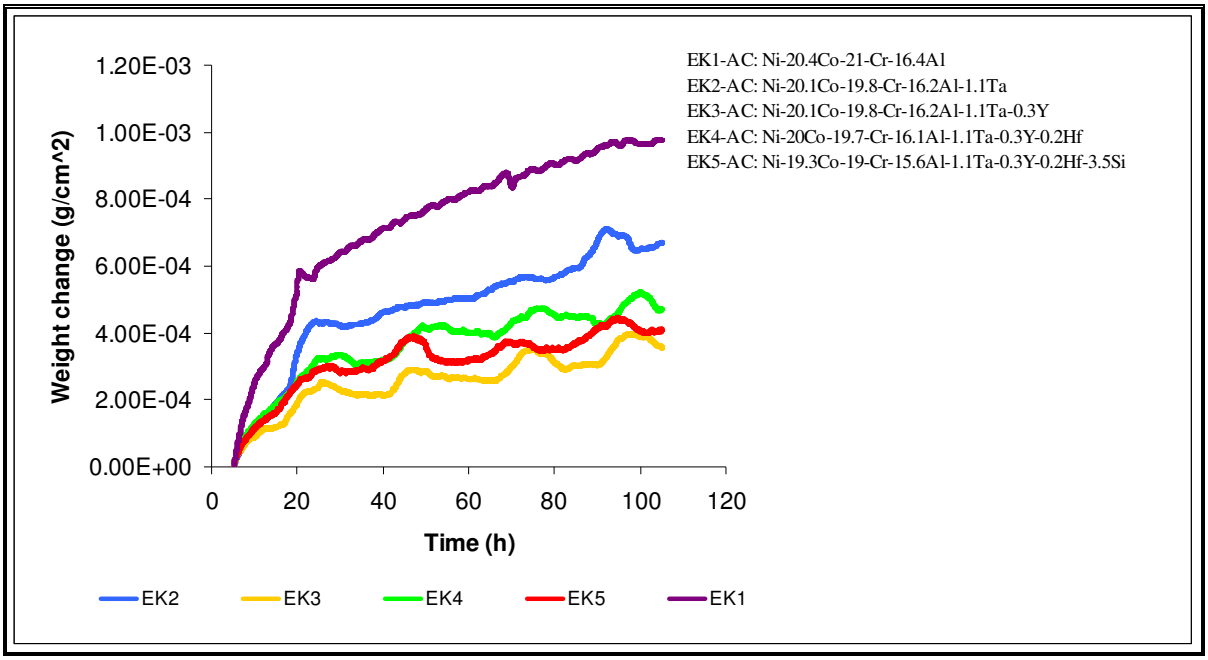

Figure 5.1 TG curves at 975 ˚C for the alloys EK1, EK2 (Ta addition), EK3 (Ta and Y additions), EK4 (Ta, Y and Hf additions), EK5 (Ta, Y, Hf and Si additions). The alloy nominal concentrations are given in at%. All alloys were tested in the as cast condition.

5.2.2 Structure of oxide scales and microstructure of oxidised alloys

The structure of oxide scales was characterized under SEI microscopy and the results showed that the EK1-TGA samples had a uniform oxide cover with islands covering the surface, the EK2-TGA had also a continuous oxide scale, the EK3-TGA showed more uniform coverage than the EK1-TGA sample, the EK4-TGA was uniform and with large oxide growths and finally the EK5-TGA had uniform oxide scale coverage. None of the samples showed evidence of spallation and in the EK1-TGA sample cracks of the alloy below the oxide scale where visible.

5.2.2.1 Ni-20.4Co-21Cr-16.4Al (alloy EK1)

5.2.2.1.1 Microscopy and glancing angle XRD

After oxidation for 100 hrs at 975 ˚C no spallation of oxide scale was observed. The surfaces of the oxidised sample were uniformly covered and had Al_2O_3 islands (figs 5.3 and 5.4). The edges of the oxidised sample were well defined (fig. 5.3). There were cracks on the oxide scale (fig. 5.5). Figures 5.4 and 5.5 show patches of Al_2O_3 of different sizes and/or morphologies. The blade-like morphology shown in figure 5.4 has also been reported by Rybicki and Smiakek (1989) and attributed to metastable θ-Al_2O_3. The EDS data in fig 5.5 cannot confirm the presence of Cr_2O_3 in the scale.

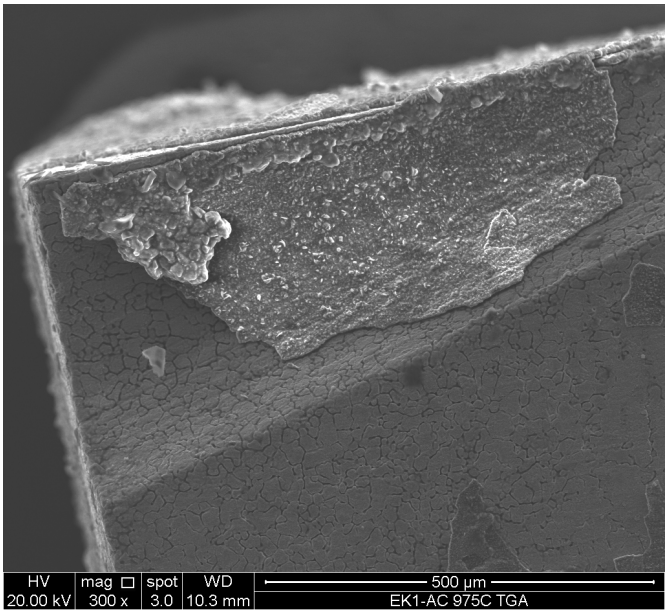

Figure 5.2 SEI image showing Al_2O_3 islands on the surface and that the edges of the alloy EK1 were well defined after oxidation at 975 ˚C.

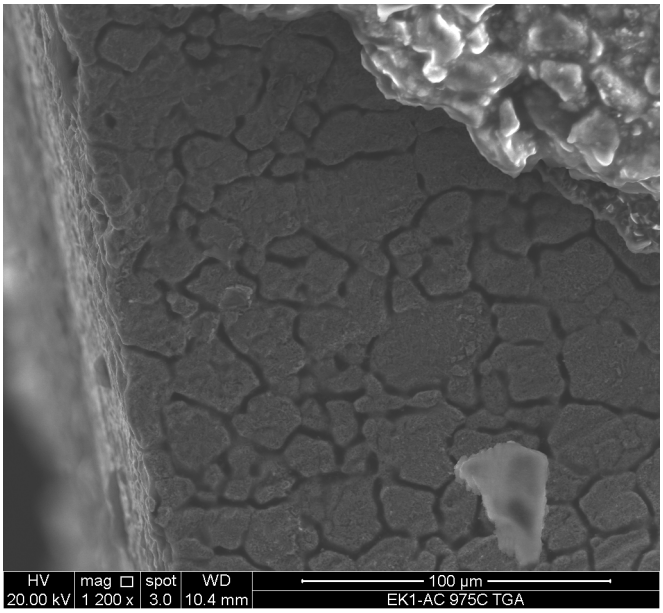

Figure 5.3 SEI image showing the metal being cracked beneath the Al_2O_3 islands that lay on the surface and that the edges of the alloy EK1 were well defined after oxidation at 975 ˚C.

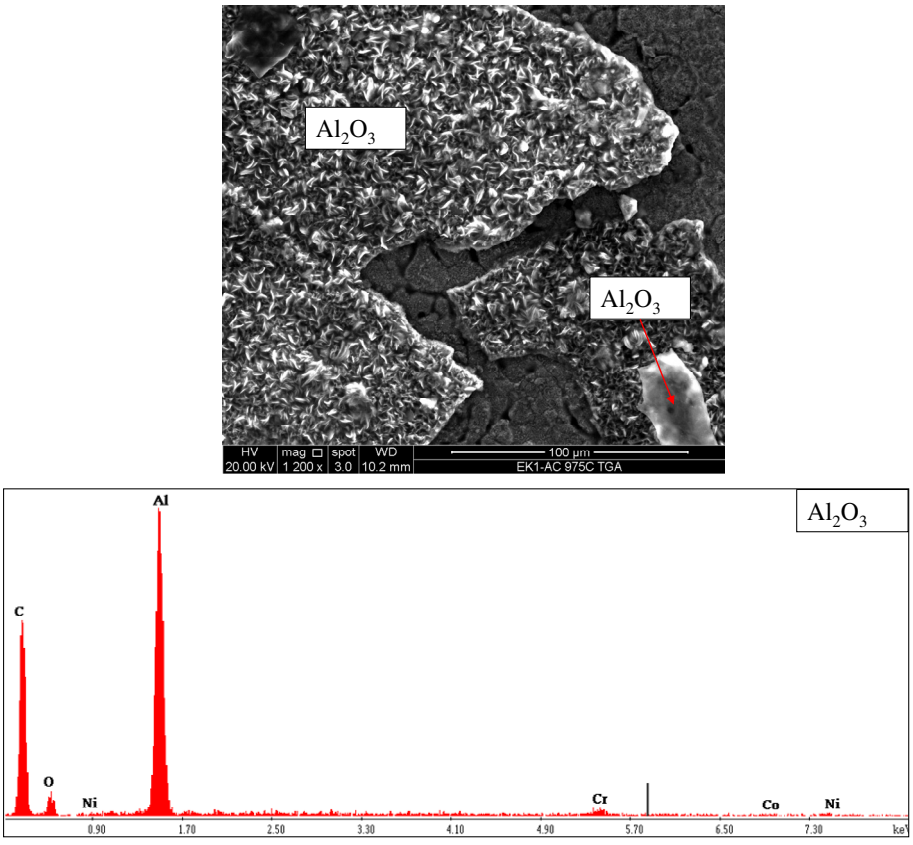

Figure 5.4 SEI image showing Al_2O_3 islands and EDS spectra from Al_2O_3 formed on the alloy EK1 after oxidation at 975 ˚C for 100 hrs.

Brumm and Grabke (1992) also reported that small fractions of Cr_2O_3 were formed with Al_2O_3 in alloys containing 7-34 at% Cr, after oxidation at temperatures over 1273 K.

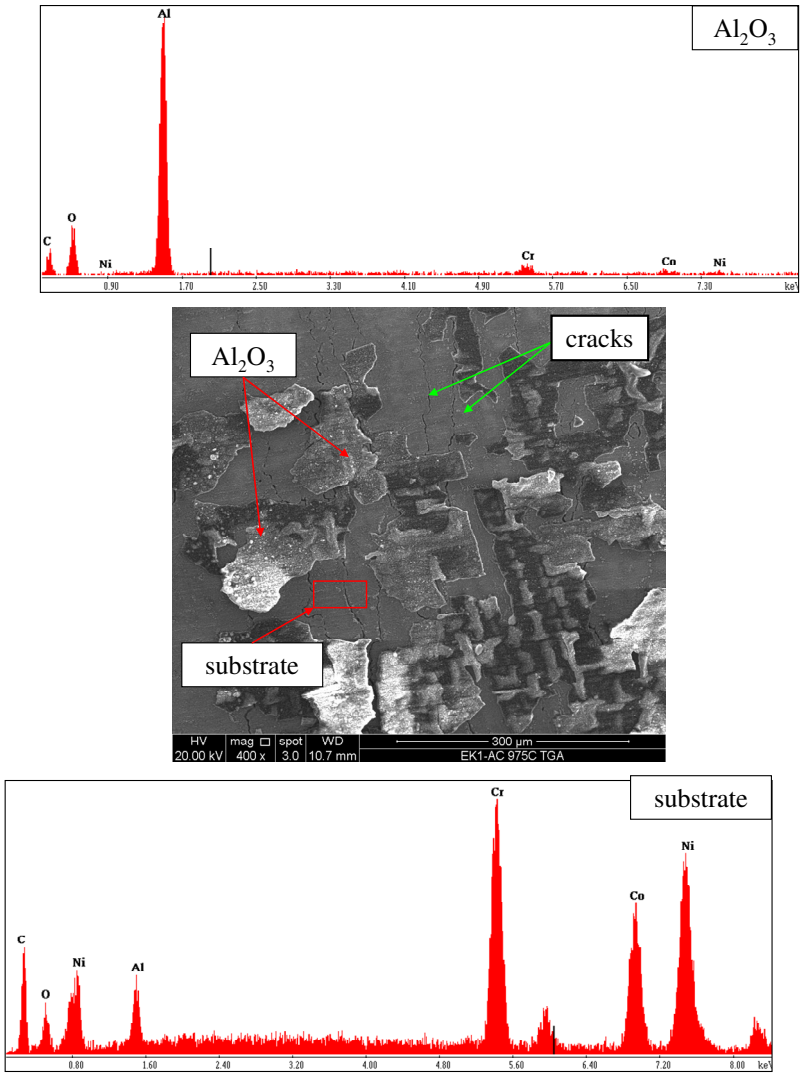

Figure 5.5 SEI image showing Al_2O_3 patches and surface cracks and EDS spectra from EK1 after oxidation at 975 ˚C for 100 hrs in air.

The glancing-angle XRD data of the alloy EK1 before and after oxidation is shown in Figures 5.6 and 5.7. X-ray peaks for the γ-Ni_{ss}, γ'-Ni_3Al and β-NiAl phases were observed in both glancing angles. Figures 5.7 shows peaks that corresponded only to γ-Al_2O_3, θ-Al_2O_3 and α-Al_2O_3 whereas the peaks for Cr_2O_3 coincided with other phases. The data also would suggest the presence of nitride phases, AlN and Cr_2N with one peak corresponding only to AlN in the γ=5˚ diffractogram (fig 5.7 b).

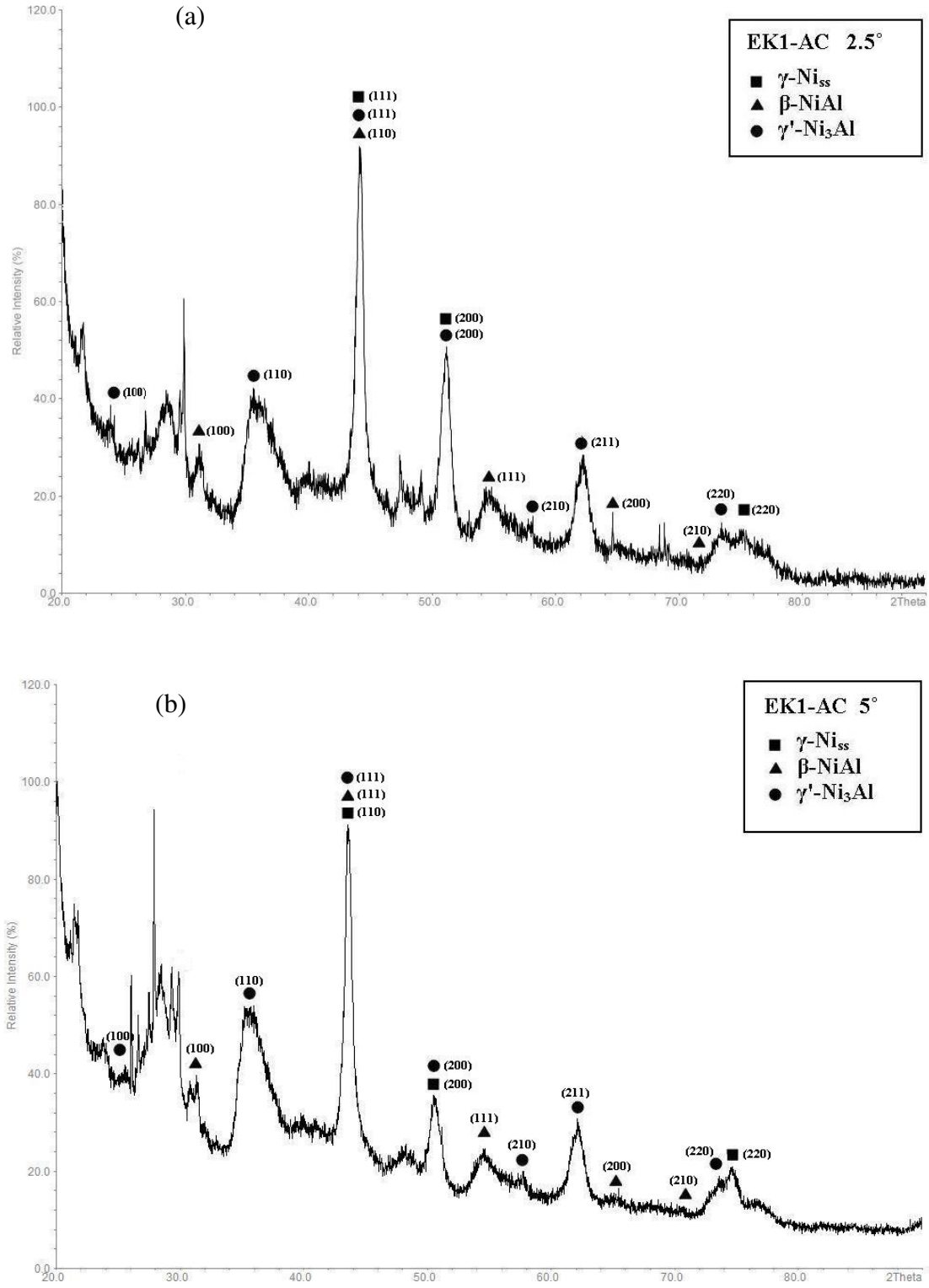

Figure 5.6 Glancing angle XRD data for the alloy EK1 before oxidation (a) γ= 2.5˚ and (b) γ= 5˚.

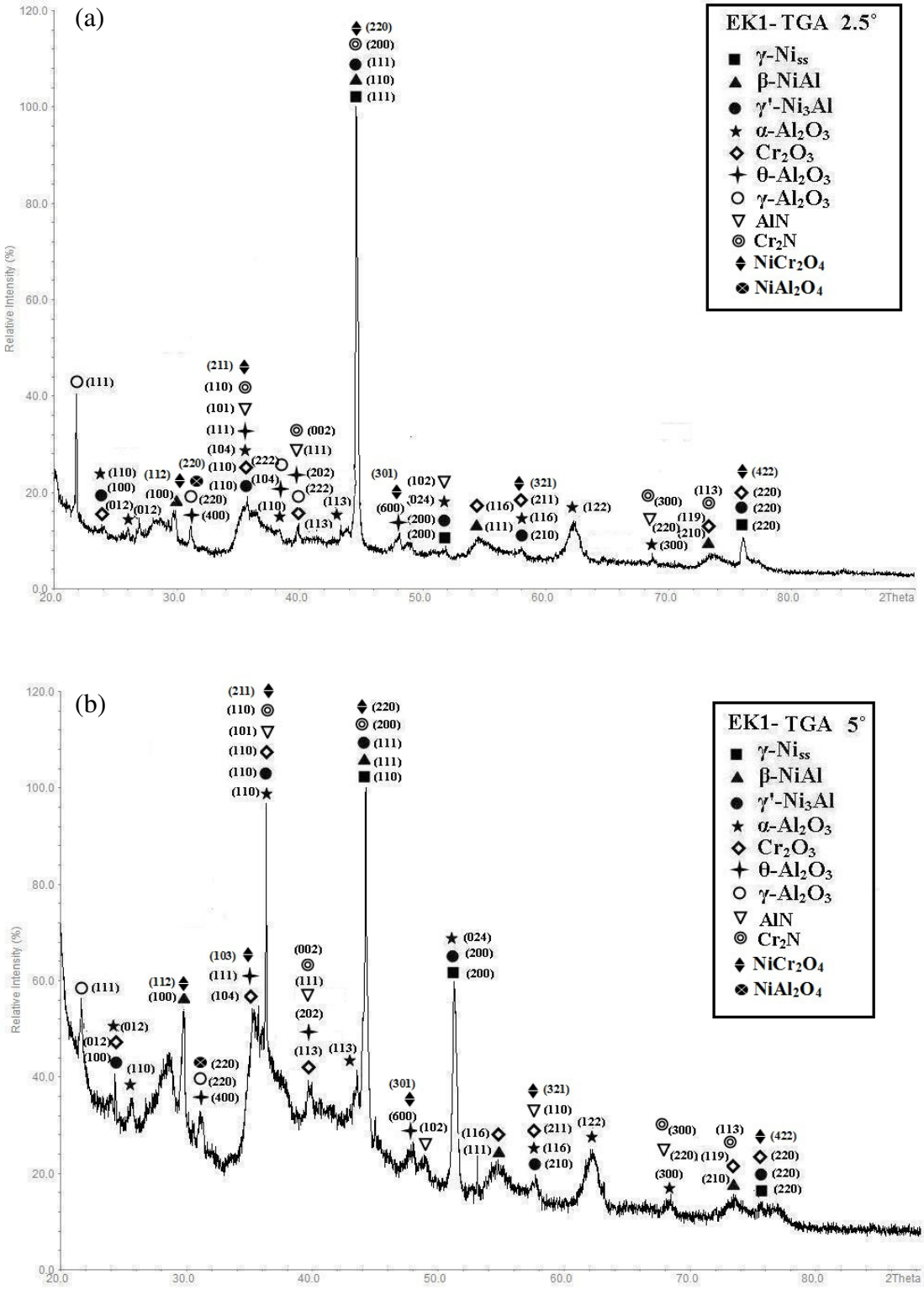

Figure 5.7 Glancing angle XRD data for the oxide scale formed on the alloy EK1 after oxidation for 100 hrs at 975 ˚C in air (a) γ= 2.5˚ and (b) γ= 5˚.

5.2.2.1.2 Microstructure of oxidised alloy

The microstructure of the oxidised alloy below the scale is shown in figure 5.8. A representative BSE image of the cross-section and the corresponding elemental distributions obtained by WDS as a function of distance from the oxide scale is shown in Fig. 5.11. The oxide scale is rich in O and Al, while the diffusion zone is characterised by its enrichment in Ni, Co and Cr. Below the internal oxidation zone the O and N and Al levels drop significantly and as the line scan goes through the bulk it crosses γ-Ni_{ss} that has high Ni, Co and Cr concentrations. The O level is low in the bulk and doesn't change below the scale whereas the N concentration seems to be the same in the γ-Ni_{ss} and β-NiAl in the bulk.

Qualitative EDS data for different parts in the cross section is shown in figures 5.9 and 5.10. The cross section microstructure exhibits four regions see fig. 5.8. Starting from the surface and going towards the bulk, there is an alumina oxide layer, see Table 5.2. A few features exhibiting dark contrast, which were rich in N (37.3 at %) and Al (43.3 at%) appeared, under the oxide scale suggesting internal oxidation and formation of aluminium nitride. Below the area of internal oxidation a diffusion zone occurred with high concentration in Ni (39 at %), Co (20.9 at %) and Cr (22.3 at %). Underneath this zone the typical bulk microstructure consisted of γ-Ni_{ss} and β-NiAl with the γ-Ni_{ss} being rich in Ni (37.5 at %), Co (22.3 at %) and Cr (23.8 at %) and the β-NiAl rich in Ni (46.1 at %) and Al (32.6 at %). The data for the γ and β phases in the as cast and oxidised alloy confirmed that as the EK1 alloy oxidised the β-NiAl became richer in Al and lost its Cr, whereas the γ-Ni_{ss} became richer in Cr and lost Al that was consumed for Al_2O_3 formation (see section 5.3).

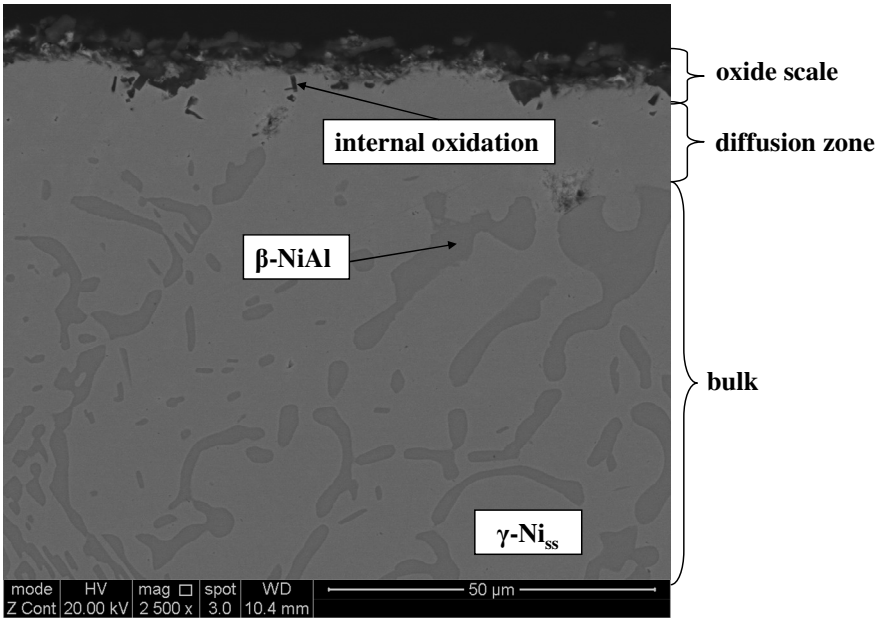

Figure 5.8 BSE image of the cross section of the oxidised specimen of alloy EK1 showing the microstructure below the scale.

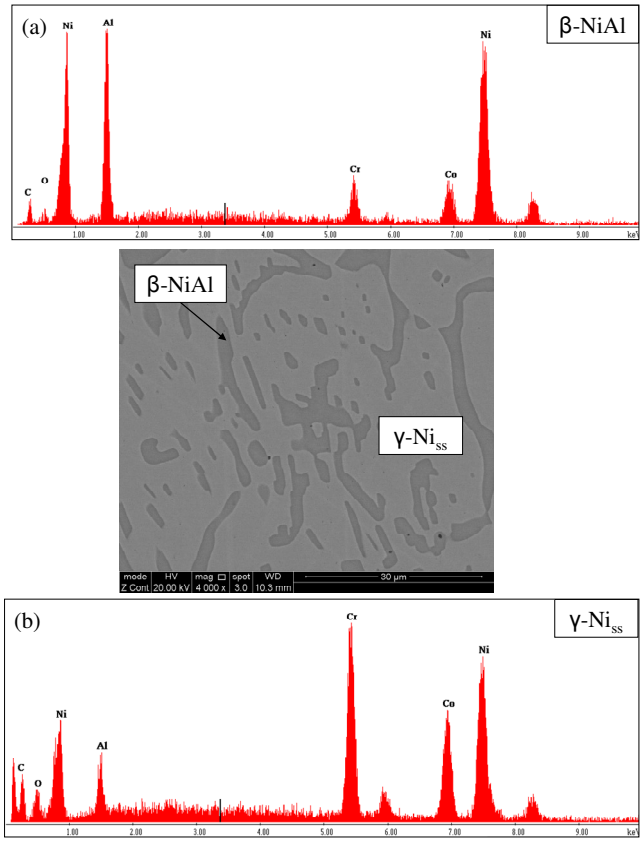

Figure 5.9 BSE image and EDS spectra taken form the bulk of the oxidised alloy showing presence of the γ-Ni_{ss} and β-NiAl phases.

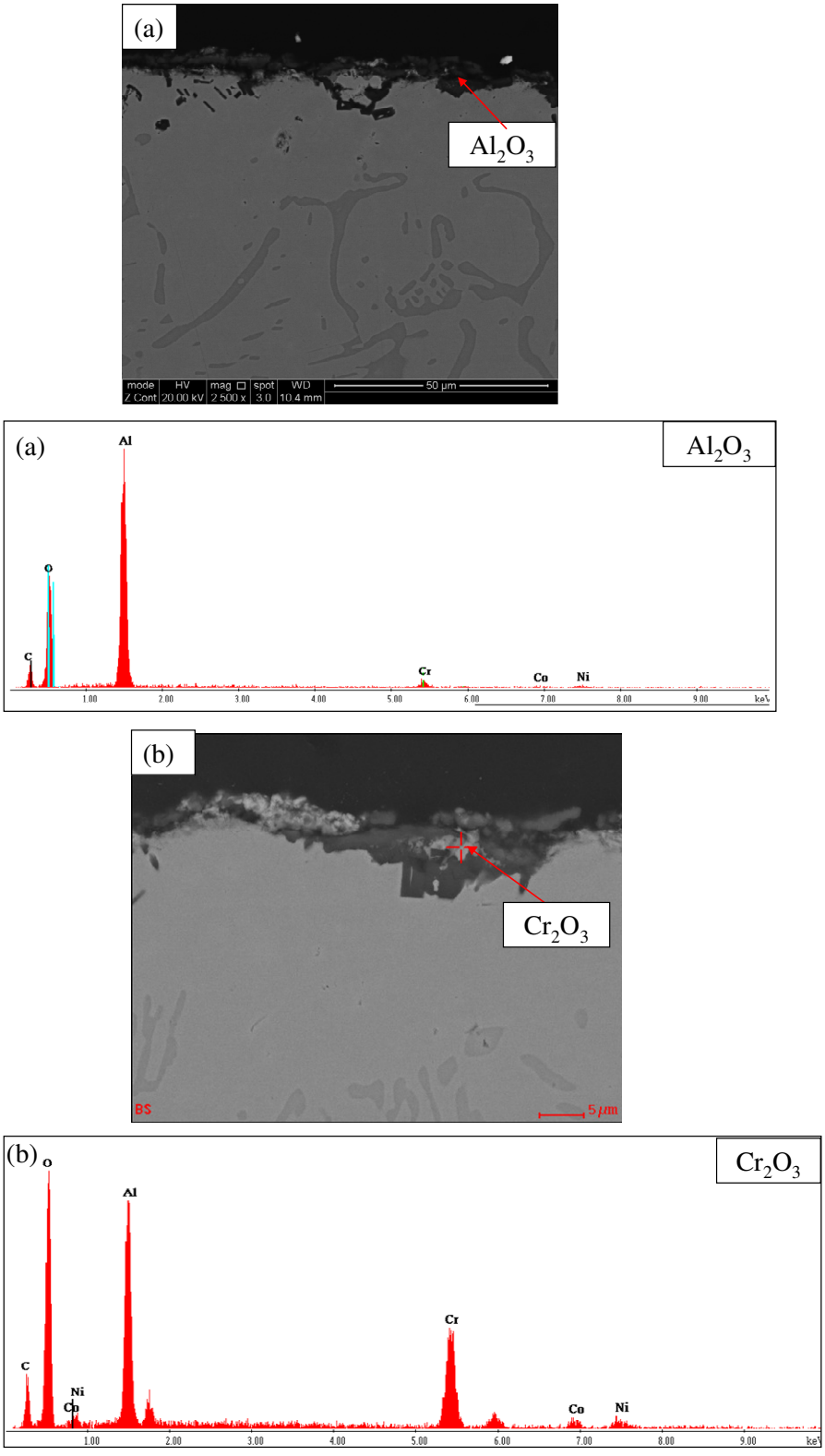

Figure 5.10 BSE images and EDS spectra of the oxide scale suggesting the presence of Al_2O_3 and Cr_2O_3.

Table 5.2 WDS analysis data (at %) of different parts of the cross section of the alloy EK1 after oxidation at 975 ˚C for 100 hrs.

Area	N	O	Ni	Co	Cr	Al
oxide scale	0	51.4±9.7	1.5±1.1	1±0.9	4.1±2.3	42.7±7.8
internal oxidation	37.3±1.2	0.7±0.04	8.3±0.4	4.7±0.1	5.5±0.1	43.4±0.4
diffusion zone	7.4±1.3	0.6±0.1	39±1	20.9±0.1	22.3±0.1	9.7±0.4
β-NiAl	6.8±1.3	0.7±0.3	46.1±0.7	8.6±0.3	5±0.08	32.6±0.5
γ-Niss	6.5±0.9	0.7±0.7	37.5±0.3	22.3±0.1	23.8±0.3	9±0.1

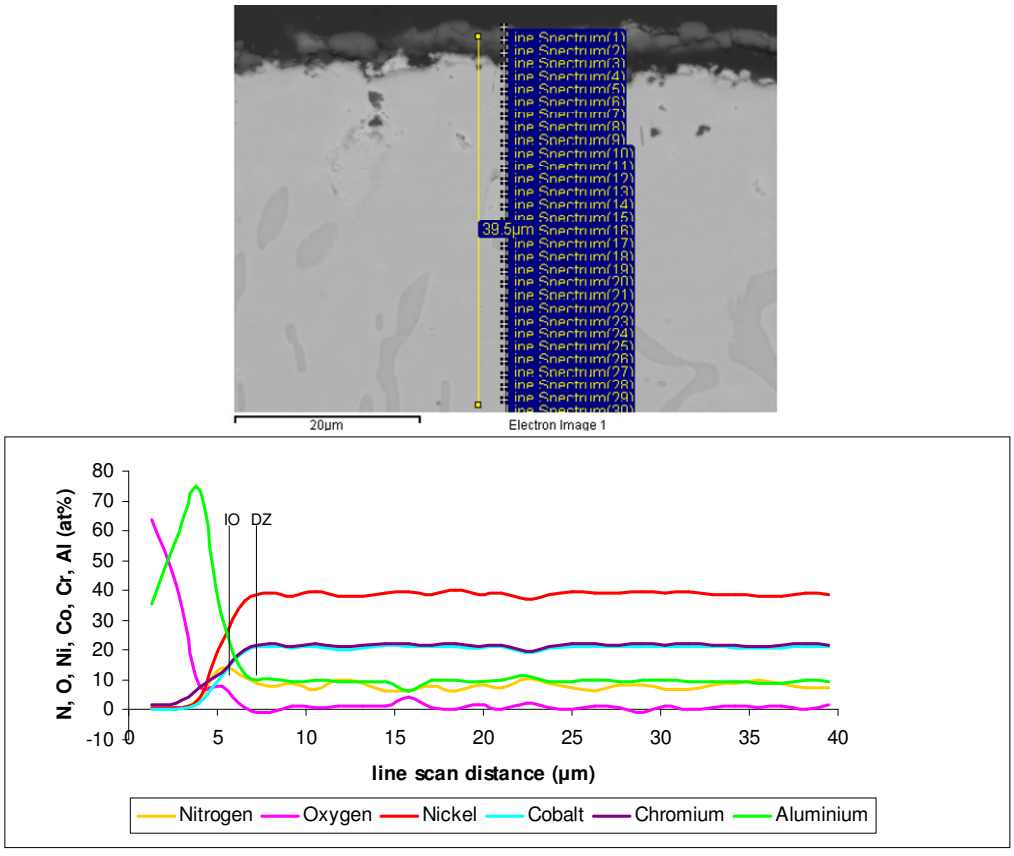

Figure 5.11 BSE image of cross section showing the distributions (by WDS data) of Ni, Co, Cr and Al as a function of distance from the surface. IO and DZ define the end of the internal oxidation and diffusion zone.

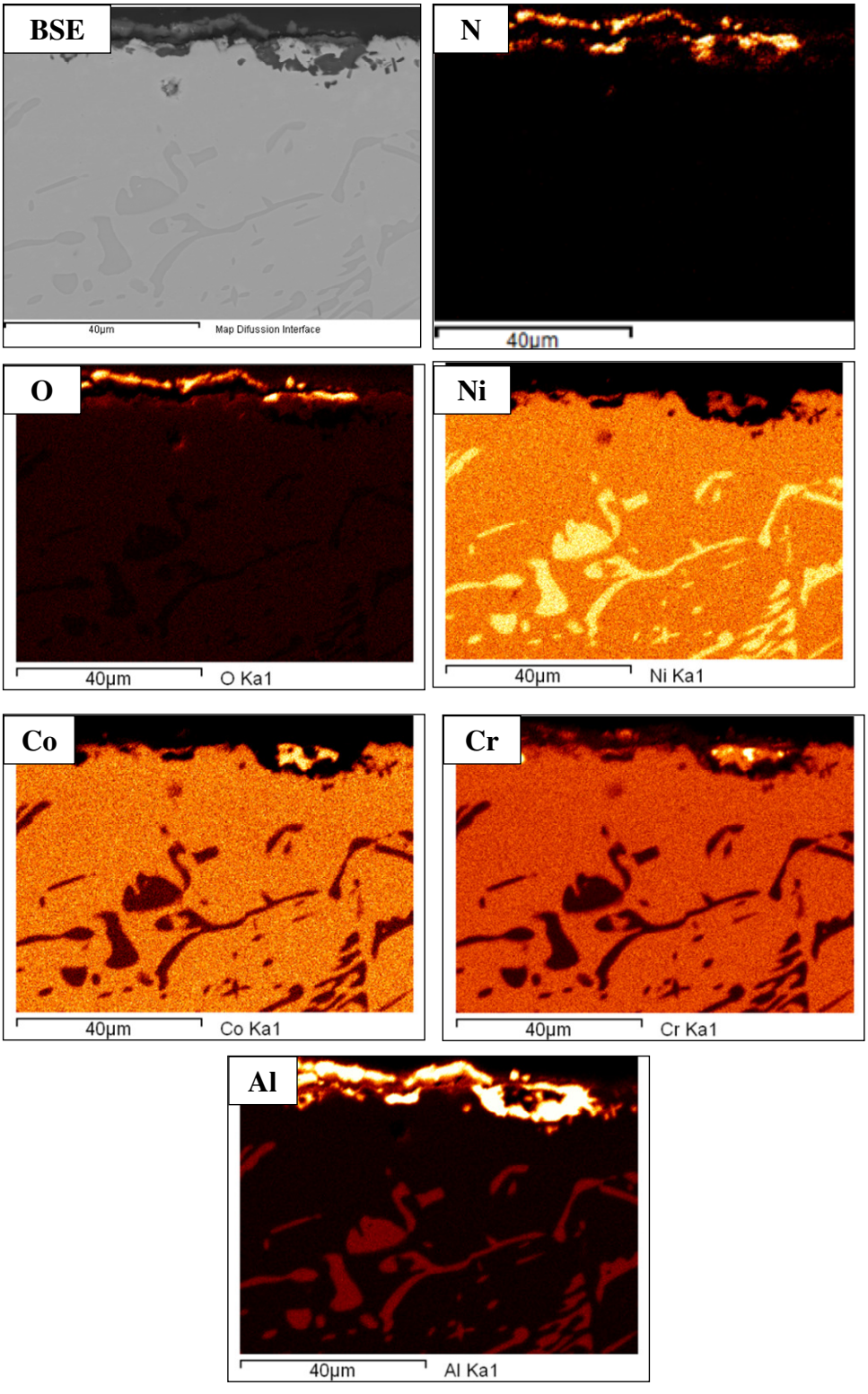

Figure 5.12 BSE image of cross section of the oxidised EK1 alloy with qualitative elemental maps of N, O, Ni, Co, Cr and Al.

X-ray maps of the cross section microstructure can be seen in Fig. 5.12 and 5.13. Both maps are from the same area, the former in qualitative and the latter quantitative. These figures show the surface to be rich in N, O and Al and support the XRD results for Al_2O_3 and AlN formation. Thickness of the former varies along the surface and in some parts of the scale Co and Cr rich areas are seen, suggesting that Cr rich oxide formed beneath the Al_2O_3. In the bulk the morphology of the β-NiAl is clear and in agreement with fig. 5.11.

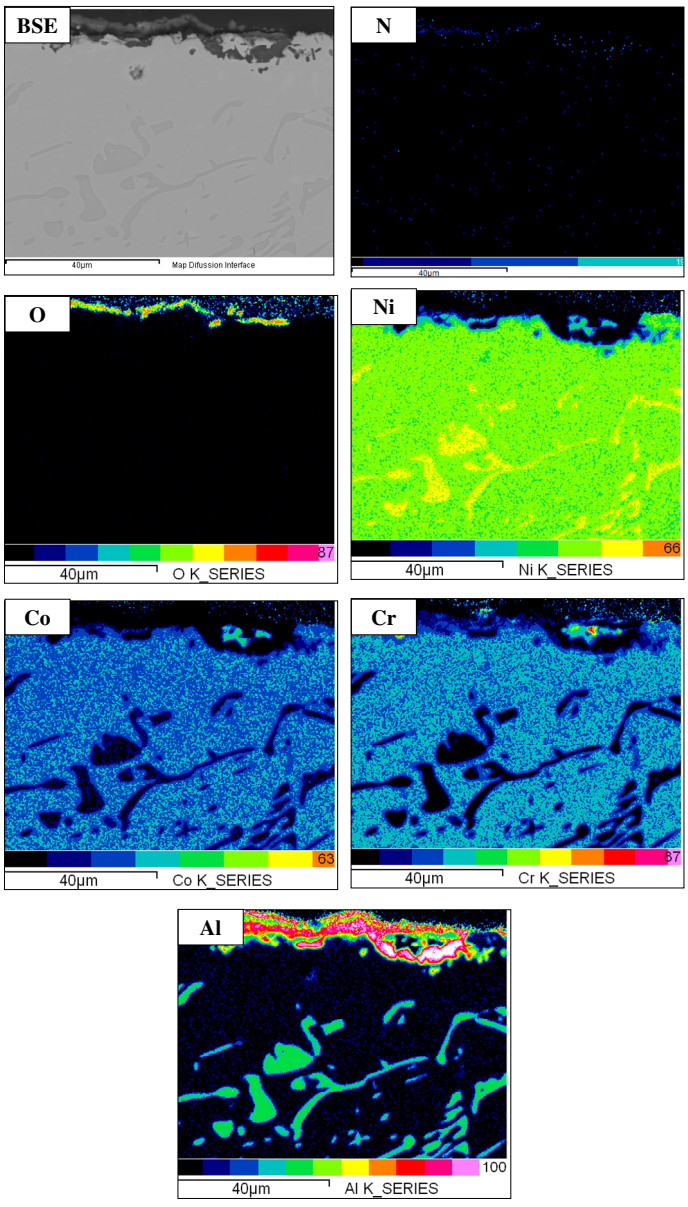

Figure 5.13 BSE image of a cross section of the oxidised EK1 alloy with quantitative elemental maps of N, O, Ni, Co, Cr and Al.

5.2.2.2 Ni-20.1Co-19.8Cr-16.2Al-1.1Ta (alloy EK2)

5.2.2.2.1 Microstructure and glancing angle XRD

The alloy EK2 had a more continuous oxide scale than the alloy EK1. The edges were well defined, see fig. 5.14. Figure 5.15 shows that were cracks and holes/voids in the scale. The latter were not observed in the oxidised alloy EK1.

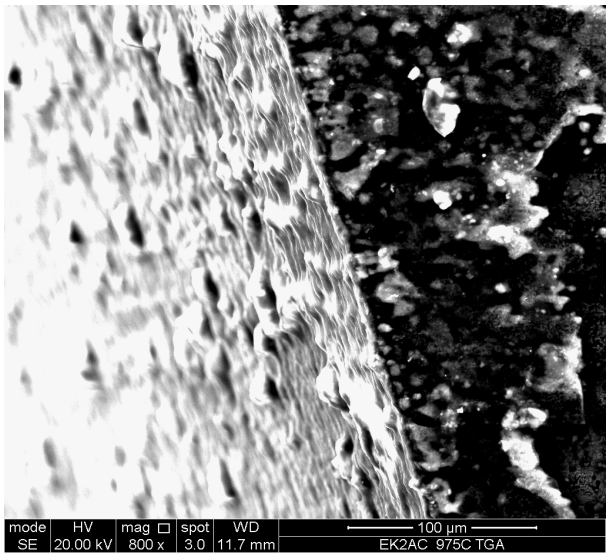

Figure 5.14 SEI image showing the edge of the alloy EK2 after oxidation at 975 ˚C for 100 hrs.

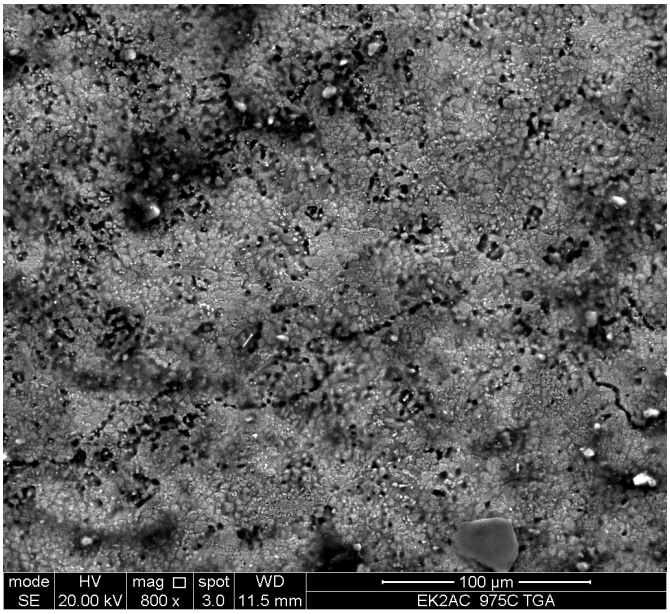

Figure 5.15 SEI image showing cracks and pores in the surface of the oxidised alloy EK2. The oxide scale exhibited a sponge like appearance.

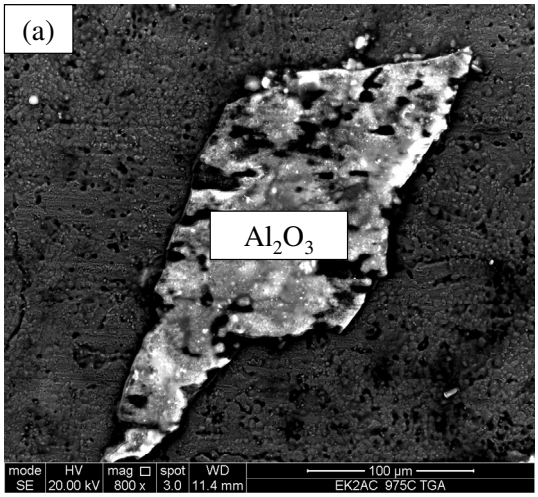

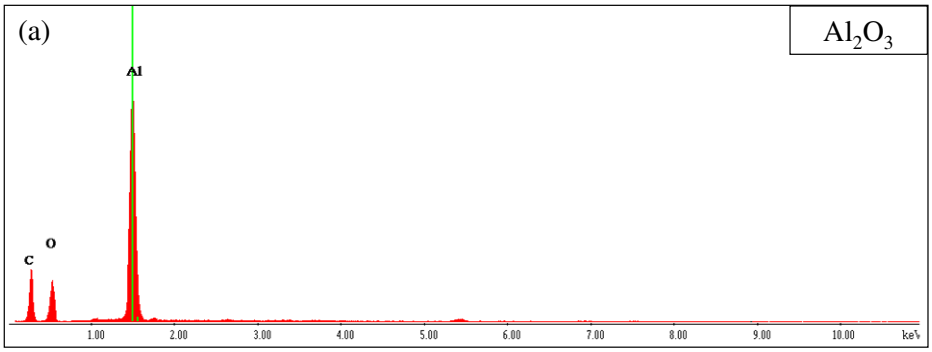

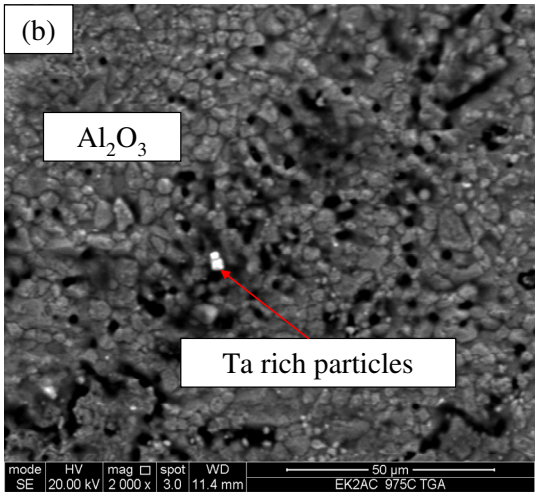

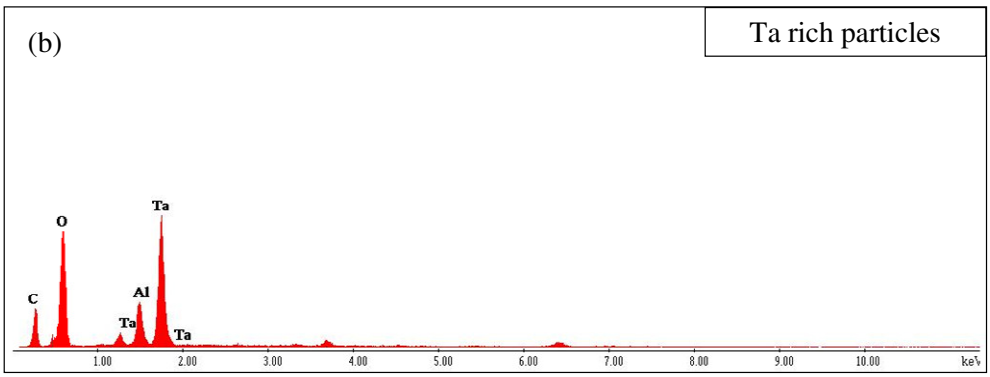

continued in the next page

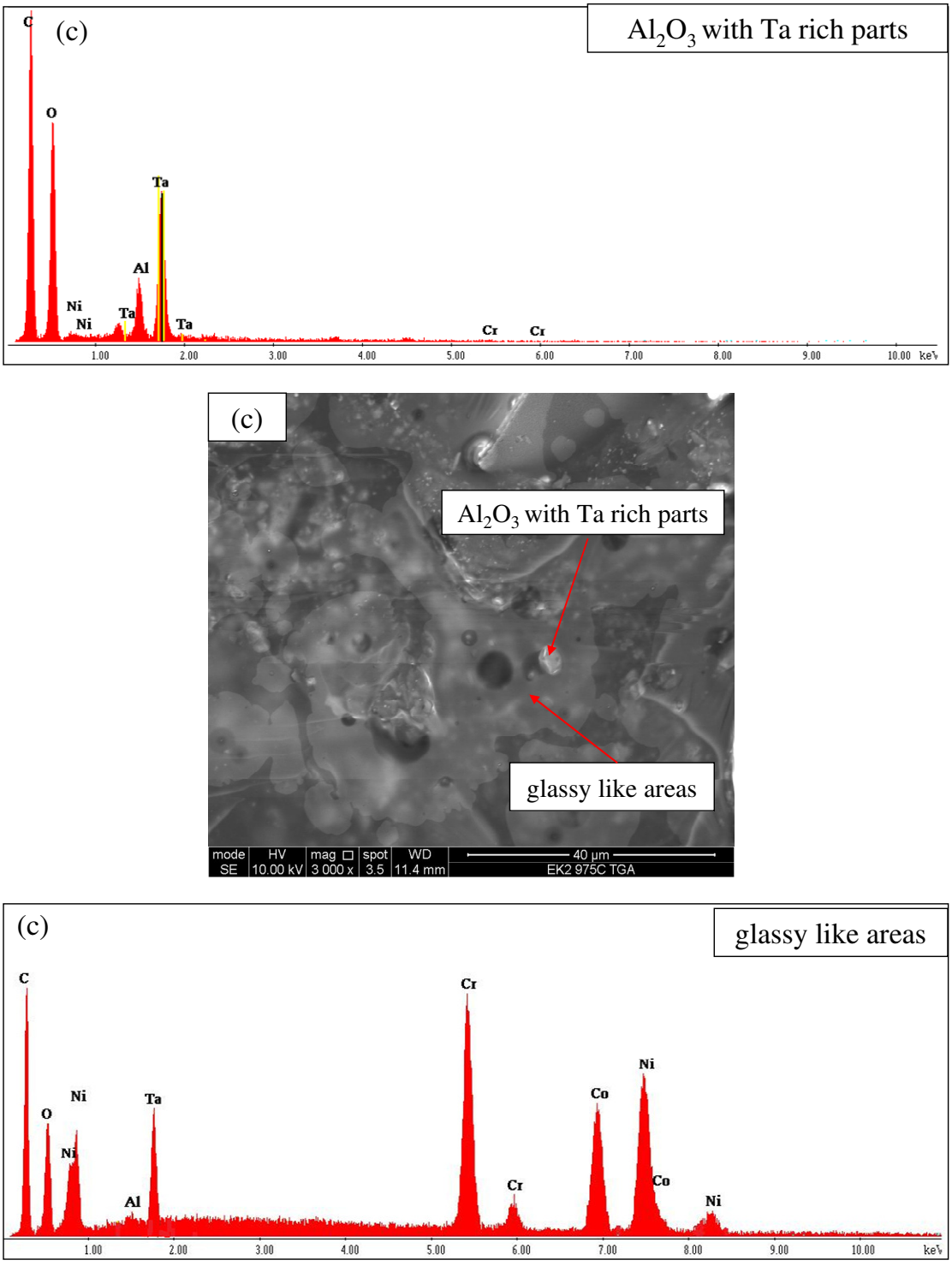

Figure 5.16 SEI images and EDS spectra showing (a) Al_2O_3 islands on the surface where some parts of the scale were rich in Ta (b) and (c) glassy like areas.

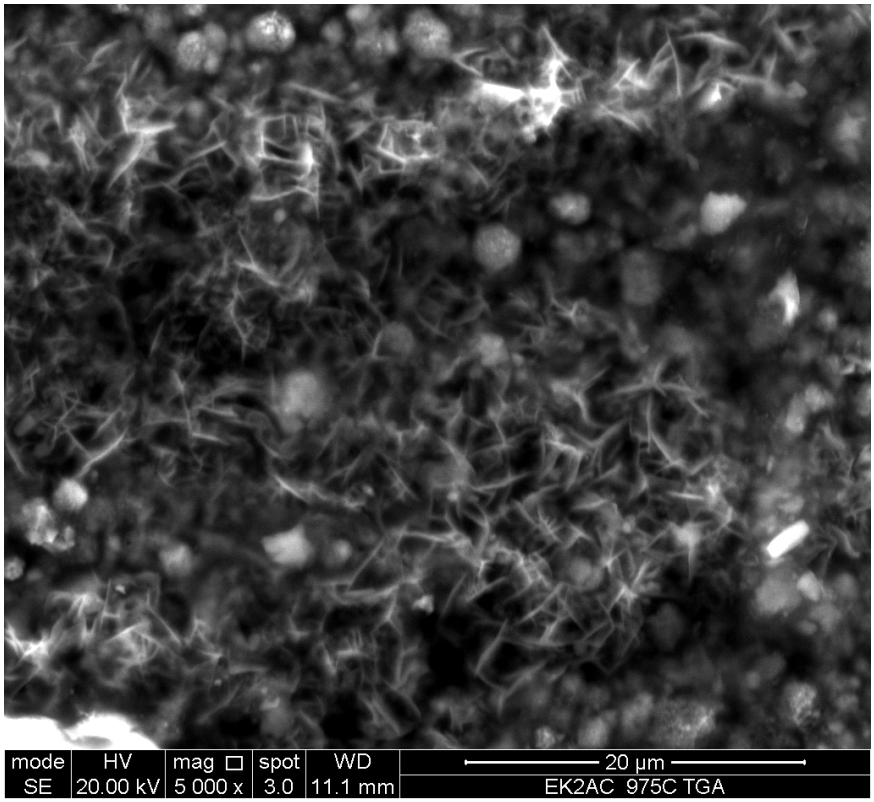

Figure 5.17 SEI image showing blade like whisker Al_2O_3 formation and bright Ta rich areas.

The majority of the oxide scale appeared like a sponge, (see figure 5.15) and there were large oxide patches covering parts of the surface of EK2, figure 5.16. The Al_2O_3 oxide patches had both fine and coarse structure. The oxide patches were larger in size compared with those formed on EK1. Another type of Al_2O_3 formed on the surface of the EK2 alloy looked more like blades and whiskers, as reported by Brumm and Grabke (1992), see figure 5.17 who attributed the different morphologies of Al_2O_3 formation to the transient aluminas forming in the scale. Tantalum was incorporated in the alumina scale and the Ta rich areas exhibited bright contrast, see figures 5.16 and 5.17.

The glancing-angle XRD data of the alloy EK2 before and after oxidation are shown in figures 5.18 and 5.19. In both figures X-ray peaks for the γ-Ni_{ss}, γ'-Ni_3Al and β-NiAl phases were observed. In fig. 5.19a as there are peaks that correspond only to γ-Al_2O_3, θ-Al_2O_3 and α-Al_2O_3, while peaks for Cr_2O_3 coincided with those of other phases. In fig. 5.23 (b) there are peaks that correspond only to θ-Al_2O_3 and α-Al_2O_3 and the peaks for γ-Al_2O_3 coincide with those for θ and α. Peaks for Cr_2O_3 coincided with those for other phases but there was a single peak of Cr_2O_3 at 2θ~53˚. The metastable γ-Al_2O_3 had the smallest number of peaks in the diffractograms, as was the case in the EK1 alloy.

Furthermore, some of the peaks could also correspond to AlN and Cr_2N with one peak corresponding only to the former for γ=2.5˚.

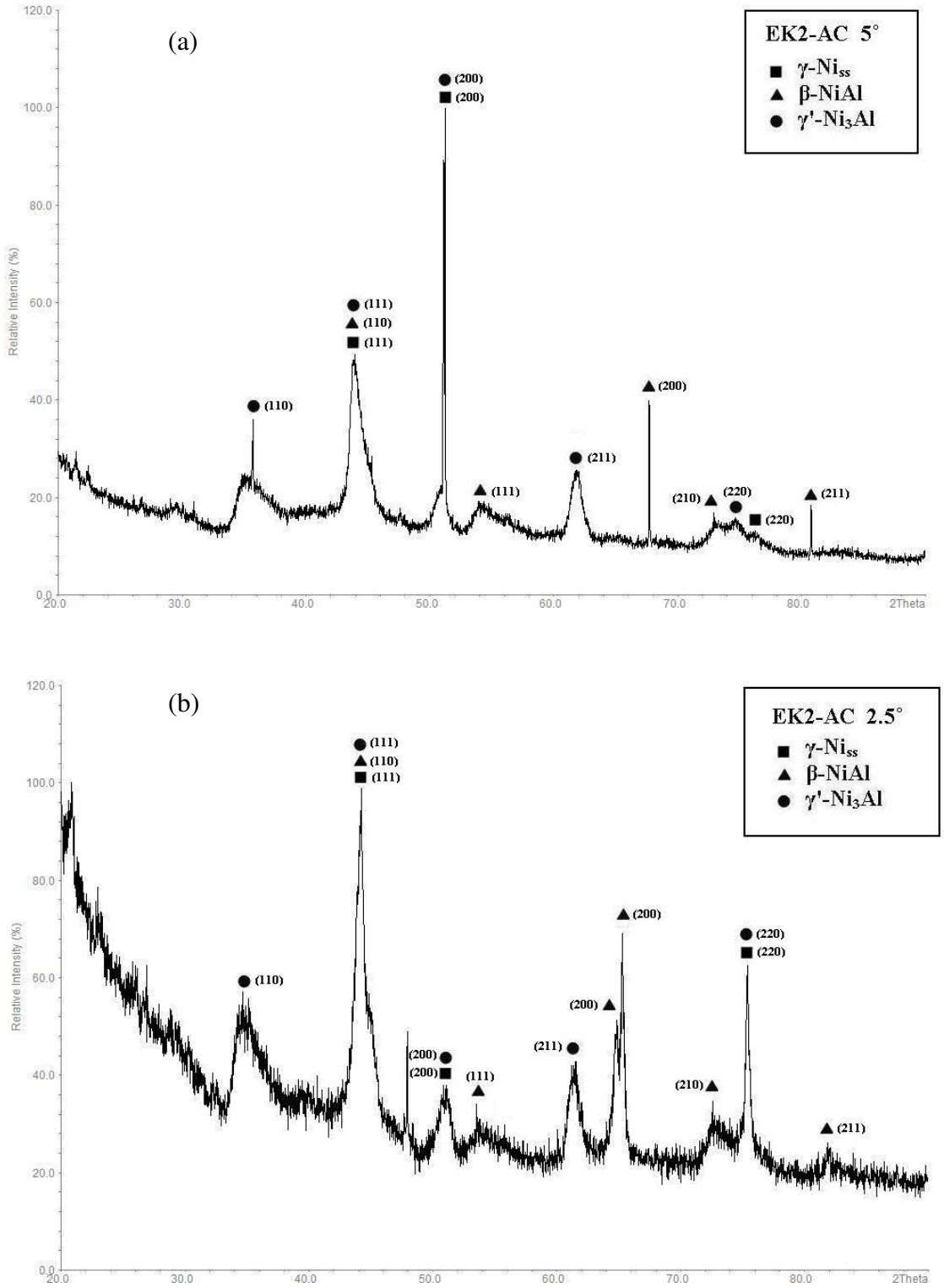

Figure 5.18 Glancing angle XRD data for the alloy EK2 before oxidation (a) γ= 2.5˚ and (b) γ= 5˚.

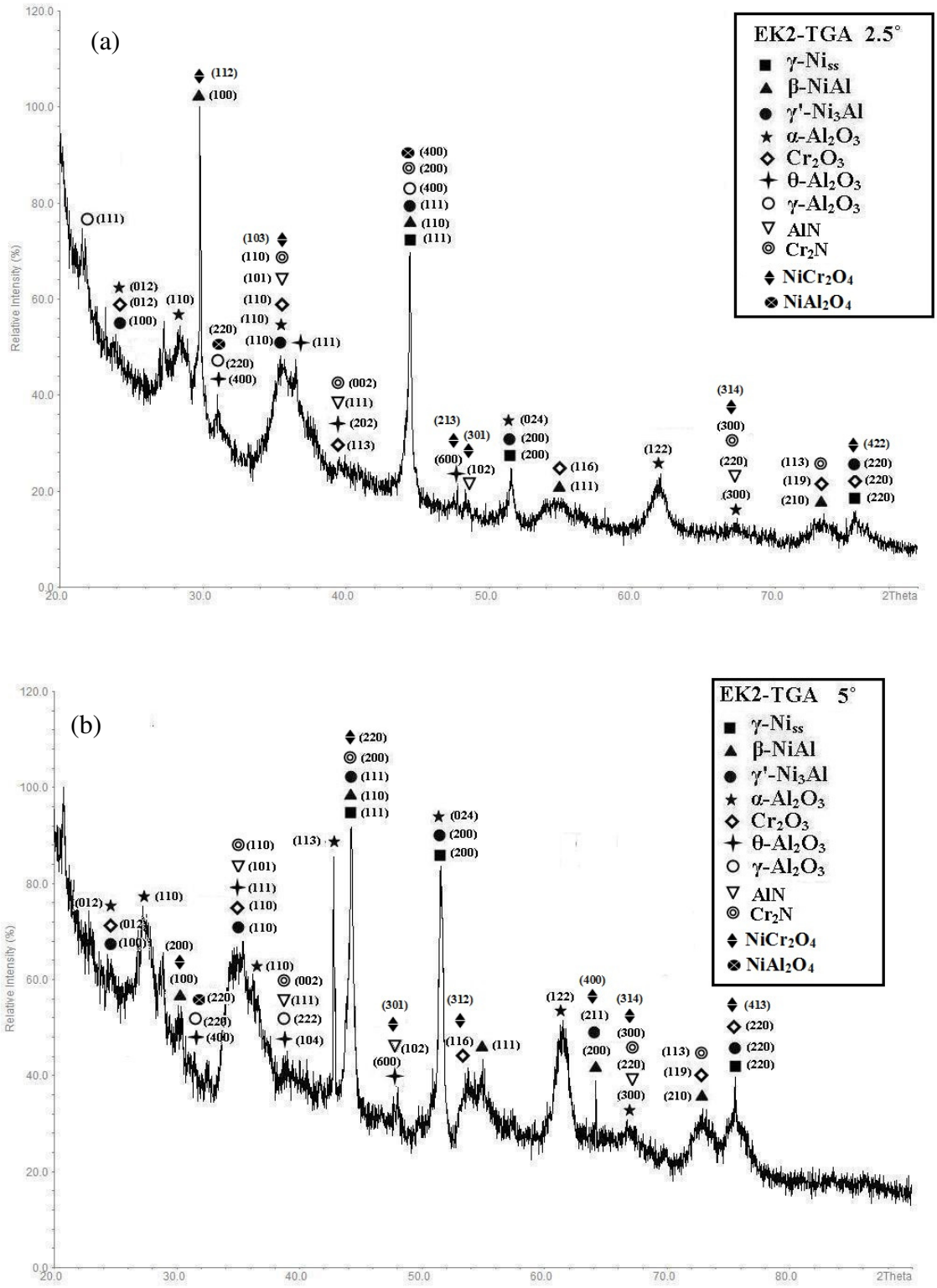

Figure 5.19 Glancing angle XRD data for the oxide scale formed on the alloy EK2 after oxidation for 100 hrs at 975 ˚C in air (a) γ= 2.5˚ and (b) γ= 5˚.

5.2.2.2.2 Microstructure of oxidised alloy

The microstructure of the oxidised alloy before the scale is shown in figure 5.20 and the WDS analysis results are summarised in Table 5.7.

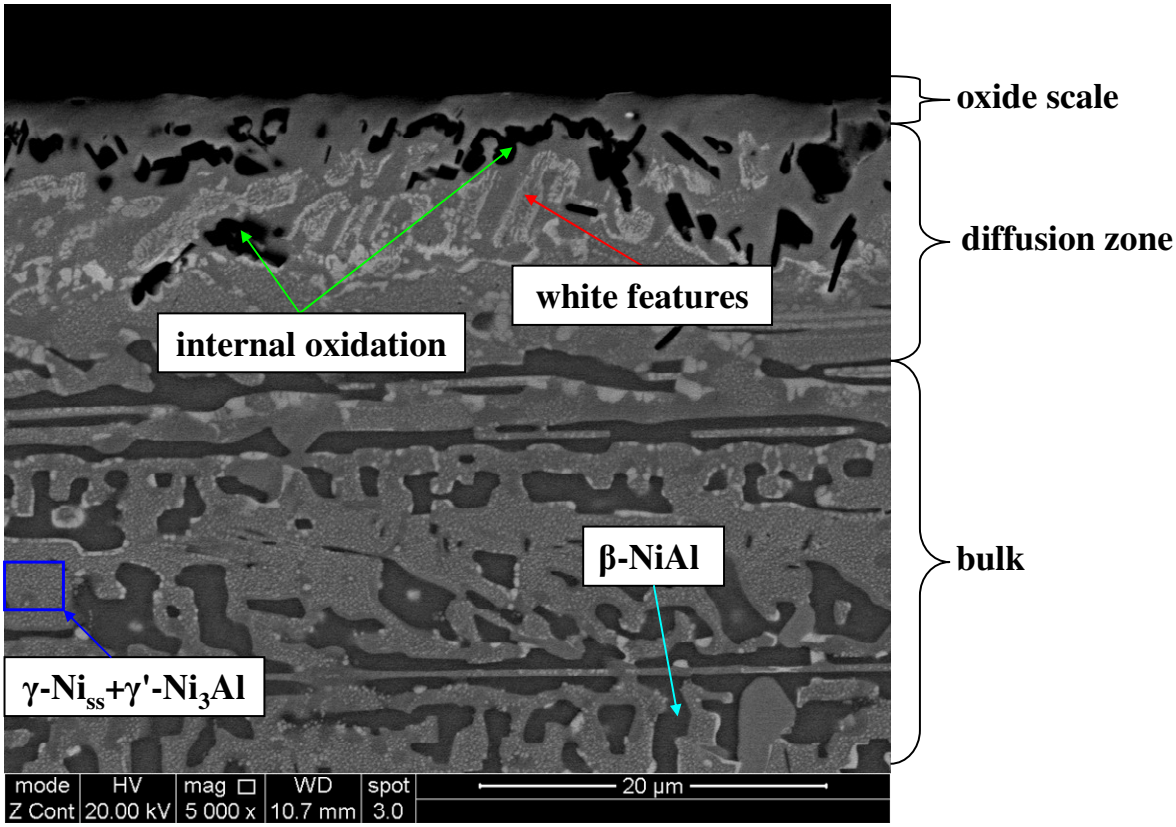

Figure 5.20 BSE image showing the microstructure of a cross section of the oxidised EK2 alloy.

After oxidation at 975 ˚C for 100 hrs the cross section of the EK2 alloy exhibited three different areas from the surface to the bulk. There was an oxide layer rich in O (43 at %) and Al (42.6 at %) and richer in Cr (13.2 at %) compared with the same layer in EK1, where the Cr content was 4.1 at %. WDS analysis of different areas in the oxide scale identified areas rich in O (36.4 at %) and Cr content (57.9 at %) with 4.4 at% Al. This data support Al_2O_3 and Cr_2O_3 formation (see fig. 5.21), as suggested by XRD (see fig. 5.19b) and EDS (figure 5.22). Beneath the oxide scale the evidence for internal oxidation was much stronger than in EK1 alloy. The internal oxidation features were coarser compared with EK1, with lower N content (12.5 at % compared with 37.3 at % in EK1) higher Cr content (12.7 at % compared with 5.5 at % in EK1) and slightly higher Al content (53.5 at % instead of 43.3 at %). A diffusion zone was also formed as was the case in EK1, but in

the EK2 there were some white features in this zone. In the lower part of the diffusion zone the N content was slightly lower than in EK1 (5.3 at % compared with 7.4 at %), the Ni content was 34 at % was lower than that in EK1 (39 at %), the Co content had slightly increased (24.8 at % compared with 20.9 at %) and finally the Cr content was 33.4 at %. WDS analysis of the white features in the upper part of the diffusion zone, showed that they were slightly richer in Ni (40.7 at %) than the overall diffusion zone, poorer in Co and Cr content (21.5 at % and 25.6 at % respectively) and with 5 at % Al and 1.1 at % of Ta.

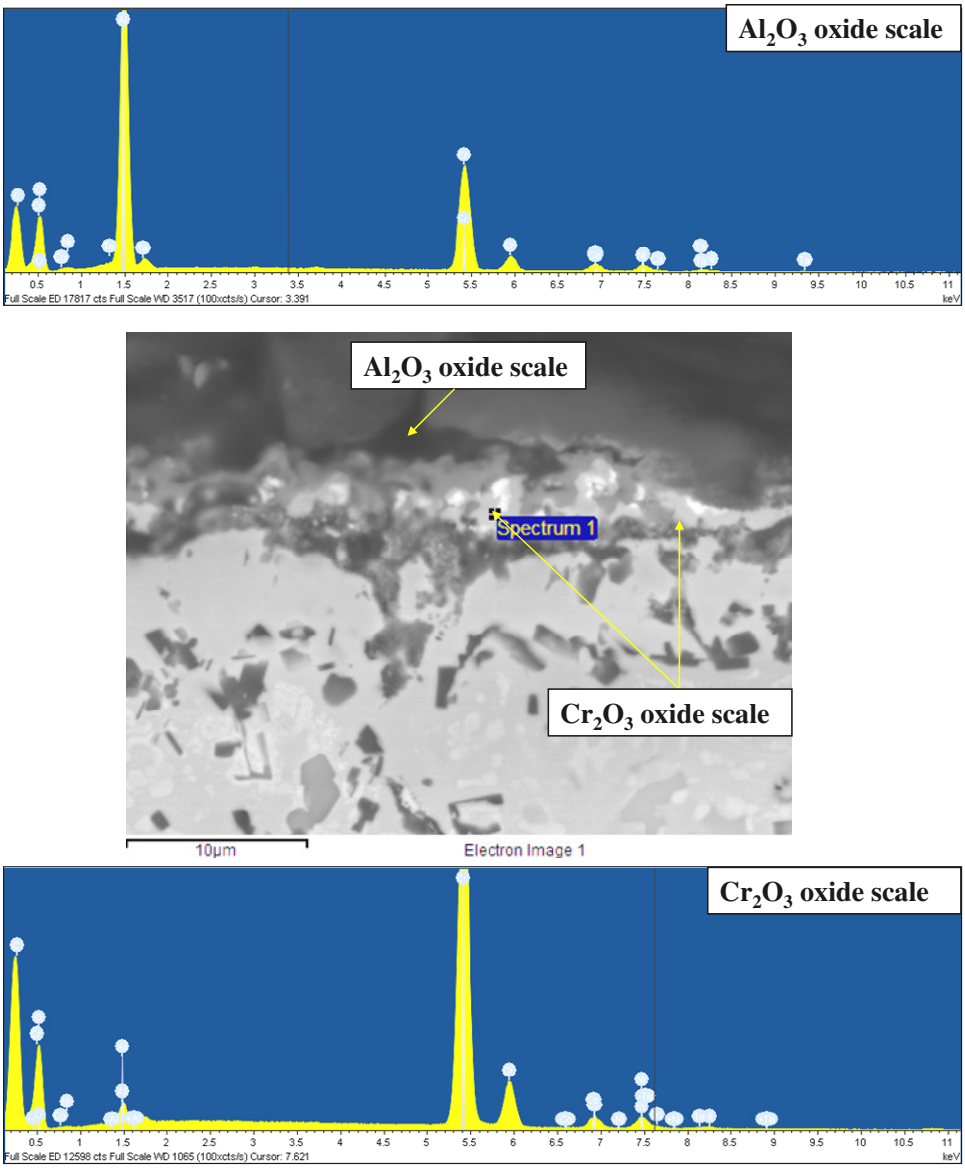

Figure 5.21 BSE image and EDS spectra showing Al_2O_3 and Cr_2O_3 oxides in the scale of EK2.

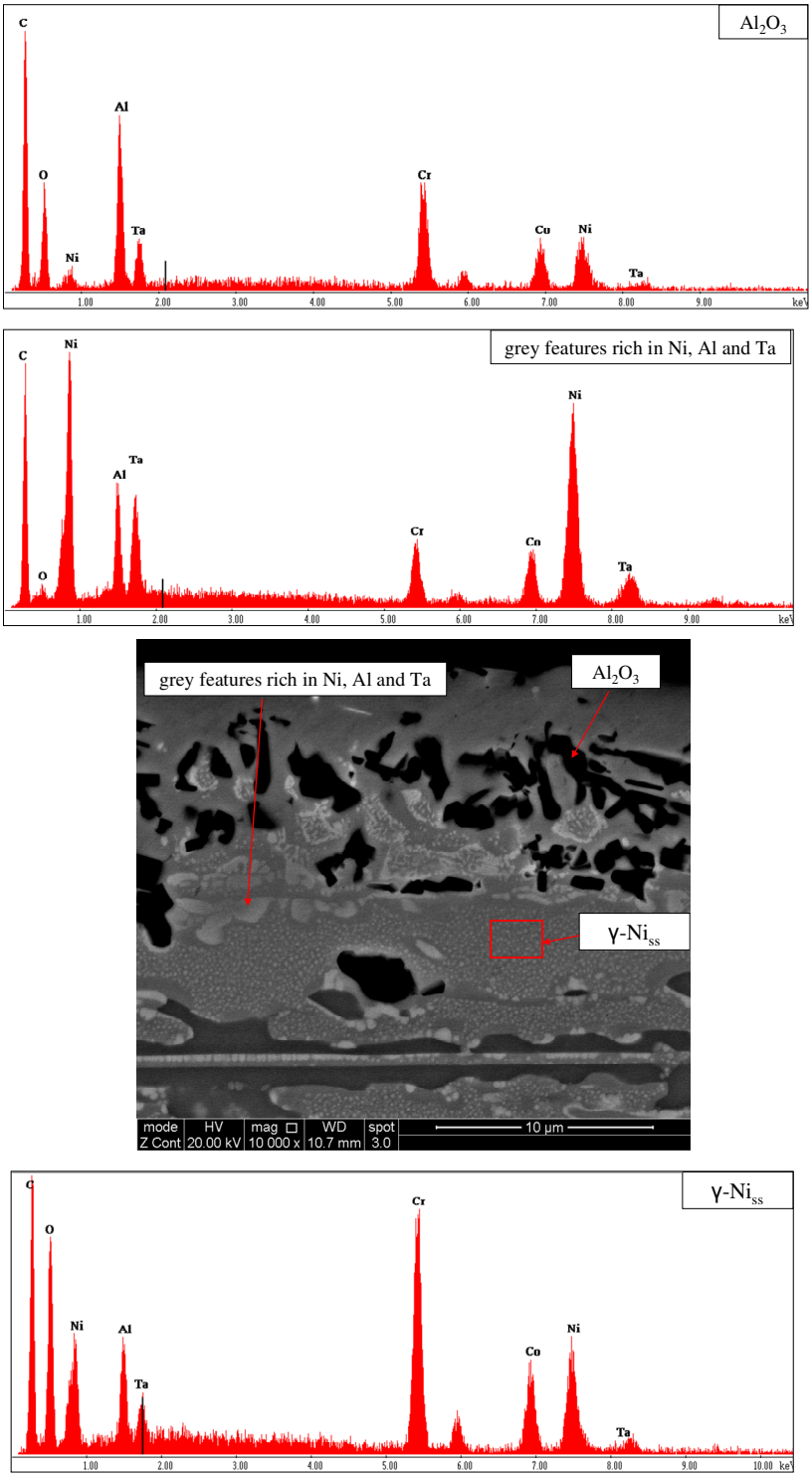

Figure 5.22 SE image and EDS spectra taken near the oxide scale suggesting the presence of γ-Ni_{ss} in between the black contrast Al_2O_3 areas and the grey features that were rich in Ni, Al and Ta.

The presence of γ-Ni_{ss}, γ'-Ni_3Al and β-NiAl that was suggested by the XRD data (fig. 5.19) was confirmed by the WDS analysis, see Table 5.7. In the oxidised EK2 alloy,

precipitation of γ'-Ni_3Al in γ-Ni_{ss} was seen as fine white precipitates of sub-micron size (see fig. 5.23). This was not observed in the oxidised EK1 alloy. The composition of γ-Ni_{ss} + γ'-Ni_3Al was similar to that of the γ-Ni_{ss} in EK1. The β-NiAl intermetallic was coarser in the bulk of EK2 compared with the EK1 alloy, and was poorer in Ni (42.3 at % and 46.1 at % respectively) and Al (31 at % and 32.6 at % respectively) and richer in Co and Cr. In the bulk of some of the NiAl intermetallics some bright precipitates had formed (fig. 5.23) which were richer in N (11.2 at %) and lower in Cr (7.4 at %) and Al (21.5 at %) contents than the plain β-NiAl, see Table 5.7. Further quantitative analysis of the bulk of the oxidised alloy EK2 revealed formation of two new phases, namely the σ-phase and a bright phase, see figs 5.23 and 5.24. The σ-phase was rich in Ni and Co (13.3 at % and 25.3 at %, respectively) and very rich in Cr (57.4 at %), see Table 5.7.

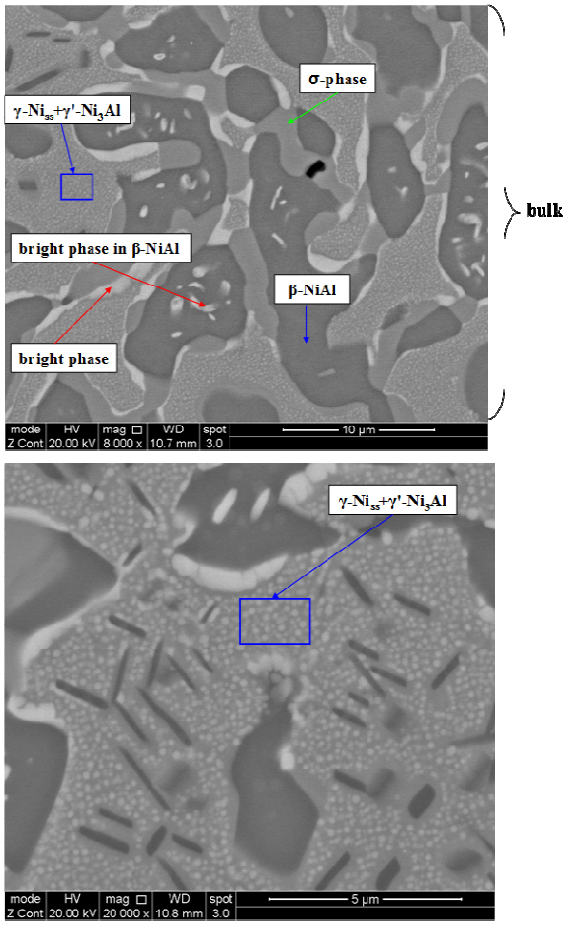

Figure 5.23 BSE images taken of the bulk microstructure of the oxidised EK2 alloy.

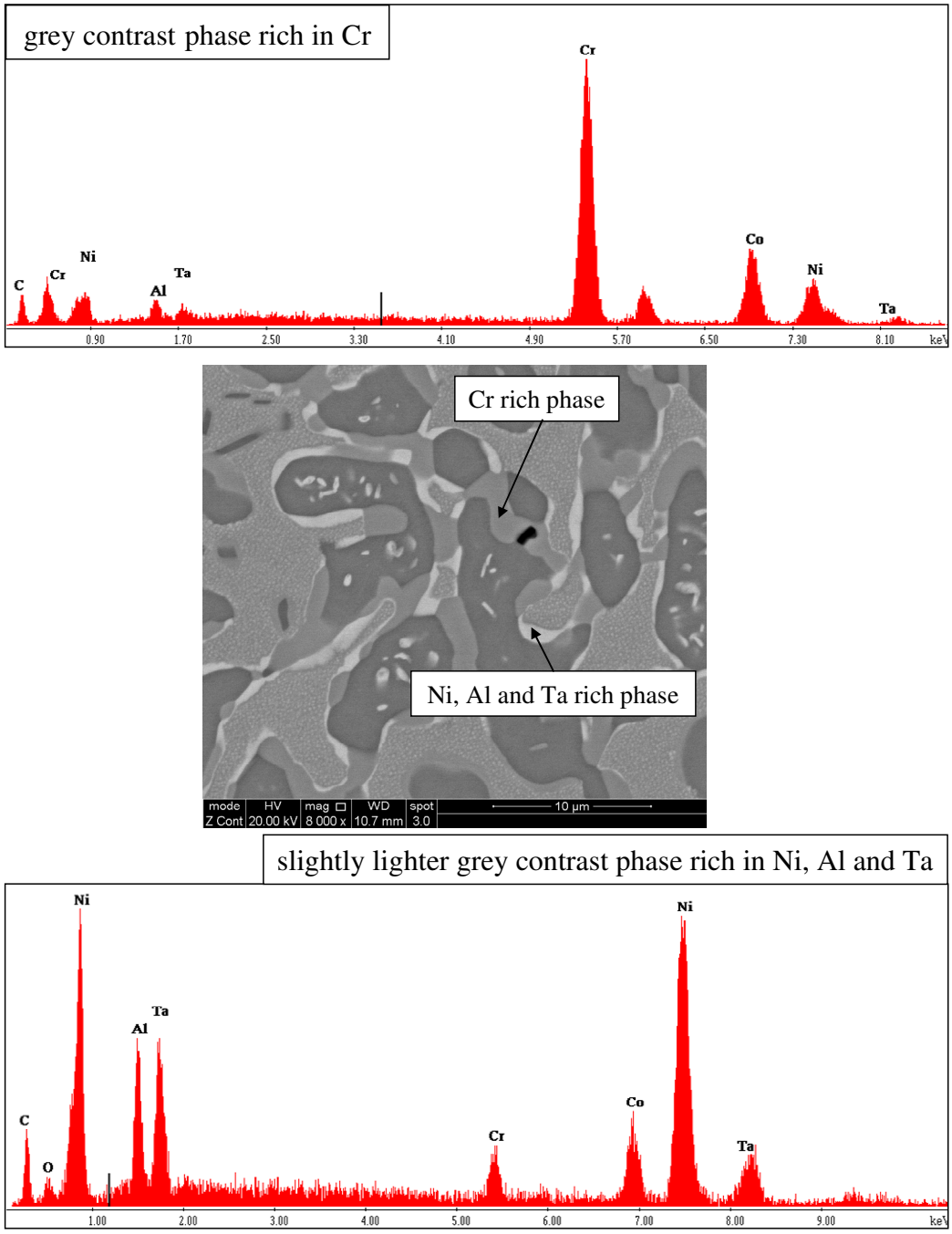

Figure 5.24 BSE image and EDS spectra of the bulk microstructure showing a Cr rich phase with grey contrast and a Ni, Al and Ta rich phase exhibiting slightly lighter grey contrast.

Table 5.7 WDS analysis data (at %) of different parts of the cross section of the EK2 alloy after oxidation at 975 ˚C for 100 hrs.

Area	N	O	Ni	Co	Cr	Al	Ta
oxide scale (Al_2O_3)	0	43.8±4.8	1.5±0.7	1.4±0.5	13.2±3	42.6±2.9	0.6±0.3
oxide scale (Cr_2O_3)	0	36.4±9.4	3.2±1.9	2.9±1.8	57.9±2.7	4.4±5.2	0.4±0.2
internal oxidation	12.5±5	0.7±0.7	11.3±2.9	9±1.7	12.7±2.3	53.5±4.8	0.3±0.1
diffusion zone	5.3±1.5	0.8±0.6	34±1.4	24.8±0.6	33.4±0.6	0.7±0.1	0.7±0.1
white features in upper bulk of diffusion zone	5.1±0.8	0.8±0.3	40.7±0.5	21.5±0.9	25.6±0.9	5±0.3	1.1±0.1
grey features in upper bulk of diffusion zone	6.3±1.2	0.8±0.2	49.9±5	11±1.2	7.3±1.1	22.3±8	2.2±2.1
β-NiAl	6.1±1.7	0.7±0.5	42.3±2.1	10.2±0.7	9.2±3.3	31±1	0.3±0.06
$\gamma Ni_{ss}+\gamma' Ni_3Al$	6.3±0.8	0.5±0.6	35.7±1.8	22.8±0.9	24.6±1.5	8.5±0.5	1.7±0.5
σ-phase	1.1±0.8	0.8±0.3	13.3±2.2	25.3±0.4	57.4±1.9	1.4±0.2	0.6±0.1
bright phase in β-NiAl	11.2	0.2	43.8	12.6	7.4	21.5	3.2
bright phase (fig. 5.27)	7.2	0.9	31.4	16.1	24.9	16.6	2.9

The distribution of elements as a function of distance along a line from the surface in a cross section of EK2 alloy that was obtained by WDS is shown in fig. 5.25. The surface was very rich in Cr and around 5 µm below the surface, where there was internal oxidation there was a high Al content and the Ni, Co and Cr contents were decreased. The N and O contents did not change along the line scan and the O content was below 1.5 at%. As the line scan moved in the bulk it met the Ni solid solution and the Ni, Co and Cr contents increased and then at around 21, 23 and 28 µm below the surface the scan crossed NiAl intermetallics and the Ni and Al contents increased.

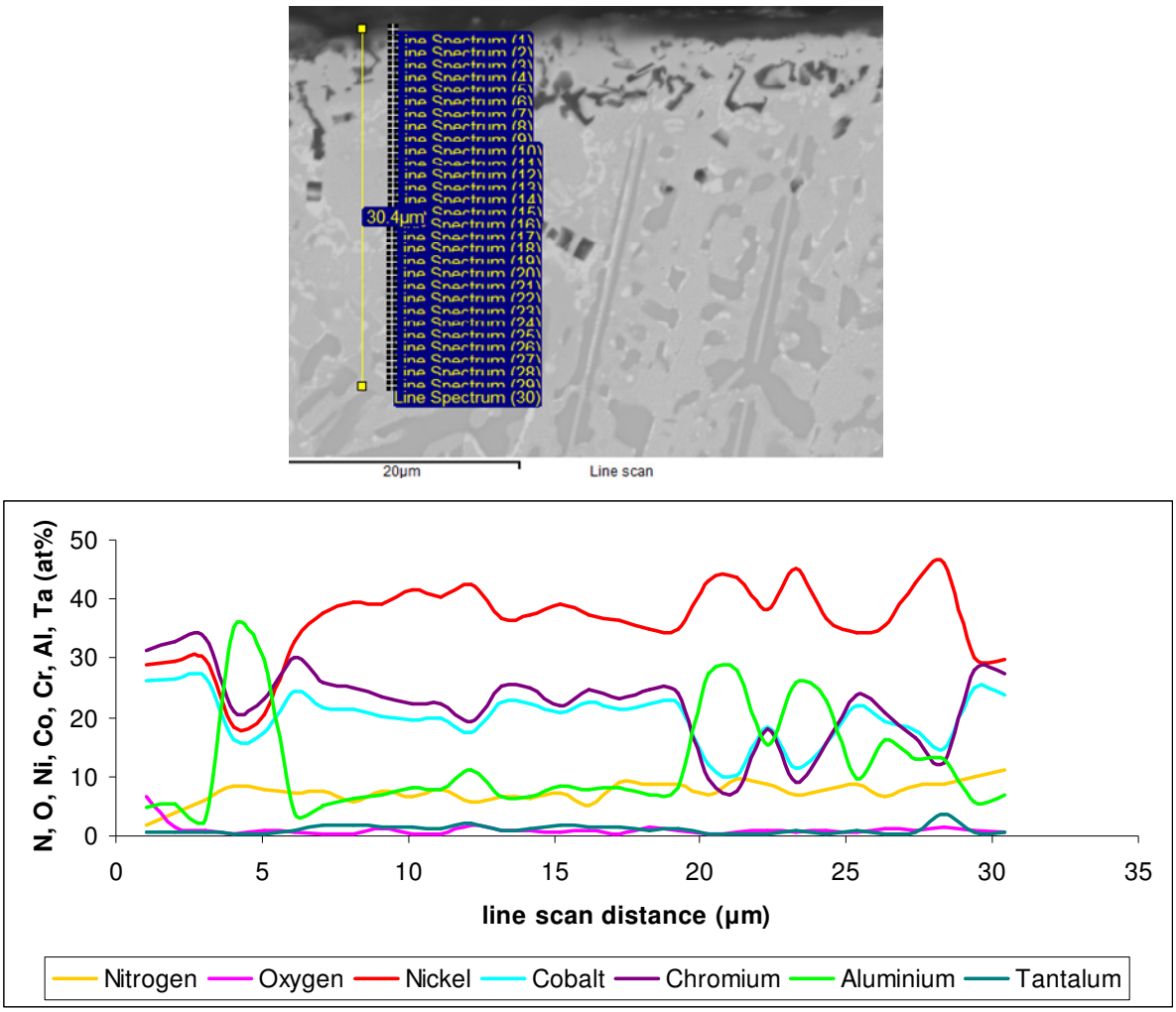

Figure 5.25 BSE image of cross section showing distributions (detected by WDS) of Ni, Co, Cr, Al and Ta as a function of distance from the surface.

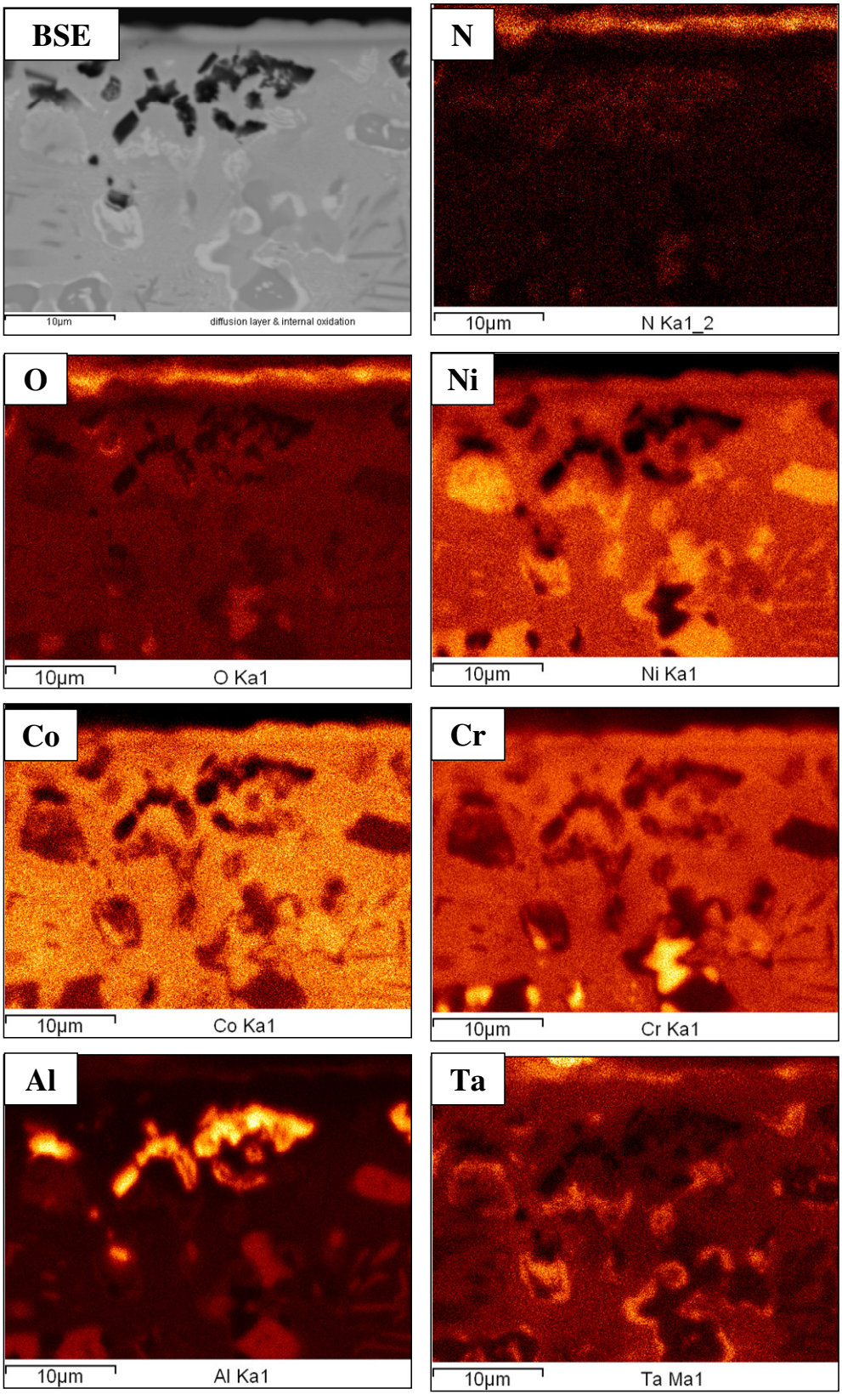

Figure 5.26 BSE image taken from the oxide scale and going towards the bulk of EK2-TGA alloy followed by qualitative elemental maps of N, O, Ni, Co, Cr, Al and Ta.

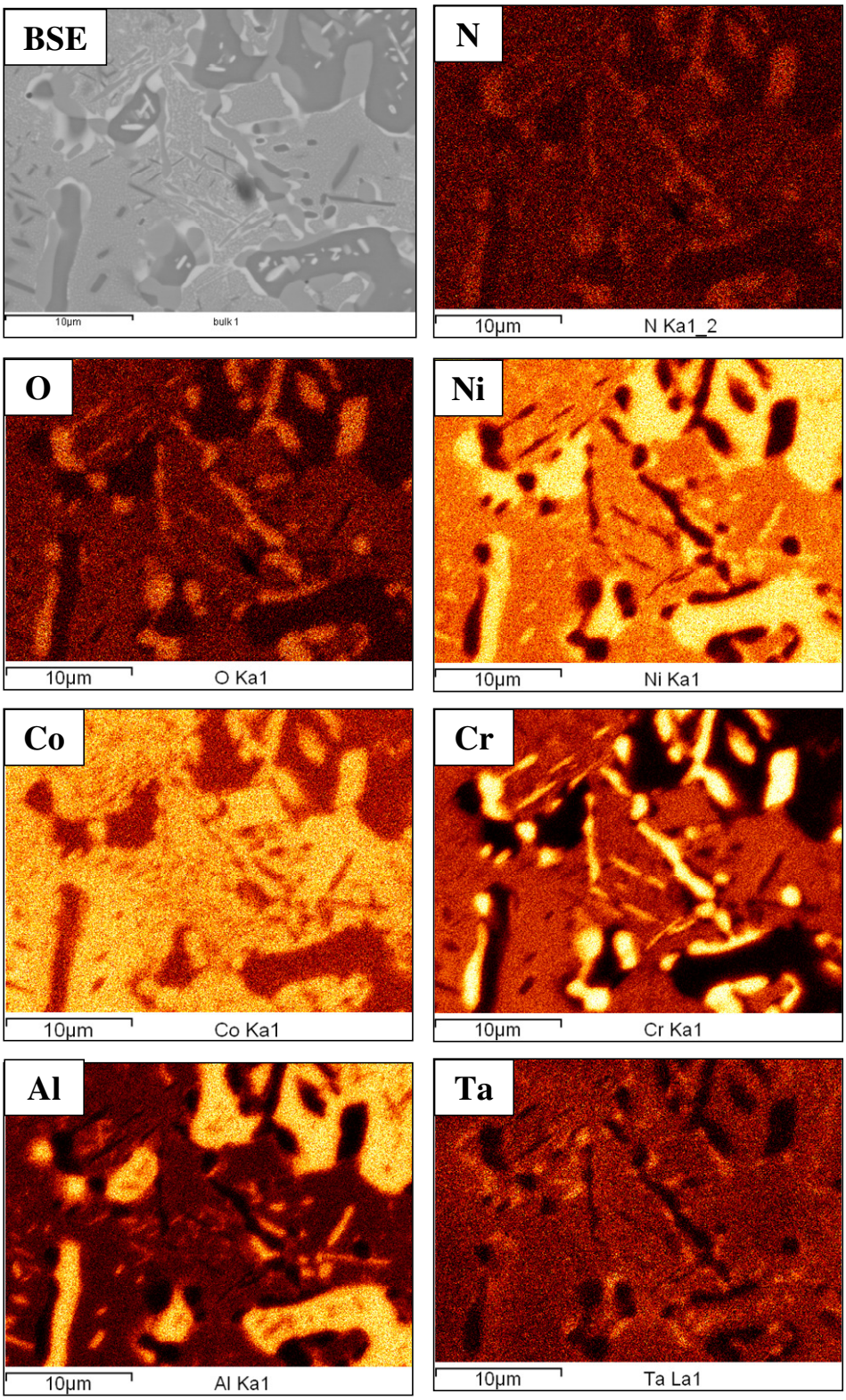

Figure 5.27 BSE image taken from the bulk of EK2-TGA alloy followed by qualitative elemental maps of N, O, Ni, Co, Cr, Al and Ta.

Qualitative X-ray maps from the near surface area and the bulk can be seen in fig. 5.26 and 5.27 and figure 5.26 shows the presence of N, O, Al and Ta in the oxide scale and white features in the diffusion zone. The Cr maps confirm the Cr content in the σ-phase. The Ta maps showed that the highest Ta content was associated with the white phases formed in the bulk and in the diffusion zone. The N and O maps showed the presence of these elements in the σ-phase.

Quantitative maps for Ni and Cr are shown in fig. 5.28. The Ni map confirmed that the white features below the oxide scale were Ni rich. The Cr map revealed highest Cr concentration in the σ-phase which had grown around the β-NiAl phase and that small white precipitates inside the intermetallics grains were Cr rich. The microstructure below the scale was richer in Cr compared with the bulk.

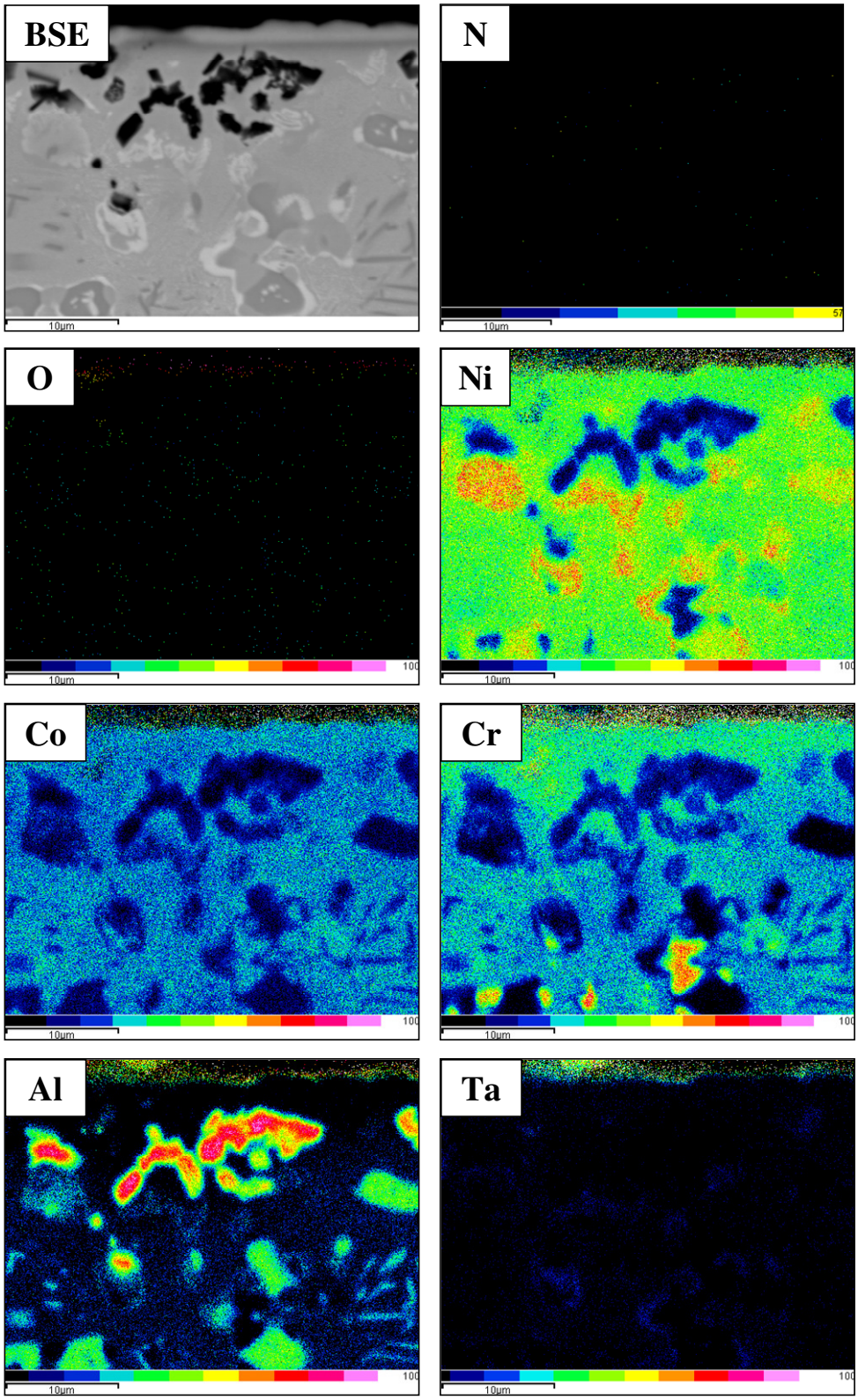

Figure 5.28 BSE image taken from the oxide scale and going towards the bulk of EK2-TGA alloy followed by quantitative elemental maps of N, O, Ni, Co, Cr, Al and Ta.

5.2.2.3 Ni-20.1Co-19.8Cr-16.2Al-1.1Ta-0.3Y (alloy EK3)

5.2.2.3.1 Microstructure and glancing angle XRD

The EK3 alloy surface had a slightly more uniform coverage by oxides compared with EK2. The edges were well defined, as was the case for the alloys EK1 and EK2. The scale seemed to be denser and no cracks were visible. Some large oxide growths were present (fig. 5.29) that were denser and bulkier than those formed on the EK1 and EK2 alloys and the rest of the scale was more uniformly spread on the whole surface.

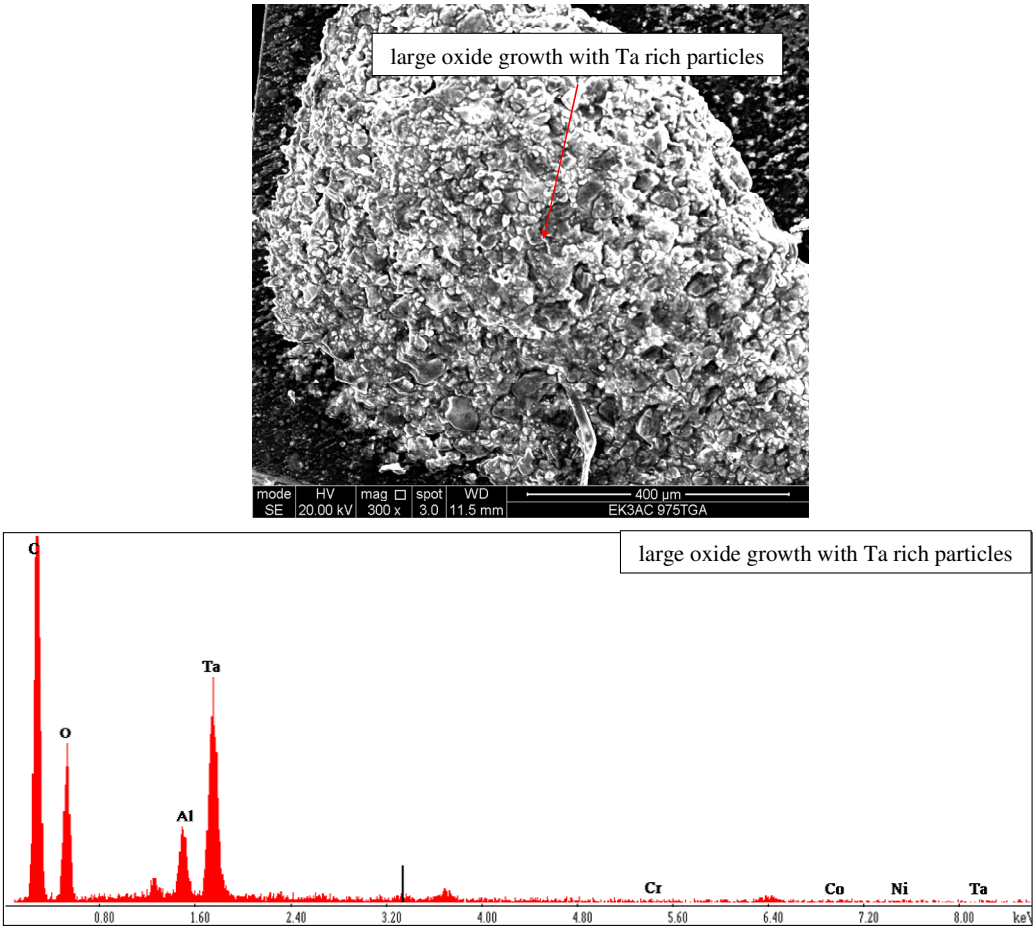

Figure 5.29 SEI image and EDS spectrum showing large oxide growth with Ta rich particles.

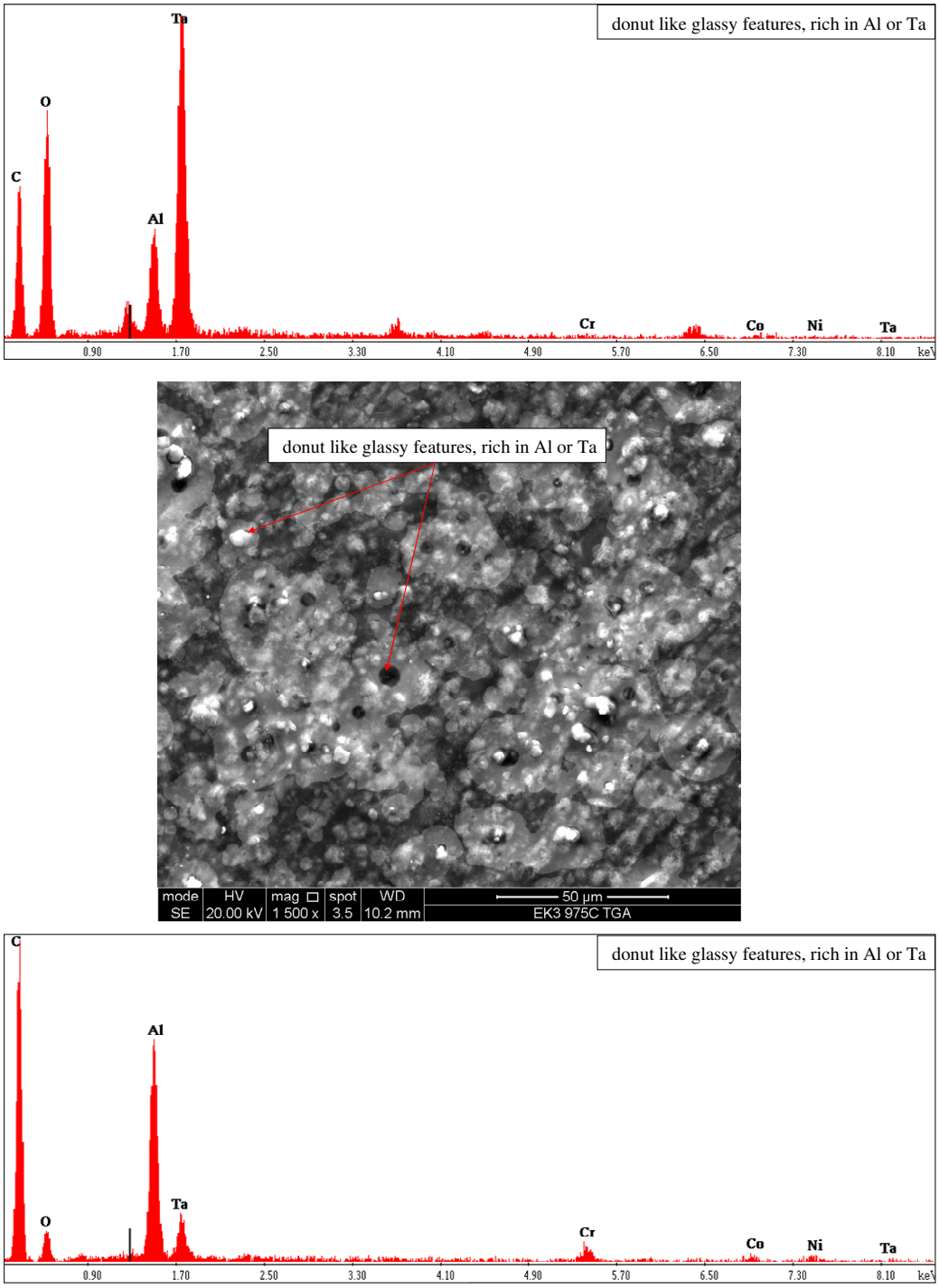

Figure 5.30 SEI image and EDS spectra showing glassy like features in the scale. The donut like glassy features were Al or Ta rich.

Glassy like features similar to the ones observed in EK2 were also formed on the EK3 alloy (fig. 5.30). The large growths and the glassy features had areas that were rich in Al or Ta. Other parts of the scale are shown in figs 5.31 and 5.32.

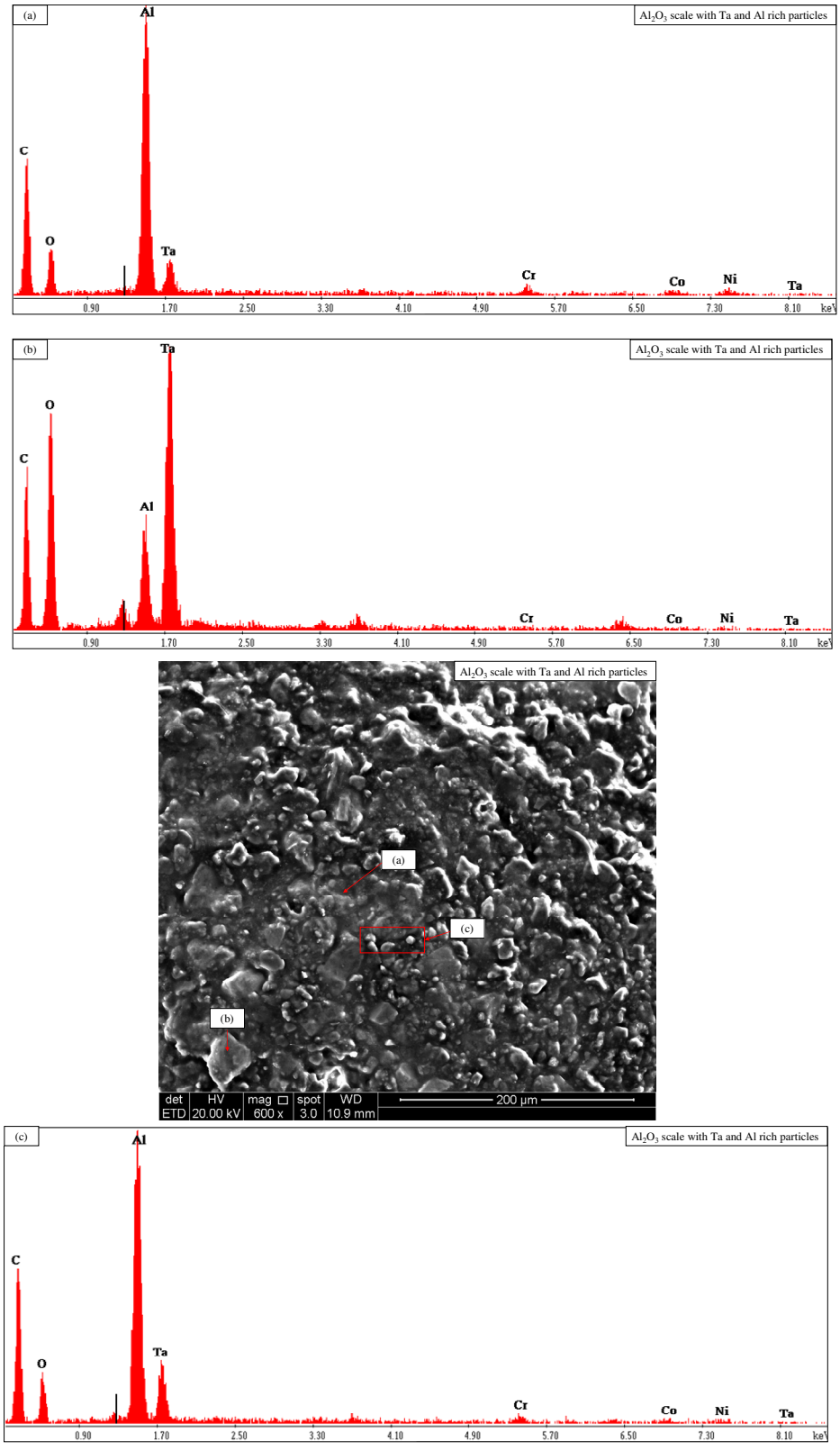

Figure 5.31 SEI image and EDS spectra showing Al_2O_3 scale with Ta and Al rich particles.

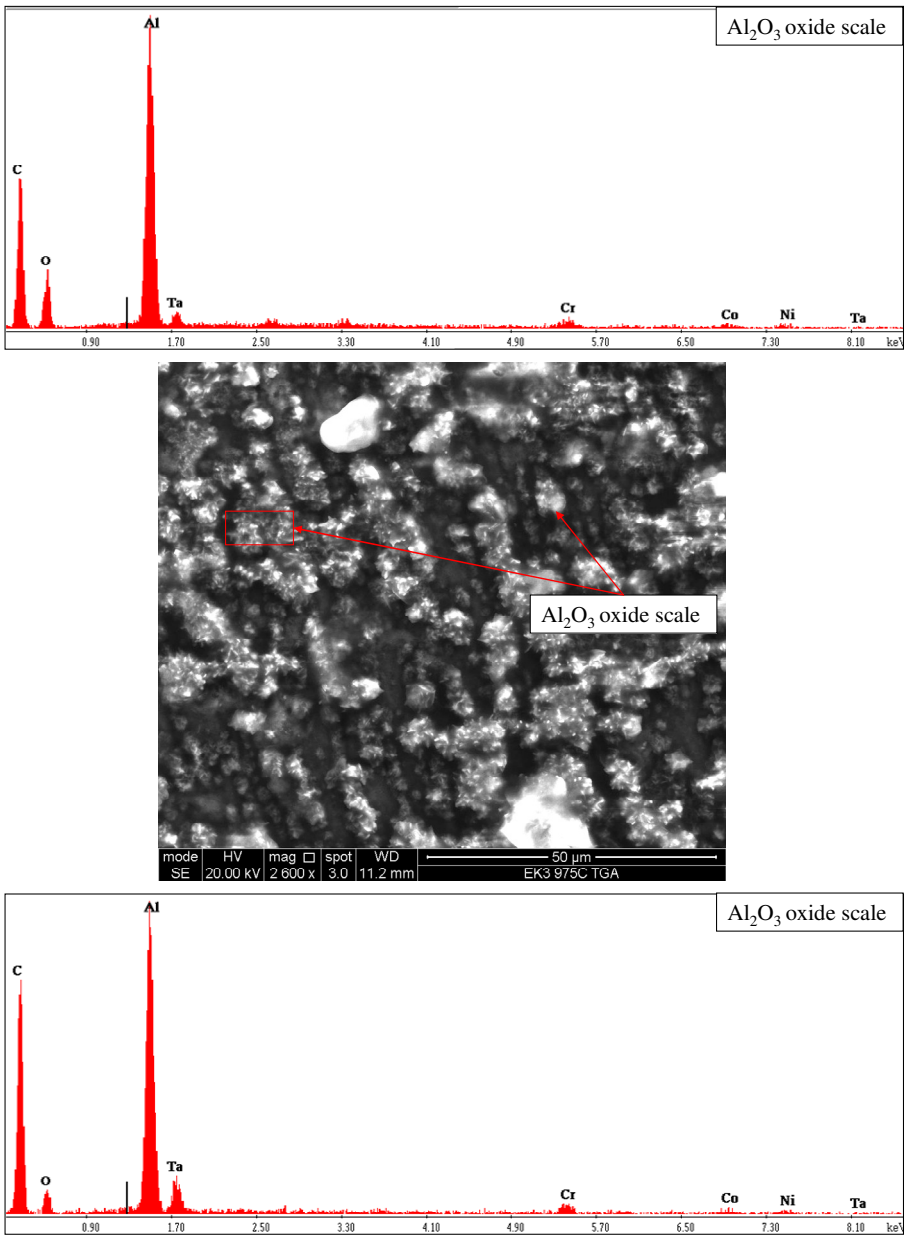

Figure 5.32 SEI image and EDS spectra showing Al_2O_3 oxide scale.

The glancing-angle XRD data of the EK3 alloy before and after oxidation is shown in figures 5.33 and 5.34. X-ray peaks for the γ-Ni_{ss}, γ'-Ni_3Al and β-NiAl peaks were identified in both glancing angles. In the lower glancing-angle, see figure 5.34 a there were peaks for α-Al_2O_3 and Cr_2O_3 and the peaks for θ-Al_2O_3 and γ-Al_2O_3 coincided with those of θ and α-Al_2O_3. In the higher glancing angle, see figure 5.34 b there were peaks for γ-Al_2O_3, α-Al_2O_3 and Cr_2O_3 and the peaks of θ-Al_2O_3 coincided with those of the other oxides. In both glancing angle peaks for AlN and Cr_2N coincides with those of the other oxides.

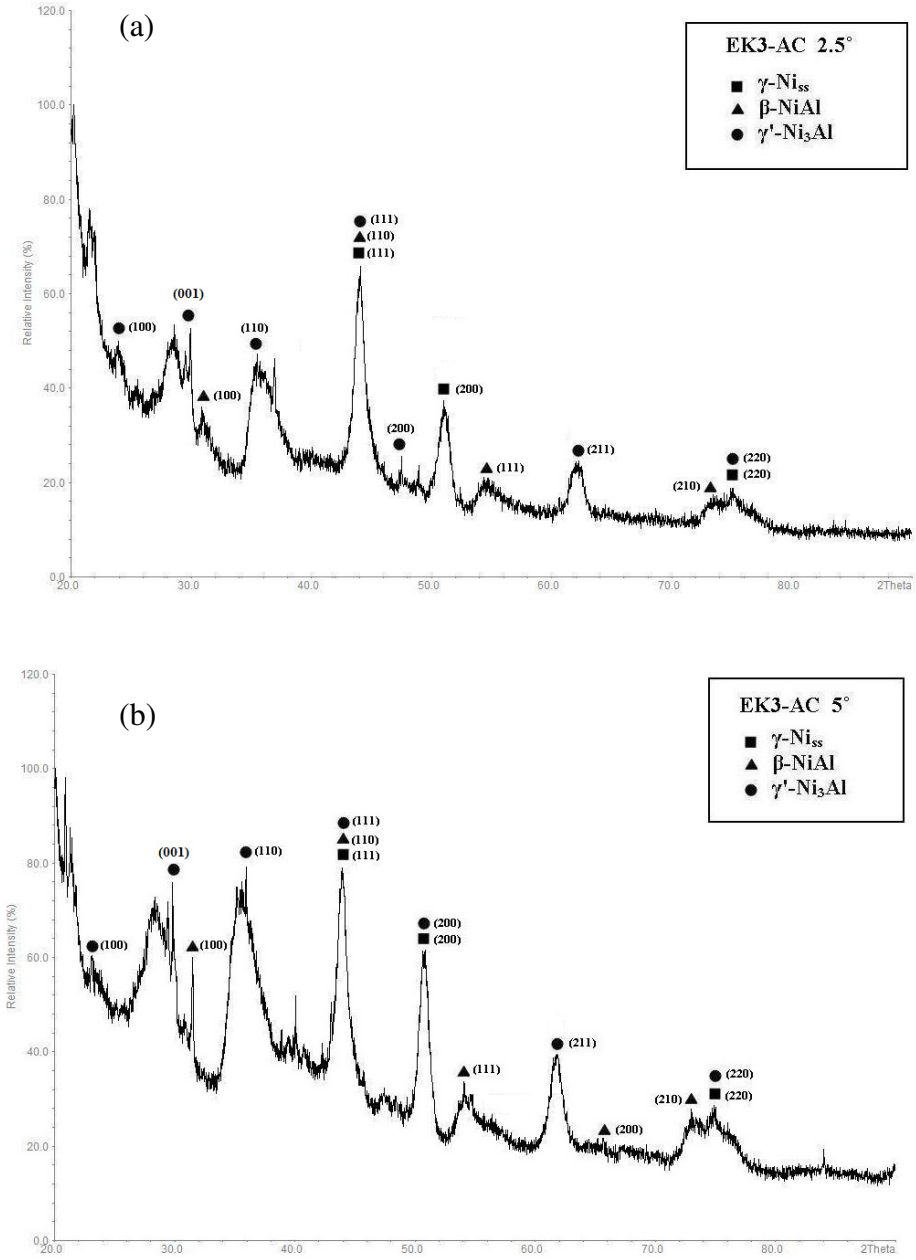

Figure 5.33 Glancing angle XRD data for the alloy EK3 before oxidation (a) γ= 2.5˚ and (b) γ= 5˚.

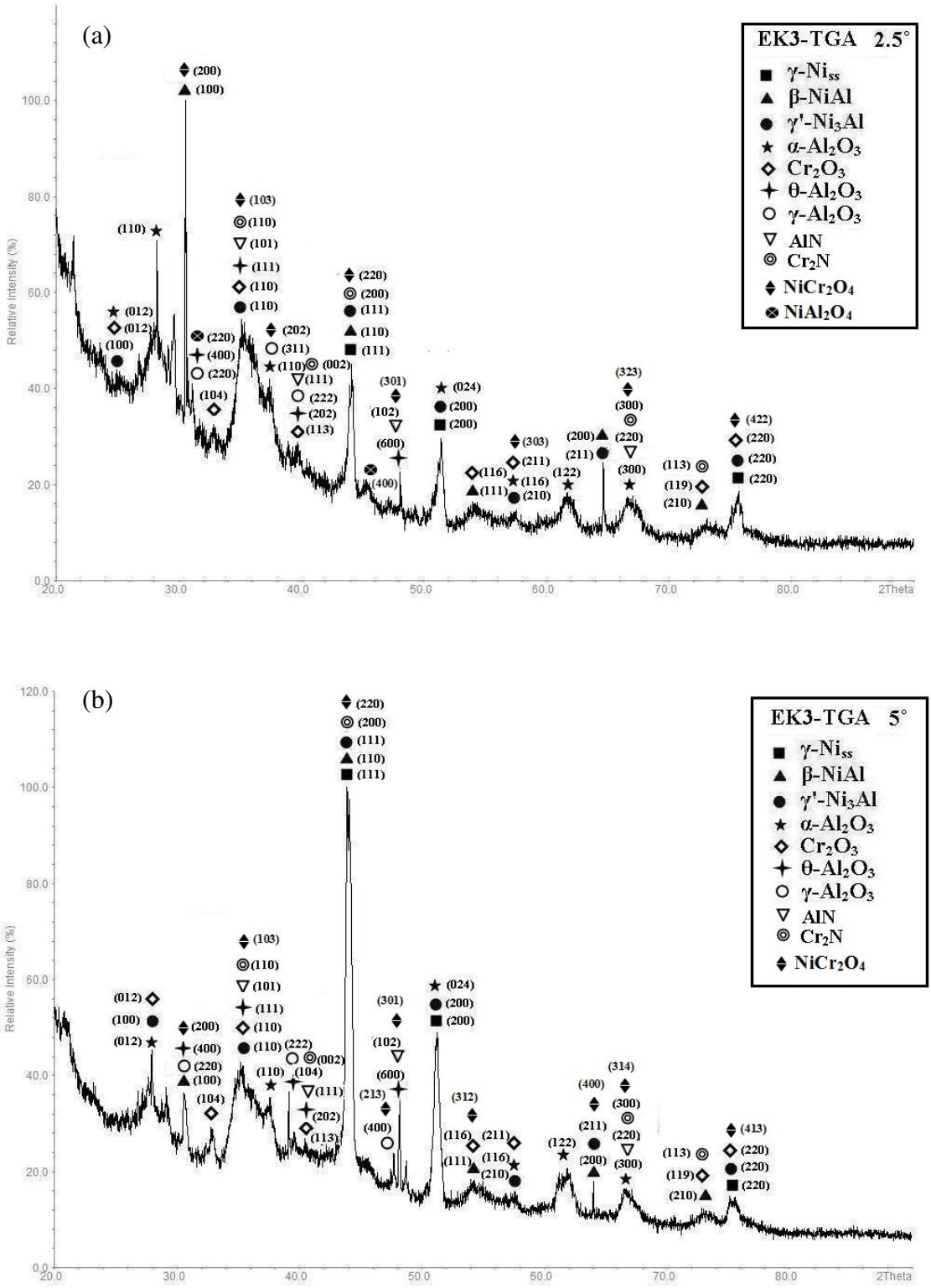

Figure 5.34 Glancing angle XRD data for the oxide scale formed on the alloy EK3 for 100 hrs at 975 ˚C in air (a) γ= 2.5˚ and (b) γ= 5˚.

5.2.2.3.2 Microstructure of oxidised alloy

WDS studies of the EK3 alloy confirmed the presence of γ-Ni_{ss}, γ'-Ni_3Al and β-NiAl. The microstructure consisted of the oxide scale on the surface, internal oxidation and a diffusion zone, see fig. 5.35 some of the β-NiAl grains contained white contrast phases and γ'-Ni_3Al had precipitated in the γ-Ni_{ss} (figs 5.35 to 5.37). Starting from the surface and going towards the bulk, there was an oxide layer rich in O (31.4 at %), Al (68.6 at %) and Ta (19.1 at %) (see Table 5.8), the latter indicated the Ta presence in the oxide scale as was also suggested by the EDS qualitative analysis of the scale, see figures 5.29 to 5.31. Below the oxide scale the internal oxidation exhibited dark contrast and was rich in O (33.5 at %) and Al (45.5 at %). The diffusion zone was rich in Ni (34.9 at %), Co (26.3 at %) and Cr (27.4 at %), as was the case in the EK1 and EK2 alloys. In the diffusion zone some white/grey contrast features were formed (figs 5.35 and 5.36) which were rich in Ni (49.3 at %) as in the EK2 alloy but slightly richer in Al and slightly poorer in Co and Cr. Fig. 5.39 also shows a Cr rich layer that was formed below the oxide layer. The bulk microstructure is shown in fig. 5.38. The microstructure consisted of γ-Ni_{ss}+ γ'-Ni_3Al, β intermetallics and a σ-phase rich in Ni (13.2 at %), Co (12.8 at %), Cr (54.4 at %) and Ta (12.1 at %). Two more phases were identified, a white phase rich in Y, see fig. 5.37 and the white contrast precipitates in β-NiAl that were rich in Ni (42.3 at %), Co (18.3 at %), Cr (13.5 at %) and Al (17.1 at %).

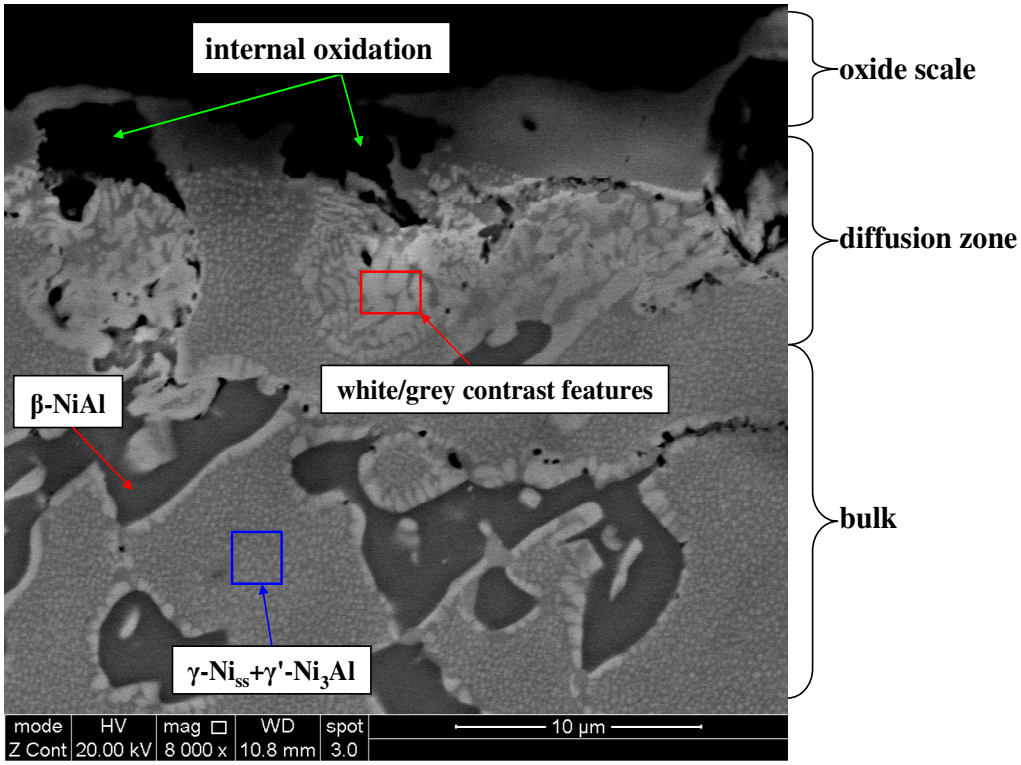

Figure 5.35 BSE image of a cross section of the oxidised EK3 alloy.

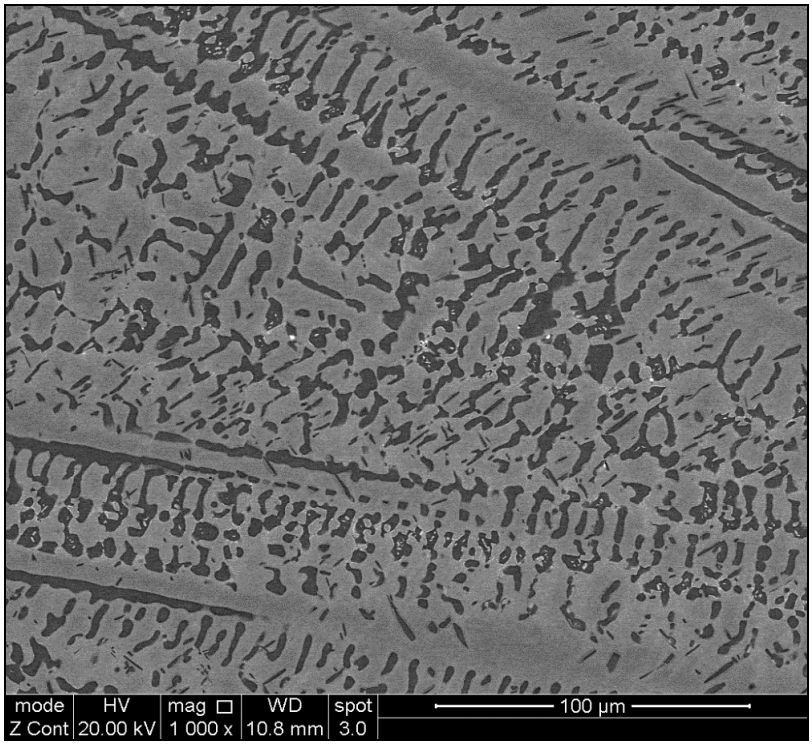

Figure 5.36 BSE image of the bulk of EK3. The dark contrast areas correspond to β-NiAl and not to internal oxidation.

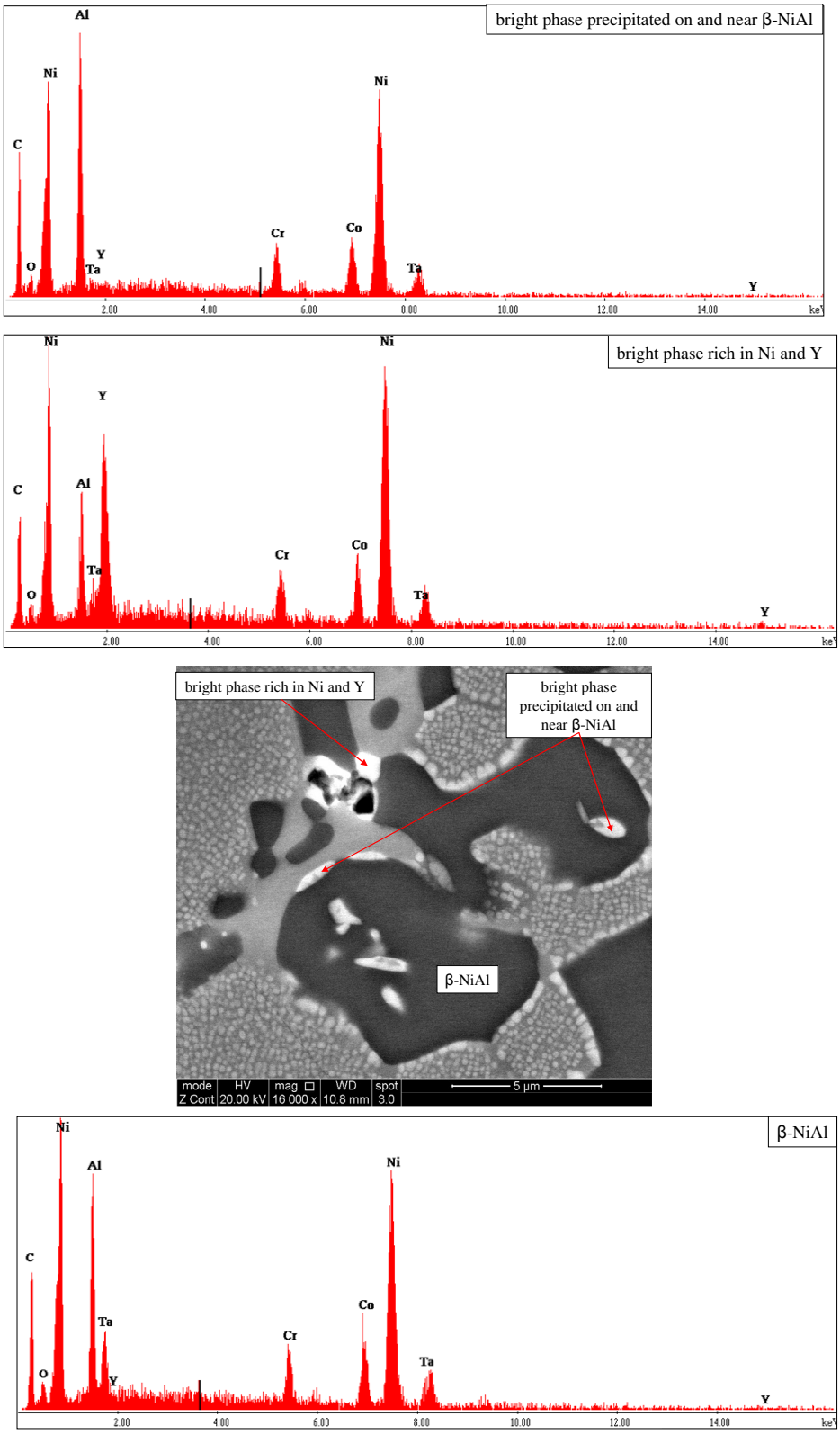

Figure 5.37 BSE image and EDS spectra taken from the bulk of EK3 showing β-NiAl and bright phases precipitated on and near it.

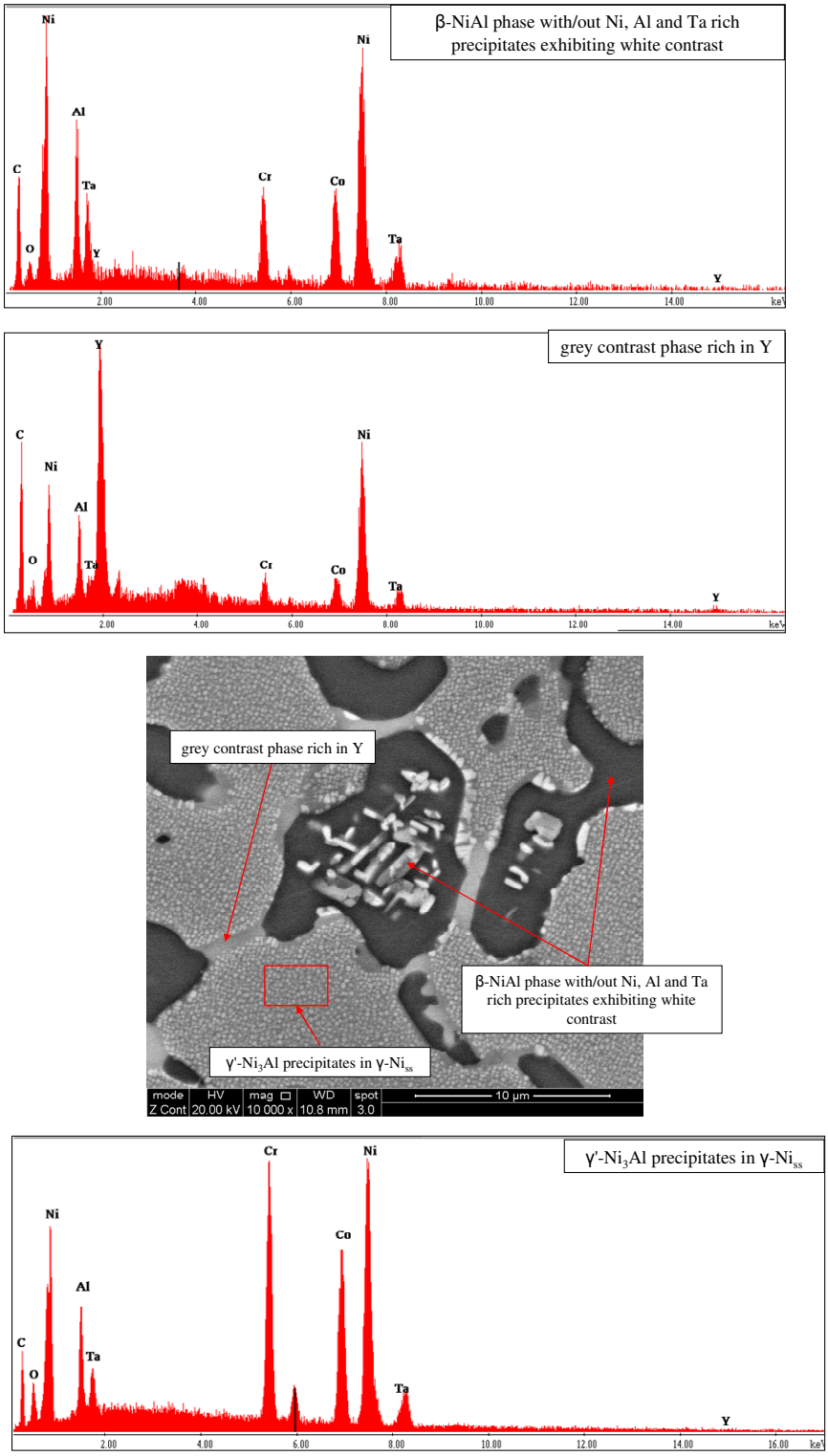

Figure 5.38 BSE image and EDS spectra taken form the bulk of the oxidised EK3 alloy showing the β-NiAl phase with/out Ni, Al and Ta rich precipitates exhibiting white contrast, and Y rich phase exhibiting grey contrast and precipitates of γ'-Ni_3Al in γ-Ni_{ss}.

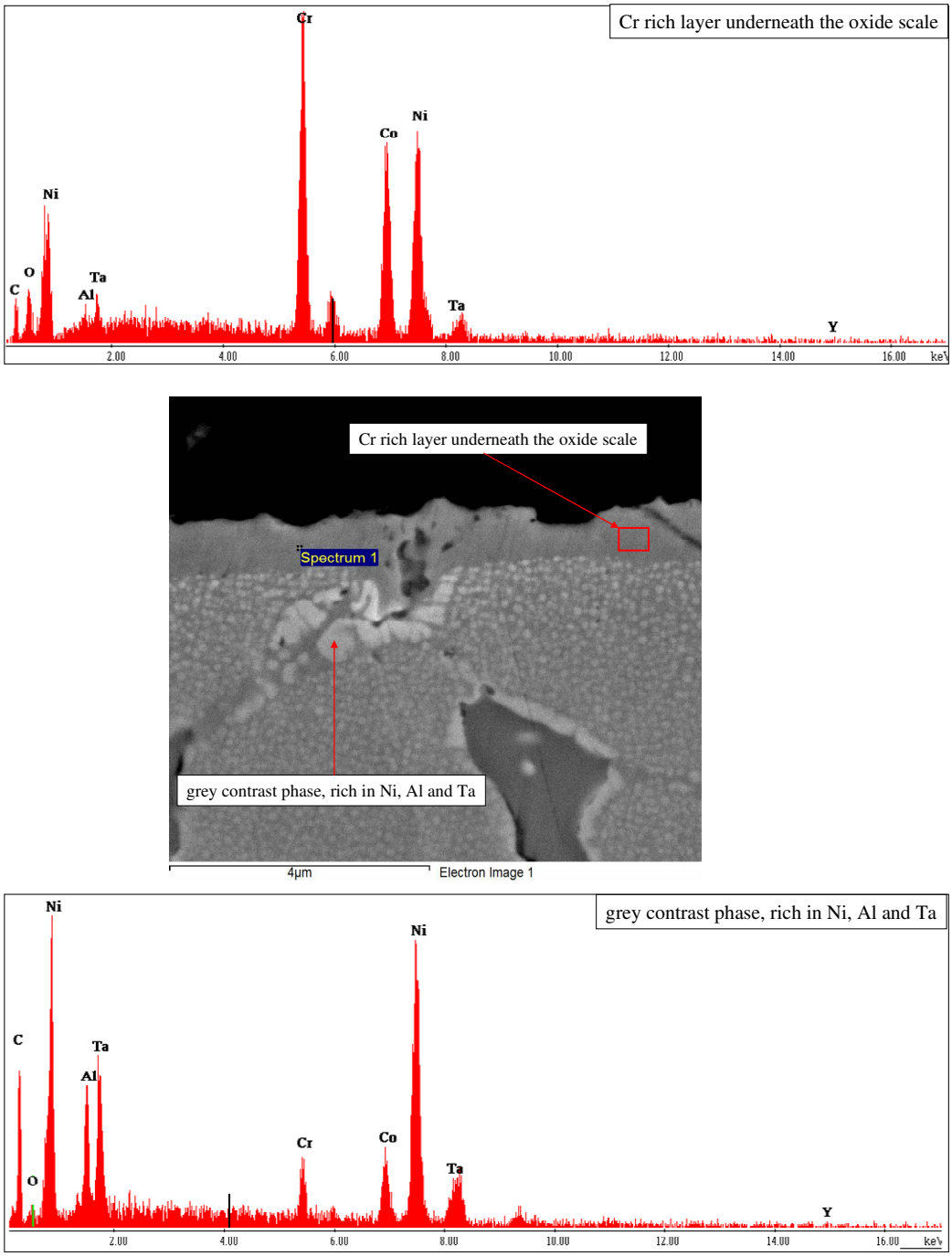

Figure 5.39 BSE image and EDS spectra suggesting presence of a Cr rich layer underneath the oxide scale and a Ni, Al and Ta rich grey contrast phase forming under the Cr rich layer.

Table 5.8 WDS analysis data (at %) of different part of the cross section of the EK3 alloy after oxidation at 975 ˚C for 100 hrs.

area	N	O	Ni	Co	Cr	Al	Ta	Y
oxide scale	0	31.4±8.2	0.3±0.07	0.2±0.03	1.3±0.2	68.6±7.4	0.8±0.4	0
internal oxidation	0	33.5±1.9	6.5±1.6	5.9±1.3	9.3±1.4	45.5±2.6	0.3	0.7±0.5
diffusion zone	5.7±0.9	0.8±0.1	34.9±1.7	26.3±1.2	27.4±1.4	3.9±0.5	0.8±0.2	0
white features in diffusion zone	6.1±0.2	0.1±0.03	49.3±1.2	15±0.4	10.7±0.9	14.4±1.6	3.7±0.7	0
β-NiAl	6.4±0.6	0.4±0.3	45.3±0.9	10.5±0.6	5.2±0.6	31.8±1.5	0.3±0.2	0.04±0.03
γ-Ni_{ss}+γ'-Ni_3Al	5.7±1.8	1.1±0.1	39±1.3	22.3±1.3	20.1±0.9	10.2±0.9	1.4±0.4	0
white features in β-NiAl	5.7±0.2	0.5±0.4	42.3±7.3	18.3±5.3	18.5±0.02	17.1±4.1	2.5±1.5	0
σ-phase in bulk	1.3±0.9	1.9±0.3	13.2±1.2	12.8±0.3	54.4±1.2	3.7±1.1	0.7±0.2	12.1±0.5

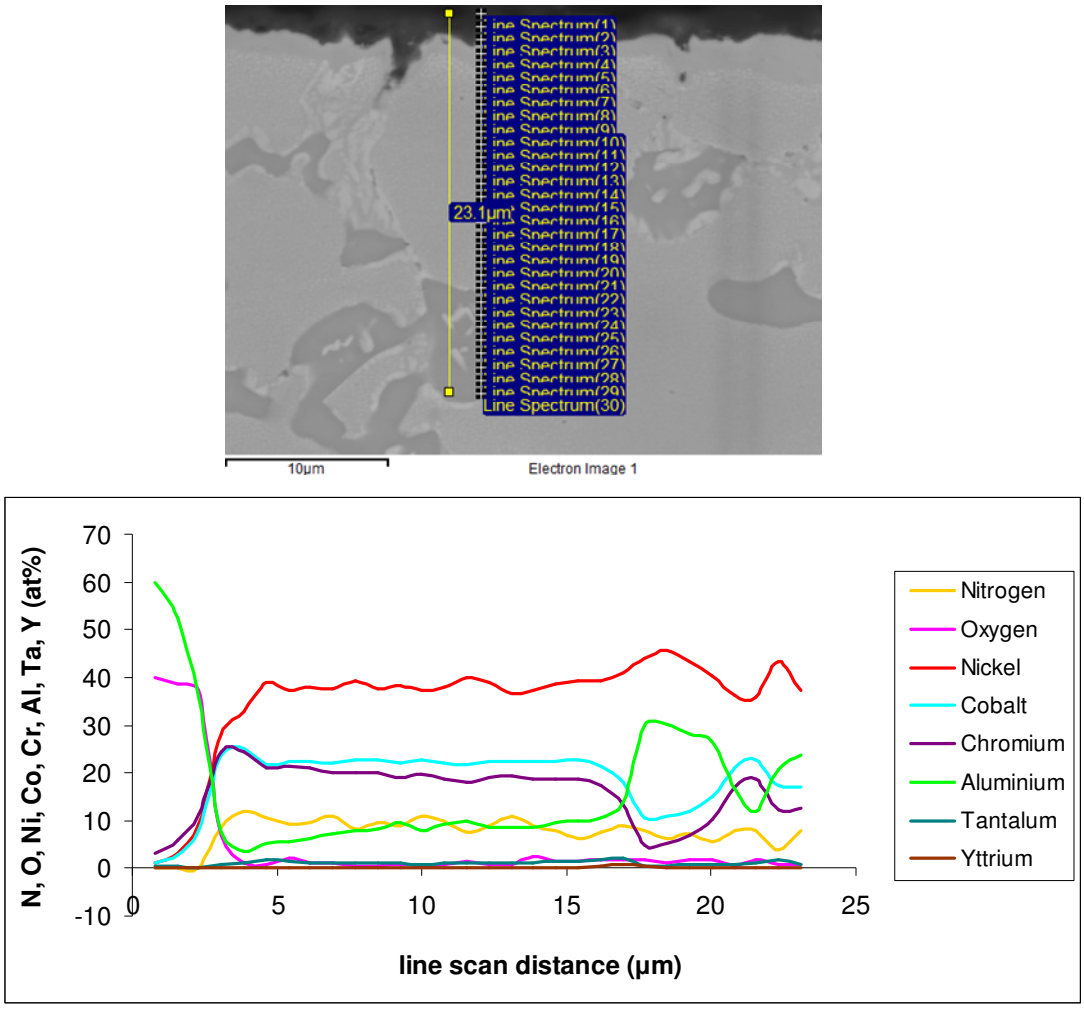

Figure 5.40 BSE image of cross section showing distributions (detected by WDS) of Ni, Co, Cr, Al, Ta and Y as a function of distance from the surface.

Elemental distributions along a cross section of the EK3 alloy obtained by WDS as a function of distance from the coating surface are shown in fig. 5.40. The oxide scale was rich in O and Al whose concentrations decreased as the scan moved from the surface towards the bulk. The diffusion zone was characterised by its enrichment in Ni, Co and Cr. As the line scan moved in the bulk the Ni, Co and Cr levels remained fairly stable as it crossed through γ-Niss+ γ'-Ni_3Al and at about ~18 µm below the surface the Ni and Al contents increased as the scan crossed a β-NiAl intermetallic grain. In the bulk the O, Ta and Y concentrations were very low. The N level increased in the diffusion zone.

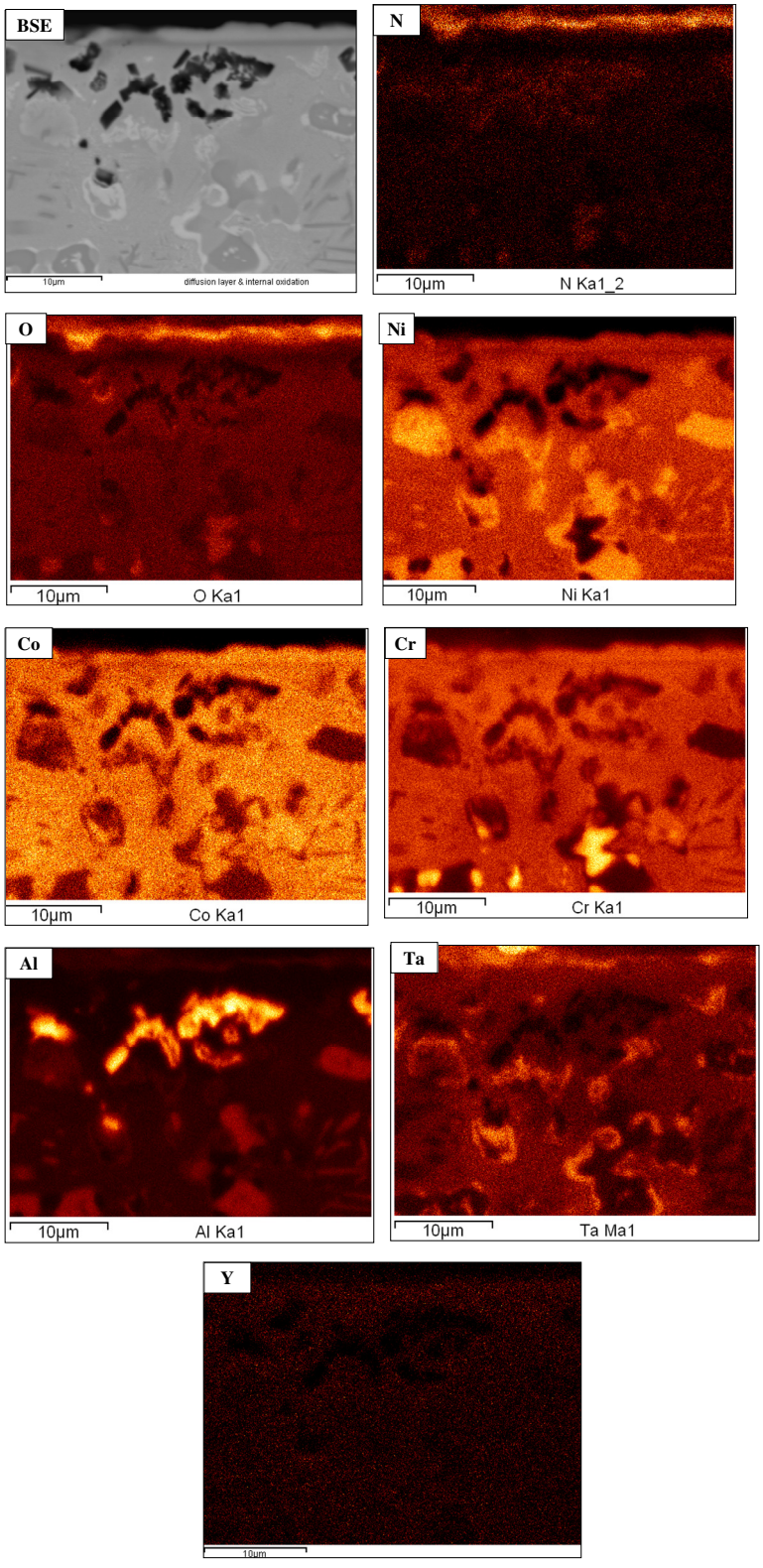

Figure 5.41 BSE image and qualitative elemental maps of N, O, Ni, Co, Cr, Al, Ta and Y taken from the oxide scale and the microstructure below it.

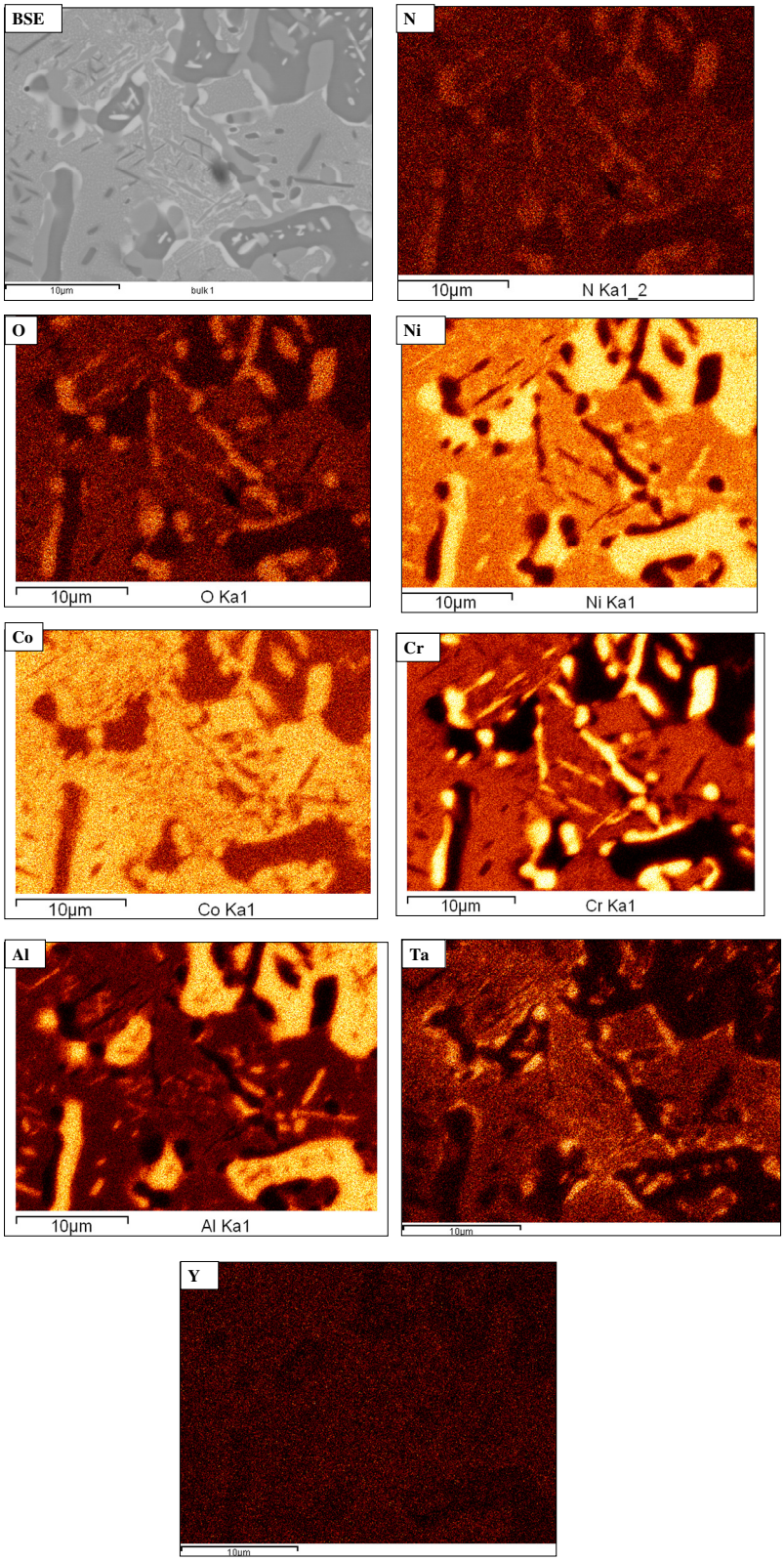

Figure 5.42 BSE image and qualitative elemental maps of N, O, Ni, Co, Cr, Al, Ta and Y taken from the bulk of EK3.

Qualitative maps collected from the surface and the bulk can be seen in figs 5.41 and 5.42 and quantitative maps in fig. 5.43. The oxide scale was rich in N, O and Al supporting the WDS and XRD results for Al_2O_3 oxide scale formation. The oxide scale appeared to be relatively thin and of varying thickness along the surface. Cr_2O_3 formation below the alumina scale and Ta rich areas in the alumina scale are indicated in the maps and confirm and lies findings. The white features in the diffusion zone and surrounding the NiAl intermetallics appear to be rich in Ni and Ta (fig. 5.41). Internal oxidation features are very rich in Al and contain N (fig. 5.41). The σ-phase is Cr rich and with N and O content. Ta rich areas are indicated around the NiAl intermetallics. In fig. 5.41 Ta appears to be present in the internal oxidation area and on the surface in fig. 5.43.

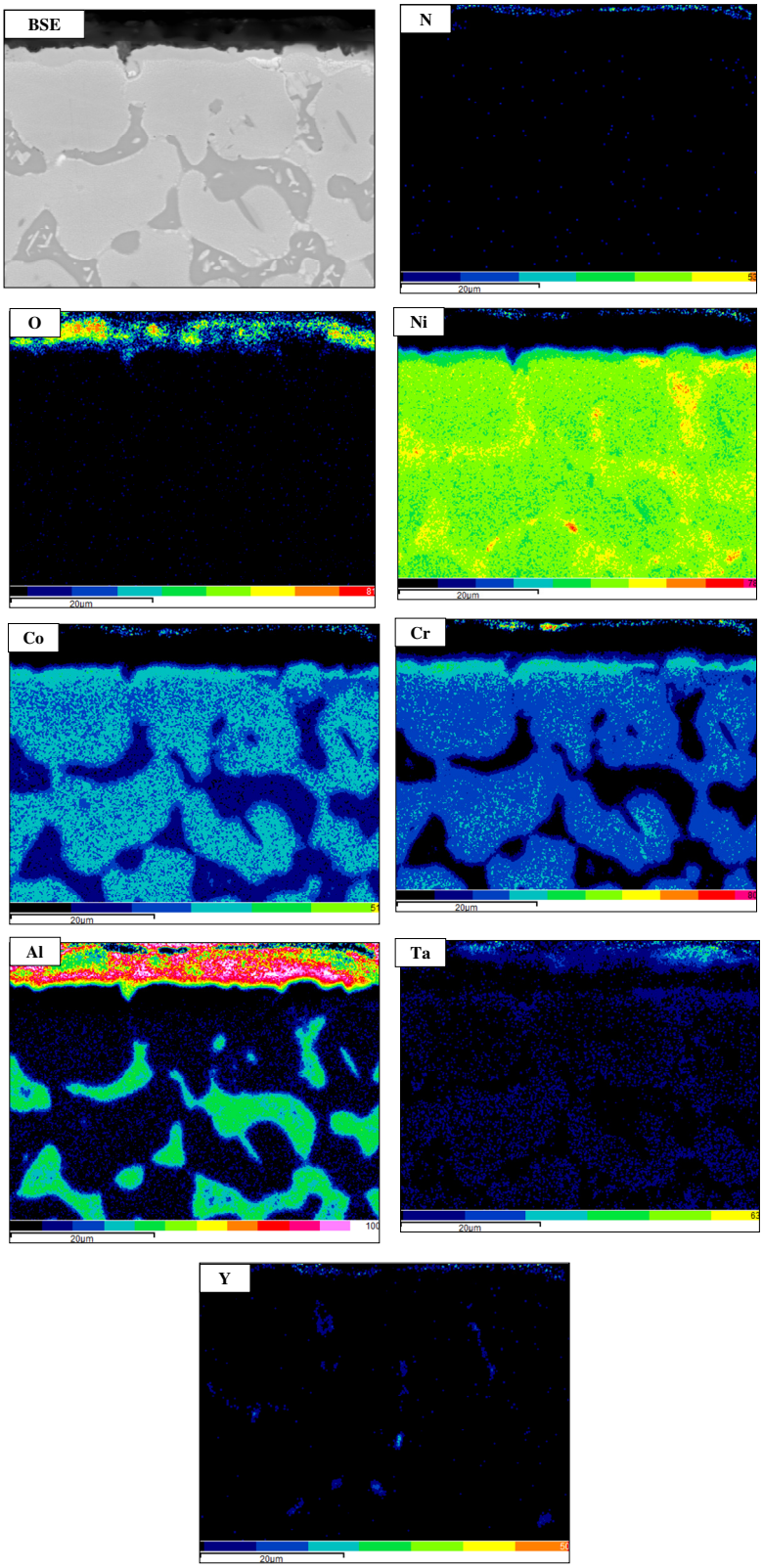

Figure 5.43 BSE image and quantitative elemental maps of N, O, Ni, Co, Cr, Al, Ta and Y taken from the oxide scale and the microstructure below it.

5.2.2.4 Ni-20Co-19.7Cr-16.1Al-1.1Ta-0.3Y-0.2Hf (alloy EK4)

5.2.2.4.1 Microstructure and glancing angle XRD

The oxide scale on the EK4 alloy was significantly more uniform than that formed on the oxidised alloy, EK1, and thinner. The edges were well defined and there were few islands of large oxide growths. No cracks were visible but there were holes in the scale (see figures 5.45 and 5.46). Unlike the alloys EK2 and EK3, in the EK4 alloy there was no evidence of glassy features in the scale. Further details of the scale formed on EK4 are shown in fig. 5.46 and 5.44. EDS confirmed the presence of Ta and Cr in the scale (fig. 5.45, 5.44).

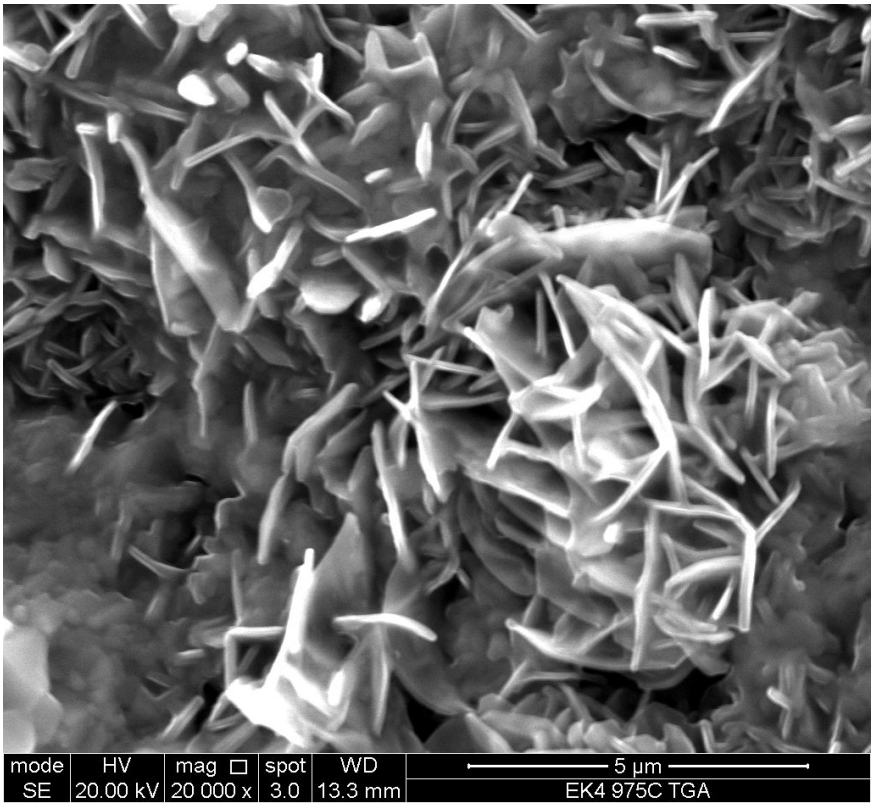

Figure 5.44 SEI image showing needle like Al_2O_3 formation.

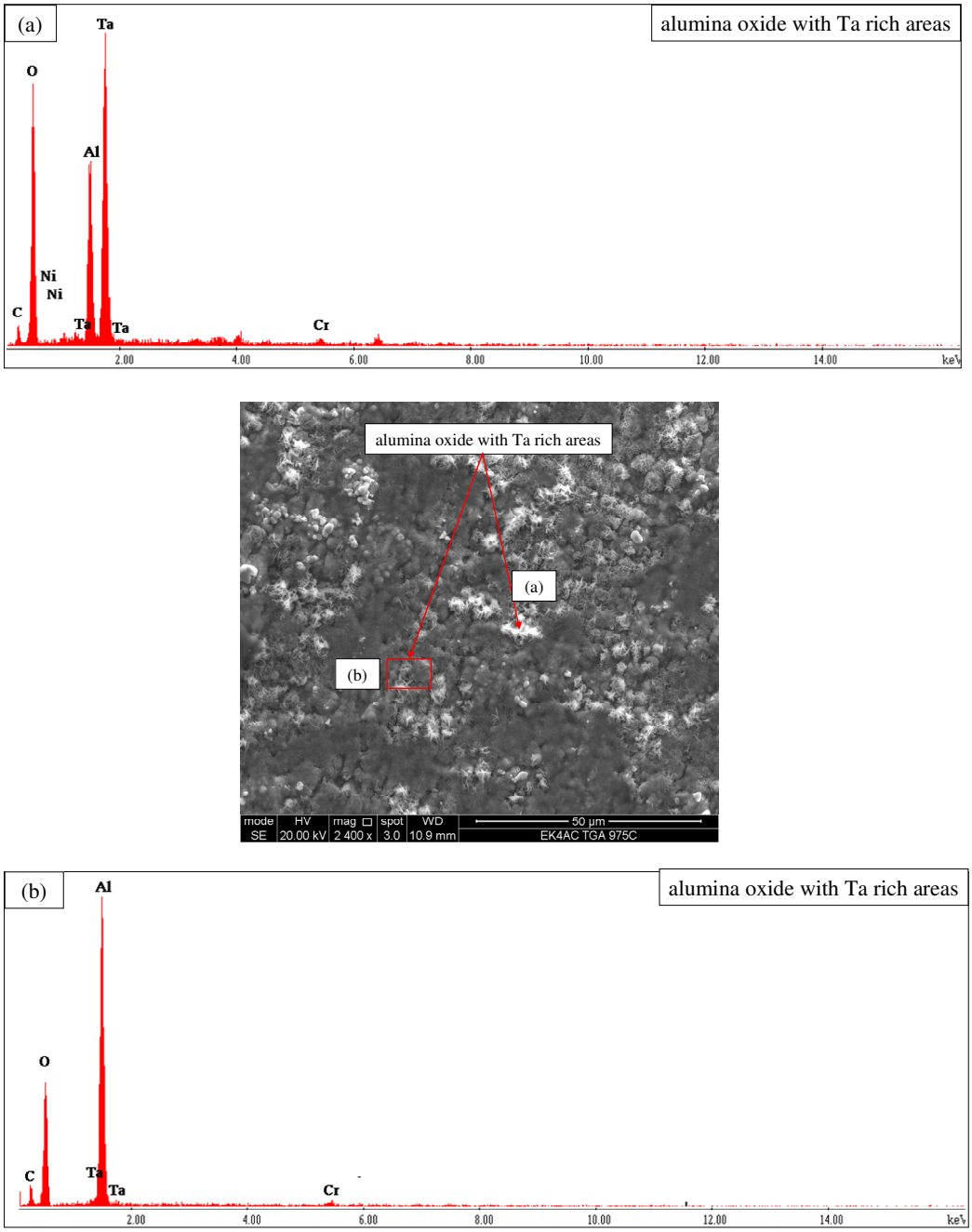

Figure 5.45 SEI image and EDS spectra of scales showing holes in the latter and alumina oxide with Ta rich areas.

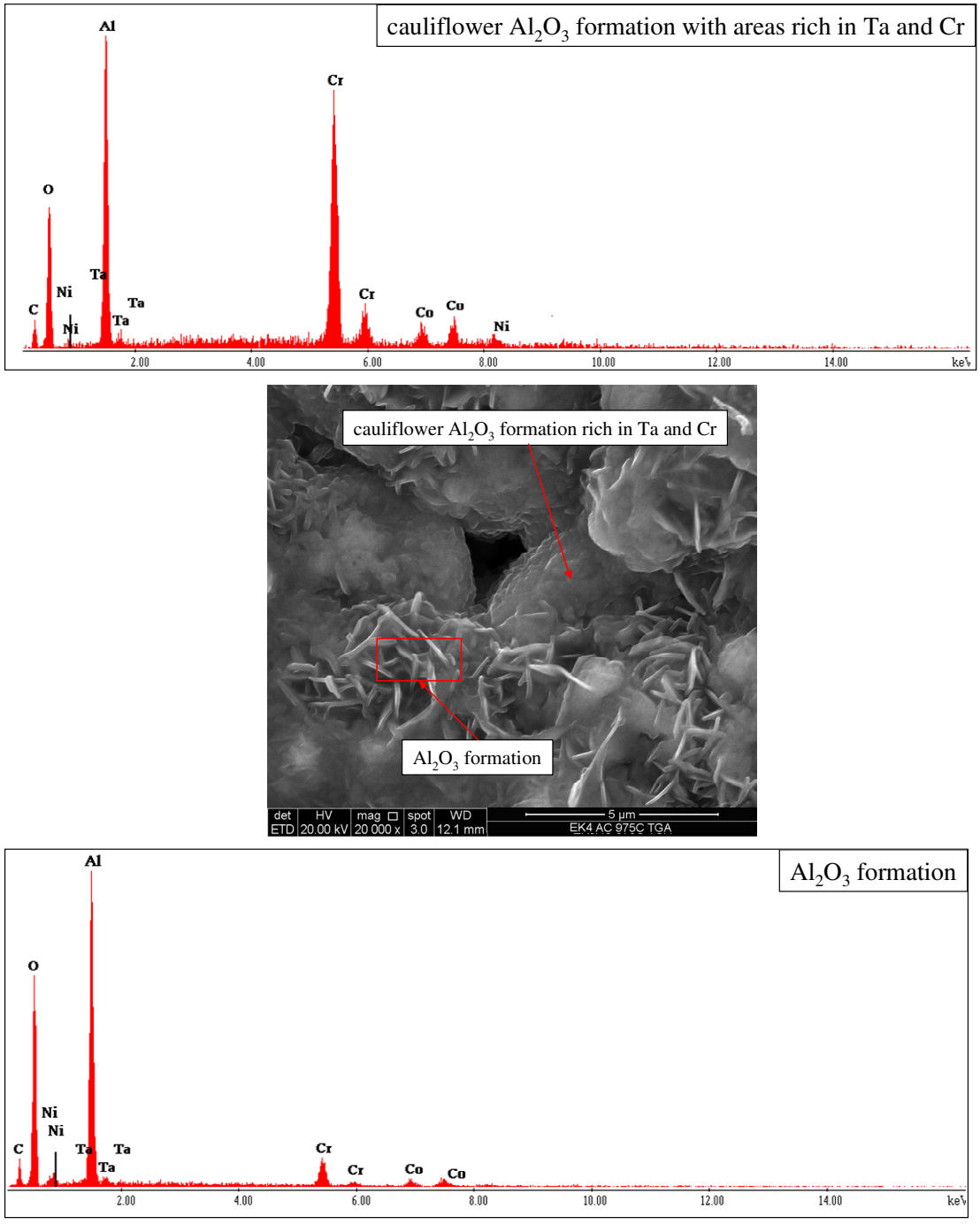

Figure 5.46 SEI image and EDS spectra showing cauliflower Al_2O_3 formation with areas rich in Ta and Cr.

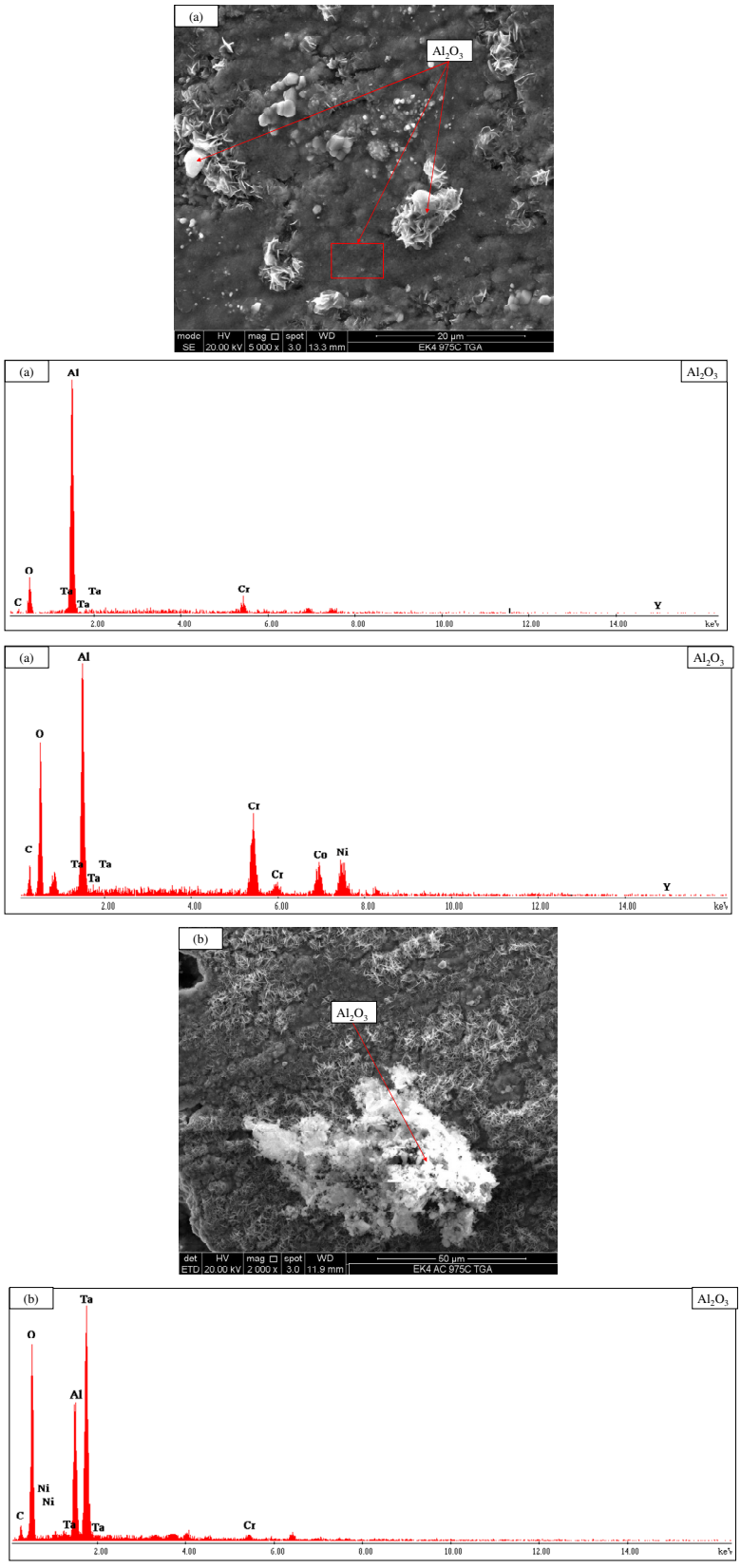

Figure 5.47 SEI image and EDS spectra showing Al_2O_3 formations.

The glancing-angle XRD data EK4 is shown in figures 5.48 and 5.49. Peaks for the γ-Ni_{ss}, γ'-Ni_3Al and β-NiAl phases were present in the diffractogram before and after oxidation. For the glancing angle γ=2.5˚ there were peaks for θ-Al_2O_3 and α-Al_2O_3 and the peaks for γ-Al_2O_3 coincided with those of θ and α-Al_2O_3 and the peaks of Cr_2O_3 coincided with those of other phases. For the glancing angle γ=5˚ there were peaks for θ-Al_2O_3, α-Al_2O_3 and Cr_2O_3 and the peaks for γ-Al_2O_3 coincided with those for θ and α-Al_2O_3. For both γ values there were peaks of AlN and Cr_2N that coincided with those of other phases but for γ=5˚ there was one peak corresponding only to AlN.

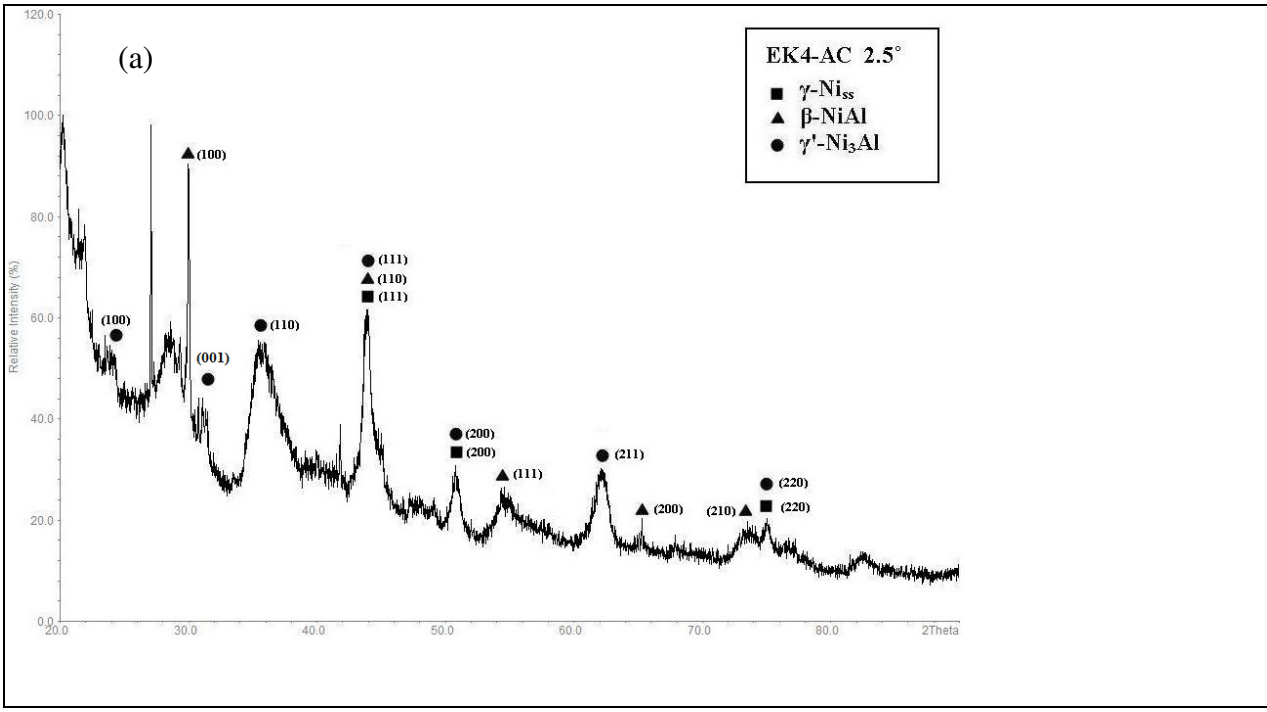

continued in the next page

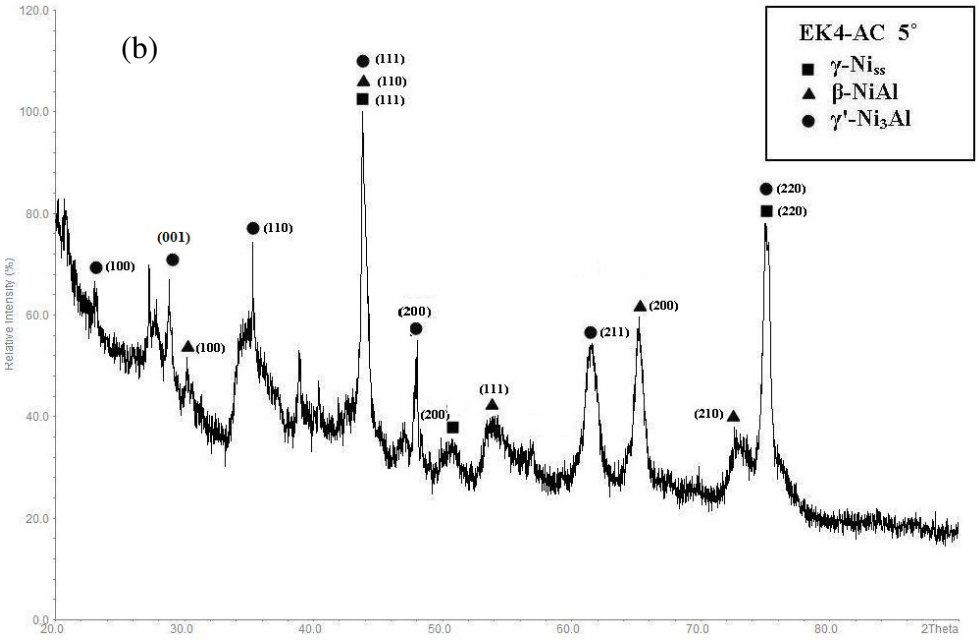

Figure 5.48 Glancing angle XRD data for the alloy EK4 before oxidation (a) γ= 2.5˚ and (b) γ= 5˚.

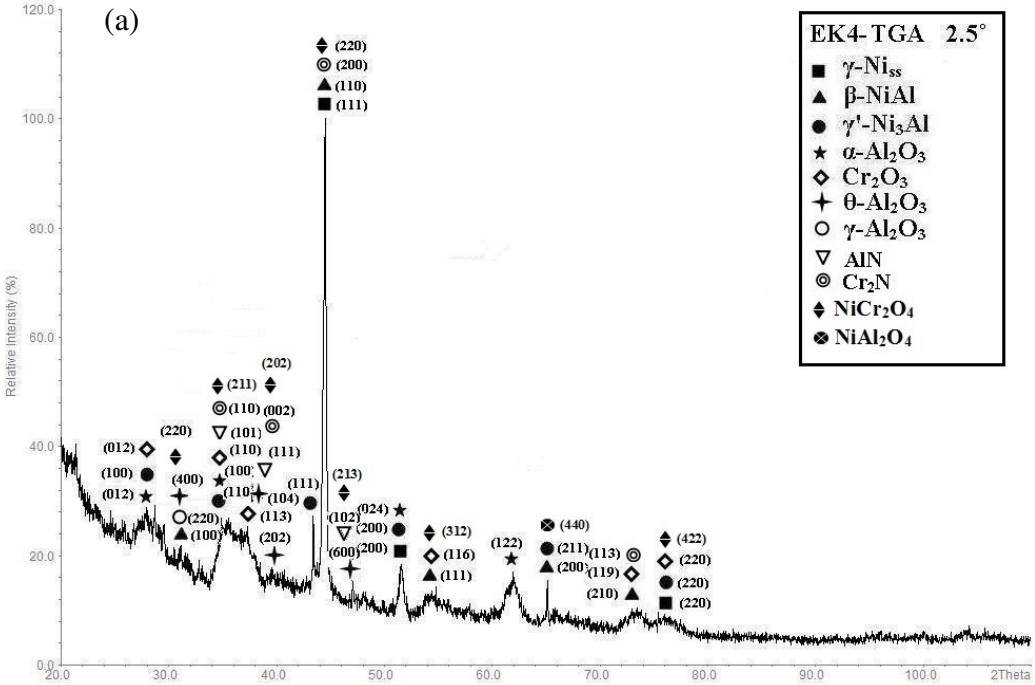

continued in the next page

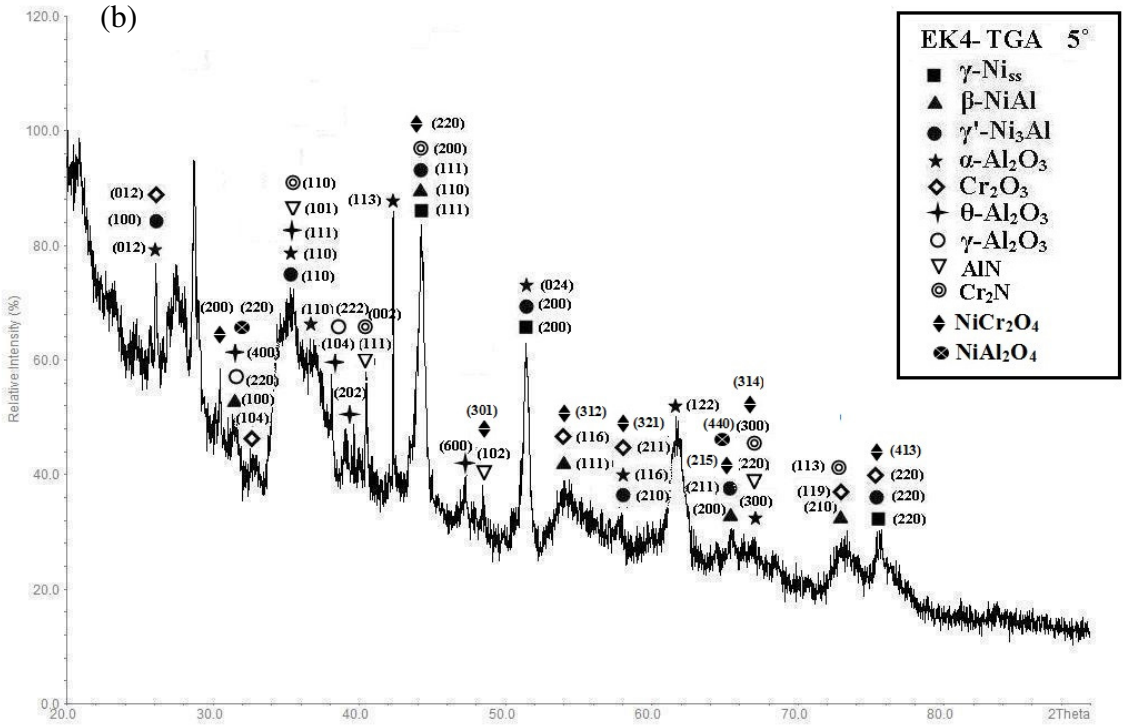

Figure 5.49 Glancing angle XRD data for the oxide scale formed on the alloy EK4 after oxidation for 100 hrs at 975 ˚C in air (a) γ= 2.5˚ and (b) γ= 5˚.

5.2.2.5.2 Microstructure of oxidised alloy

A cross section of the oxidised alloy is shown in figure 5.50. The surface of EK4 was covered by an oxide scale rich in O (38.3 at %) and Al (52 at %) with high Cr content (8 at %), see Table 5.9. The diffusion zone was rich in Ni (28.7 at %), Co (22.1 at %) and Cr (22.5 at %) and had high Al content (15.8 at %) compared with the diffusion zone in the previous alloys EK1 to EK3. In the diffusion zone, some white features had formed and there were rich in Ni (48.2 at %), and slightly poorer in Co (14.9 at %) and Cr (10.2 at %) compared with the alloy EK3, see Table 5.9. The Al content (17 at %) in these white features was similar with those formed in the EK3 and higher than in EK2. Internal oxidation was also evident and this was more severe than in the alloys EK2 and EK3, see figs 5.50 and 5.51. The internal oxidation was rich in O (30.3 at %) and Al (34.4 at %) which were slightly lower than in the EK3 alloy and very different than in the EK1 and EK2 alloys where the O content was very low and the Al content was significantly high. As seen in figs 5.50 and 5.51 the internal oxidation had penetrated deep in this alloy and reached its bulk. This was not the case in the alloys EK1, EK2 and EK3. Precipitation of

γ'-Ni_3Al in γ-Ni_{ss} was evident both near the scale and in the bulk (figs 5.50, 5.52). Compared with EK2 and EK3 the β-NiAl was free of second phases. One phase formed at the interface of β-NiAl with the γ-Ni_{ss} grains had a morphology similar to the σ-phase observed in EK2 and EK3 but higher Ni (47.2 at %) and Ta (4.7 at %) and lower Cr (10.1 at %) contents. Another phase exhibited bright/white contrast, was formed in the area of internal oxidation and had high Y (4.1 at %), Ta (7.4 at %) and Hf (19.5 at %) contents. The O concentration below the surface area was low with the exception of the internal oxidation areas and the bright/white contrast phase.

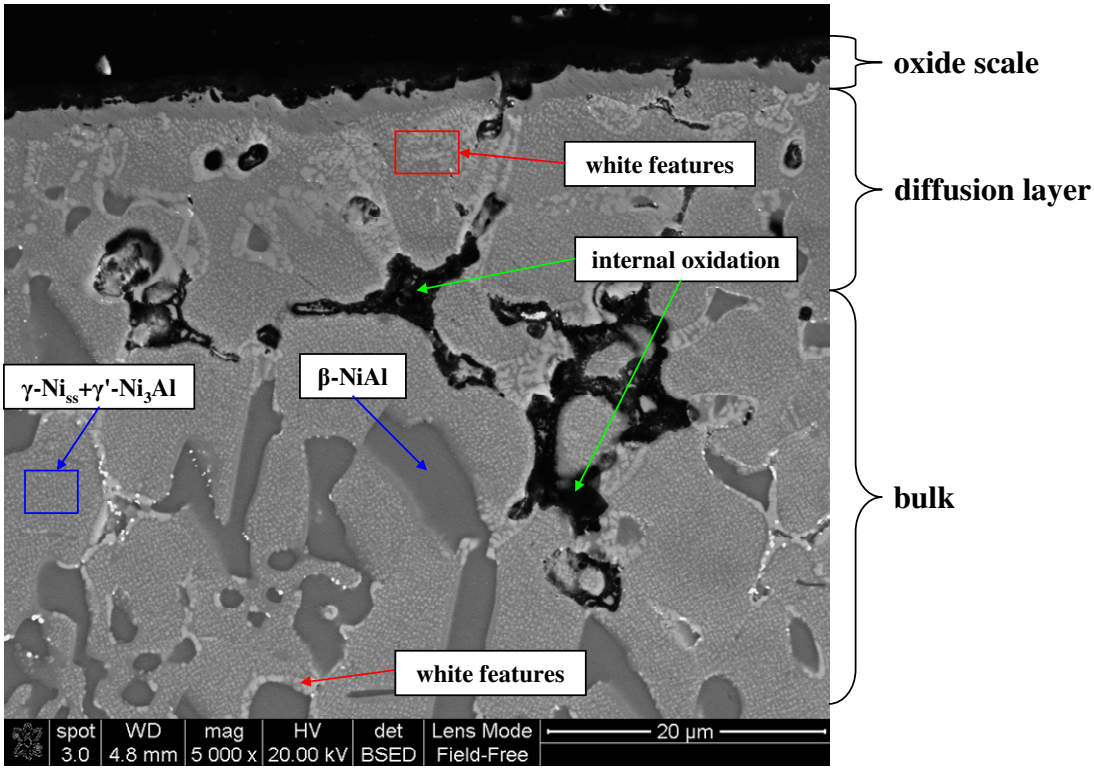

Figure 5.50 BSE image illustrating different phases and layers of the oxidised EK4 alloy.

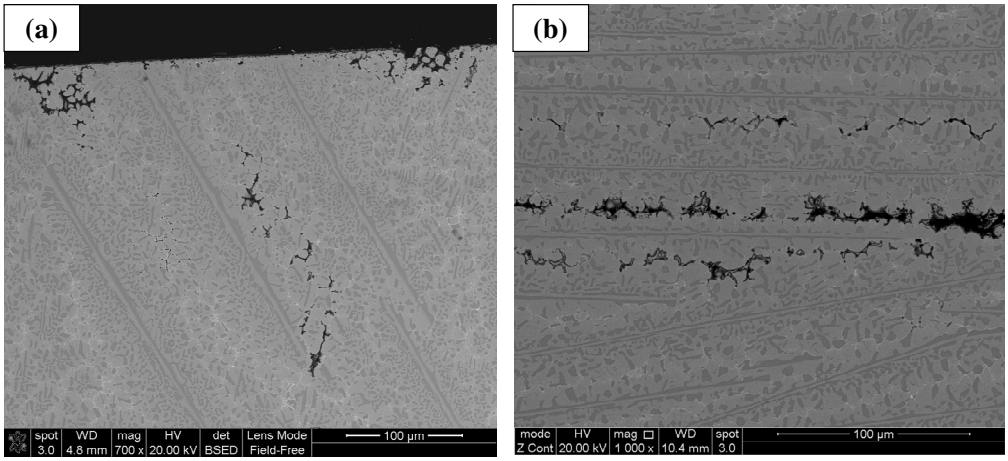

Figure 5.51 BSE images showing (a) internal oxidation below the surface, (b) internal oxidation in the bulk.

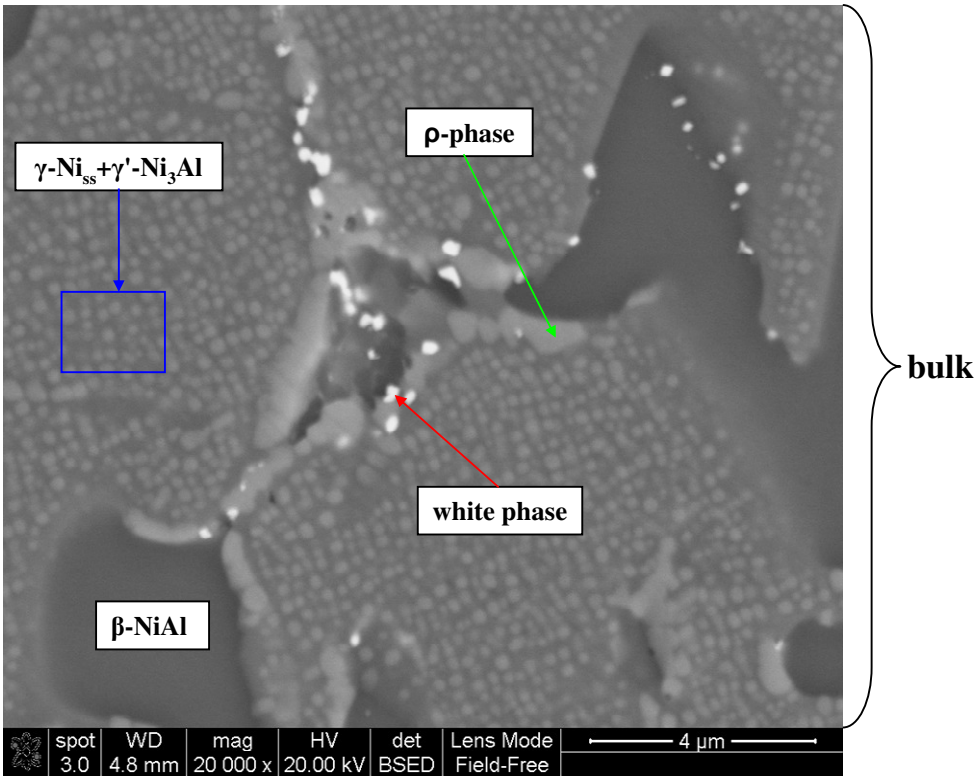

Figure 5.52 BSE image showing different phases in the bulk microstructure of the oxidised EK4 alloy.

Table 5.9 WDS analysis data (at %) of different parts of the cross section of the EK4 alloy after oxidation at 975 ˚C for 100 hrs.

area	N	O	Ni	Co	Cr	Al	Ta	Y	Hf
oxide scale	0	38.3±4.3	2±0.4	1.8±0.4	8±2	52±2.6	0.9±0.3	0	0
internal oxidation	0	32.2±8.5	11.9±4.7	8.3±3.4	11.2±4.6	36.7±5.9	0.6±0.6	0.04±0.04	0.3±0.2
diffusion zone	5.2±1.2	5±2.5	28.7±2.8	22.1±2	22.5±2.2	15.8±6.2	0.5	0	0
white features in diffusion zone	6.2±0.8	1±0.6	48.2±2.9	14.9±1.9	10.2±3.2	17±2.9	2.9±0.1	0	0
β-NiAl	6.7±1.8	0.9±0.1	43.1±0.8	10.3±0.04	5.5±0.2	33.3±1.4	0.3±0.1	0	0
$\gamma Ni_{ss}+\gamma' Ni_3Al$	5.4±1.2	1±0.5	36.2±3.1	23.7±2.5	22.1±3.3	10.2±1.5	1.5±0.8	0	0
ρ-phase in bulk	4.4±0.8	1.2±0.3	47.2±3.1	15.3±1.5	10.1±2.7	16.4±2.6	4.7±0.2	0	0.7±0.5
bright/white features in bulk	6.7±1.8	5.9±2.3	25.5±1.2	10.3±0.8	8.7±1	11.7±2.1	7.4±1	4.1±3	19.5±4.2

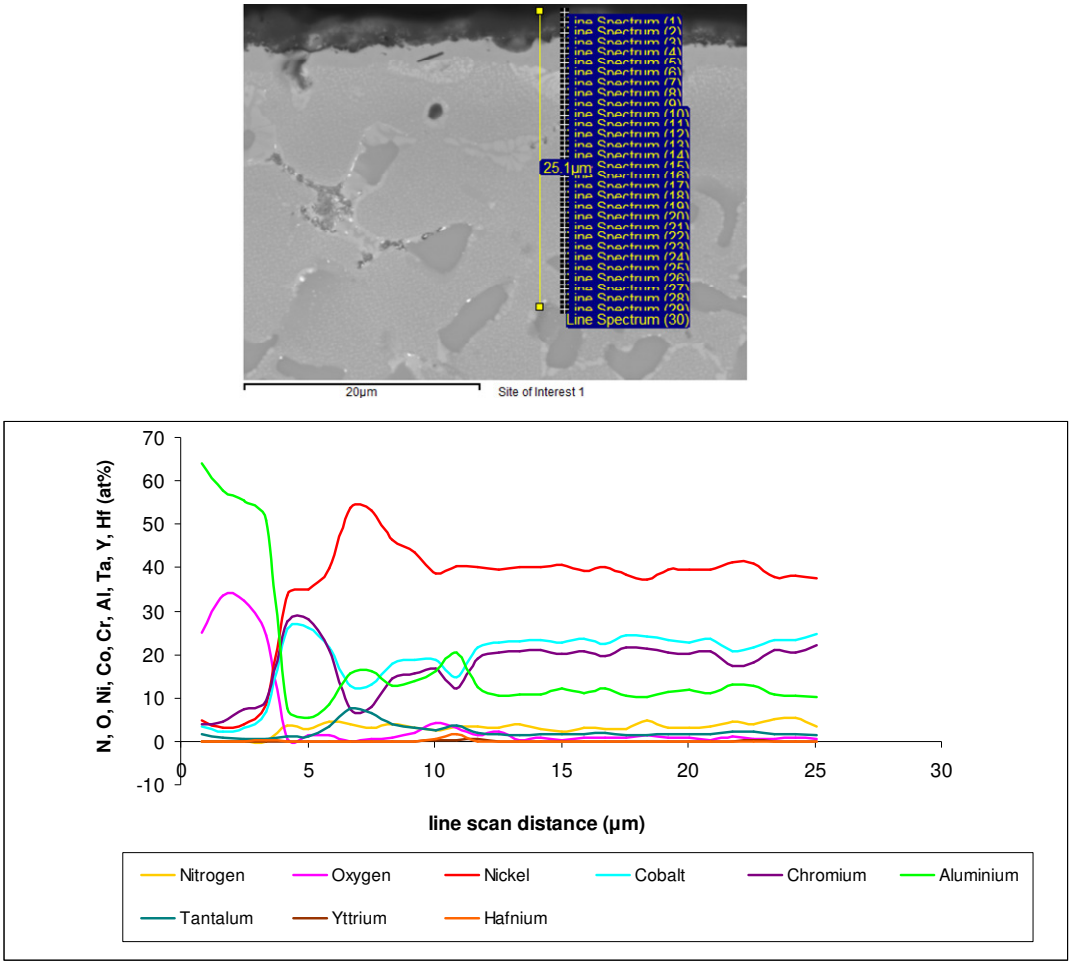

Figure 5.53 BSE image of cross section showing distributions (detected by WDS) of Ni, Co, Cr, Al, Ta, Y and Hf as a function of distance from the surface.

Elemental distributions along a cross section of the oxidised EK4 alloy obtained by WDS as a function of distance from the scale are shown in fig. 5.53. The surface was rich in O, Al and N according to the X-ray maps and there was also presence of Hf and Ta and possibly Y. In the diffusion zone the O and Al contents decreased significantly and the Ni, Co and Cr contents increased. As the scan moved towards the bulk it reached the γ-Ni_{ss}+γ'-Ni_3Al areas where the Ni, Co and Cr distributions remained stable throughout the whole scan as it did not cross any β-NiAl grains. The Y and Hf contents were very low throughout the whole scan, below 1 at%, whereas the N content was up to 4 at%. The O content was very low beyond the diffusion zone towards the bulk. Ta content increased slightly around 5-9 µm below the surface when the scan crossed the white phases in the diffusion zone.

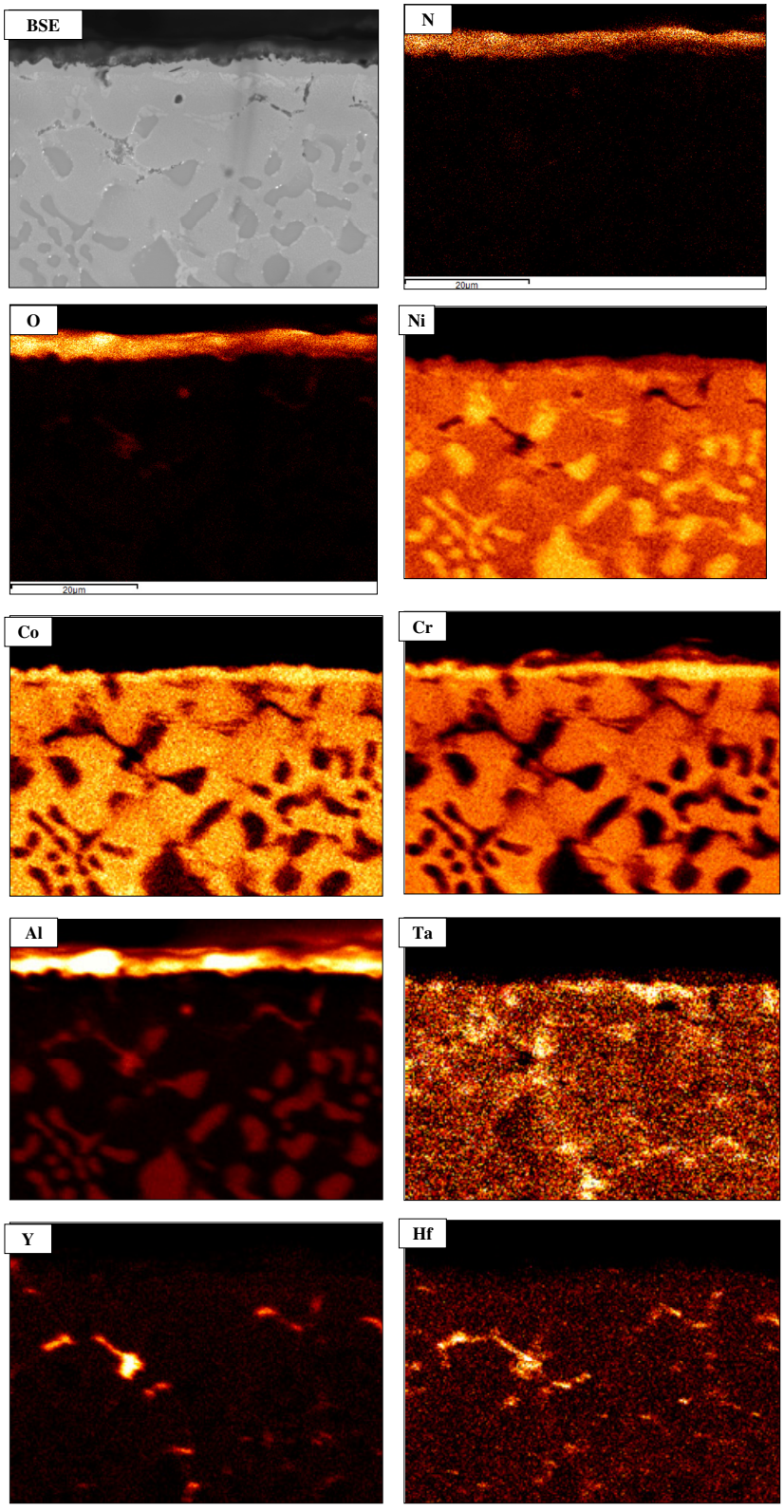

Figure 5.54 BSE image and qualitative elemental maps of N, O, Ni, Co, Cr, Al, Ta, Y and Hf taken from the oxide scale and the microstructure below it in the oxidised EK4 alloy.

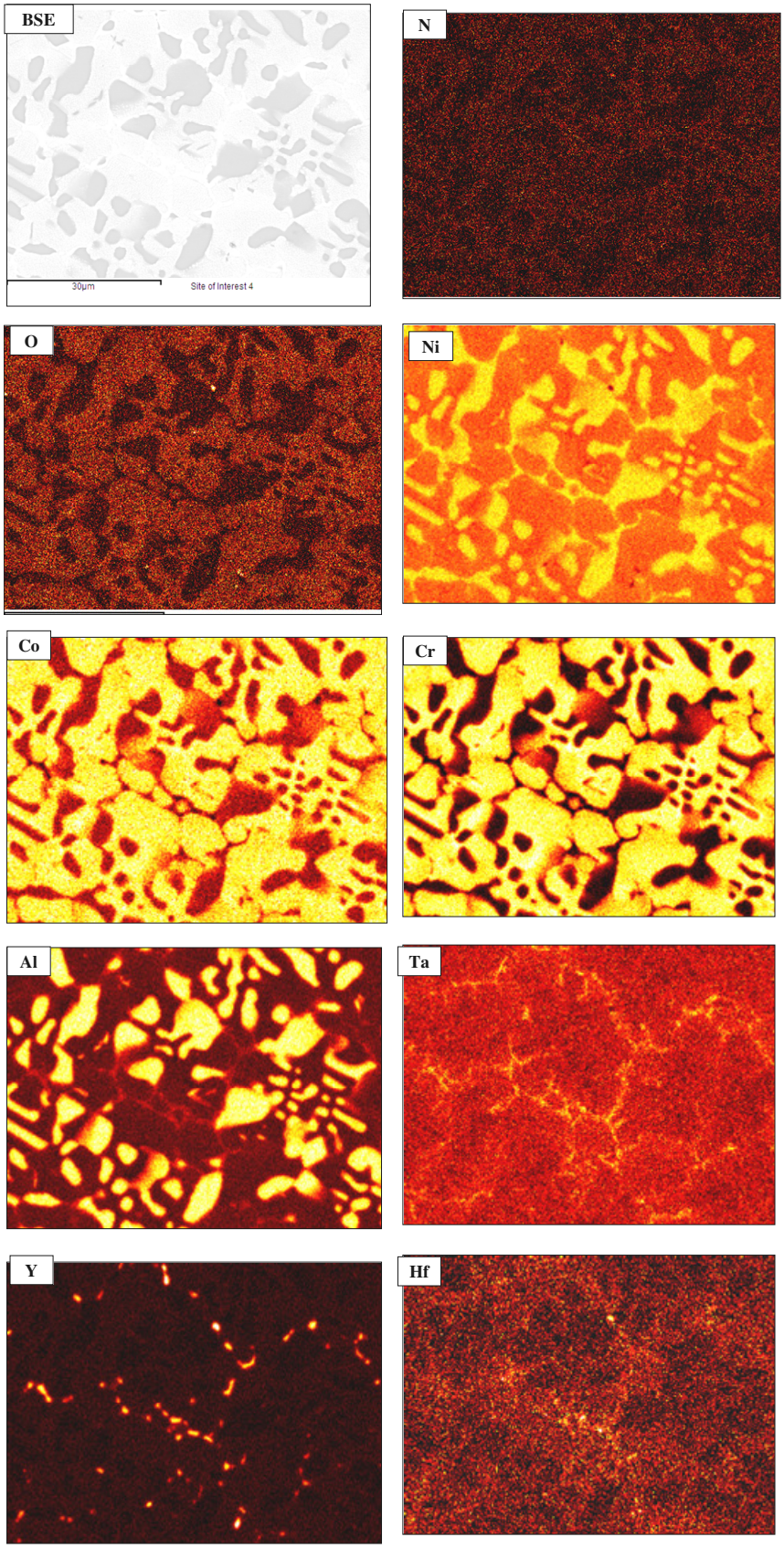

Figure 5.55 BSE image and qualitative elemental maps of N, O, Ni, Co, Cr, Al, Ta, Y and Hf taken from the bulk of oxidised EK4 alloy.

Qualitative and quantitative data maps of the surface areas and the bulk are shown in figs 5.54 to 5.57. According to the X-ray maps the N, O and Al concentrations were high in the oxide scale where some Cr was also detected that would be attributed to Cr_2O_3 formation, as suggested by the XRD. Below the scale in the diffusion zone the Ni, Co and Cr contents increased. The Ni and Al concentrations were high in the β intermetallics. The γ-Ni_{ss}+γ'-Ni_3Al areas were rich in Ni, Co and Cr but the Ni content was lower than in the β-NiAl and the Co and Cr were lower than in the σ-phase. The brighter regions in the Ta maps corresponded to the white phases in the diffusion zone and bulk, whereas for Y the lighter contrast in the maps indicated the white phase or internal oxidation. The Hf appeared to be associated with Ta and Y.

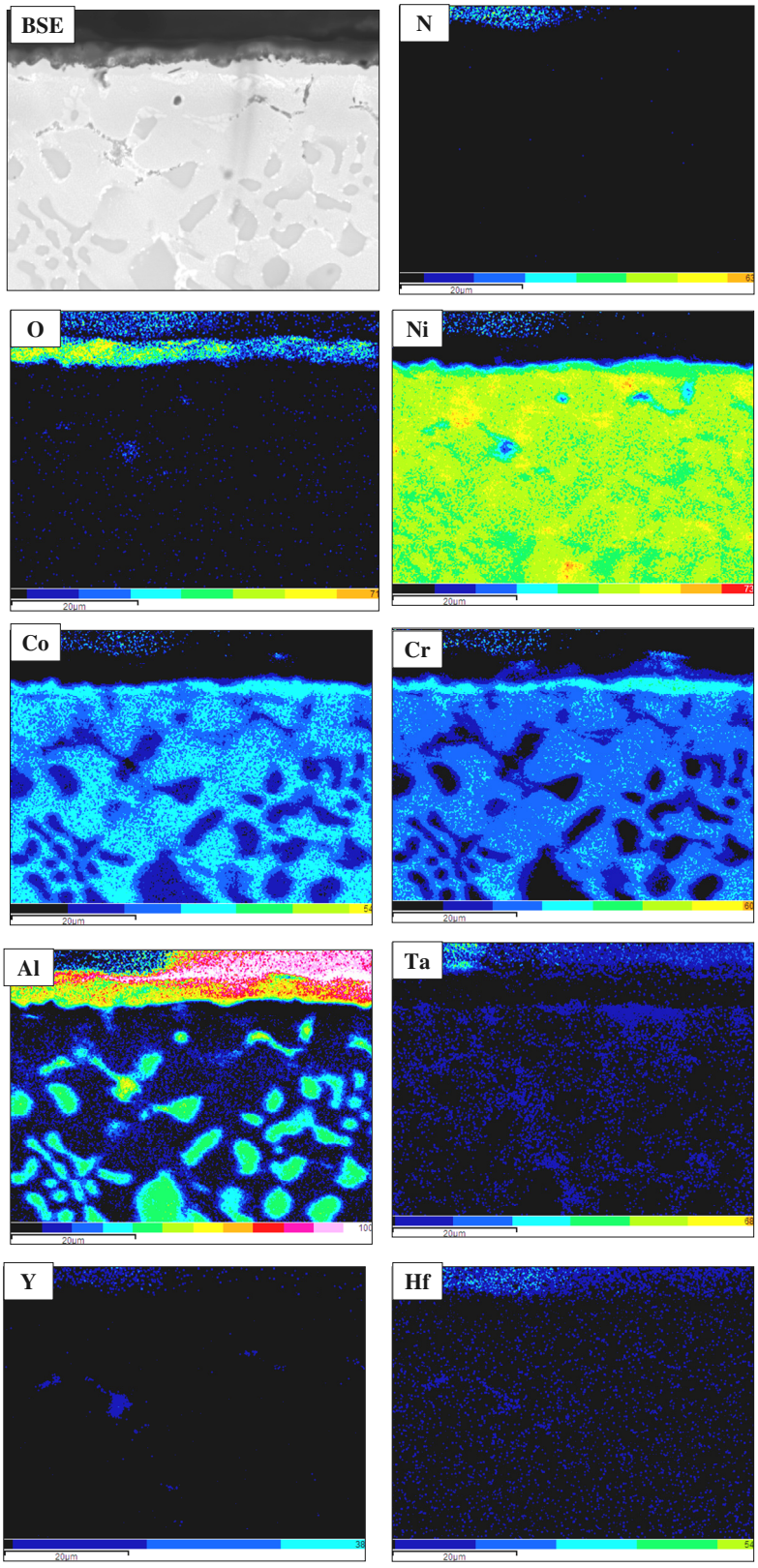

Figure 5.56 BSE image taken from the oxide scale and going towards the bulk of EK4-TGA alloy followed by quantitative elemental maps of N, O, Ni, Co, Cr, Al, Ta, Y and Hf.

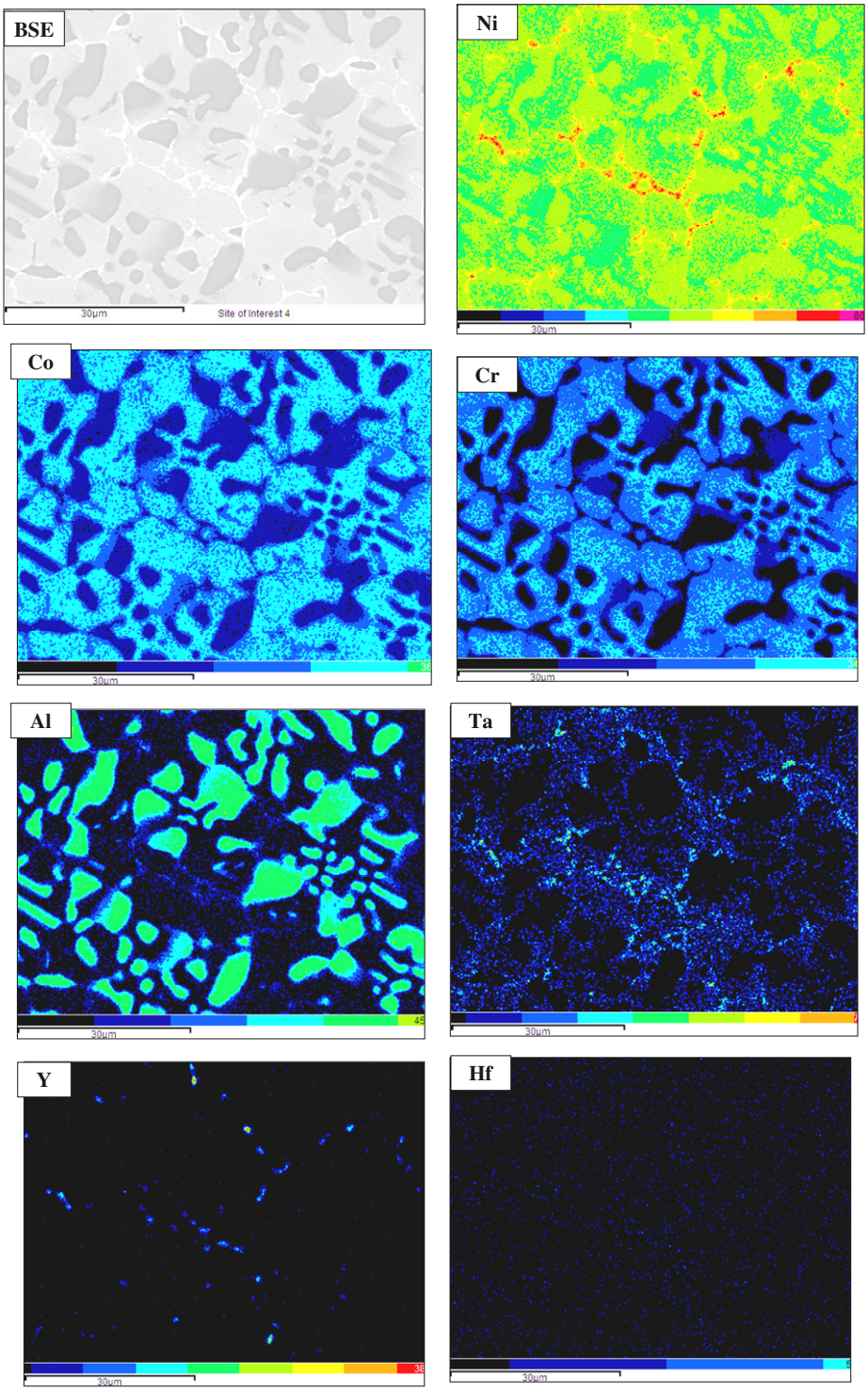

Figure 5.57 BSE image and quantitative elemental maps of N, O, Ni, Co, Cr, Al, Ta, Y and Hf taken from the bulk of the oxidised EK4 alloy.

The quantitative maps showed Ta, Y and Hf participation in the scale and Ta enrichment of the diffusion zone below the scale in the areas that were rich in Co and Cr. The Ni concentration increased in the σ-phase.

5.2.2.5 Ni-19.3Co-19Cr-15.6Al-1.1Ta-0.3Y-0.2Hf-3.5Si (alloy EK5)

5.2.2.5.1 Microstructure and glancing angle XRD

The surface of the oxidised EK5 alloy had the most uniform coverage by oxide scale with no cracks in the majority of the surface, no holes and no large growths of oxide, see fig. 5.58. The EDS studies suggested the presence of Al_2O_3 and SiO_2, Cr and Ta content in the latter and Cr in the former see figs 5.59 and 5.60. There were Al_2O_3 needles forming cauliflower like structures (see figure 5.61) and coarsen Al_2O_3 (see figure 5.60), probably due to the different transient types of aluminas.

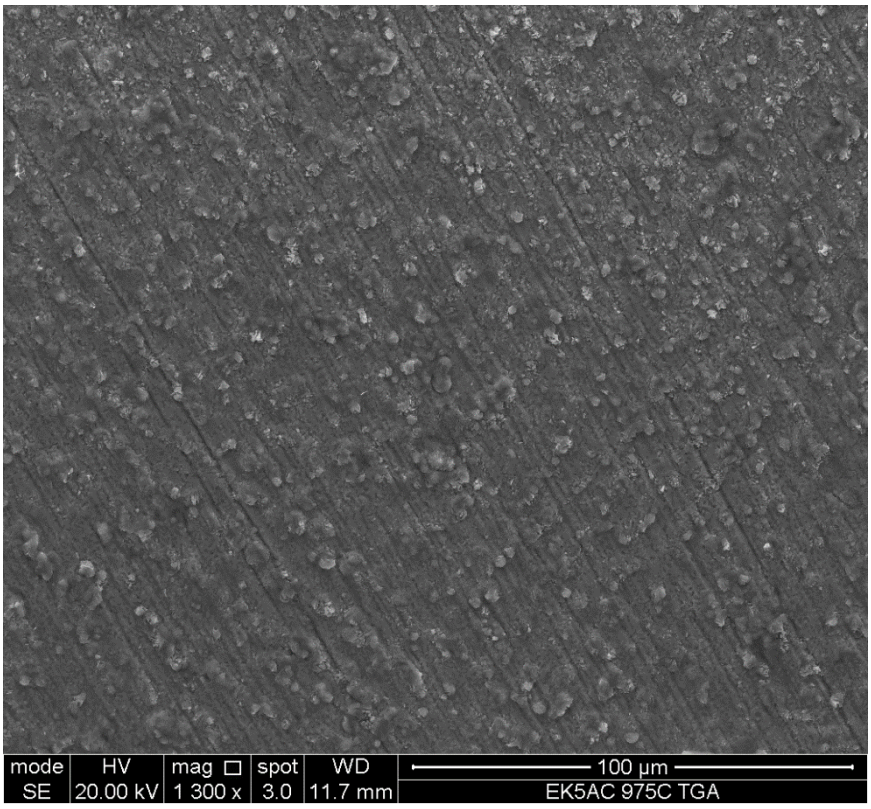

Figure 5.58 SEI image of the surface of the EK5 alloy oxidised at 975 ˚C for 100 hrs in air, showing a uniform oxide coverage with no large oxide growths.

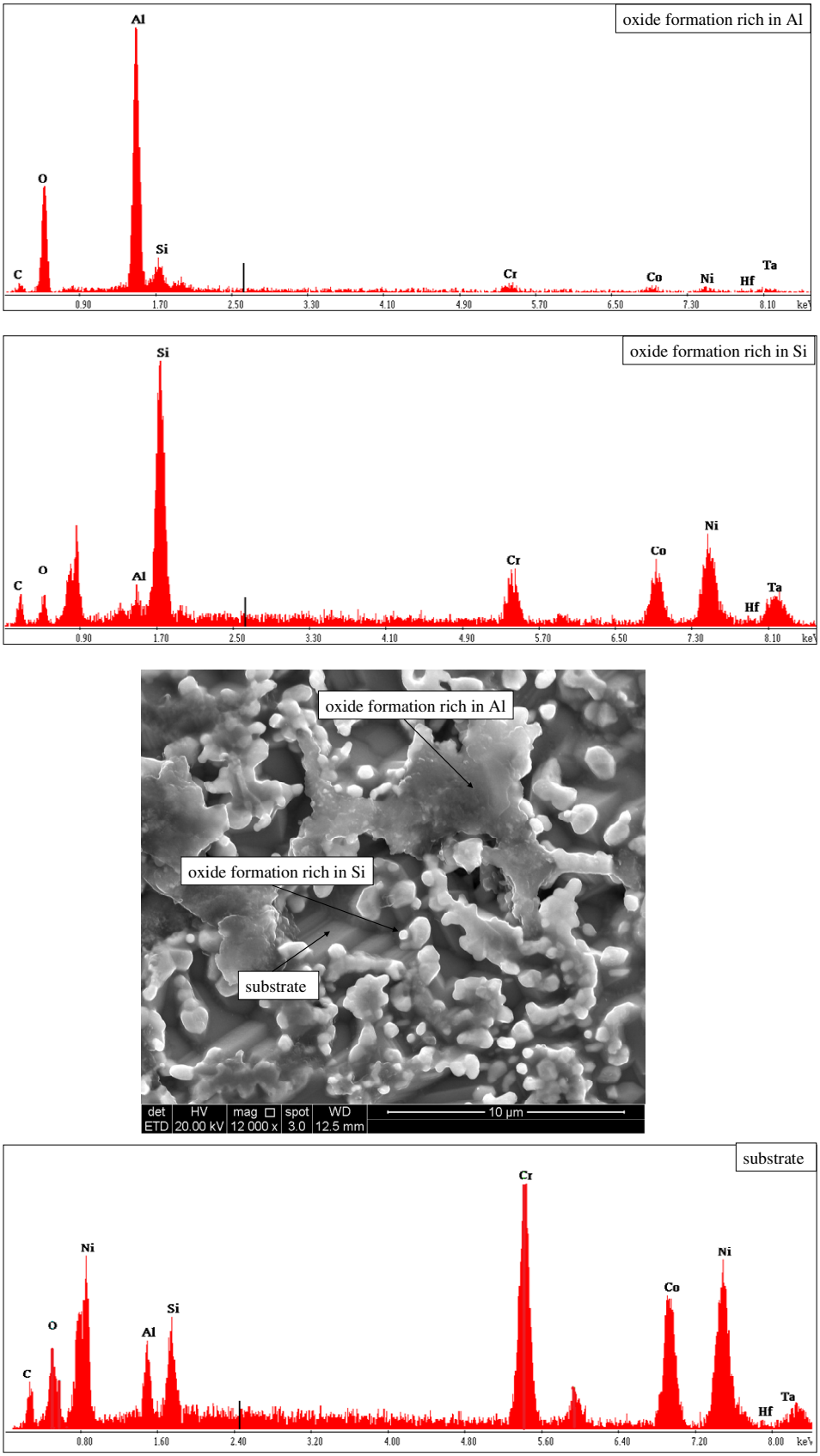

Figure 5.59 SEI image and EDS spectra showing different oxide formations and substrate in EK5.

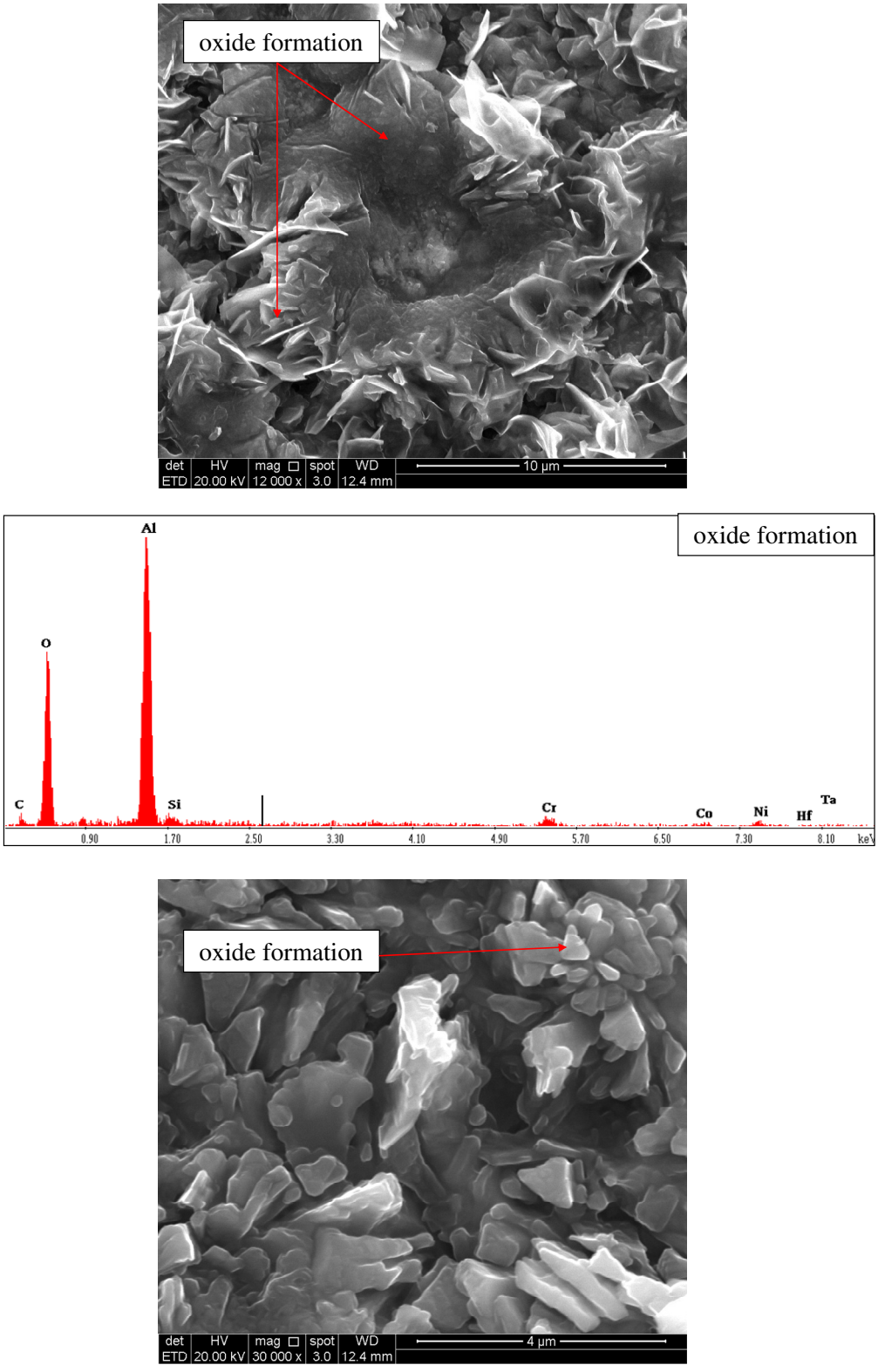

Figure 5.60 SEI images and EDS spectra showing different oxide formations.

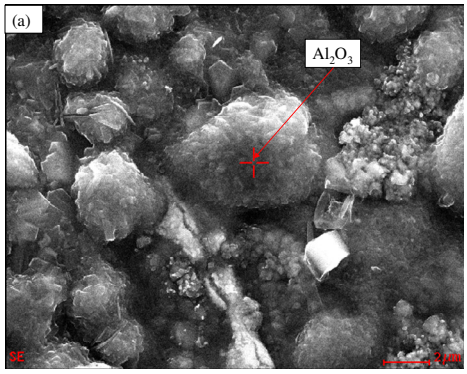

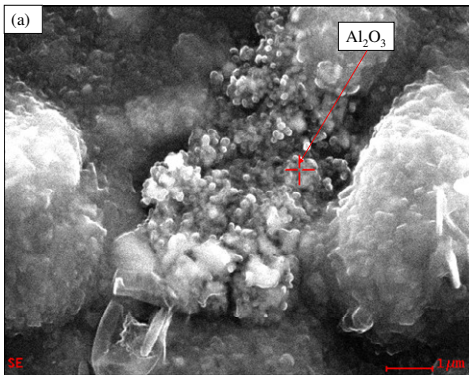

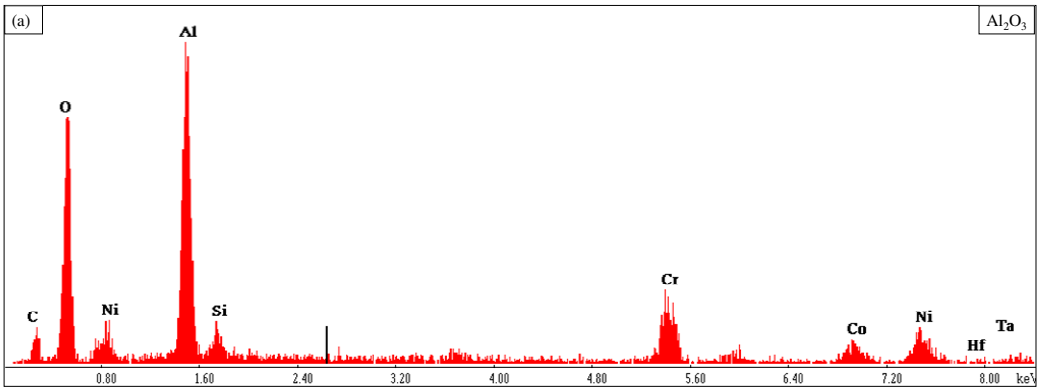

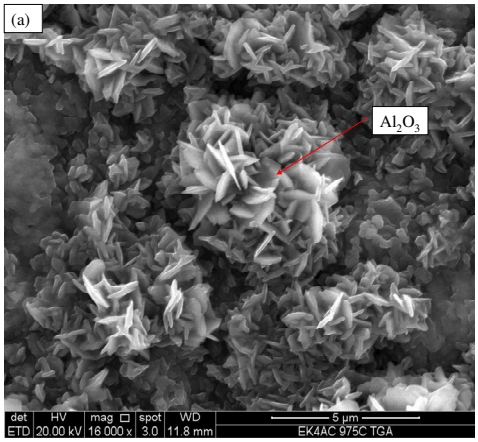

continued in the next page

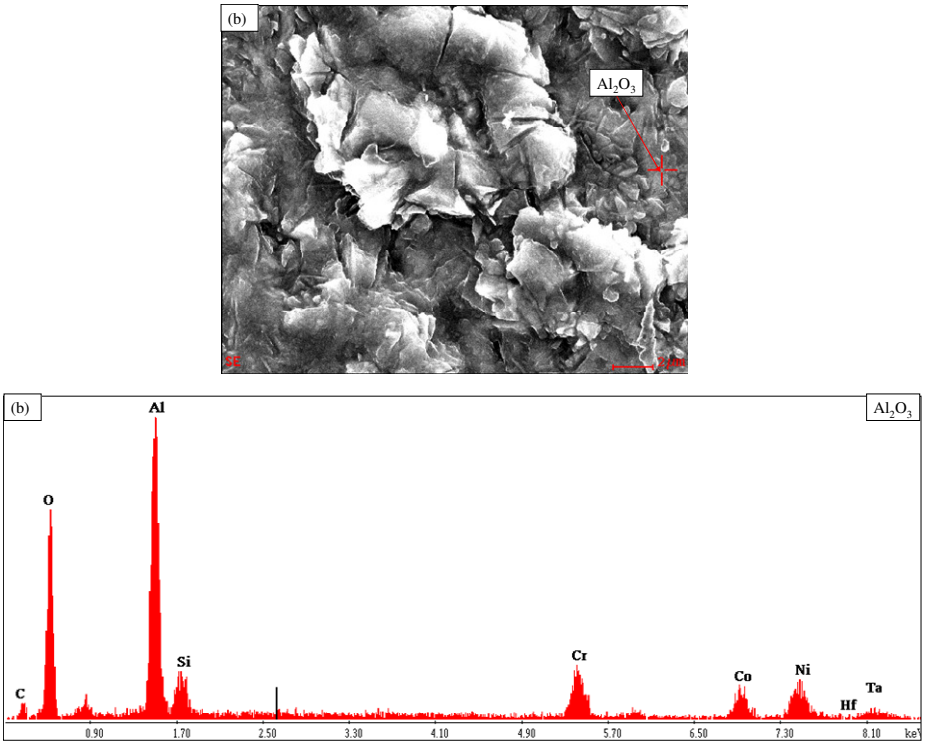

Figure 5.61 SEI images and EDS spectra showing different Al_2O_3 growths.

The glancing-angle XRD data is shown in figures 5.62 and 5.63. Peaks of the γ-Ni_{ss}, γ'-Ni_3Al and β-NiAl were present in the as cast condition and after oxidation. At the low glancing-angle there were peaks for θ-Al_2O_3 and α-Al_2O_3, the peaks for γ-Al_2O_3 coincided with those of the θ and α-Al_2O_3 and the peaks for Cr_2O_3 coincided with those of other oxides. For the higher glancing-angle there were peaks for γ-Al_2O_3, θ-Al_2O_3 and α-Al_2O_3 and Cr_2O_3. In both glancing angles the peaks for AlN and Cr_2N coincided with those of the oxides.

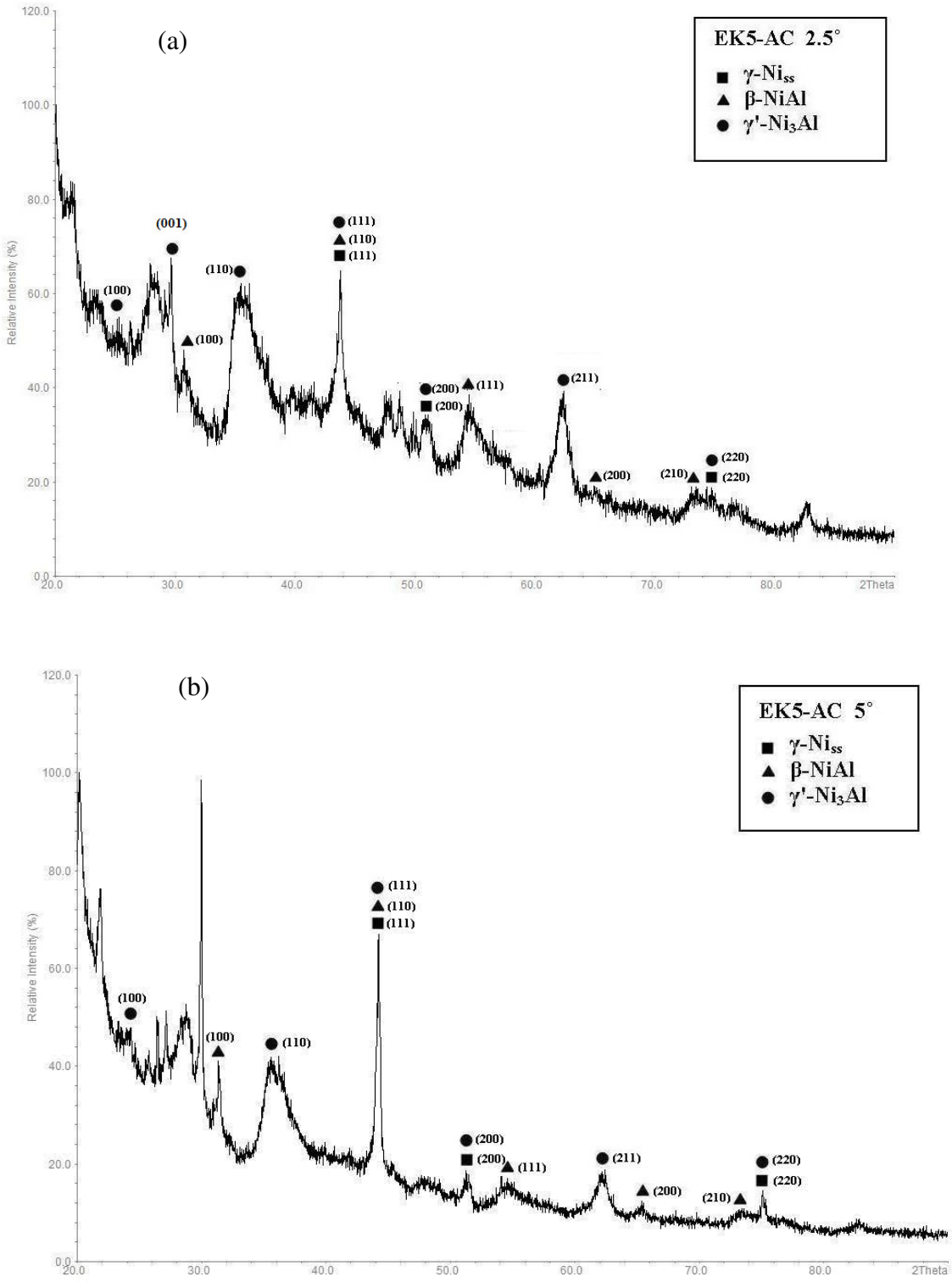

Figure 5.62 Glancing angle XRD data for the alloy EK5 before oxidation (a) γ= 2.5˚ and (b) γ= 5˚.

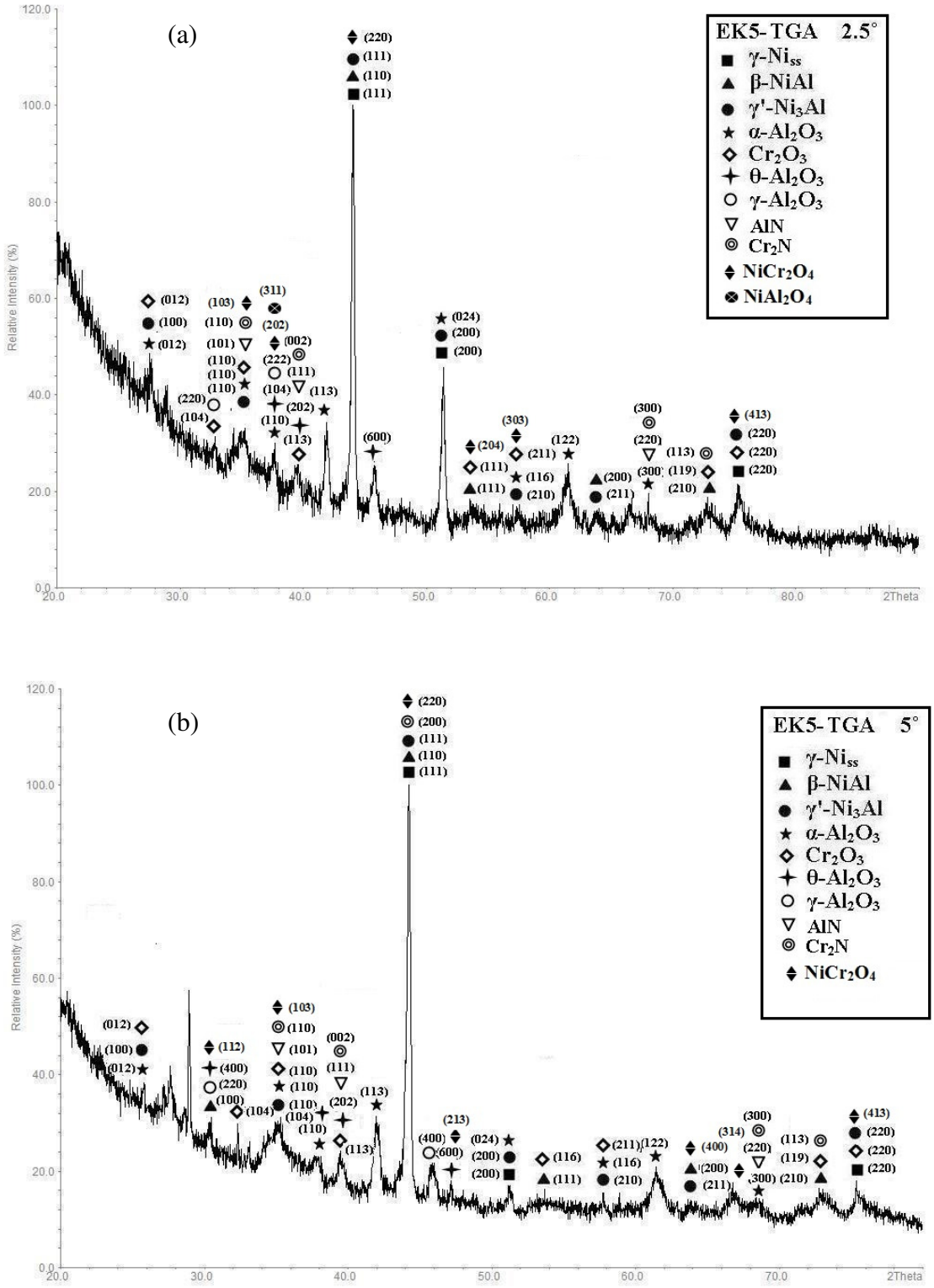

Figure 5.63 Glancing angle XRD data for the oxide scale formed on the alloy EK5 after oxidation for 100 hrs at 975 ˚C in air (a) γ= 2.5˚ and (b) γ= 5˚.

5.2.2.5.2 Microstructure of the oxidised alloy

The microstructures near the surface and in the bulk **of** the oxidised alloy EK5 are shown in fig. 5.64 and EDS spectra from different phases in these areas are given in figs 5.65 to 5.68. Quantitative WDS analysis is summarised in Table 5.10.

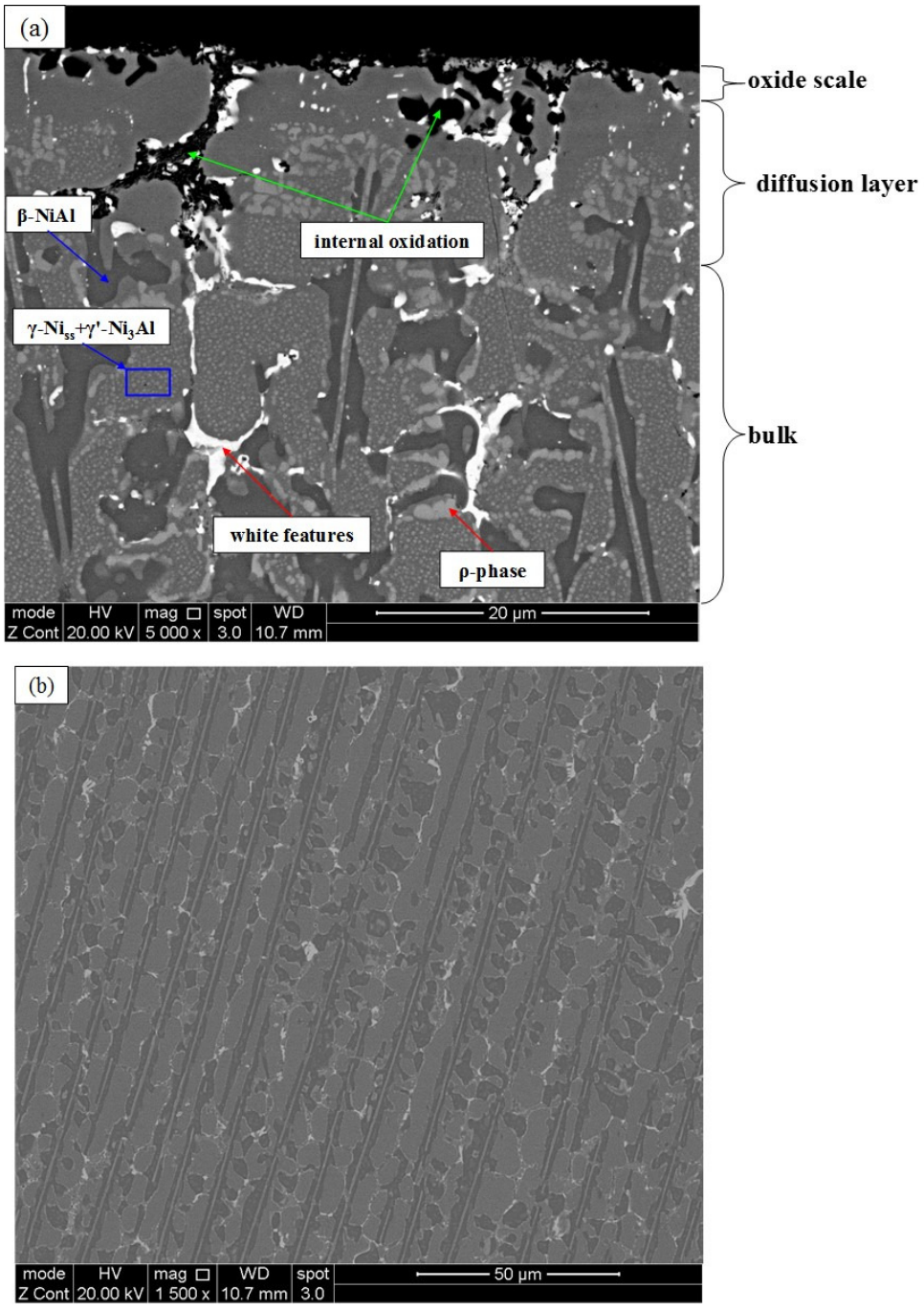

Figure 5.64 BSE images of the microstructure of the oxidised EK5 alloy (a) below the oxide scale and (b) in the bulk.

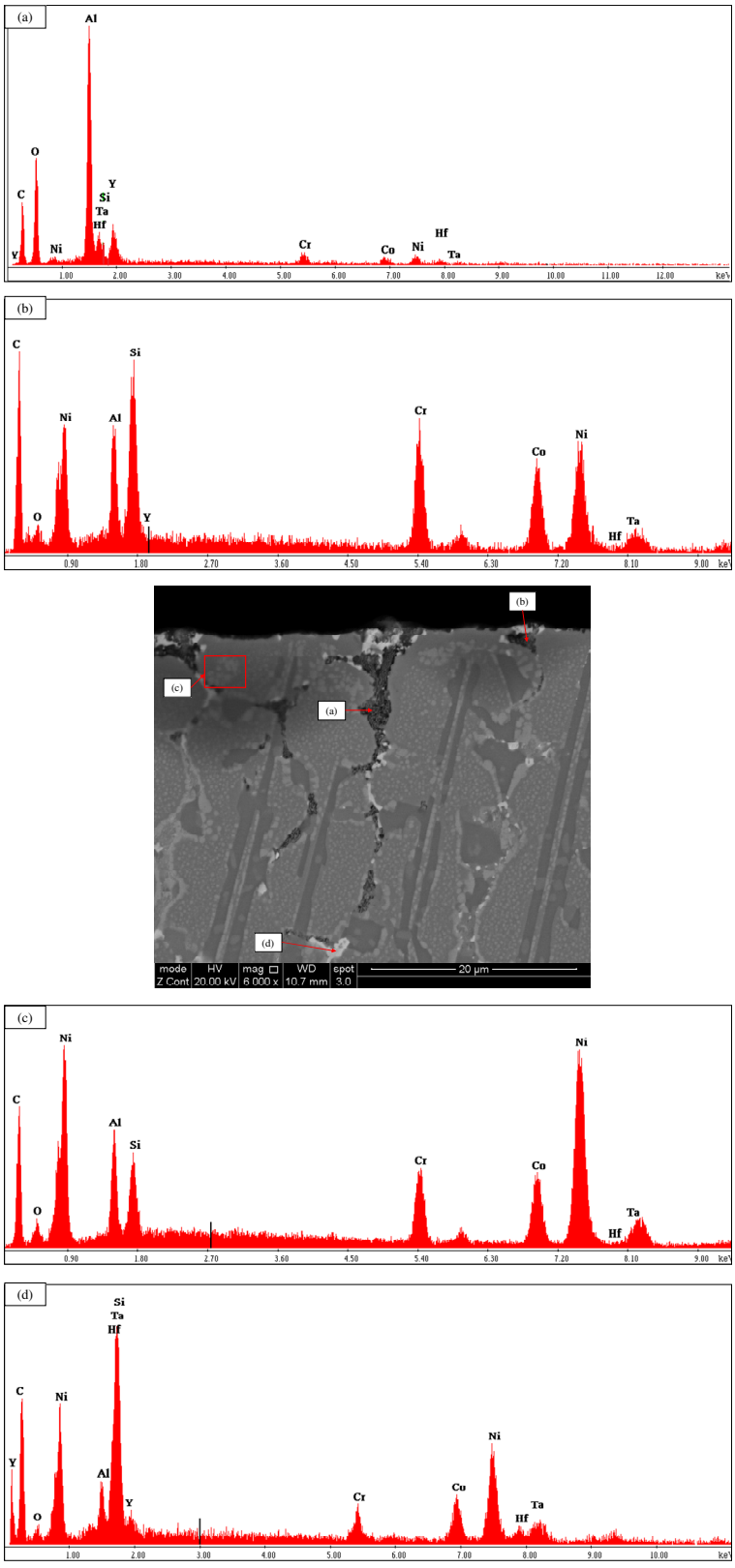

Figure 5.65 BSE images and EDS spectra taken near the surface of the oxidised EK5 alloy.

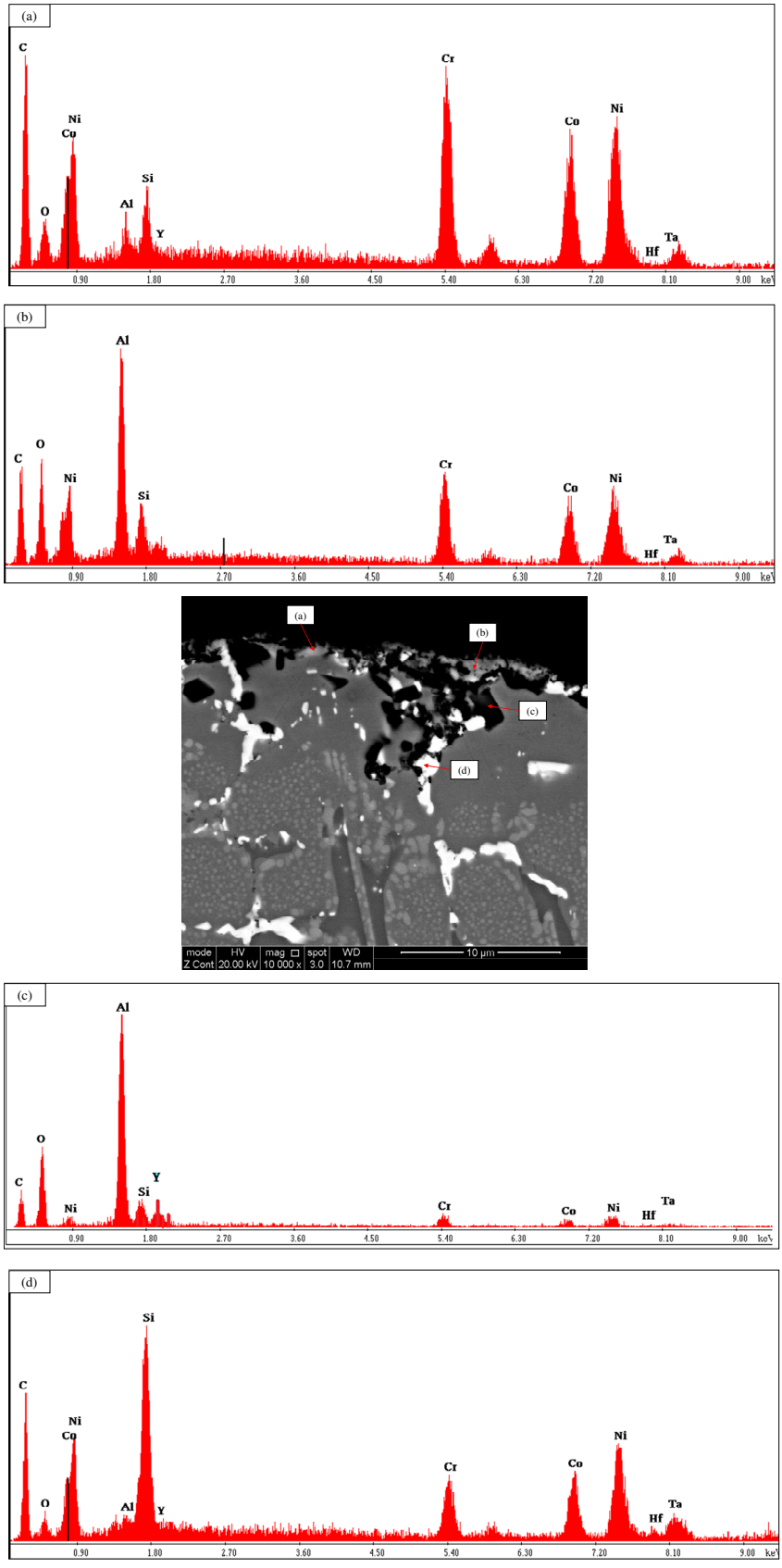

Figure 5.66 BSE image and EDS spectra from the microstructure near the surface of the oxidised EK5 alloy.

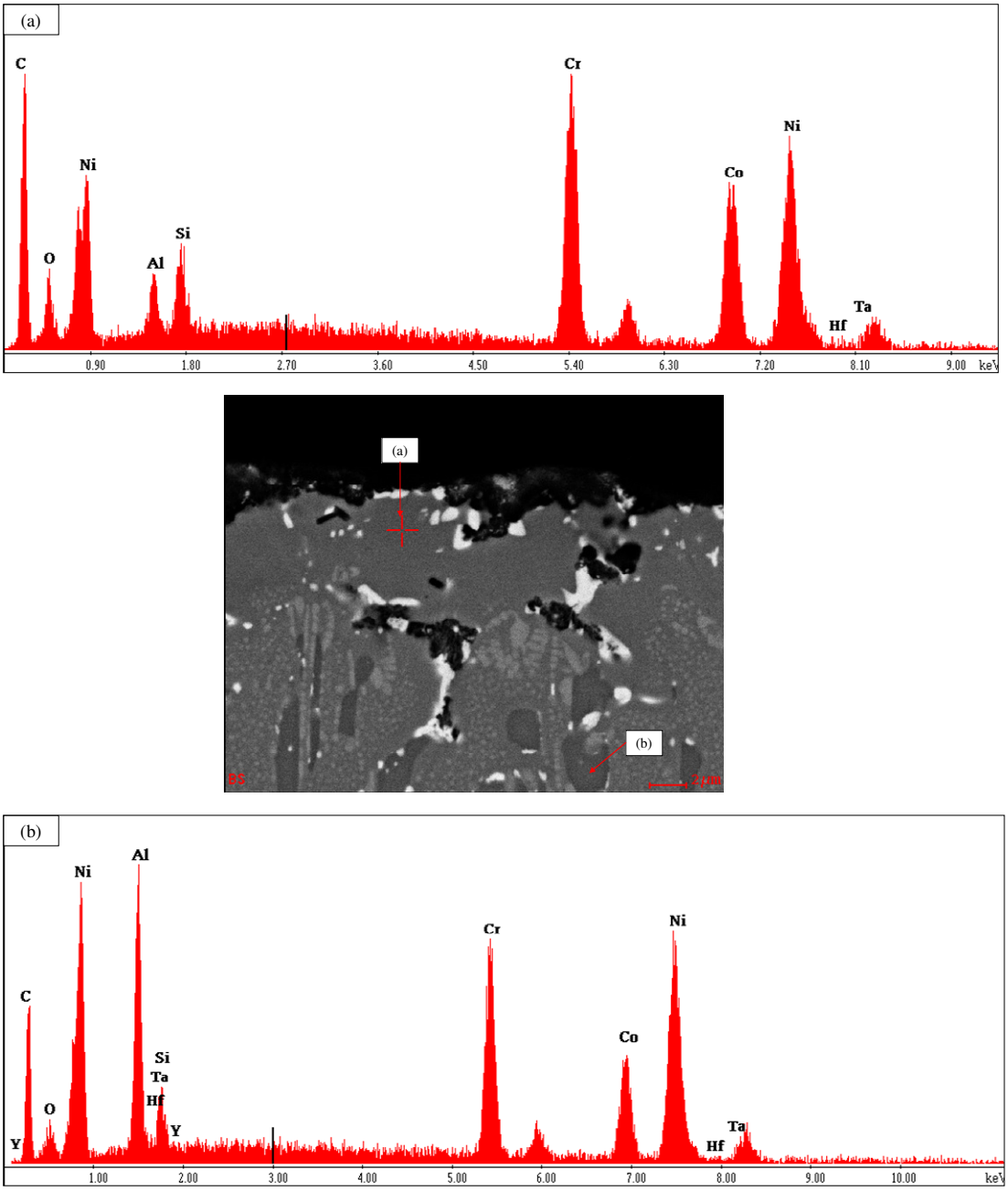

Figure 5.67 BSE images and EDS spectra taken near the oxide scale.

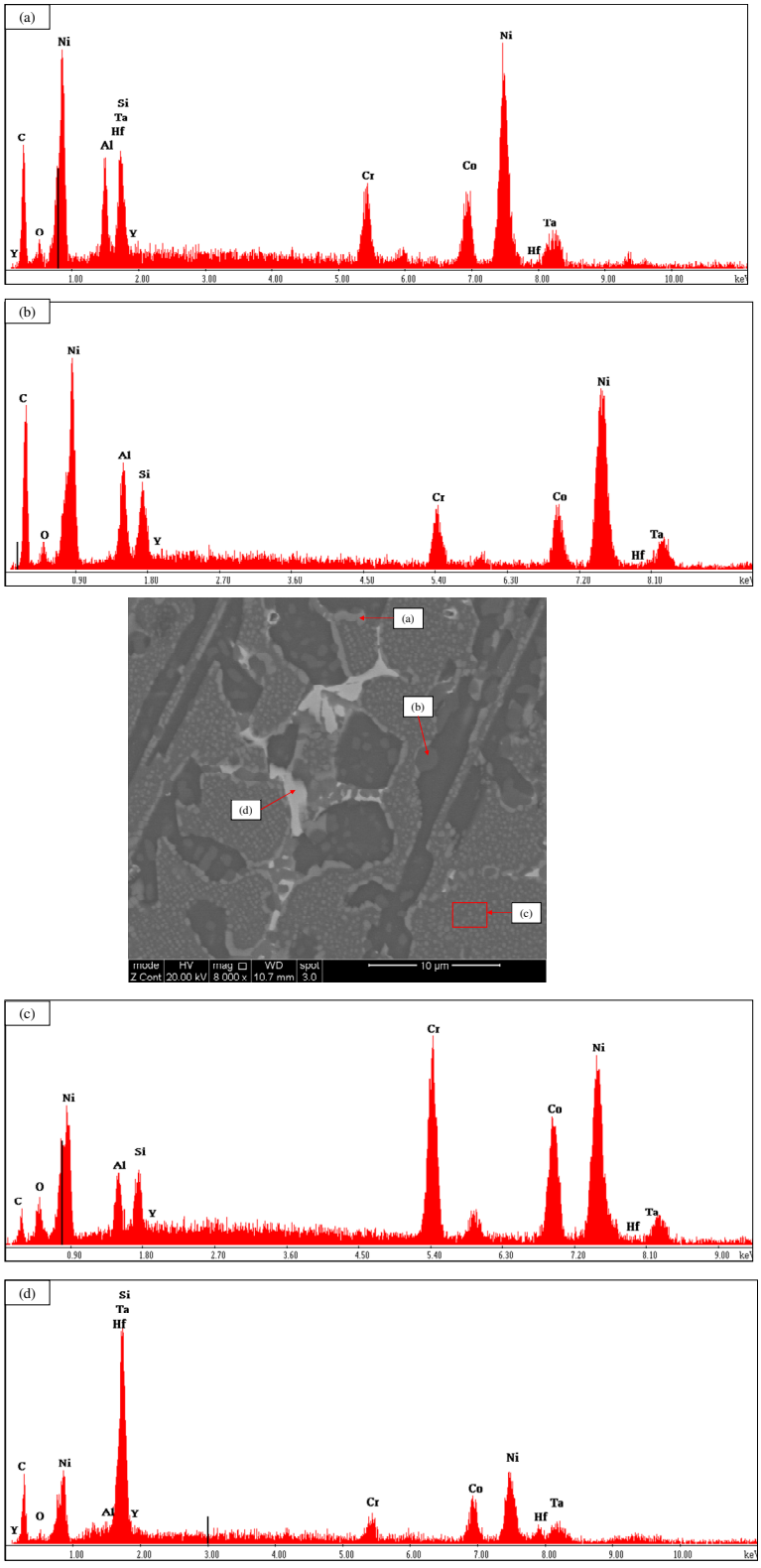

Figure 5.68 BSE image and EDS spectra taken from phases in the bulk of the oxidised EK5 alloy showing γ-Ni_{ss}+γ'-Ni_3Al, β-NiAl and three other phases with different contrast one rich in Ni, Al, Si, Hf and Ta, one rich in Ni, Al and Si and another with brighter contrast and rich in Si, Hf and Ta.

Table 5.10 WDS analysis data (at %) of different peaks of the cross section of the EK5 alloy after oxidation at 975 ˚C for 100 hrs.

Area	N	O	Ni	Co	Cr	Al	Ta	Y	Hf	Si
oxide scale	0	56.1±1.9	0.2	0.2	0.8±0.1	46.8±1.8	0	0	0	0
internal oxidation	0.1	33.8±6	12.1±6.3	6.7±3.1	6.9±3.4	32.6±7.2	0.8±0.2	5±1.2	1.2±0.6	1.4±0.5
diffusion zone	8.1±2.2	1.2±0.3	32±0.7	23.8±0.7	26.8±1	3.6±0.9	0.1±0.05	0	0	4.4±0.3
ρ-phase in bulk	6.2±0.9	0.8±0.7	47.4±4.4	14.2±2.1	11.1±3.6	13.3±5.6	2.1±1	1.3±2.3	0	3.5±2.7
β-NiAl	6.4±0.8	1.1±0.4	43.5±1.9	10.2±0.7	6.5±1.7	30.3±0.8	0	0	0	1.8±0.2
$\gamma Ni_{ss}+\gamma' Ni_3Al$	7.4±1	0.5±0.08	37.5	21.1±0.3	20.9±0.5	8.4±0.9	1±0.5	0	0	3±0.7
bright/white features	9.8±1.7	2.6±1.4	34.6±5	14.8±0.6	9.3±2.3	5.6±1.2	6.5±2.5	1.3±1.2	2.7±1.1	12.5±3.3

The oxide scale was rich in O (56.1 at %) and Al (46.8 at %). There were internal oxidation areas which were rich in O (33.8 at %), Al (32.6 at %) and Y (5 at %). The diffusion zone was rich in Ni (32 at %), Co (23.8 at %), Cr (26.8 at %) and Si (4.4 at %). A phase resembling the σ-phase was formed in the diffusion zone and in the bulk. This phase was rich in Ni (47.4 at %), Co (14.2 at %), Cr (11.1 at %), Al (13.3 at %) and Si (3.6 at %). WDS analyse in the bulk gave γ-Ni_{ss}+γ'-Ni_3Al with Ni 37.5 at%, Co 21.1 at% and Cr 20.9 at% and β-NiAl with Ni (43.5 at %) and Al (30.3 at %). The white contrast phases in the microstructure had the highest N (9.8 at %) concentration of all the phases present in this alloy as well as high Ni (34.6 at %), Co (14.8 at %) and Si (12.5 at %) contents. The highest Ta, Hf and Si contents were observed in the white phase.

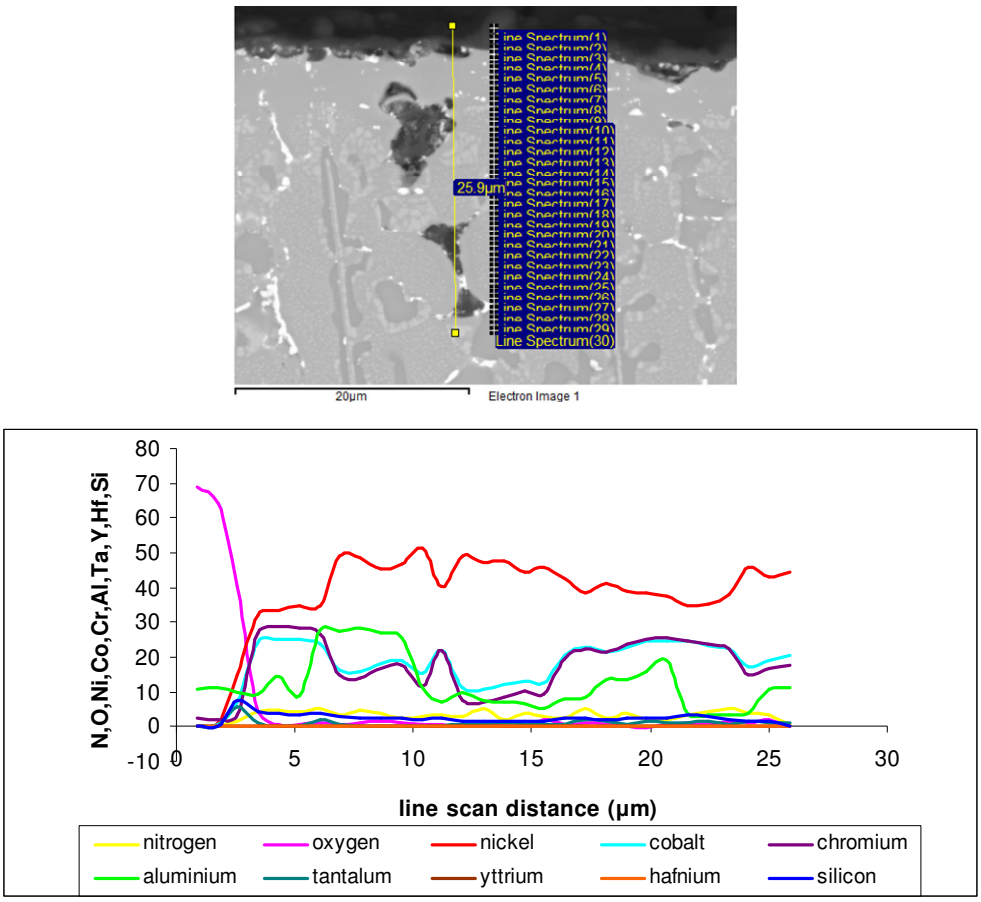

Figure 5.69 BSE image of cross section showing distributions (detected by WDS) of Ni, Co, Cr, Al, Ta, Y, Hf and Si as a function of distance from the surface.

Figure 5.69 shows elemental distributions along a cross section of the EK5 alloy after oxidation as a function of distance from the surface to the bulk. Figs 5.70 and 5.71 show qualitative and quantitative elemental maps for the near the surface areas and figs

5.72 and 5.73 for the bulk. The oxide scale was rich in Al, O and N and the quantitative maps also indicated the presence of Cr, Ta, Hf, Y, Si and Ni. Beneath the scale the O and Al levels were reduced and the Ni, Co and Cr levels were increased. To around 5 μm below the surface these levels remained stable as the scans went through γ-Ni_{ss}+γ'-Ni_3Al phases. When the scan crossed the internal oxidation areas the Al levels were slightly increased and the Ni, Co and Cr levels were decreased. The elemental maps in figs 5.70 and 5.71 also indicated Cr, Si and Co enrichment and Ni and Ta depletion below the scale. The elemental maps in figs 5.72 and 5.73 confirmed the presence of O, Al, Y, Si and Hf in the internal oxidation areas.

The Ni maps showed that the highest content was in the β intermetallics where the Al content was also high but always lower than in the oxide scale and internal oxidation areas. From the Co and Cr maps it was noticeable that in the diffusion zone these elements appeared to be in high concentration, then these concentrations decreased slightly in the ρ-phase and more in the γ-Ni_{ss}+γ'-Ni_3Al. The highest Ta content was in the white features formed below the surface and in the bulk whereas significant amounts of Ta were found very close to the oxide scale. Regarding the Y, Hf and Si these elements seemed to concentrate in the white features and close to the internal oxidation areas whereas the Ta, Y and Si showed significant amounts in the ρ-phase too, which was in agreement with the WDS data, see in Table 5.10.

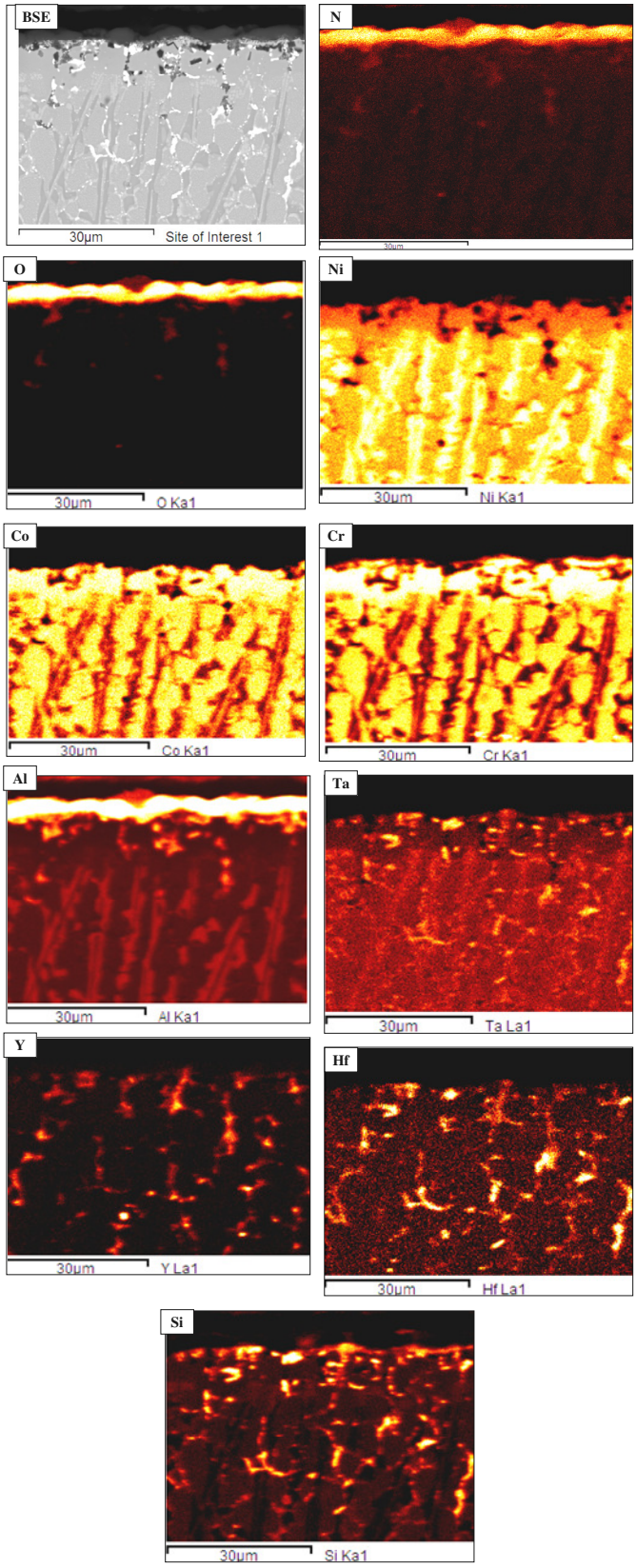

Figure 5.70 BSE image and qualitative elemental maps of N, O, Ni, Co, Cr, Al, Ta, Y, Hf and Si taken from the area near the oxide scale of the oxidised EK5 alloy.

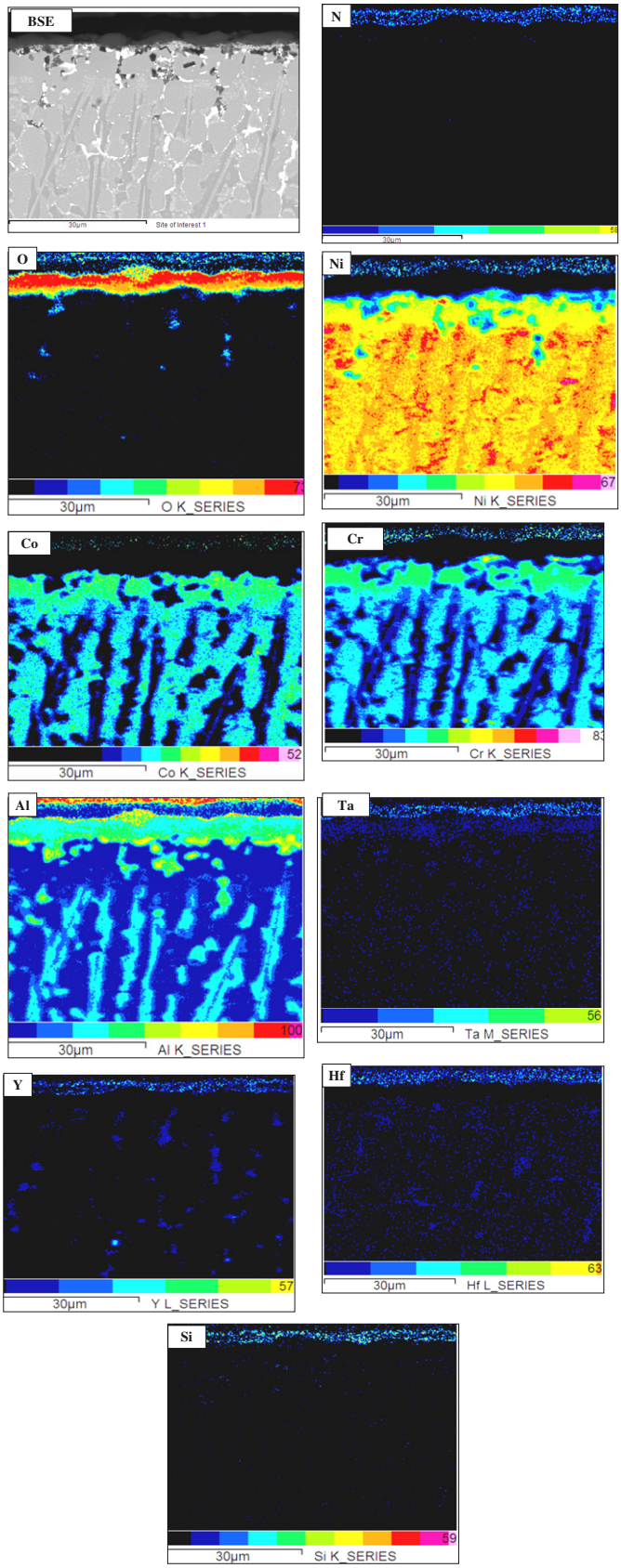

Figure 5.71 BSE image and quantitative elemental maps of N, O, Ni, Co, Cr, Al, Ta, Y, Hf and Si taken from areas near the oxide scale of the EK5 alloy.

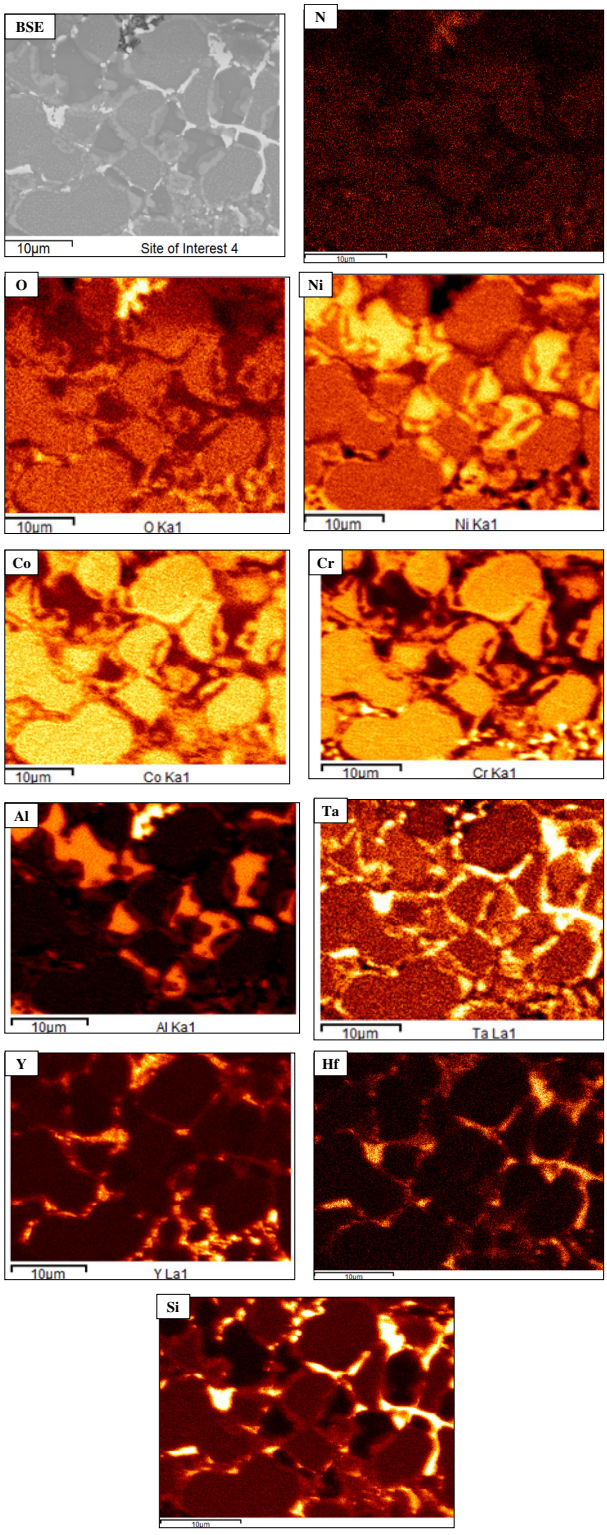

Figure 5.72 BSE image and qualitative elemental maps of N, O, Ni, Co, Cr, Al, Ta, Y, Hf and Si taken from the bulk of EK5 alloy.

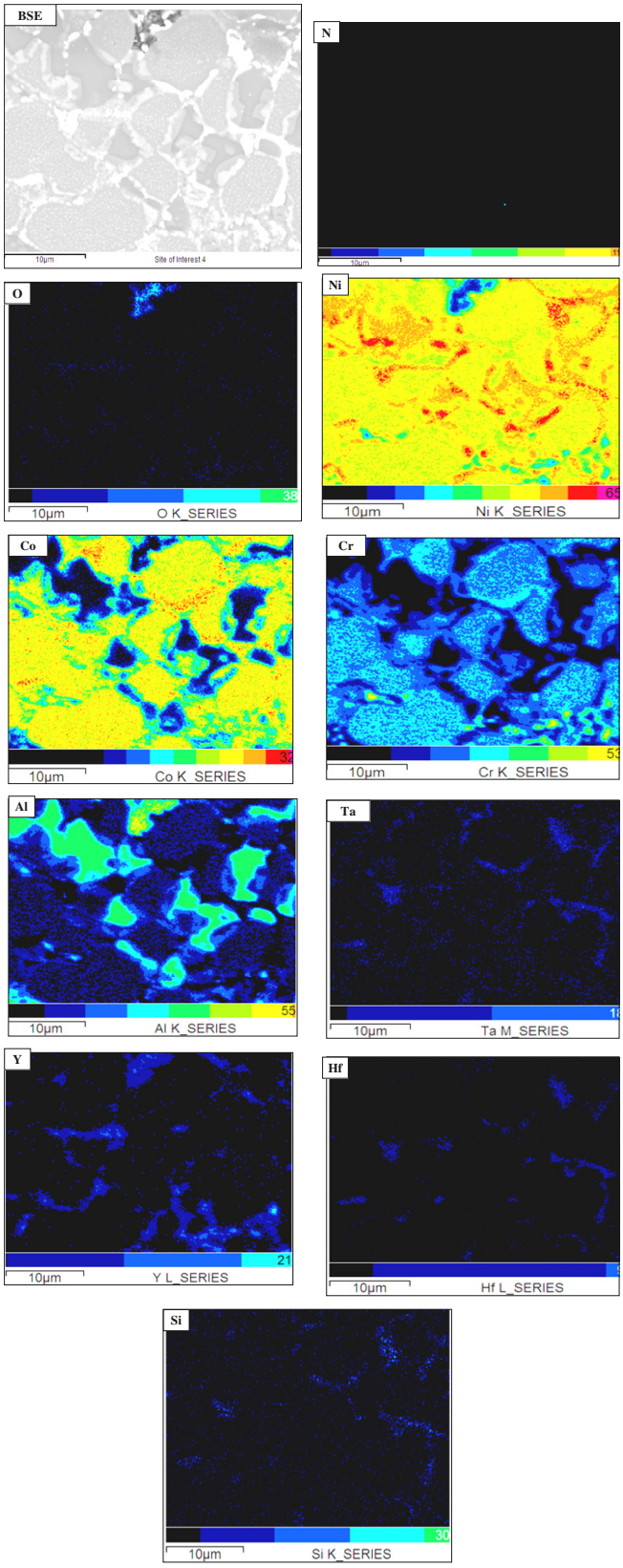

Figure 5.73 BSE image and quantitative elemental maps of N, O, Ni, Co, Cr, Al, Ta, Y, Hf and Si taken from the bulk of EK5 alloy.

5.3 Discussion

The multicomponent alloys of this study were designed to resist type I and type II high temperature corrosion and form alumina scales, in particular the desirable α-Al_2O_3. The key alloying elements in the alloys were the Al and Cr. The alloys were designed to have Al rich oxidation resistant Ni intermetallic phases, such as β-NiAl and γ'-Ni_3Al, and the Ni solid solution (γ-Ni_{ss}) in their microstructures. There is solubility of Al and Cr in all three phases.

The β-NiAl, γ'-Ni_3Al and the γ-Ni_{ss} would be the "reservoirs" of Al and Cr and were expected to "ensure" the formation of alumina scale on the alloys. Since Cr_2O_3 forms a complete solid solution with Al_2O_3, it was expected that Cr would dissolve in Al_2O_3 and not segregate on its grain boundaries. As the scale formed, depletion of species in the microstructure below the scale could lead to phase transformation(s), for example formation of leaner in Al and/or Cr phases, which in turn could affect scale formation on the alloy when cracks in the scale exposed the substrate to the oxidising environment. Thus, scale chemistry (e.g., type(s) of oxide(s)), structure (e.g., continuity and uniformity) and performance upon cooling from the oxidation temperature (e.g., adhesion), would be affected by the whole microstructure (size, volume fraction and distribution of phases and their chemistry) and the way the latter "evolves" below the scale as oxidation proceeds, in other words not just by the presence of Al and Cr in the alloy and the concentrations of these elements in the relevant phases in the alloy.

In designing/selecting the alloys of this study and for interpreting their oxidation behaviour a vast literature on the oxidation of alumina and chromia forming alloys had to be taken into account. Some of the important issues regarding phase equilibria, the effects of alloying on oxidation rate, oxide grain size, oxide adhesion and oxidation mechanism and subscale phase formation are highlighted below and the discussion expands on the most important ones later on when the results reported in this chapter are considered.

According to the Ni-Al-O ternary, at 800 – 1400 °C the α-Al_2O_3 is in equilibrium with all Ni aluminides and according to the NiAl-Cr-O ternary the NiAl is not in equilibrium with Cr_2O_3 oxide; they interact to form a reaction zone of variable composition $Al_{2-x}Cr_xO_3$ and Ni_3Al [Povarova et al, 2007].

In Ni-Al based alloys the addition of reactive elements (see below) is reported to be very effective. In chromia forming alloys, the addition of Y (e.g. in FeCrAl with Y added

as Y_2O_3) leads to reduction of oxidation rate, decrease of the oxide grain size, improvement of oxide adhesion and change of the oxidation mechanism to anion diffusion [Whittle and Stringer, 1980]. In alumina forming alloys with Y addition changes in the microstructure of the oxide and improvement of its adherence have been reported but the reduction in oxidation rate is about a factor of 2 or less compared with $_X$10 to 100 reductions in chromia forming alloys. When Y is the RE addition, the change in oxidation behaviour has been linked with its interaction with sulphur (see below) and/or its segregation in g.bs (see below).

Reactive elements also affect oxide morphology (see below) and oxide type (see below). In the case of NiAl with/out Y addition the scale formed at 1000 °C on the alloyed intermetallic consisted of plates and whiskers of θ-Al_2O_3 as compared with nodules in the un-alloyed phase that formed α-Al_2O_3 [Pint et al. 1991]. For NiAl the θ-Al_2O_3 → α-Al_2O_3 transformation occurs below 1000 °C [Rybicki and Smialek, 1989] while for T > 1000 °C the θ-Al_2O_3 forms first and then transforms to α-Al_2O_3. Pint et al (1991) suggested that the θ-Al_2O_3 → α-Al_2O_3 transformation may explain the conflicting results about the growth mechanism for alumina scales: θ-Al_2O_3 growing by Al transport out and α-Al_2O_3 by oxygen transport in. In the isothermal oxidation at 1000 °C of NiAl+ Al_2O_3 with/out Y the oxidation product was α-Al_2O_3 in both cases but the addition of Y changed the scale morphology as it led to the disappearance of the ridge structures [Xu et al, 2011]. In isothermal oxidation at 900 °C, 1000 °C and 1100 °C of a sputtered NiCrAlY coating the θ-Al_2O_3 → α-Al_2O_3 transformation was faster as the oxidation temperature increased.

Cross sections of oxidised specimens consisted of the substrate, a diffusion layer, a zone below the scale and the scale. During oxidation the β-NiAl transformed to γ′-Ni_3Al and γ-Ni_{ss} [Li et al, 2003]. Zhang et al (2011) reported that γ′-Ni_3Al formed in the vicinity of the NiAl/γ-Al_2O_3 interface after 1 h oxidation at 750 °C and that the formation of γ′-Ni_3Al coincided with significant void formation. Subsequent study by Zhang et al (2012) of oxidised NiAl (110) showed that at T > 850 °C or T < 650 °C the γ′-Ni_3Al was not formed below the surface after 1 h. They concluded that in cases where subsurface formation of the γ′-Ni_3Al occurs during the early stages of oxidation its existence can be transient, as shown by the results for oxidation at 750 °C.

Oxidation can affect the mechanical behaviour of NiAl. Noebe and Gibala (1995) reported surface film softening of NiAl based on their study of oxidised impure non-

stoichiometric NiAl single crystals with axial orientation near [123]. They observed softening at room temperature in compression. The softening increased with oxide thickness and the amount of softening appeared to be related to the stress state of the oxide. The flow stress was ~ 20% lower and the strains to failure were larger than that of the un-oxidised specimen. In a few instances the ductility enhancement was as much as four times. The larger effect was observed at 1000 °C with 350 nm δ-Al_2O_3. Overall the softening effect observed for the α-Al_2O_3 was small compared with that seen for the $NiAl_2O_4$ spinel.

The magnitude of the thermal stress σ in an oxide can be estimated from $\sigma = [E\Delta T(a_c - a_m)]/(1-\nu)$ where σ is assumed to be biaxial ($\sigma \approx \sigma_x \approx \sigma_y >> \sigma_z$), E is the elastic modulus, ν is the Poisson ratio, a_c is the CTE of the oxide and a_m the CTE of the substrate and ΔT is the temperature difference between the oxidation and ambient temperatures [Oxx, 1995]. For α-Al_2O_3 the E is significantly larger than that of the spinel but the a_c values are essentially the same [Kingery et al, 1976]. Therefore the stress σ will be greater in α-Al_2O_3 compared with the spinel.

In order to be protective, the scale formed on a high-temperature structural material should be dense, slow-growing and adherent [Yang et al, 2001]. Experimental work has shown that the adhesion of the α-Al_2O_3 scale significantly improved by alloying additions. Calculations by Jarvis and Carter (2002) based on Density Functional Theory (DFT) of the ideal cleavage energy at 0 K of Ni (111) and Al_2O_3 (001) gave values respectively about 3800 and 3000 mJ/m^2. The calculated values for the adhesion of ideal Ni/Al_2O_3 interfaces with increasing Al_2O_3 thickness were 618, 943 and 456 mJ/m^2 respectively for one, two and three layer coating. The latter values are very weak indicating that the alumina/Ni interfaces of a Ni substrate with Al_2O_3 are unfavourable and that the metal/ceramic adhesion dramatically decreases for the thickest oxide films. However, DFT based calculations showed that alloying (doping) the substrate with early transition metals improves adhesion of Ni/Al_2O_3 interfaces by a 100 percent increase. The interface adhesion values for doped Ni/Al_2O_3 interfaces with half-monolayer element doping were 1882, 1493, 1244, 3242, 3685 and 3213 mJ/m^2 respectively for Ni, Al, Si, Y, Ti and Zr. These values show, for example, that the Al_2O_3 interface doped with Ni is stronger than the ideal Ni/Al_2O_3 interface and the strong effect of Y.

As an oxide scale grows, stresses invariably develop. Although the mechanisms by which scale failure may eventually occur depend on factors such as the particular material

being oxidized (see above), its surface preparation, the oxidation conditions and the presence of impurities (alloying additions), there is a prevailing consensus that failure occurs when the stored elastic strain energy in the scale (the product of the scale thickness and the square of the stress) attains a critical value. Therefore, the stress state in an oxidized scale is a critical parameter in predicting the loss of integrity of the scale, and hence in assessing the long-term protection afforded by the underlying alloy. Because scale failure can occur under a wide range of oxidation conditions, there has been considerable interest in identifying the mechanisms by which stresses develop within a growing oxide scale. At any instance in the thermo-mechanical history of the scale-alloy system, the stress represents a complex interaction between several contributions: the growth stresses, mediated by diffusional stress relaxation and augmented by thermal expansion mismatch. The results show that, after a transient period, the stress in the oxide scale is essentially independent of oxidation time. This is attributed to a steady-state balance being established between the rate of stress relaxation by diffusional flow and the rate of stress generation.

The value of the steady-state stress is expected to depend on the diffusional flow properties of the alumina scale and hence on its grain size, porosity and impurity (dopant) level. The transient period is attributed to the formation of a continuous α-Al_2O_3 scale from initially metastable alumina phase(s). The growth stress in the alumina grains is deduced to be tensile during this transient period. The tensile strain is attributed to the molar volume change associated with the transformation to α-Al_2O_3. While it is generally understood that the alumina scales on pure NiAl grow primarily by the outward diffusion of aluminium at early times and a combination of inward diffusion of oxygen and outward diffusion of aluminium at later stages, the growth rate of new oxide is not homogeneous through the scale thickness [Lipkin et al, 1997]. Cracking and spallation are the main modes that weaken the protective properties of the scale because they can expose the sub-surface of the matrix to the atmosphere and lead to secondary oxidation. For NiAl-based materials, the cracking of the scale is mainly caused by two factors, thermal stress and the transformation of transition (metastable) aluminas to α-Al_2O_3. During cooling, due to the mismatch of the coefficients of thermal expansion (CTE) (~ 8-9*10^{-6} C^{-1} for α-Al_2O_3 and ~ 13-16*10^{-6} C^{-1} for MCrAlY [Wright and Evans, 1999]), there is a large thermal stress between the scale and the matrix, which can induce cracking during oxidation.

Spallation of scale is caused by the cracking and formation of voids. During oxidation, the stable α-Al_2O_3 scale forms through diffusion involving simultaneous

outward diffusion of Al and inward diffusion of O. The consumption of Al near the matrix/scale interface causes Ni diffusion to the bulk to compensate for the Al depletion and consequently leads to formation of voids along the matrix/scale interface. These voids reduce the contact between the scale and matrix and weaken the adhesion of the scale [Brumm and Grabke, 1993].

The above considerations were taken into account when designing (selecting) the alloys to be studied in this thesis. Thus, in this work, the effects of alloying with a refractory metal (Ta), reactive elements (REs) Hf and Y, and Si on phase stability, architecture of microstructure (size, volume fraction and distribution of phases) and oxidation behaviour were studied. The characterisation of the microstructures gave particular emphasis on the analysis of the chemical compositions of the phases present in the cast and heat treated conditions and in particular on the parameters Al/Cr and Al + Cr in β-NiAl (see Table 4.9), as well as on the volume fractions of the β-NiAl and Ni (see Table 4.14). The microstructure characterisation work also sought to determine the compositions of the β-NiAl and Ni_{ss} after oxidation (see below) and to investigate the microstructure below the scale in order to establish which phase(s) supplied the Al and Cr used in the formation of the scales.

Alumina scales are formed on Al-containing alloys by the faster species moving along its fastest path. In all the alloys of this study it was expected (i) that the scale formed in the early stages of oxidation would contain concentrations of the base alloy metals (in all alloys at ambient atmosphere a few nanometres thick oxide layer is present in their surfaces), (ii) that the concentrations of the base alloy metals would decrease as the scale developed into a complete layer of alumina, (iii) that the alumina would become "purer" as its thickness increased with oxidation time and (iv) that oxides or spinels of the base alloy metals might be incorporated in the final scale. The glancing angle XRD data for the alloys provided evidence that the (iv) was indeed the case as $NiCr_2O_4$ and/or $NiAl_2O_4$ were detected in the scales (see figures 5.7, 5.19, 5.34, 5.49 and 5.66). The WDS data from the study of cross sections of the oxidised alloy specimens confirmed the presence of alumina in all scales and that chromia and alumina in the scale formed on the alloy EK2 (see Tables 5.2, 5.7, 5.8, 5.9, and 5.10). It was also expected that concentrations of base alloy metals in the scale would vary from point to point owing to small grain size of base metal oxides or spinels formed during oxidation. In other words it was expected that the scale will be doped with elements present in the substrate.

In this work REs were added in low concentrations (aimed to be less than 1 at%) as dissolved metals (i.e., not as oxide dispersions). According to the literature, the REs have a strong effect on scale formation and improve oxidation (oxidation rates in Ni based alloys are reduced at least by a factor of 2). The effect of REs is stronger on the intermetallics of interest in this study. For example, Pint reported reduced oxidation rate by a factor of ~ 10 for NiAl alloyed with Hf [Pint 1998]. The distribution [Stringer and Hou, 1986] and concentration [Whittle et al, 1982] of REs are crucial for their effectiveness in the oxidation behaviour of an alloy. Furthermore, the same REs used in different alloy types may show different effects [Pint, 1998].

Reactive elements (REs) suppress the outward diffusion of Al, reduce scale formation kinetics and affect the θ-$Al_2O_3 \rightarrow \alpha$-$Al_2O_3$ transformation. For example, Y addition in NiAl reduces the formation of θ-Al_2O_3, enhances the nucleation of α-Al_2O_3 and accelerates the θ-$Al_2O_3 \rightarrow \alpha$-$Al_2O_3$ transformation [Grabke, 1999]. However, the latter has been disputed, for example by Pint et al, according to whom Y (like Hf) retards the transformation of metastable aluminas to α-Al_2O_3 [Pint et al, 1996]. Water vapour promoted the θ-$Al_2O_3 \rightarrow \alpha$-$Al_2O_3$ transformation in the work of Zhaohui Zhou et al (2011). However, the literature on the influence of water vapour on this transformation is contradictory.

Studies [Doychak and Ruhle 1989, Schumann and Ruhle 1994, Doychak et al 1989, Yang et al 1998] of the transformation of metastable (transition) aluminas in the oxidation of β-Ni(Al,Cr) and γ'-Ni_3(Al,Cr) have confirmed a nucleation and growth transition. First well-defined orientation relationships between transition aluminas and their substrates are established. The subsequent transformation of the transition aluminas to the stable α-Al_2O_3 occurs via nucleation at the scale-gas interface [Doychak et al, 1998] or the scale-metal interface [Doychak and Ruhle 1988, Schumann and Ruhle 1994]. Close packed planes in the transition aluminas are parallel to close packed planes in the α-Al_2O_3.

Regarding the intermetallic β-NiAl, slow growing Al_2O_3 scale with no Ni oxides and spinels forms on oxidised pure (unalloyed or un-doped) β-NiAl [Pettit, 1967]. The latter, however, is not a line (stoichiometric) compound, and when oxidised in its unalloyed form its parabolic rate constant decreases with decreasing Al content, which would suggest that the Al supply to the scale has an effect on its growth (see above). Formation of voids at the oxide/intermetallic (i.e., NiAl) interface has been reported. It should be noted that voids were observed in the scale formed on the alloys EK2-TGA

figure 5.15 and EK4-TGA figures 5.44 and 5.45 in this study and are attributed to variations in the supply of Al to the scale. Regarding the other intermetallic of interest in the alloys studied in this research, depending on oxidation conditions, other oxides than Al_2O_3 can form on the γ'-Ni_3Al [Kuenzly and Douglass, 1974].

In the growth of alumina scales, so-called transition aluminas (all have cubic or pseudo-cubic spinel structures) can form preferentially during the early stages of oxidation before transferring to corundum (α-Al_2O_3), which is the stable polymorph of aluminium oxide at ambient pressure. This was confirmed by the glancing angle XRD studies of the surfaces of the oxidised alloys, see figures 5.7, 5.19, 5.34, 5.49 and 5.66. Furthermore, the fast oxidation exhibited by the alloys in the early stages of oxidation (figure 5.1) is believed to be because of the formation of transient aluminas. The change of slope of the weight gain curves exhibited by all the alloys is usually considered to be due to the transformation of transient aluminas to stable α-Al_2O_3.

The α-Al_2O_3 is denser than the transition aluminas and the transformation of the latter to the former involves ~ 8% unit cell volume change and therefore can result to substantial stresses in the scale [Doychack et al, 1989] that contribute to scale spallation. Thus, the transformations discussed above are crucial to coating performance and life. Furthermore, according to the literature compressive stresses in RE free alumina, which can be significant (100 – 200 MPa), become tensile in the presence of Res [Veal et al. 2007 and Veal and Paulikas 2008]. The origin of the tensile stresses in the scales formed on alloys with REs is not clear [Heuer eta al., 2011] As shown in this chapter, the characterisation of the scales identified evidence of spallation and scale cracking, which are attributed to the formation and transformation(s) of transition aluminas to α-Al_2O_3 and the presence of REs in the alloys EK3 to EK5, for example see alloy EK1-TGA figure 5.4 and 5.5 where cracks are visible on the surface of the whole oxidised sample and EK2-TGA figure 5.15.

The grain boundary area in alumina scales is very significant, making grain boundaries dominant transport paths through the scale. The grain size of transition aluminas can be of the order of nanometres [Smialek and Gibala, 1983]. As the latter transform the grain size of α-Al_2O_3 nucleated at the scale/alloy interface is of submicron size [Yang et al., 1995] and as the scale becomes thicker the grain size tends to be about 2 μm [Pint and Hobbs, 1994]. The doping of the scale can lead to changes in grain structure and equiaxed and/or columnar scales can form.

As discussed above and supported by the results reported in this thesis, alumina was formed in the scale of the oxidised alloy. The formation of alumina involved inward oxygen diffusion and outward Al diffusion. Oxidation kinetics was controlled by the faster of Al or oxygen grain boundary diffusion. The inward oxygen diffusion was dominant but the outward Al diffusion was significant. If outward Al transport (or inward diffusion of Al vacancies) dominated new oxide would appear at the scale-gas interface (cation vacancies will be annihilated at the scale-substrate interface and there will be recession (displacement) of the latter) and the vacancies would be injected into the substrate and annihilated at vacancy sinks. If inward oxygen diffusion occurred oxygen vacancies would be annihilated at the scale-gas interface and the metal vacancies created would be annihilated in a sink in the substrate.

It was discussed above that the microstructure of the scale is important for the transport processes during oxidation. Regarding volume (lattice) diffusion, following the work of Paladino and Kingery (1962) it was accepted that $D_{Al} >> D_{oxygen}$ and this is still believed to be true [Heuer, 2008] even though there have been doubts as to what Paladino and Kingery measured (i.e., volume or g.b diffusion). Heuer, in his paper "Oxygen and aluminium diffusion in α-Al_2O_3: How much do we really understand?" concluded "the answer to the question is not a great deal" and went on to identify eight areas that future research should address [Heuer, 2008].

Lattice (volume) diffusion of oxygen in α-Al_2O_3 occurs by vacancy migration. Regarding grain boundary diffusion, D_{gb}^{oxygen} is significantly enhanced compared with lattice diffusion D_{oxygen}. There is no data for D_{gb}^{Al} [Heuer, 2008]. There have been only two reports of Al self-diffusion in alumina, one by Paladino and Kingery (1962) and another by LeGall et al (1994). Using the data of these researchers for lattice (volume) Al diffusion in α-Al_2O_3 given in [Heuer 2008] the diffusion distance x of Al in α-Al_2O_3 after 100 h at 975 °C respectively would be $2.2\ 10^{-9}$ m and 0.42 m, which clearly shows the inconsistencies of the existing data in the literature.

Further complications would arise if the alumina were to be doped (alloyed). According to Tsubasa Nakagawa et al (2007), Y doping retards the grain boundary diffusivity of oxygen by ~ 10 times compared with the un-doped alumina and the segregation of Y at g.bs affects grain boundary sliding for stress relaxation at triple junctions (in other words doping with Y affects the creep of alumina). In practice, doping of the scale can occur from elements from the Ni superalloy substrate that diffuse in the

BC (e.g., Ti) or by elements deliberately added in the alloy, for example REs. As the latter has indeed been the case in the alloys EK3 to EK5 of this study it is highly likely that the oxygen diffusivity in α-Al_2O_3 was affected compared with the pure (i.e., non-doped) case. Using the diffusivity data for oxygen from Tsubasa Nakagawa et al the diffusion distance x ($=2.4\sqrt{Dt}$) of oxygen after 100 h oxidation at 975 °C would be ~ $3.9\ 10^{-11}$ m according to the volume diffusion data for un-doped and Y doped α-Al_2O_3, and $1\ 10^{-8}$ m and $6.4\ 10^{-10}$ m for grain boundary diffusion along pristine and Y-doped Σ31 grain boundaries of 1 nm thickness.

Doping by transition metals can also affect the shape of alumina as well as the transformation of transition aluminas to α-Al_2O_3, for example the shape anisotropy of α-Al_2O_3 platelets increased when doped with Ti (according to Hsing-I Hsiang et al 2010) Titania segregation of Ti at the g.bs of alumina would hinder the growth of specific surfaces, thereby enhancing the development of platelet-shaped alumina grains), and the γ-$Al_2O_3 \rightarrow \alpha$-$Al_2O_3$ transformation was promoted. Fielitz et al (2008) reported that the diffusivity of Al is orders of magnitude higher than the oxygen diffusivity in Ti doped α-Al_2O_3 owing to an increase of the concentration of mobile Al vacancies which enable the transport of Al by a vacancy mechanism. Using their data for the diffusion of Al in Ti-doped alumina the diffusion distance x of Al in Ti doped α-Al_2O_3 would be in the range $1.2\ 10^{-8}$ m to $8\ 10^{-8}$ m, higher than the diffusion distance of Al calculated above for un-doped alumina. Even though there is no data in the literature for the effect of Ta, it is likely that the addition of Ta in the alloys EK2 to EK5 qualitatively had a similar effect as that of Ti.

Regarding the morphologies exhibited by metastable aluminas and α-Al_2O_3, for the θ-Al_2O_3 blades and whiskers and for the α-Al_2O_3 network of ridges on the oxide layer are reported as being the typical ones. In particular, the α-Al_2O_3 scale morphology is that of a thin textured oxide with thick ridges at g.bs (owing to grain boundary diffusion) extending inwards and outwards [Doychak, 1989]. These morphologies were exhibited by scales formed on the alloys of this study, see EK2-TGA alloy figure 5.17, EK3-TGA alloy figure 5.32, EK4-TGA alloy figures 5.45 and 5.47.

Oxidation induced stresses also arose from formation of new alumina within the scale and at the oxide-gas and oxide-substrate interfaces when counter current inward diffusion of oxygen and outward diffusion of Al could contribute almost equally to growth of the scale [Quadakkers et al, 1991].

Such stresses would in turn also influence scale adhesion. The latter however would also be affected by impurities. Indeed, it has been reported that sulphur in Ni-Al based alloys, even when present at ppm level, can promote scale spallation by segregating at the oxide/scale interfaces where it causes a loss of adhesion. The REs Hf and Y are believed to counteract this effect of sulphur impurities. Prussner et al (1997) and Khanna et al (1989) showed that the oxidation rate increased in sulphur doped NiAl and NiCrAl alloys. TEM was used in these studies to detect the sulphur in the scale where it had segregated at the alumina g.bs. However, sulphur under the TEM desorbs quickly with time, which makes it very difficult to detect accurately its concentration(s), particularly when the latter are very small. In the research described in this thesis the characterisation of the microstructures did not find evidence of sulphur using the techniques described in the experimental chapter. There was evidence for contamination by nitrogen from the oxidising environment, as suggested by the identification of AlN and Cr_2N nitride peaks in the glancing angle XRD in the alloys EK1, EK2, EK3, EK4 and EK5 of this study, see figures 5.7, 5.19, 5.34, 5.49 and 5.66 and the WDS analysis data which showed the presence of nitrogen below the scale (see below). The Cr_2N is less stable than AlN. Furthermore, the AlN is in equilibrium with NiAl and does not interact with it [Povarova et al, 2007]. Formation of Al nitride has been reported by Zhong et al (2000) in NiAl containing sputtered Ni-Al thin films. The nitrogen content in the latter increased with the amount of N_2 in the sputtering atmosphere. Thus, on the basis of the limited data in this thesis and the aforementioned literature data the AlN is the most likely nitride phase to be present. It should be noted that Noebe et al suggested that the formation of nitride(s) could be beneficial for cyclic oxidation resistance [Noebe et al, 1993].

The sluggish diffusion kinetics of Al and O are responsible for the protection afforded by the alumina scales. Alloying additions however significantly affect diffusion (see above discussion regarding the doping of alumina and the effect of the latter on the diffusivity of oxygen and [Reddy and Cooper, 1982]. It is suggested that scale formation kinetics was dominated by grain boundary diffusion owing to the microstructure of alumina scales (see above) and the low lattice (volume) diffusivities. As discussed above reactive elements (e.g., Y) segregate to grain boundaries in the oxide [Tsubasa et al, 2007] and inhibit the outward diffusion of Al (i.e., reduce oxidation kinetics). Regarding Y, in the literature it has been suggested that it decreases the oxygen mobility along the alumina scale g.bs owing to the Y-O bonds being considerably stronger than the Al-O bonds (the melting point of Y_2O_3 is 2425 ^oC and of Al_2O_3 is 2040 ^oC). The results of this research

were not sufficient to support or refute the segregation of Y at grain boundary of the scale. TEM investigations would be required to address this. Such studies were outside the scope of the present study.

In the literature, the mechanism(s) by which REs inhibit Al diffusion is(are) not well understood. Three explanations have been offered for the effectiveness of REs, namely (i) "site blocking", meaning that REs segregate to grain boundaries of the scale and impede the outward diffusion of Al along the grain boundary, (ii) the "swamp out" mechanism in which preferential RE segregation at g.bs prevents segregation of other alloying elements that would otherwise affect the local point defect populations in the grain boundaries and enhance grain boundary diffusion [Pint at al 1998 and Nakagawa et al, 2007] and (iii) REs, rather than blocking diffusion paths, affect the electronic structure of alumina, i.e., REs cause modification of the near-band edge grain boundary defect states relative to those present in pure alumina (i.e., alumina without REs) [Heuer et al, 2013]. Regarding the Y effect, the study of the Y doping effect on g.b diffusion of oxygen using pristine (un-doped) and Y doped α-Al_2O_3 bicrystals with the same geometrical configuration led Tsubasa Nakagawa et al to conclude that the Y effect can be explained by a "site blocking" mechanism or a "swamp out" mechanism, or by both of these. On the basis of the results of this research it is not possible to select any of the above mechanisms. The results however clearly indicated the beneficial effect of RE addition in the alloys EK3 to EK5 when their oxidation is compared with that of the alloy EK1.

Diffusion controlled scale formation should follow parabolic law. Wagner (1993) considered both mass and charge transport across a growing oxide. He assumed growth of a neutral oxide that was compact and free of short-circuit migration paths (in other words Wagner ignored grain boundaries) and local equilibrium at any point in the oxide and showed that the oxidation rate is dependent on the oxygen partial pressure when metal vacancies or oxygen interstitials predominate in the oxide and that the rate is independent of the oxygen partial pressure when oxygen vacancies or metal interstitials predominate. However, as it has been discussed above, the oxidation kinetics is almost certainly controlled by grain boundary diffusion and the microstructure of the scale formed is also important regarding transport processes during oxidation. According to the literature, the microstructure can be largely columnar for most of the scale thickness and equiaxed near the scale/gas interface and gradients in oxygen chemical activity (oxygen potential) can exist across the thickness of a growing alumina scale.

The oxidation rates of the alloys EK2 and EK3 were one order of magnitude lower than for the alloys EK1, EK4 and EK5. The Ni-20.4Co-21Cr-16.4Al alloy (EK1) exhibited the highest weight gain and worst oxidation behaviour at 975 ˚C. After 100 hrs of exposure in air the weight gain was 0.97 mg/cm^2 (Fig. 5.74 and Table 5.11). The additions of Ta and Ta and Y (alloys EK2 and EK3 retrospectively) increased the oxidation resistance at 975 ˚C. The Hf and Hf and Si additions did not have such a dramatic effect on the oxidation behaviour of the alloys EK4 and EK5. However, the simultaneous addition of Ta, Y, Hf and Si increased significantly the oxidation resistance at 975 ˚C when compared with the base alloy (EK1-AC).

After exposure of 100 hrs at 975 ˚C in air the weight gains of the alloys EK2 (Ta present), EK3 (Ta and Y present), EK4 (Ta, Y and Hf present) and EK5 (Ta, Y, Hf and Si present) were 0.67, 0.36, 0.47 and 0.41 mg/cm^2, respectively. There was no evidence of oxide spallation during oxidation for any of the alloys (Fig. 5.2). The weight change curves in Fig 5.74 showed that the Ta and Y containing alloy EK3 exhibited far better oxidation resistance at 975 ˚C, compared with the Ta containing alloy EK2 and the base alloy EK1. The alloys EK3, EK4 and EK5 had better oxidation resistance than EK1 and EK2, and showed near identical oxidation during the initial oxidation, up to ~ 18 hrs. At 975 ˚C, the n value (see Table 5.1) for the alloys EK1, EK3 and EK4 would suggest parabolic oxidation and the alloy EK2 showed faster than parabolic kinetic behaviour.

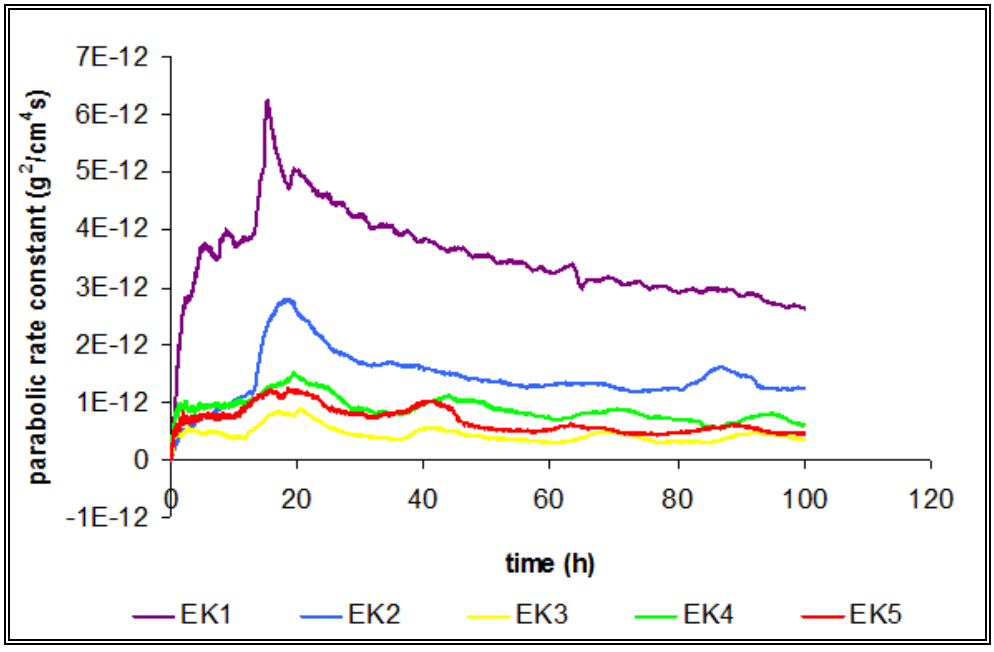

Figure 5.74 Plot of parabolic rate constants k_p of the alloys EK1-AC: Ni-20.4Co-21Cr-16.4Al, EK2-AC: Ni-20.1Co-19.8Cr-16.2Al-1.1Ta, EK3-AC: Ni-20.1Co-19.8Cr-16.2Al-

1.1Ta-0.3Y, EK4-AC: Ni-20Co-19.7Cr-16.1Al-1.1Ta-0.3Y-0.2Hf, EK5-AC: Ni-19.3Co-19Cr15.6Al-1.1Ta-0.3Y-0.2Hf-3.5Si, at 975 ˚C as a function of time. Nominal alloy compositions in at%. Alloys tested in the as cast condition. This figure shows the development of the maximum values of the parabolic rate constant after 18 to 20 hours and this corresponds to the time of development of the protective oxide layer. After this, a drop in the oxidation rate is observed

Brumm and Grabke (1992) suggested that in alumina-forming alloys, the case with the alloys in this project, fast growing transient aluminas like γ-Al_2O_3 and θ-Al_2O_3 transform to slow growing α-Al_2O_3 and the latter controls the oxidation rate in the final stages. The fact that fast growing metastable aluminas cause a high oxidation rate in the early stages of oxidation introduces a deviation t_0 to the time axis and the rate law becomes:

$$(\Delta w/A)^2 = k_p(t+t_0) \qquad (5.3)$$

$$d(\Delta w/A)^2/dt = k_p \qquad (5.4)$$

When equation (5.3) is differentiated the differential yields the value of k_p as a function of time, equation (5.4). Thus, the k_p can be plotted as a function of time, see Fig 5.74.

Table 5.11 Oxide scale thickness x, parabolic rate constant k_p and parabolic rate growth k_x. The calculation of x assumed that the oxide scale is only alumina.

Alloy code	**Parabolic growth constant k_x (cm^2/sec)**	**Oxide scale thickness x (cm)**	**Parabolic rate constant k_p ($g^2/cm^4 * sec^1$)**
EK1	$2.9*10^{-12}$	$1*10^{-3}$	$2.6*10^{-12}$
EK2	$1.4*10^{-12}$	$7*10^{-4}$	$1.2*10^{-12}$
EK3	$4.1*10^{-13}$	$3.8*10^{-4}$	$3.6*10^{-13}$
EK4	$7*10^{-13}$	$5*10^{-4}$	$6.1*10^{-13}$
EK5	$5.3*10^{-13}$	$4.4*10^{-4}$	$4.6*10^{-13}$

According to Hindam and Whittle (1982), if the oxide scale is envisaged as a moving grain boundary of fixed composition, then its boundaries follow a parabolic law and

$$x^2 = D_{eff}t = k_x t \quad (5.5) \quad \text{and}$$

$$k_p = [p_{Al2O3} * W_{O2}/W_{Al2O3}]^2 * k_x \quad (5.6)$$

where x is the scale thickness, D_{eff} is an effective diffusion coefficient and k_x is the parabolic growth constant in terms of scale thickness. The effective diffusion coefficient D_{eff} is obtained from the gravimetric constant using the density of Al_2O_3 = 3.98 g/cm^3 and the ratio of weight of oxygen in Al_2O_3 to weight of Al_2O_3 (3/2 M_{O2}/M_{Al2O3} = 0.235). The calculated oxide thicknesses are given in Table 5.11 which shows that the oxide thickness was highest for the base alloy and thinnest for the alloys EK3 and EK5. Figure 5.1 shows that the oxidation rate constants of the alloys EK1 to EK5 changed with time from a high value after about 20 h of oxidation to a lower one after 100 h. Indeed, for the alloy EK1 the k_p values changed from 6.2 10^{-12} g^2/cm^4 *sec^1 at 15.5 h to 2.6 10^{-12} g^2/cm^4 *sec^1 at 100 h, for the alloy EK2 the k_p values changed from 2.7 10^{-12} g^2/cm^4 *sec^1 at 19 h to 1.2 10^{-12} g^2/cm^4 *sec^1 at 100 h, for the alloy EK3 the k_p values changed from 7.8 10^{-13} g^2/cm^4 *sec^1 at 21.7 h to 3.5 10^{-13} g^2/cm^4 *sec^1 at 100 h, for the alloy EK4 the k_p values changed from 1.4 10^{-12} g^2/cm^4 *sec^1 at 20 h to 6.2 10^{-13} g^2/cm^4 *sec^1 at 100 h and for the alloy EK5 the k_p values changed from 1.2 10^{-12} g^2/cm^4 *sec^1 at 17 h to 4.7 10^{-13} g^2/cm^4 *sec^1 at 100 h.

The Arrhenius plot of alumina formation on the intermetallic NiAl is shown in figure 5.75 where the oxidation temperature used in this study is indicated by a vertical line. All the aforementioned k_p values fall between the data corresponding to the θ-Al_2O_3 and α-Al_2O_3 suggesting the formation of transient aluminas and α-Al_2O_3, which is consistent with the glancing angle XRD data for each alloy. Indeed the glancing angle XRD data confirmed the presence of transient γ-Al_2O_3 and θ-Al_2O_3 and stable α-Al_2O_3 Li et al (2003) reported the formation of different aluminas on a Ni-30Cr-12Al-0.3Y (wt%) BC alloy with β-NiAl and traces of γ-Ni_{ss} in its microstructure. Furthermore Brumm and Grabke (1992) reported formation of different aluminas on β-NiAl. According to Brumm and Grabke in the early stages of oxidation (800 – 950˚C), metastable oxides like γ-Al_2O_3 grew. Later on, these oxides transformed to monoclinic θ-Al_2O_3 that finally transformed to α-Al_2O_3 at higher temperatures > 950˚C. A major difference between this work and Li et al (2003) and Brumm and Grabke (1992) is that this work studied the oxidation of different

alloys containing γ-Ni_{ss}, γ'-Ni_3Al and β-NiAl and other phases in the alloys EK2, EK3, EK4 and EK5 with different volume fractions of γ-Ni_{ss} and β-NiAl, see Table 4.14. Thus, this work would suggest the formation of transient aluminas and α-Al_2O_3 on MCrAlY type bond coat alloys with $0.8 < [\text{vol }\%]_{Niss} / [\text{vol}\%]_{NiAl} < 2.85$.

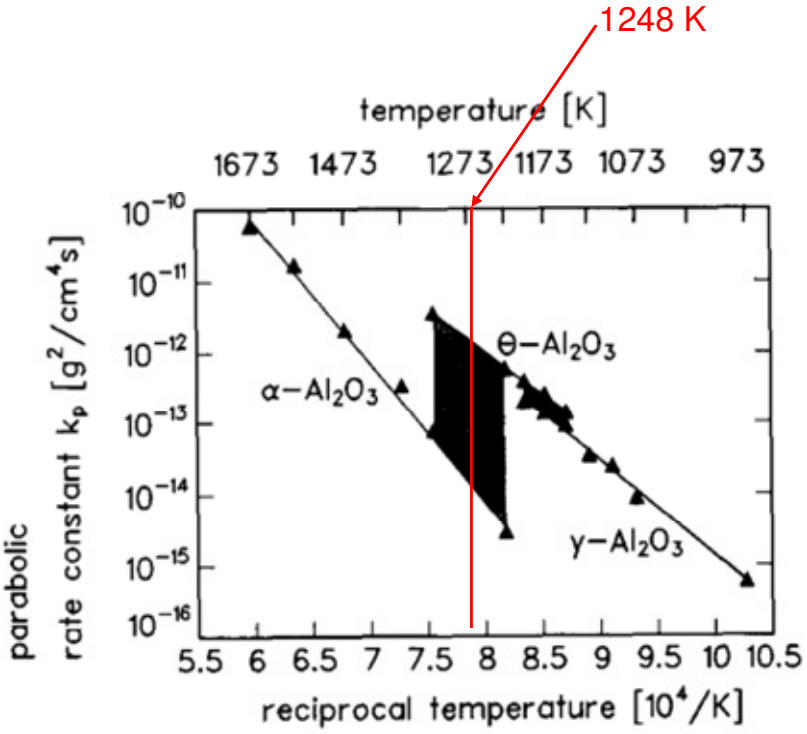

Figure 5.75 Arrhenius plot of the parabolic rate constants k_p of NiAl oxidation [Brumm and Grabke, 1992]. The vertical line at T= 1248 K indicates the oxidation temperature used in this study.

Tables 5.12 and 5.13 respectively give the compositions of the β-NiAl and γ-Ni_{ss} phases in the as-cast condition and after oxidation (975 ˚C for 100 hrs) for the alloys EK1, EK2, EK3, EK4 and EK5. The data show that the γ-Ni_{ss} and β-NiAl acted as the Al and Cr reservoirs during oxidation. Similar data for γ'-Ni_3Al cannot be provided because accurate chemical analysis of this phase could not be performed. The data in Table 5.12 also shows significant reductions in the concentrations of Co, Ta, Y and Si in the NiAl phase after oxidation while the data in Table 5.13 shows small changes in the concentrations of Co and Cr in the γNi_{ss}. However, compared with the NiAl, there was no consistent trend in the changes of Co and Cr content in the solid solution after oxidation. The data in Tables 5.12 and 5.13 would thus suggest a prominent role for the NiAl phase during the oxidation of the alloys EK1 to EK5. Furthermore, the alloy EK3 exhibited the lowest percentage

increase in Al in the NiAl, and the lowest [$(Al/(Cr+Co)_{NiAl})/(Al/(Cr+Co)_{Ni})$] ratio after oxidation.

Table 5.12 Average composition (at%) of the β-NiAl phase in the alloys EK1, EK2, EK3, EK4 and EK5 in the as-cast condition (bulk) and after oxidation (25 to 40 μm below scale) at 975 ˚C for 100 hrs.

Alloy and condition	Ni	Co	Cr	Al	Ta	Y	Hf	Si
EK1-AC	43.7	13	12.6	30.7	-	-	-	-
EK1-TGA	46.1	8.6	5	32.6	-	-	-	-
EK2-AC	39.6	15.7	15	28.4	1.1	-	-	-
EK2-TGA	42.3	10.2	9.2	31	0.3	-	-	-
EK3-AC	42.4	14.4	10.6	30.9	1.6	0	-	-
EK3-TGA	45.3	10.5	5.2	31.8	0.3	0.04	-	-
EK4-AC	42.3	15.5	10.9	29.8	1.4	0	0	-
EK4-TGA	43.1	10.3	5.5	33.3	0.3	0	0	-
EK5-AC	40.8	14.1	11.4	26.7	0.6	0.5	0.3	6
EK5-TGA	43.5	10.2	6.5	30.3	0	0	0	1.8

Table 5.13 Avergae composition (at%) of the γ-Ni_{ss} phase in the alloys EK1, EK2, EK3, EK4 and EK5 in the as-cast (bulk) and after oxidation (25 to 40 μm below scale) at 975 ˚C for 100 hrs.

Alloy and condition	Ni	Co	Cr	Al	Ta	Y	Hf	Si
EK1-AC	42.5	21.4	20.5	15.7	-	-	-	-
EK1-TGA	37.5	22.3	23.8	9	-	-	-	-
EK2-AC	36.3	22.2	25.2	15.1	1.2	-	-	-
EK2-TGA	35.7	22.8	24.6	8.5	1.7	-	-	-
EK3-AC	40.6	22.5	19.3	15.8	1.4	0.2	-	-
EK3-TGA	39	22.3	20.1	10.2	1.4	0	-	-
EK4-AC	40.5	22.2	20.2	15.4	1.7	0	0	-
EK4-TGA	36.2	23.7	22.1	10.2	1.5	0	0	-
EK5-AC	37.1	21.8	23.3	10.9	1.1	0.2	0.1	5.3
EK5-TGA	37.5	21.1	20.9	8.4	1	0	0	3

The data for the volume fractions of Ni_{ss} and NiAl in the alloys would suggest that the "best" oxidation behaviour as suggested by the oxidation rates at 100 h at 975 °C was exhibited by the alloy that tended to form equal volume fractions of the two phases, i.e., the alloy EK3.

Hou (2003) re-evaluated data on parabolic oxidation rate constants of alumina forming alloys that was compiled by Whittle and Hindam (1982) by making distinction of the different types of alloys with/out RE additions. Hou's figure is reproduced here as figure 5.76.

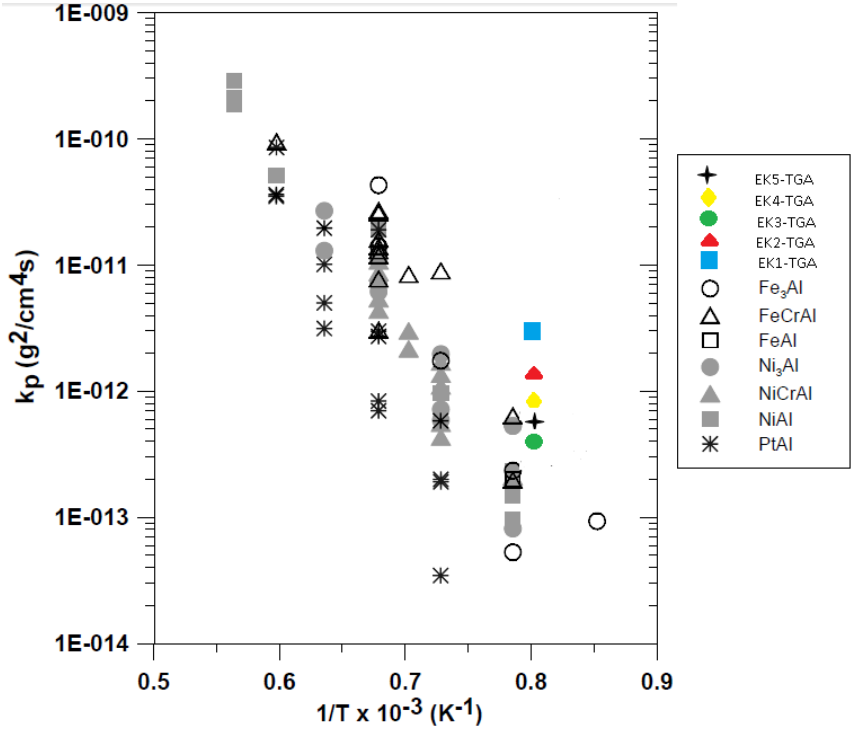

Figure 5.76 Parabolic rate constants from Hou (2003) and results from this work showing the Al_2O_3 scale growth rate on different types of Fe, Ni and Pt based alloys.

The data compiled by Hou shows scatter from study to study even for alloys of the same composition. According to Hou, the presence of Cr in some alloys did not seem to make any difference on oxidation rates. The rates of the alloys of this study fall in the upper band of the data for the specific temperature of study.

This figure also shows that PtAl has the slowest oxidation rate, and that the alloys of Fe and Ni oxidised up to 10 times faster compared with PtAl. When the effect of REs on oxidation rates was considered by Hou for the alloys used by Whittle and Hindam in their compilation of data, Hou found out that the result was a scatter band about 2 orders of magnitude wide that showed no apparent effect of RE on scale growth rate, as was concluded by Whittle and Hindam. This was attributed by Hou to differences in the distribution and concentration of REs in the alloys, which are extremely critical for their effectiveness in oxidation (see above). However, when Hou compared more recent data with/out RE additions obtained by the same research group on the same type of alloy the results showed consistent reduction of oxidation rate by the RE addition. This data from Hou is shown in Table 5.14 with the data for the alloys of this study. The data in this table shows that the "effectiveness" of RE addition(s) is compromised when the latter are in synergy with a refractory metal (Ta in this case) or two REs are in synergy.

Table 5.14 Data for parabolic oxidation rate constant of phases and alloys with/out REs.

Phase or alloy	$T_{oxidation}$ (°C)	k_p without RE (g^2/cm^4s)	RE type	k_p with RE (g^2/cm^4s)	Reference
NiAl	1200	$1.4\pm0.4\ 10^{-11}$	Hf, Y	$8\pm4.1\ 10^{-12}$	Referenced in Hou (2003)
Ni_3Al	1200	$7.1\ 10^{-12}$	Y	$4.3\pm3.1\ 10^{-12}$	Hou (2003)
NiCrAl	1100	$1.1\ 10^{-12}$	Hf, Y	$4.5\pm2.1\ 10^{-13}$	Hou (2003)
EK2	975	$1.2\ 10^{-12}$	+ Hf	$3.6\ 10^{-13}$ (EK3)	this work
EK2	975	$1.2\ 10^{-12}$	+Hf+Y	$6.1\ 10^{-13}$ (EK4)	this work

Tawancy (1996) suggested that the addition of Si in certain BC alloys could improve oxidation significantly. The data for the alloy EK5 does not support this and also shows that alloying with Si increased the depth below the scale where internal oxidation occurred.

With the addition of REs a significant amount of Al outward transport is reduced [Hou 2003]. This is supported by the data in Table 5.13 which shows the composition of the Ni_{ss} in the alloys before and after oxidation. The data shows that the latter phase was the main supplier of Al for the growth of the scale and that indeed the additions of Hf and Y alone and in synergy had a positive effect on the concentration of Al in the Ni_{ss} below the substrate compared with the alloys EK1 and EK2 (the percentage reduction in the Al concentration in the Ni_{ss} after oxidation was 22.9%, 33.7%, 35.4% in EK5, EK4, EK3 compared with 43.7% and 42.7% in EK2 and EK1 respectively).

As discussed above, the oxidation of the alloys and thus the consumption of Al and Cr from the precursor phases in the alloys was expected to modify the composition of the substrate below the scale, which in turn could shift phase equilibria in different parts of the phase diagram, induce phase transformations that could cause volume changes, which could in turn affect both the growth of the scale and possibly lead to internal oxidation. The characterisation of the microstructures sought to quantify the chemical composition(s) of phase in these areas and also to find out whether "contamination" of the sub-(scale-substrate) interface by interstitials (nitrogen and oxygen) had occurred.

The WDS studies confirmed the presence of alumina in the scales of all five alloys and of chromia in the scale of EK2. As discussed above, alumina formation in all the alloys was confirmed by GXRD, which also provided evidence for the existence of chromia. The internal oxidation (IO) zones, which were formed below the scale, showed changes in simple metal (Al, Si), transition metal (TM) and oxygen and nitrogen content. All the IOs were rich in Al. The IO in EK2 was richer in Cr and Ni and leaner in N compared with EK1. No nitrogen was analysed by WDS in the IOs formed in EK3, EK4 and EK5 and no oxygen in the IO in EK1. In the alloy EK5, the IO was leaner in Co, Cr compared with EK2 and rich in Y compared with EK3 and EK4. The diffusion zone (DZ), which were formed below the IO zones, were rich in Cr (in other words all the DZs were rich in Cr and all the IOs were rich in Al). In all the DZs Nitrogen was present as well as Co and in the DZs formed in EK2, EK3, EK4 and EK5 Ni was also analysed with its concentration exhibiting opposite trends in EK3 and EK4 (higher in the former). The concentrations of Al and oxygen in the DZ in EK4 were higher than in the other alloys.

New Ni rich phases were observed in the DZs of EK2, EK3 and EK4 that contained Al, Co and Cr. In the substrate below the diffusion zone γ and γ′-Ni_3Al was observed in the alloys EK2, EK3, EK4 and EK5. In these phases and the β-NiAl that was observed in all five alloys and the β-NiAl and γ that were observed in EK1 the concentration of nitrogen was around 5 to at% but that of oxygen was low (< 1 at%). This suggested that in all five alloys the contamination by nitrogen extended below the DZs. Below the DZs in EK2 and EK3 a Cr rich phase (identified as σ phase in the Tables 5.7 and 5.8) was formed. The σ contained Co and was rich in Y in EK3. However, in the alloys EK4 and EK5 the σ phase was absent and instead a Ni rich phase with solubilities of Al, Co and Cr (identified as ρ phase in Tables 5.9 and 5.10) was formed. The ρ phase contained nitrogen and respectively was rich in Ta and Si, Ta and Y in the alloys EK4 and EK5. Formation of other phases occurred in the NiAl in the alloys EK2 and EK3 and bright contrast precipitates were observed below the DZ in EK5. The above data would thus suggest that new phase equilibria was established in the alloys EK2 to EK5 below the scale owing to the consumption of Al and Cr to form the scale and the contamination by oxygen and nitrogen. The aforementioned phases cannot be explained by existing phase equilibria data. Only the phases β-NiAl, γ′-Ni_3Al, γ-Ni_{ss} and Cr rich σ phase in EK2 can be accounted for by the existing phase equilibria data for 975 °C, see figure 3.23 that shows thermodynamic calculation for the two alloys.

Chapter 6 – Conclusions and future work

6.1 Conclusions

In the research described in this thesis five NiCrCoAl based bond coat type alloys, namely Ni-23Co-20Cr-8.5Al (EK1), Ni-23Co-20Cr-8.5Al-4Ta (EK2), Ni-23Co-20Cr-8.5Al-4Ta-0.6Y (EK3), Ni-23Co-20Cr-8.5Al-4Ta-0.6Y-0.8Hf (EK4) and Ni-23Co-20Cr-8.5Al-4Ta-0.6Y-0.8Hf-2Si (EK5) (wt%), were studied in the as cast, heat treated (1200 °C) and oxidised (975 °C in air) conditions. The microstructures of the alloys EK1-EK5 determined by quantitative EDS analysis and XRD were as follows:

1. The microstructure of the cast alloy EK1 consisted of the γ-Ni_{ss} and β-NiAl phases in the cast and heat treated (1200 °C/48hrs) conditions with the two phases forming a eutectic in the cast alloy.
2. The microstructure of the cast alloy EK2 consisted of the γ-Ni_{ss} and β-NiAl phases in the cast and heat treated conditions (1200 °C/48hrs) with γ + β eutectic and Ta rich areas in the γ-Ni_{ss} in the cast ingot.
3. The microstructure of the cast alloy EK3 consisted of the γ-Ni_{ss} and β-NiAl phases and an Y rich intermetallic and after the heat treatment (1200 °C/48hrs) of the former two phases and M_5Y and M_xY_z intermetallics.
4. The microstructure of the cast alloy EK4 consisted of γ-Ni_{ss} and β-NiAl phases, a eutectic formed of these phases and Y and Hf rich areas that exhibited white contrast under BSE imaging. The same phases without the lamellar microstructure were present after the heat treatment (1200 °C/48hrs) with the white contrast areas now being either Hf or Y rich.
5. The microstructure of the cast alloy EK5 consisted of γ-Ni_{ss} and β-NiAl phases and white contrast areas that were rich in Si, Hf and Ta and grey contrast areas that were rich in Si and Y. After the heat treatment (1200 °C/48hrs) the same phases were present with the white contrast areas being richer in Ta, Hf and Si compared with the cast condition. Furthermore there was severe microckracking in the microstructure and evidence of internal oxidation.

6. The phase equilibria that was "established" by the synergy of Ni-Co-Cr-Al in the alloy EK1, namely the stable γ-Ni_{ss} and β-NiAl phases, was not altered by the synergy of Ta with Y, Ta, Y and Hf and Ta, Y, Hf and Si.
7. XRD and imaging in the SEM suggested the presence of γ′-Ni_3Al, the former technique in all alloys and the latter in the alloys EK2-HT2, EK3-AC, EK3-HT2, EK5-HT1 AND EK5-HT2. The synergy of Ta with Y, Ta with Y and Hf and Ta with Y, Hf and Si had an effect on the stability of γ′-Ni_3Al and the γ + β eutectic. The γ + β eutectic was not observed in the alloys EK3 and EK5, which would suggest that Y and Si suppress its formation.
8. The synergy of Ta and Y and of Ta, Y and Si enhanced the stability of the γ′-Ni_3Al, according to the SEM data.
9. During solidification the formation of the γ-Ni_{ss} was accompanied by partitioning of Al, Si and Ta to the melt; the only exception was the alloy EK5 where the Ta partitioned to the γ-Ni_{ss} rather than the melt.
10. The formation of the β-NiAl during solidification was accompanied by partitioning of Co, Cr, Si and Ta to the melt and of Al to the β-NiAl, with the data for Ta for the alloy EK3 suggesting partitioning of Ta to the β-NiAl.
11. In the solidified microstructures the partitioning of Al and Co between the γ-Ni_{ss} and β-NiAl phases was not changed by the synergies of different alloying elements.
12. The partitioning of Cr to the γ-Ni_{ss} was increased by the synergy of Ta and Y and Ta, Y and Si.
13. Alloying with Ta resulted to the highest Al + Cr and Cr contents in Ni_{ss} and NiAl in the cast condition and this was maintained after the heat treatments.
14. The Al + Cr content in the γ + β eutectic was essentially the same in the three alloys where the eutectic was formed but the Al/Cr ratio increased dramatically when the Ta was in synergy with Hf.
15. Alloying with Ta had a dramatic effect on the volume fractions of the two main phases. In the as cast condition the vol% of the β-NiAl was higher than the vol% of the γ-Ni_{ss} in the alloys EK2 and EK5, suggesting that alloying with Y and Hf tends to favour the γ-Ni_{ss} rather than the β-NiAl. There were changes in the vol% of the aforementioned phases after the heat treatment, with the vol% of the β-NiAl increasing in all alloys. The higher vol% of β-NiAl was still observed in the alloys EK2 and EK5.

16. The reactive element addition(s) clearly had a beneficial effect on oxidation. The oxidation of the alloys EK3, EK4 and EK5 improved compared with that of the alloy EK1.
17. With the addition of reactive elements a significant amount of Al outward transport was reduced.
18. Alloying with Si did not improve the oxidation rate and increased the depth below the scale where internal oxidation occurred.
19. The "effectiveness" of reactive elements was compromised when the latter were simultaneously in synergy with Ta.
20. The Ni_{ss} was the main supplier of Al for the growth of the scale.
21. The NiAl was the main supplier of Cr for the growth of the scale.
22. Overall, the "best" oxidation behaviour was exhibited by the alloy that tended to form equal volume fractions of γ-Ni_{ss} and β-NiAl, i.e., the alloy EK3.
23. Alumina, chromia, spinels and most likely AlN were present in the scales formed on all the alloys. The GXRD confirmed the presence of transition aluminas and α-Al_2O_3.
24. The morphologies of the aluminas were consistent with those reported in the literature.
25. The spallation and cracking of scales was attributed to the formation and transformation(s) of transition aluminas to α-Al_2O_3 and the presence of reactive elements in the alloys EK3 to EK5.
26. New phase equilibria was established in the alloys EK2 to EK5 below the scale owing to the consumption of Al and Cr to form the scale and the contamination by oxygen and nitrogen.

6.2 Suggestions for future work

One of the "problems" for understanding the performance of BC alloys is that with no exception bond coats have been studied "in the prepared" condition, meaning the BC was deposited on a specific substrate using a selected deposition technique and then the BC/substrate system was given the "typical" heat treatment for the substrate. This means that BC alloys have not been studied as solidified after deposition using a spray technique (APS, LPPS, and HFOV) or vapour deposition technique (EBPVD etc). The latter techniques are all non-equilibrium processes but there are differences between them (say

LPPS and HVOF) and between the same technique depending on deposition parameters (e.g., deposition distance, spray temperature, fraction liquid all of which (and other parameters like the powder size distribution used for spray) have implications for the phase transformations (L→S, S→S) occurring in the deposit). Furthermore, the "typical" heat treatment almost certainly will be accompanied by inter-diffusion at the BC/substrate interface, meaning that both BC and substrate will be "doped" with other elements and thus the chances of "doping" oxides forming the scale are increased. Thus, future research should aim to study the microstructures and properties of a selected BC alloy, say EK3, in the as cast condition (cast using any "traditional" technique) and in the as sprayed condition using powders of the same size distribution, same spray distance but with spraying done using different technique(s), say APS, LPPS, HVOF.

Another area of interest, particularly from a physical metallurgy perspective, would be to extent the microstructure characterisation work to detailed TEM studies of the BC below the scale, in the areas where the microstructure of the substrate is affected by contamination.

References

1. Adelpour E., Thermal Barrier Coating for Gas Turbine Engine, Department of Mechanical and Aerospace Engineering, University of California, San Diego, MAE 221, http://courses.ucsd.edu/rherz/mae221a/reports/Adelpour_221A_F07.pdf, visited on 22/10/2010.
2. Achar D. R. G., Munoz-Arroyo R., Singheiser L., Quadakkers W. J. (2004), Modelling of phase equilibria in MCrAlY coating systems, Surface and Coatings Technology, vol.187, pp. 272-283.
3. ALD Vacuum Technologies GmbH, http://web.ald-vt.de/cms/en/vacuum-technology/systems/ebpvd/, visited on 30/09/2010.
4. Alexander W.O. and Vaughan N.B. (1937), The Constitution of the Nickel-Aluminum System, J. Inst. Met., vol. 61, pp.247-63.
5. Allam I.M., Whittle D.P., Stringer J. (1978), The oxidation behavior of CoCrAI systems containing active element additions, Oxidation of Metals, vol. 12, pp. 35–66.
6. Assadi H., Greer A. L. (1995), Application of disorder trapping theory to the solidification of Ni3Al, ISIJ International, vol. 35, pp. 574-579.
7. Assadi H., Barth M., Greer A. L., Herlach D. M. (1998), Kinetics of solidification of intermetallic compounds in the Ni–Al system, Acta Materialia, vol. 46, pp. 491-500.
8. Assadi H., Reutzel S. and Herlach D. M. (2006), Kinetics of solidification of B2 intermetallic phase in the Ni–Al system, Acta Materialia, vol. 54, pp. 2793-2800.
9. ASM metals handbook (1990), vol. 03, Alloy phase diagrams.
10. ASM metals handbook (1990), vol. 01, Properties and Selection: Irons, Steels, and High-Performance Alloys.
11. Barron R. A. (2010), Chemical vapor deposition of alumina, Connexions http://cnx.org/content/m24918/latest/, visited on 30/10/10.
12. Bernstein HL. (1991), Analysis of cracked gas turbine blades. Proceedings of International Gas Turbine and Aeroengine Congress and Exposition, Orlando, New York: ASME, p. 1–12.
13. Bezencon C., Schnell A .and Kurz W. (2003), Epitaxial deposition of MCrAlY coatings on a Ni-base superalloy by laser cladding, Scripta Materialia, vol. 49, pp. 705-709.

14. Borom M.P., Johnson C.A. and Peluso L.A. (1996), Role of environmental deposits and operating surface temperature in spallation of air plasma sprayed thermal barrier coatings, Surface and Coatings Technology, vol. 86-87, pp. 116-126.
15. Brandl W., Toma D., Kruger J., Grabke H. J., Matthaus G. (1997), The oxidation behaviour of HVOF thermal sprayed MCrAlY, Surface and Coatings Technology, vol. 94-95, pp. 21-26.
16. Brodin H., Jinnestrand M., Johansson S. and Sjöström S. (2006), Thermal barrier coating fatigue life assessment (Siemens report, private communication with P.Tsakiropoulos).
17. Brumm M. W. and Grabke H. J. (1992), The oxidation behaviour of NiAl-I. Phase transformations in the alumina scale during oxidation of NiAl and NiAl-Cr alloys, Corrosion Science, vol. 33, pp. 1677-1690.
18. Brumm M. W. and Grabke H. J. (1993), Oxidation behaviour of NiAl-II. Cavity formation beneath the oxide scale of NiAl of different stoichiometries, Corrosion Science, vol. 34, pp. 541-561.
19. Brumm M. W. and Grabke H. J. (1994), The oxidation of NiAl-III. Internal and intergranular oxidation, Corrosion Science, vol. 36, pp. 37-53.
20. Bose Sudhangshu (2007), High temperature coatings, Elsevier Butterworth-Heinemann.
21. Cambridge Structural Database System (Cds), http://cds.dl.ac.uk/cds/datasets/crys/csd/csd.html, last visited on 21/02/2013.
22. Cao X.Q., Vassen R., Stoever D. (2004), Ceramic materials for thermal barrier coatings, Journal of Europian Ceramic Society, vol. 24, pp. 1-10.
23. Chandrasekaran K., Richter K. W., Ipser H. (2006), The Al–Ni–Si phase diagram—Part III: Phase equilibria in the nickel rich part, Intermetallics, vol. 14, pp. 491-497.
24. Chart 1027 °C, A-B-C Phase Diagram, ASM Alloy Phase Diagrams Database, P. Villars, editor-in-chief; H. Okamoto and K. Cenzual, section editors; http://www1.asminternational.org/AsmEnterprise/APD, ASM International, Materials Park, OH, 2006.
25. Chart 1127 °C, A-B-C Phase Diagram, ASM Alloy Phase Diagrams Database, P. Villars, editor-in-chief; H. Okamoto and K. Cenzual, section editors;

http://www1.asminternational.org/AsmEnterprise/APD, ASM International, Materials Park, OH, 2006.

26. Corderman Reed Roeder, Pfaendtner Jeffrey Allan, Rigney Joseph David, Ramgopal Darolia, Nardi Richard Arthur Jr. (2003), Nickel aluminide coating containing hafnium and coating systems formed therewith. Gen Electric, US patent EP 1329536-A1.
27. Clarke D.R. and. Levi C.G. (2003), Materials design for the next generation thermal barrier coatings, Annual Review of Materials Research, vol. 33, pages 395-397.
28. Creech G. E., Barber M. J. (1991), Method of forming platinum-silicon-enriched diffused aluminide coating on a superalloy substrate, United States Patent 5057196.
29. Czech N., Schmitz F. and Stamm W. (1994), Improvement of MCrAlY coatings by additions of rhenium, Surface and Coatings Technology, vol. 68-69, pp. 17-21.
30. Dahl K. V., Hald J.and Horsewell A. (2006), Interdiffusion between Ni-based superalloy and MCrAlY coating, Defect and Diffusion Forum, Trans Tech Publications, vol. 258-260, pp. 73-78.
31. Das D.K., Singh V. and Joshi S.V. (2000), The Cyclic Oxidation Performance of Aluminide and Pt-Aluminide Coatings on Cast Ni-Based Superalloy CM-247, The Minerals, Metals and Materials Society, JOM-e, vol. 52, http://www.tms.org/pubs/journals/JOM/0001/Das/Das-0001.html, visited on 19/10/10.
32. Deloro Stellite Group, http://www.stellite.com/Home/TermsofUse/tabid/64/Default.aspx, visited on 30/09/2010.
33. Doychak J., Ruhle M. (1989), TEM studies of oxidized NiAl and Ni3Al cross sections, Oxid. Metals, vol. 31, pp. 431-452.
34. Doychak J., Smialek J. L., Mitchell T. E. (1989), Transient oxidation of Single-Crystal β-NiAl, Metall. Trans., vol. 20, pp. 499-517.
35. Dupin N. (1995), PhD Thesis, Institut National Polytechnique, Grenoble.
36. Dupin N., Ansara I., and Sundman B. (2001), Thermodynamic Re-Assessment of the Ternary System Al-Cr-Ni, Calphad, vol 25, pp. 279-298.
37. Ellison Surface Technologies, http://www.ellisonsurfacetech.com/pages/hvof.htm, visited on 30/09/2010.

38. Eliaz N., Shemesh G, Latanision R.M. (2002), Hot corrosion in gas turbine components, Engineering Failure Analysis, vol. 9, pp. 31–43.
39. Evans A.G., Mumm D.R., Hutchinson J.W., Meier G.H., Pettit F.S. (2001), Mechanisms controlling the durability of thermal barrier coatings, Progress in Materials Science, vol. 46, issue 5, pp. 505–553.
40. Felten E. J. and Pettit F. S. (1976), Development, growth and adhesion of Al2O3 on platinum-aluminium alloys, Oxid Met, vol. 10, pp. 189-223.
41. Fielitz P., Borchardt G., Ganschow S., Bertram R., Markwitz A. (2008), Al tracer diffusion in titanium doped single crystalline α-Al2O3, Solid State Ionics, vol. 179, pp. 373-379.
42. Fritscher K. (2003), Eutectic structures in the Ni–Co–Cr–Al system obtained by plasma spraying and by Bridgman growth, Journal of Crystal Growth, vol. 250, pp. 546–557.
43. Fritscher K. and Lee Y. T. (2005), Investigation of an as-sprayed NiCoCrAlY overlay coating – microstructure and evolution of the coating, Materials and Corrosion, vol. 56, pp. 5-14.
44. Gall M. Le, Lesage B., Bernardini J. (1994), Self-diffusion in α-Al2O3 I. Aluminium diffusion in single crystals, Phil. Mag., vol. 70, pp. 761-773.
45. Grabke H. J. (1999), Oxidation of NiAl and FeAl, Intermetallics, vol. 7, pp. 1153-1158.
46. Gandara R. D. (2009), Forecastle, Coahuila Mexico, http://us.monografias.com/docs69/vof-spraying/vof-spraying2.shtml, visited on 14/01/2013.
47. Gurrappa I. (2008), Identification of a smart bond coating for gas turbine engine applications, Journal of Coatings Technology and Research, vol. 5, pp. 385-391.
48. Goward G.W. (1986), Protective coatings-purpose, role, and design, Materials Science and Technology, vol. 2, pp. 194-200.
49. Goward G.W. (1998), Progress in coatings for gas turbine airfoils, Surface Coating Technology, vol. 109, pp. 73–79.
50. Gupta D. K. and Duvall D. S. (1984), A silicon and hafnium modified plasma sprayed MCrAlY coating for single crystal superalloys, TMS-proceedings of conference on superalloys, Pratt and Whitney Aircraft, East Hartford, CT 06108.
51. Grunling H.W., Bauer R. (1982), The role of silicon in corrosion-resistant high temperature coatings, Thin Solid Films, vol. 95, pp. 3–20.

52. Hancock P. (1987), Vanadic and choride of superalloys, Materials Science and Technology, vol. 3, pp. 536-544.
53. Hansen M. and Anderko K. (1958), Constitution of Binary Alloy, 2nd edition, McGraw Hill, NY, pp. 118-121. Huang S. C., Hall E. L., Chang K. M., Laforce R. P. (1986), L12-type Ni-Al-Cr alloys processed by rapid solidification, Metallurgical and Materials Transactions A, vol. 17, pp. 1685-1692.
54. Harris K. and Erickson G.L. (1991), Low carbon directional solidification alloy, United States Patent 5069873.
55. Heuer A. H. (2008), Oxygen and aluminum diffusion in α-Al2O3: How much do we really understand?, J. European Ceram. Soc., vol. 28, pp. 1495.
56. Heuer A. H., Hovis D. B., Smialek J. L., Gleeson B. (2011), Alumina Scale Formation: A New Perspective, J. Am. Ceram. Soc., vol. 94, pp. 146-153.
57. Heuer A. H., Nakagawa T., Azar M. Z., Hovis D. B., Smailek J. L., Gleeson B., Hine N. D. M., Guhl H., Lee H-S, Tangney P., Foulkes W. M. C., Finnis M. W. (2013), On the growth of Al2O3 scales, Acta Mater., vol. 61, pp. 6670-6683.
58. Hilpert K., Kobertz D., Venugopal V., Miller M., Gerads H., Bremer F. J. and Wenzl H. (1988), Phase diagram studies on the aluminium nickel system, Journal of Crystal Growth, vol. 87 (2-3), pp.185-192.
59. Hindam H. M. and Smeltzer W. W. (1980), Growth and Microstructure of α-Al_2O_3 on β-Ni-Al alloys, Journal of the Electrochemical Society, vol. 127, pp.1630-1635.
60. Hindam H. and Whittle D. P. (1982), Microstructure, adhesion and growth kinetics of protective scales on metals and alloys, Oxidation of Metals, vol. 18, pp. 245-284.
61. Hou P. Y. (2003), Impurity effects on alumina scale growth, J. Am. Ceram. Soc., vol. 86, pp. 660-668.
62. Hsiang Hsing-I, Chuang Chia-Che, Chen Tsung-Hao, Fu-Su Yen (2010), Ti4+ addition effect on α-Al2O3 flakes synthesis using a mixture of boehmite and potassium sulphate, Ceramics International, vol. 36, pp. 1467-1472.
63. Huang W, Chang Y. A. (1999), A thermodynamic description of the Ni–Al –Cr – Re system, Materials Science and Engineering, vol. 259, issue 1, pp. 110-119.
64. Huang W. and Chang Y.A. (1999), Thermodynamic properties of the Ni-Al-Cr system, Intermetallics 7, pp. 863-874.

65. Hunziker O. and Kurz W. (1999), Directional solidification and phase equilibria in the Ni-Al system, Metallurgical and Materials Transactions A, vol. 12, pp3167-3175.
66. http://iweb.tms.org/Communities/FTAttachments/superalloystable_castcomp.pdf, visited on 18/05/2015.
67. http://www.h2-igcc.eu/, visited on 10/01/2013.
68. http://www.minormetals.com/content/html/minormetals/about/AboutChrome.htm, visited on 30/09/2010.
69. http://www.tms.org/meetings/specialty/superalloys2000/superalloyshistory.html, visited on 29/09/2010.
70. http://www4.nau.edu/microanalysis/Microprobe-SEM/Signals.html, types of signals in SEM, last visited on 07/08/2013.
71. http://www.thomas-sourmail.org/coatings/index.html, visited on 28/01/2013.
72. http://www.plasmatronindia.com/techdetail.php?articleid=50, visited on 15/01/2013.
73. http://www.steelforge.com/inconel-738/, visited on 18/05/2015.
74. http://www.wikelectro.com/electron_beam_physical_vapor_deposition.php, visited on 30/09/2010.
75. Ibegazene H., Alperine S., Diot C (1995), Yttria-stabilized hafnia-zirconia thermal barrier coatings: the influence of hafnia addition on TBC structure and high-temperature behaviour, Journal of Material Science, pp.938-951.
76. Itoh Y., Tamura M. (1999), Reaction diffusion behaviours for interface between Ni-based super alloys and vacuum plasma sprayed MCrAlY coatings, Journal of Engineering for Gas Turbine and Power, vol. 121, pp. 476–483.
77. Jackson M. R. and Rairden J. R. (1977), The aluminization of platinum and platinum-coated IN-738, Metallurgical and Materials Transactions A, vol. 8, pp. 1697-1707.
78. Jackson 1060 °C, A-B-C Phase Diagram, ASM Alloy Phase Diagrams Database, P. Villars, editor-in-chief; H. Okamoto and K. Cenzual, section editors; http://www1.asminternational.org/AsmEnterprise/APD, ASM International, Materials Park, OH, 2006.
79. Kang N.L., Protective coatings for gas turbines, Cleveland State University, NASA Glenn Research Center Cleveland,

http://www.netl.doe.gov/technologies/coalpower/turbines/refshelf/handbook/4.4.2.pdf, visited on 17/10/10.

80. Jarvis E. A. and Carter E. A. (2002), The role of reactive elements in thermal barrier coatings, Princeton University, www.princeton.edu/mae/people/faculty/carter/ecdocs/EAC-121.pdf

81. Jiang S. M., Xu C. Z., Li H. Q., Liu S. C., Gong J., Sun C. (2010), Preparation and oxidation behaviour of an AlSiY diffusion coating on a Ni-based single crystal superalloy, Corrosion Science, vol. 52, pp. 435–440.

82. Jianqiang L., Tang Y. L., Shen N. and Pan W. (2001), Effects of solidification kinetics on phase selection of Ni–Al alloys, Journal of Alloys and Compounds, vol. 329, pp. 157-161.

83. Kainuma R. (1996), Isothermal section of Ni-Co-Al at 1100 ˚C, in ASM-alloy phase diagram database.

84. Karadge M., Zhao X., Preuss M., Xiao P. (2005), Microtexture of the thermally grown alumina in commercial thermal barrier coatings, Scripta Materialia, vol. 54, issue 4, pp. 639-644.

85. Kedward E.C. (1969), Electrodeposited composite coatings for tribological applications, Metallurgia, vol. 79, p. 225.

86. Keienburg K. H., Esser W., Deblon B. (1985), Refurbishing procedures for blades of large stationary gas turbines, Material Science Technology, vol. 1, pp. 620-628.

87. Khanna A. S. (2002), Introduction to High Temperature Oxidation and Corrosion, ASM International.

88. Khanna A. S., Wasserfuuhr C., Quadakkers W. J., Nickel H. (1989), Addition of yttrium, cerium and hafnium to combat the deleterious effect of sulphur impurity during oxidation of an NiCrAl alloy, Mater. Sci. Eng. A., vol. 120-121, pp. 185-191.

89. Kingery W. D., Bowen H. K., Uhlmann D. R. (1976), Introduction to Ceramics, 2nd edition, John Wiley and Sons, New York.

90. Krämer S., Yang J., Levi C.G. and Curtis A. J. (2006), Thermochemical Interaction of Thermal Barrier Coatings with Molten CaO–MgO–Al2O3–SiO2 (CMAS) Deposits, Journal of the American Ceramic Society, issue 10, vol. 89, pp. 3167-3175 .

91. Krämer S., Faulhaber S., Chambers M., Clarke D.R., Levi C.G., Hutchinson J.W., Evans A.G. (2008), Mechanisms of cracking and delamination within thick thermal

barrier systems in aero-engines subject to calcium-magnesium alumino-silicate (CMAS) penetration, Materials Science and Engineering, vol. 490, pp. 26–35.

92. Kuenzly J.D. and Douglass D.L. (1974), The oxidation mechanism of Ni3Al containing yttrium, Oxidation of Metals, vol. 8, pp. 139–178.
93. Lee J. H. and Verhoeven J. D. (1994 (a)), Metastable Eutectic Formation In Ni- Al Alloys, Journal of Phase Equilibria, vol. 15 (2), pp. 136-146.
94. Lee J. H. and Verhoeven J. D. (1994 (b)), Eutectic formation in the Ni-Al system Journal of Phase Equilibria, vol. 143, pp. 86-102.
95. Lee J. H. and Verhoeven J. D. (1994 (c)), Peritectic formation in the Ni-Al systemJournal of Phase Equilibria, vol. 144, pp. 353-366.
96. Levi C. G., Sommer E., Terry S. G., Catanoiu A, Ruhle M (2003), Alumina Grown during Deposition of Thermal Barrier Coatings on NiCrAlY, Journal of Ceramic Society, vol. 86, pp. 676-85.
97. Levi C.G. (2004), Emerging materials and processes for thermal barrier systems, Current opinion in solid state and materials science, vol. 8, pp. 77–91.
98. Levi C. G., Hutchinson J. W., Vidal-Sétif M. H., Johnson C. A. (2012), Environmental degradation of thermal barrier coatings by molten deposits, Materials Research Society, vol. 37, pp. 932-940.
99. Levitin V. (2006), High Temperature Strain of Metals and Alloys: Physical
100. Fundamentals, Wiley-VCH.
101. Li Y., Li C-J., Zhang Q, Yang G-J, Li C-X (2010), Influence of TGO Composition
102. the Thermal Shock Lifetime of Thermal Barrier Coatings with Cold-sprayed MCrAlY Bond Coat, Journal of Thermal Spray Tachnology, vol. 19, pp. 168-177.
103. Li M. H., Zhang Z. Y., Sun X. F., Li J. G., Yin F. S., Hu W. Y., Guan H. R., Hu Z. Q. (2003), Oxidation behavior of sputter-deposited NiCrAlY coating, Surface and Coatings Technology, vol. 165, pp. 241-24.
104. Li H., Hesnawi A., Fan X., Gong S. And Xu H. (2006), Inter-diffusion and oxidation behaviour in electron-beam evaporated NiAl coatings, vol. 81, pp. 329-337.
105. Lima C.R.C. and Guilemany J. M. (2007), Adhesion improvements of Thermal Barrier Coatings with HVOF thermally sprayed bond coats, Surface Coatings and Technology, vol 201, pp. 4694- 4701.

106. Lipkin D. M., Clarke D. R., Hollatz M., Bobeth M. and Pompe W. (1997), Stress development in alumina scales formed upon oxidation of (111) NiAl single crystals, Corrosion Science, vol. 39, pp. 231-242.
107. McGaw M.A., Kalluri S., Bressers J. and Peteves S.D. (2003), Thermomechanical fatigue behaviour of materials, ASTM standards international, vol. 4.
108. McNallan Michae (2000), High Temperature Corrosion and Materials Chemistry: Proceedings of the Per Kofstad Memorial Symposium, The Electrochemical Society, p. 220.
109. Menon E. S. K, Mendiratta M. G., Dimiduk D. M (2001), Hight temperature oxidation mechanisms in Nb-silicide bearing multicomponent alloys, Materials Science Forum, vol. 475-479, pp. 717-720.
110. Monceau D., Oquab D., Estournes C., Selezneff S., Thebault Y., Cadoret Y. (2009), Pt-modified Ni aluminides, MCrAlY-base multilayer coatings and TBC systems fabricated by Spark Plasma Sintering for the protection of Ni-base superalloys, Surface & Coatings Technology, vol. 204, pp. 771–778.
111. Mumm D.R., Evans A.G., Spitsberg I.T. (2001), Characterization of a cyclic displacement instability for a thermally grown oxide in a thermal barrier system, Acta Materialia, vol. 49, issue 12, pp. 2329–2340.
112. Musil J., Alaya M., Oberacker R. (1997), Plasma-Sprayed Duplex and Graded Partially Stabilized Zirconia Thermal Barrier Coatings: Deposition Process and Properties, Journal of Thermal Spray Technology, vol. 6(4), pp. 449-455.
113. Nakagawa Tsubasa, Sakaguchi Isao, Shibata Naoya, Matsunaga Katsuyuki, Mizoguchi Teruyasu, Yamamoto Takahisa, Haneda Hajime, Ikuhara Yuichi (2007), Yttrium doping effect on oxygen grain boundary diffusion in α-Al2O3, Acta Materialia, vol. 55, p. 6627-6633.
114. Narita T., Thosin K.Z., Fengqun L., Hayashi S., Murakami H., Gleeson B., Young D. (2005), Development of Re-based diffusion barrier coatings on nickel based superalloys, Materials and Corrosion, vol. 56, issue 12, pp. 923 – 929.
115. Naumenko D., Shemet V., Singheiser L., Quadakkers W. J. (2009), Failure mechanisms of thermal barrier coatings on MCrAlY-type bondcoats associated with the formation of the thermally grown oxide, Journal of Materials Science, vol. 44, pp. 1687-1703.

116. Nicholls J. R., Hancock P., Al Yasiri L. H. (1989), Optimising oxidation resistance of MCrAl coating systems using vapour phase alloy design, Materials Science and Technology, vol. 5, pp. 799-805(7).
117. Nicholls J. R. (2000), Designing Oxidation-Resistant Coatings, JOM, vol. 52, issue 1, pp. 1.
118. Nicholls J. R. (2003), Advances in coating design for high performance gas turbines, MRS bulletin [0883-7694], vol.28, issue 9, pp. 659.
119. Nicholls J. R., Simms N. J., Chan W. Y., Evans H. E. (2002), Smart Overlay Coatings – Concept and Practice, Surface and Coatings Technology, vol. 149, issues 2-3, pp. 236-244.
120. Noebe R. D., Bowman R. R., Nathal M. V. (1993), Physical and mechanical properties of the B2 compound NiAl, Int. Mater. Rev., vol. 38, 193-233.
121. Noebe R. D., Gibala R. (1995), The effect of surface oxide films on the mechanical behaviour of NiAl, Mat. Res. Soc. Symp. Proc., vol. 39, pp. 319-326.
122. Oforka 1150 °C, A-B-C Phase Diagram, ASM Alloy Phase Diagrams Database, P. Villars, editor-in-chief; H. Okamoto and K. Cenzual, section editors; http://www1.asminternational.org/AsmEnterprise/APD, ASM International, Materials Park, OH, 2006.
123. Oxx G. D. (1995), referenced in Noebe R. D., Gibala R. (1995), The effect of surface oxide films on the mechanical behaviour of NiAl, Mat. Res. Soc. Symp. Proc., vol. 39, pp. 319-326.
124. Padture N.P., Gell M., Jordan E. H. (2002), Thermal Barrier Coatings for Gas-Turbine Engine Applications, Science, vol. 296, pp. 280-284.
125. Paladino A. E., Kingery W. D. (1962), Aluminum ion diffusion in aluminium oxide, J Chem. Phys., vol. 37, pp. 957-962.
126. Perez E., Patterson T. and Sohn Y. (2006), Interdiffusion analysis for NiAl versus superalloys diffusion couples, Journal of Phase Equilibria and Diffusion, vol. 27, pp. 659-664.
127. Perez E., Patterson T. and Sohn Y. (2005), Superalloy dependent stability of β-NiAl phase in NiCoCrAlY coatings, http://www.ctcms.nist.gov/~cecamp/NIST%20Sp05%20Diffusion%20copy.pdf, visited on 22/10/10.
128. Perkins R. A., Chiang K. T., Meier G. H. (1987), Effect of alloying, rapid solidification, and surface kinetics on the high temperature environmental

resistance on niobium, Technical rept. Nov 1985-Jan 1989, Accession Number : ADA209934.

129. Perkins R. A., Chiang K. T., Meier G. H., Miller R. (1989), Formation of alumina on niobium and titanium alloys, Oxidation of high temperature intermetallics, pp. 157-169, Ref. Number 21070392, Publ. Year1988, INIS vol. 21, INIS Issue18.

130. Pettit F. S. (1967), Oxidation Mechanisms for Ni-Al Alloys at Temperatures Between 900 and 1300 C, Trans. Met Soc AIME, vol. 239, pp. 1296.

131. Pichoir R. (1978), Aluminide coatings on nickel or cobalt-base superalloys in high temperature alloys for gas turbines, American Journal of Applied Sciences, p.191, http://www.thomas-sourmail.org/coatings/aluminides.html, visited on 22/10/10.

132. Pichoir R. and Hauser JM. (1980), Current status of coatings for high temperature applications in environmental degradation of high temperature materials, Spring Residential Conference, Institute of Metallurgists, vol. 1, p. 6/1 6/21.

133. Pint B. A., Jain A., Hobbs L. W. (1991), The Effect of Ion-Implanted Elements on the θ to α Phase Transformation of Al2O3 Scales Grown on β-NiAl, Mat. Res. Soc., Symp Proc, vol. 288, pp. 981-986.

134. Pint B. A., Martin J. R. and Hobbs L. W. (1993), SIMS characterization of the growth mechanism of doped and undoped α-Al2O3, Oxidation of Metals, vol. 39, pp. 167-195.

135. Pint B. A., Hobbs L. W. (1994), Limitations on the Use of Ion Implantation for the Study of the Reactive Element Effect in β - NiAl, Oxid. Met., vol. 41, pp. 203-233.

136. Pint B. A., Treska M., Hobbs L. W. (1996), The effect of various oxide dispersions on the phase composition and morphology of Al2O3 scales grown on β-NiAl, Oxid. Met., vol. 47, pp. 1-20.

137. Pint B. A., Treska M. and Hobbs L. (1997), The effect of various oxide dispersions on the phase composition and morphology of Al2O3 scales grown on β-NiAl, Oxidation of Metals, vol. 47, pp.1-20.

138. Pint B.A., Wright I. G., Lee W. Y., Zhang Y., Prüßner, Alexander K. B., (1998), Substrate and bond coat compositions: factors affecting alumina scale adhesion, Materials Science and Engineering A, vol. 245, pp. 201–211.

139. Pint B. A. (1998), The Oxidation Behavior of Oxide-Dispersed β-NiAl: I. Short-Term Performance at 1200°C, Oxid. Met., vol. 49, pp.531-559.

140. Pint B. A., Alexander K. B. (1998), Grain Boundary Segregation of Cation Dopants in α-Al2O3 Scales, J. Electrochem. Soc., vol. 145, pp. 1819-1829.

141. Pint B. A., Haynes J. A., More K. L., Wright I. G., Leyens C. (2000), Compositional Effects on Aluminide Oxidation Performance: Objectives for Improved Bond Coats," in Pollock T. M. , Kissinger R. D., Bowman R. R., Green K. A., McLean M., Olson S. and Shirra J. J., Superalloys 2000, TMS, pp. 629-38.

142. Pint B. A., More K. L. and Wright I. G. (2003), Effect of quaternary additions on the oxidation behavior of Hf-doped NiAl, Oxidation of Metals, vol. 59, pp. 257-283.

143. Pint B. A., Haynes J. A., and Besmann T. M. (2010) ,Effect of Hf and Y alloy additions on aluminide coating performance, Surface and Coating Technology, vol. 204, pp. 3287-3293.

144. Pochet L. F. (1996), Factors Influencing the Formation of Single Phase Platinum Aluminide Coatings in Proceeding of the 13th International Conference of Chemical Vapour Deposition, editors Bessman T. M., Allendorf M. D.,. Robinson McD, Ulrich R K, published by the Electrochemical Society 1996.

145. Pomeroy M.J. (2005), Coatings for gas turbine materials and long term stability issues, Materials and Design 26, pp. 223–231.

146. Povarova K.B., Kazanskaya N. K., Drozdov A. A., Morozov A. E. (2007), Physicochemical laws of the interaction of nickel aluminides with alloying elements: II. Interaction of nickel aluminides with alloying elements and/or interstitial phases, Russian Metallurgy (Metally), vol. 2007, pp. 380-386.

147. Prescott R. and Graham M. J. (1992), The formation of aluminium oxide scales on high-temperature alloys, Oxidation of Metals, vol. 38, pp. 233-254.

148. Prescott R., Mitchell D. F., Graham M. J. and Doychak J. (1995), Oxidation mechanisms of β-NiAl + Zr determined by SIMS, Corrosion Science, vol. 37, pp. 1341-1364.

149. Prussner K., Schumann E., Ruhle M. (1997), Oxidation of S-doped β-NiAl in H2/H2O and in air, in Proceedings Electrochemical Society, vol. 96, Fundamental aspects of high temperature corrosion, eds D A Shores, R A Rapp, P Y Hou, Electrochemical Society, Pennington, PA, pp. 344-351.

150. Protopopescu H. M. (1991), Isothermal section of Ni-Co-Al at 25 ˚C, in ASM-alloy phase diagram database.

151. Quadakkers W. J., Elschner A., Speier W., Nickel H. (1991), Composition and growth mechanisms of alumina scales on FeCrAl-based alloys determined by SNMS, Appl. Surf. Sci., vol. 52, pp. 271-287.

152. Reddy K. P. R., Cooper A. R. (1982), Oxygen Diffusion in Sapphire, J. Am. Ceram. Soc., vol.65, pp. 634-638.
153. Reed R.C. (2008), The Superalloys: Fundamentals and Applications, Cambridge University Press.
154. Rhines F. N. and Wolf J. S. (1970), The role of oxide microstructure and growth stresses in the high-temperature scaling of nickel, Metallurgical Transactions, vol. 1, pp. 1701-1710.
155. Rhys-Jones T.N. (1989), Coatings for blades and vane applications in gas turbine. Corrosion Science, vol. 29, pp. 623–646.
156. Rogl P., in: Petzow G., Effenberg G. (Eds.) (1991), Ternary Alloys, Wiley-VCH, Weinheim, vol. 4, pp. 400–415.
157. Russo L. and Dorfman M. (2003), High-Temperature Oxidation of MCrAlY Coatings Produced by HVOF, Proc. Int. Thermal Spray Conference, ed. A. Ohmori (Japan: High Temperature Society of Japan), pp. 1179–1194.
158. Rybicki G. C. and Smialek J. L. (1989), Effect of θ-α-Al2O3 transformation on the oxidation behaviour of β-NiAl + Zr, Oxidation of Metals, vol. 31, pp. 275-304.
159. Sartwell B.D. (2012), Papers Presented at the Combined 17th International Conference on Metallurgical Coatings and 8th International Conference on Thin Films, San Diego, CA, U.S.A., April 2-6, 1990, Elsevier, p.453.
160. Schumann E., Ruhle M. (1994), Microstructural observations on the oxidation of γ′-Ni3Al at high oxygen partial pressure, Acta Metal. Mater., vol. 42, pp. 1481-1487.
161. Schumann E., Ynag J. C., Graham M. J. and Ruhle M. (1996), The effect of Y and Zr on the oxidation of NiAl, Materials and Corrosion, vol. 47, pp. 631-632.
162. Schütze M. (1997), Protective oxide scales and their breakdown, Wiley-VCH.
163. Schütze M. (2000), Corrosion and Environmental Degradation, vol. 2, Wiley-VCH.
164. Schütze M. I., Cahn R. W., Haasen P., Kramer E.J. (2000), Material science and technology: corrosion and environmental degradation, vol. I. Weinheim, Germany: Wiley-VCH, pp. 83.
165. Schramm J. (1941), The binary Nickel-NiAl subsystem, Z. Metallkd., vol. 33 (10), pp. 347-55.
166. Scrivani A. S., Bardi U., Carrafiello C., Lavacchi A., Niccolai F., Rizz G (2003), A comperative study of high velocity oxygen fuel, vacuum plasma spray, and axial

plasma spray for the deposition of CoNiCrAlY bond coat alloy, Journal of Thermal Spray Technology, issue 4, vol.12, pp. 504-507.

167. Shirvani K., Saremi M., Nishikata A., Tsuru T. (2004), The effect of silicon on cyclic oxidation behavior of aluminide coatings on superalloy IN-738LC, Material Science Forum, pp. 335–342.

168. Sims C. T., Stoloff N.S., Hagel W. C. (1987 , 1992 again), Superalloys II: High Temperature Materials for Aerospace and Industrial Power, Materials and Manufacturing Processes A Wiley-Interscience Publication John Wiley & Sons, vol. 7, issue 3, pp. 463-468.

169. Singleton M. F., Murray J. L. and Nash P. (1986), Binary Alloy Phase Diagrams: Al-Ni, ASM, Metals Park, OH, pp.140-142.

170. Smialek J. L. (1978), Oxide Morphology and Spalling Model for NiAl, Metall. Mater. Trans. A, vol. 9A, pp. 309–320.

171. Smialek J. L., Gibala R. (1983), Structure of transient oxides formed on NiCrAl alloys, Metall. Trans. A, 14A, pp. 2143-2161.

172. Smialek J.L., Jayne D.T., Schaeffer J.C., Murphy W.H. (1994), Effects of hydrogen annealing, sulfur segregation and diffusion on the cyclic oxidation resistance of superalloys: a review, Thin Solid Films, vol. 253, pp. 285-292.

173. Smeggil J.L. (1987), Some comments on the role of yttrium in protective oxide scale adherence, Materials Science and Engineering, vol. 87, pp. 261-265.

174. Smialek J. L., Lowell C. E. (1974), Effects of Diffusion on Aluminum Depletion and Degradation of NiAl Coatings, Journal of the electrochemical society, vol. 121, pp. 800-805.

175. Spitsberg I., Moreb K. (2005), Effect of thermally grown oxide (TGO) microstructure on the durability of TBCs with PtNiAl diffusion bond coats, Materials Science and Engineering A., vol. 417, issue 1-2, pp. 322-333.

176. Spitsberg I.T., Mumm D.R., Evans A.G. (2005), On the failure mechanisms of thermal barrier coatings with diffusion aluminide bond coatings, Materials Science and Engineering A, vol. 394, issues 1-2, pp. 176-191.

177. Stiller Krystyna, Pt modified aluminide diffusion coatings for Ni-based superalloys, Experimental Physics, Chalmers Industrial partners: Volvo Aero Corporation, Demag Delaval Industrial Turbomachinery AB, http://www.htc.chalmers.se/projects/project3.htm, visited on 19/10/10.

178. Stringer J. (1986), High-temperature corrosion of superalloys, Materials Science and Technology, vol. 7, pp. 482-493.
179. Stringer J., Hou P. Y. (1986), The effect of surface-applied reactive metal oxides on the high temperature oxidation of alloys in Proceedings Symp. Corrosion and Particle Erosions at High Temperatures, eds V Srinivasan, K Vedula, TMS, Warrendale, pp. 383-401.
180. Stöver Detlev (2007), Advanced Thermal Barrier Coatings (TBC), New TBC concepts, IEF-1: Materials Synthesis and processing, Institute of Energy Research (IEF), http://www.fz-juelich.de/ief/ief-1/datapool/page/109/TBC-Flyer2007.pdf,visited on 29/09/2010.
181. Strangman E.T. (1985), Thermal barrier coatings for turbine airfoils, Thin solid films, vol.127, issues 1-2, pp. 93-106.
182. Stringer J. (1987), Role of coatings in energy producing systems: an overview, Material Science Engineering, vol. 87, pp. 1–10.
183. Surface Modification Systems INC, http://www.surfacemodificationsystems.com/lowpressureplasmaspray.htm, visited on 30/09/2010.
184. Tang F., Ajdelsztajn L., Kim G. E., Provenzano V., Schoenung J. M. (2004), Effects of surface oxidation during HVOF processing on the primary stage oxidation of a CoNiCrAlY coating, Surface and Coating Technology, vol. 185, pp.228-233.
185. Tawancy H. M. (1996), High-temperature oxidation behavior of a wrought Ni-Cr-W-Mn-Si-La alloy, Oxid. Met., vol. 45, pp. 323-348.
186. Trivedi R. (1995), Metall. Mater. Trans. A., vol. 26A, pp.1583-1590.
187. Toscano J., Vaßen R., Gil A., Subanovic M., Naumenko D. and Singheiser L., Quadakkers W.J. (2006), Parameters Affecting TGO Growth and Adherence on McrAlY-Bond Coats for TBC's, Surface and Coatings Technology, vol. 201, issue 7, pp. 3906-3910.
188. Tsakiropoulos P. (2010), Private Communication, University of Sheffield.
189. TSET-advanced equipment refurbishment services, http://www.tosohset.com/, visited on 30/09/2010.
190. Unocic K. A. and Pint B. A. (2010), Characterization of alumina scale formed in a commercial MCrAlYHfSi coating, Surface and Coating Technology, vol. 205, issue 5, pp. 1178-1182.

191. Vande Put Aurélie, Lafont Marie-Christine, Oquab Djar, Raffaitin Aymeric, Monceau Daniel (2010), Effect of modification by Pt and manufacturing processes on the microstructure of two NiCoCrAlYTa bond coatings intended for thermal barrier system applications, Surface and Coatings Technology, vol. 205, pp. 717-727.

192. Vargas J.R., Ulion N.E., Gobel J.A. (1980), Advanced coating development for industrial/utility gas turbine engines, Thin Solid Films, vol. 73, pp. 407–413.

193. Veal B. W., Paulikas A. P., Gleeson B., Hou P. Y. (2007), Creep in α-Al2O3 thermally grown on β-NiAl and NiAlPt alloys, Surf. Coat. Techn., vol. 202, pp. 608-612.

194. Veal B. W., Paulikas A. P. (2008), Growth strains and creep in thermally grown alumina: Oxide growth mechanisms, J. Appl. Phys., vol. 104.

195. Verhoeven J. D., Lee J. H., Laabs F. C. and Jones L. L. (1991), Journal of Phase Equilibria, vol. 12 (1), pp.15-23.

196. Vidhu (2006), Thermal barrier coatings for power plant gas turbine and aircraft engines, private communication P.Tsakiropoulos.

197. Viswanathan R. (2001), An investigation of blade failures in combustion turbines, Engineering Failure Analysis, vol. 8, pp. 493–511.

198. Wagner C. (1933), Z. Phys. Chem., vol. B21, pp. 25.

199. Wallwork G. R. and Hed A. Z. (1970), Some limiting factors in the use of alloys at high temperatures, Oxidation of Metals, vol. 3, pp. 171-184.

200. Wang Q.M., Wu Y.N., Ke P.L., Cao H.T., Gong J., Sun C., Wen L.S. (2004), Hot corrosion behavior of AIP NiCoCrAlY(SiB) coatings on nickel base superalloys, Surface and Coating Technology, vol. 186, pp. 389–397.

201. Whittle D.P., Stringer J. (1980), Improvements in High Temperature Oxidation Resistance by Additions of Reactive Elements or Oxide Dispersions, Philosophical Transactions Royal Society of London, vol. 295, no. 1413, pp. 309–329.

202. Wright P. K. and Evans A. G. (1999), Mechanisms governing the performance of thermal barrier coatings, Solid state and Materials Science, vol. 4, pp. 255-265.

203. Wolfe E. D. and Singh J. (2000), Titanium carbide coatings deposited by reactive ion beam-assisted, electron beam–physical vapour deposition, Surface and Coatings Technology, vol. 124, issues 2-3, pp. 142-153.

204. Woodford D. A. (2006), Gas phase embrittlement and time dependent cracking of nickel based superalloys, Energy Materials: Materials Science and Engineering for Energy Systems, vol. 1, pp. 59-79.
205. Wright I.G. and Pint B.A. (2005), Bond coating issues in thermal barrier coatings for industrial gas turbines, Journal of Power and Energy A, vol. 219, pp. 101-107.
206. www.h2-igcc.eu/ last visited on 07/08/2013.
207. www.fz-juelich.de/ last visited on 07/08/2013.
208. Xu G. H., Wang G. F. and Zhang K. F. (2011), Effect of rare earth Y on oxidation behaviour of NiAl-Al2O3, Trans. Nonferrous Met. Soc. China, vol. 21, pp. 362-368.
209. Yang J. C., Nadarzinski K., Schumann E., Ruhle M. (1995), Electron microscopy studies of NiAl/γ-Al_2O_3 interfaces, Scripta Metall., vol. 33, pp. 1043-1048.
210. Yang J. C., Schumann E., Levin I., Ruhle M. (1998), Transient oxidation of NiAl, Acta Mater., vol. 46, pp.2195-2201.
211. Yang S, Wang F. and Wu W. (2001), Effect of microcrystallization on the cyclic oxidation behaviour of β-NiAl intermetallics at 1000 ˚C in air, Intermetallics, vol. 9, pp. 741-744.
212. Yu Z., Hass D.D., Wadley H.N.G. (2004), NiAl bond coats made by a directed vapour deposition approach, Materials Science and Engineering A, vol. 394, issues 1-2, pp. 43-52.
213. Zhang L.C. and Heuer A.H. (2005), Microstructural evolution of the nickel platinum–aluminide bond coat on electron-beam physical-vapour deposition thermal-barrier coatings during high-temperature service, Metallurgical and Materials Transactions A, vol. 36, pp. 43-53.
214. Zhang G., Zhang H., and Guo J. (2006), Improvement of cyclic oxidation resistance of a NiAl-based alloy modified by Dy, Surface and Coating Technology, vol. 201, pp. 2270-2275.
215. Zhang Z., Li L., Yang J. C. (2011), γ-Al2O3 thin film formation via oxidation of β-NiAl(1 1 0), Acta Materialia, vol. 59, pp. 5905-5916.
216. Zhang Z, Gleeson B., Jung K., Li L. and Yang J. C. (2012), A diffusion analysis of transient subsurface γ'-Ni3Al formation during β-NiAl oxidation, Acta Materialia, vol. 60, pp. 5273-5283.
217. Zhang Zhongfan, Gleeson Brian, Jung Keeyoung, Li Long, Yang Judith C (2012), Acta Materialia, vol. 60, pp. 5273-5283.

218. Zhong D., Moore J. J., Ohno T. R., Disam J., Thield S., Dahan I. (2000), Deposition and characterization of NiAl and Ni–Al–N thin films from a NiAl compound target, Surface and Coatings Technology, vol. 130, pp. 33-38.

219. Zhou Z, Guo H, Abbas M. And Gong S. (2011), Effect of water vapor on the phase transformation of alumina grown on NiAl at 950 ˚C, Corrosion Science, vol. 53, pp. 2943-2947.